Jennifer M. Collins · Kevin Walsh *Editors*

Hurricanes and Climate Change

Volume 3

Aegean
Conferences

Springer

Hurricanes and Climate Change

Jennifer M. Collins • Kevin Walsh
Editors

Hurricanes and Climate Change

Volume 3

Aegean
Conferences

Springer

Editors
Jennifer M. Collins
School of Geosciences
University of South Florida
Tampa, FL, USA

Kevin Walsh
School of Earth Sciences
The University of Melbourne
Parkville, VIC, Australia

Preface

This book was inspired by the 5th International Summit on Hurricanes and Climate Change, held in Chania, Greece, in June 2015. This ongoing series of conferences brings together leading experts from around the world to discuss work on the relationship between hurricanes, climate, and the assessment of hurricane risk. Hurricanes are among nature's most powerful and destructive phenomena. They have captured the interest of atmospheric researchers for more than 75 years, as before satellite observations became routinely available, they often struck with little or no warning. Tropical cyclones cause physical and economic disruption not only to societies in the tropics and subtropics but to the mid-latitude regions as well. Their destructive power comes not only from high winds and heavy rains but from storm surge and the potential to spawn tornadoes as they make landfall. The impacts of tropical cyclones fall most heavily on less developed nations, but developed nations have also suffered extreme hardship.

Early research established an understanding of the climatological and dynamic character of tropical cyclones, as well as their evolution and lifecycle. These advances led to an increase in forecast skill. The development of technologies, such as radar and satellite techniques, along with better monitoring methods, has led to a reduction in error for track and intensity forecasts. Additionally, studies have examined changes and variability in the occurrence of tropical cyclones. By understanding the interannual and interdecadal variability in tropical cyclone occurrence, societies can be better prepared and can position resources better for aiding impacted areas.

Today we understand that there is an intimate relationship and cooperation between atmospheric and oceanic conditions and processes leading to the development of tropical cyclones. Changes in climate will influence the occurrence and intensity of tropical cyclones in the future, even though the nature of these changes is not yet entirely clear. This book is comprised of ten chapters that present cutting-edge research which attempts to answer outstanding questions that remain in our understanding of tropical cyclones, whether this research endeavors to uncover their historical character, dynamics, societal impacts, and what the future may bring.

The first and second chapters discuss the climatological history of tropical cyclones. The first reviews research from the last decade in the subject of paleotempestology. This field endeavors to piece together the occurrence of tropical cyclones on the timescale of centuries and millennia or the climatological behavior of tropical cyclones before the observational record (about 160 years). These studies find that long-period behavior in the El Niño and Southern Oscillation phenomenon, the North Atlantic Oscillation, and location of the ITCZ are some factors that control periodicity on the century and millennial timescales. This work also reveals that tropical cyclone activity today is not at an historical high level going back to the mid-Holocene. The second chapter focuses on tropical cyclone landfalls along the southeast US coast, and the authors find that the locus of landfalls has shifted about 1° latitude further north. Thus, this study provides critical guidance for policy makers and those whose responsibility includes disaster preparedness.

The dynamic, thermodynamic, and kinematic behavior of tropical cyclones is another topic of wide interest, and Chaps. 3, 4, and 5 explore various aspects of tropical cyclone lifecycles. Chapter 3 examines the relationship between sea surface temperatures and tropical cyclone intensity in the eastern North Pacific, an area that has not been studied as extensively as other tropical cyclone basins. Using statistical methods, the authors find generally that sea surface temperatures exert a greater influence on tropical cyclone intensity than in other basins, in particular when compared with the North Atlantic.

The next chapter reviews both in situ and remote sensing methods that have been developed for estimating tropical cyclone winds. Better estimates will lead to better forecasts, which is of benefit to societies exposed to tropical cyclone risks. The authors note that each method has their strengths and weaknesses, but the use of different methodologies could, for example, lead to differing conclusions about trends in tropical storm intensity. They recommend the continued improvement of satellite-based techniques in order to improve the current state of the art.

The fifth study examines a new concept impacting tropical cyclone genesis over land called the "Brown Ocean." In recent years, there have been a few notable cases of tropical cyclones intensifying over land. Conventional wisdom holds that these storms should decay once over land. However, if enough surface moisture is present, then tropical cyclones can actually strengthen over land if the latent heat flux is sufficient.

The techniques of risk management have become increasingly important in tropical cyclone studies, and the next chapter proposes a novel statistical analysis of tropical cyclone risk, both in the Atlantic basin and along the coast of China. The authors conclude that standard methods of risk assessment may underestimate tropical cyclone risk factors such as storm surge and wave height.

The topic of the final four chapters is the ability of models to project aspects of tropical cyclone occurrence on the timescales of decades or longer. Decadal projection of various phenomena in atmospheric science has been a topic of considerable interest in the last 5 years. The first of these chapters studies the use of the next generation general circulation models in assessing tropical cyclone risk in a warmer world. The authors propose that these models, with increased resolution,

will be able to reveal smaller-scale structures in future events, as well as provide the basis for the study of topics such as teleconnectivity between tropical cyclone basins and occurrence-to-landfall rates. The second of these chapters examines multidecadal simulations of tropical cyclone occurrences by basin. However, the authors also discuss the limitations of the models and tracking algorithms, the influence of model physics, and an overview of our current understanding and future direction of tropical cyclone activity research.

Forecasting the frequency of landfalling storms in the Atlantic basin on the seasonal and decadal timescales is the subject of the third modeling chapter. The authors use the UK Met Office's seasonal forecasting algorithm and demonstrate that there is significant skill in some regions due to the strong El Niño and Southern Oscillation signal, but lower skill in other places where this signal is not strong. The Met Office algorithm does produce successful multi-year forecasts of landfalling storms, and the authors point out that their methodology will identify decadal-scale active and inactive regimes for subregions within the Atlantic basin. The final chapter studies future changes in rainfall intensities associated with tropical cyclones, with a focus on landfalling storms. The authors performed a model sensitivity study to examine the relative impact of warmer sea surface temperatures only versus a doubling of atmospheric carbon dioxide concentration only and compare these to a control run. They found that tropical cyclone precipitation is more intense when sea surface temperatures increase. When atmospheric carbon dioxide concentration is doubled, tropical cyclone rainfall actually decreased slightly. Lastly, the study found that rainfall accompanying landfalling tropical cyclones increases and that the greater uplift of moist low-level air forced by landfall plays a significant role in increased vulnerability of coastal regions to tropical cyclone impacts.

Tampa, FL, USA   Jennifer M. Collins
Columbia, MO, USA   Anthony R. Lupo
Melbourne, Australia   Kevin Walsh

Acknowledgments

Contents

Contributors

Theresa Andersen Research Square, Durham, NC, USA

George Arhonditsis Department of Physical and Environmental Sciences, University of Toronto Scarborough, Scarborough, Ontario, Canada

Brian H. Bossak Department of Health and Human Performance, College of Charleston, Charleston, SC, USA

Ken Butler Department of Computer and Mathematical Sciences, University of Toronto Scarborough, Scarborough, Ontario, Canada

Joanne Camp Met Office Hadley Centre, Exeter, UK

Louis-Philippe Caron Earth Science Department, Barcelona Supercomputing Center, Barcelona, Spain

Vincent Cheng Department of Physical and Environmental Sciences, University of Toronto Scarborough, Scarborough, Ontario, Canada

Alison Cobb Imperial College London, London, UK

Jennifer M. Collins School of Geosciences, University of South Florida, Tampa, FL, USA

Liu Defu Ocean University of China, Qingdao, China

James Done National Center for Atmospheric Research, Boulder, CO, USA

Wang Fengqing Ocean University of China, Qingdao, China

Ethan J. Gibney NOAA National Weather Service Forecast Office, San Diego, CA, USA

Samantha Gibson Department of Marine and Ecological Sciences, Florida Gulf Coast University, Fort Myers, FL, USA

William A. Gough Department of Physical and Environmental Sciences, University of Toronto Scarborough, Scarborough, Ontario, Canada

Silvio Gualdi Istituto Nazionale di Geofisica e Vulcanologia, INGV Italy, Centro euro-Mediterraneo sui Cambiamenti Climatici, CMCC, Bologna, Italy

Liu Guilin Ocean University of China, Qingdao, China

Christopher C. Hennon Department of Atmospheric Sciences, University of North Carolina at Asheville, Asheville, NC, USA

Jerry Y. Jien Department of Physical and Environmental Sciences, University of Toronto Scarborough, Scarborough, Ontario, Canada

Han Longzhi Ocean University of China, Qingdao, China

Anthony Lupo Department of Soil, Environmental and Atmospheric Sciences, University of Missouri, Columbia, MO, USA

Joanne Muller Department of Marine and Ecological Sciences, Florida Gulf Coast University, Fort Myers, FL, USA

Antonio Navarra Istituto Nazionale di Geofisica e Vulcanologia, INGV Italy, Centro euro-Mediterraneo sui Cambiamenti Climatici, CMCC, Bologna, Italy

Leilani Paxton School of Geosciences, University of South Florida, Tampa, FL, USA

Kevin A. Reed School of Marine and Atmospheric Sciences, Stony Brook University, Stony Brook, NY, USA

Enrico Scoccimarro Istituto Nazionale di Geofisica e Vulcanologia, INGV Italy, Centro euro-Mediterraneo sui Cambiamenti Climatici, CMCC, Bologna, Italy

Marshall Shepherd Department of Geography, University of Georgia, Athens, GA, USA

Gabriel Vecchi NOAA/Geophysical Fluid Dynamics Laboratory (GFDL), Princeton, NJ, USA

Gabriele Villarini IIHR-Hydroscience & Engineering, The University of Iowa, Iowa City, IA, USA

Kevin Walsh School of Earth Sciences, The University of Melbourne, Parkville, VIC, Australia

Michael F. Wehner Lawrence Berkeley National Laboratory, Berkeley, CA, USA

Mark R. Welford Department of Geology and Geography, Georgia Southern University, Statesboro, GA, USA

Ethan E. Wright Department of Atmospheric Sciences, University of North Carolina at Asheville, Asheville, NC, USA

Colin M. Zarzycki National Center for Atmospheric Research, Boulder, CO, USA

Ming Zhao NOAA/Geophysical Fluid Dynamics Laboratory (GFDL), Princeton, NJ, USA

Chapter 1
Recent Advances in the Emerging Field of Paleotempestology

Joanne Muller, Jennifer M. Collins, Samantha Gibson, and Leilani Paxton

Abstract Roughly 35 % of the world's 7.4 billion people are in the path of tropical cyclones, and coastal populations are expected to increase in the coming century. To understand the future damage that tropical cyclones could impose on an ever-growing coastal population, it is critically important to better understand the relationships between tropical cyclones and climate. Large-scale features of the climate system have been shown to affect tropical cyclone activity, for example, the El Niño Southern Oscillation (ENSO) has been shown to influence tropical cyclone frequency in all oceanic basins on seasonal, yearly, and decadal timescales. However, the relatively short observational record (<160 years) is inadequate for identifying the climatic influences on tropical cyclones over centennial to millennial timescales. Paleotempestology, a relatively new science, helps to resolve this issue by extending the instrumental record back several thousands of years. Over the past two decades, the number of paleotempestology records has increased substantially for sites along the Northwest Atlantic Ocean, Gulf of Mexico and Caribbean Sea, the South Pacific Ocean, and the Northwest Pacific and Indian Ocean regions. The most obvious characteristic of these records is that they reveal extended alternating periods of either greater or lesser tropical cyclone activity over centennial and millennial timescales. In these studies, researchers have shown that large-scale climatic features such as ENSO, sea surface temperatures (SSTs), the latitudinal position of the intertropical convergence zone (ITCZ), and the North Atlantic Oscillation (NAO) are likely driving the alternating long-term behavior of tropical cyclones in global oceanic basins. This review paper will focus on recent paleotempestology studies from multiple global sites and endeavor to synthesize the results and interpretations.

J. Muller (✉) • S. Gibson
Department of Marine and Ecological Sciences, Florida Gulf Coast University, Fort Myers, FL 33965, USA
e-mail: jmuller@fgcu.edu; smgibson0089@eagle.fgcu.edu

J.M. Collins • L. Paxton
School of Geosciences, University of South Florida, Tampa, FL 33620, USA
e-mail: collinsjm@usf.edu; lpaxton@mail.usf.edu

1 Introduction

The North Atlantic Basin provides the longest observational record of tropical cyclone activities spanning the past 160 years (Landsea et al. 2012). Examination of this record reveals significant interannual and interdecadal variability in tropical cyclone activity, which can be related to regional- and global-scale climatic phenomena such as sub-Saharan drought, El Niño Southern Oscillation (ENSO) events, and changes in sea surface temperatures (SSTs) in the Main Development Region (MDR; Gray 1990; Landsea et al. 1996; Elsner and Kara 1999). However, due to the brevity of the historical record, it is impossible to assess whether such variability occurs at longer centennial to millennial timescales. This question can be addressed by means of paleotempestology, a relatively new research field that utilizes geological, biological, and written documentary techniques to study past tropical cyclone activity (Liu and Fearn 1993; Donnelly et al. 2001a; Hippensteel 2011; among others).

Paleotempestology seeks to develop tropical cyclone activities over a large range of timescales, from day-by-day reconstructions to millennial-scale reconstructions. Since the early 1990s significant progress has been made in the field of paleotempestology with new developments in research theory, methodology, and understanding. As a result, paleotempestology has become an important component of quaternary paleoclimatology (Liu 2004; Nott 2004; Fan and Liu 2008) not only in its basic scientific research application but also in its practical application to society. This research has allowed for tropical cyclone return period calculations that extend back beyond the historical record for selected coastal areas, potentially providing empirical data for risk assessments by insurance companies, civil planners, and emergency management officials (Liu 2004).

In 2008, Fan and Liu (2008) published a comprehensive review on the development of paleotempestology proxy techniques, methodologies, and research achievements at the global scale. The review outlined all potential paleotempestology archives and their relevant proxies, in addition to the widely accepted climatic interpretations in the field of paleotempestology in 2008. Since the publication of this review paper, there have been a number of advances in the field. This review chapter presents recent paleotempestology advances that have contributed important information to our understanding of paleotempestology dynamics. We will summarize these studies and their findings in the following pages.

2 Recent Developments in Paleotempestology Proxies

As discussed in Fan and Liu (2008), there are a number of archives that provide information on past tropical cyclone activity. The more commonly used archives include (1) historical documentary records; (2) speleothem, coral-ring, and tree-ring archives; (3) beach ridges and cheniers; and (4) coastal lacustrine, lagoonal, and marsh overwash facies, while less common archives include (5) shallow-marine storm sequences, (6) estuarine storm-related rhythmites, and (7) storm deposits in atoll lagoons and inner reef flats. Since Fan and Liu's review paper publication in 2008, advances in the field are mostly confined to the more commonly used archives outlined above and coastal karst basins, a relatively new type of paleotempestology archive. Therefore, this review chapter will focus on these paleotempestology archives and the climatological interpretations from these recent works. In addition we will provide some information on the potential difficulties facing the field of paleotempestology.

2.1 Historical Documentary Records

Tropical cyclones are often catastrophic disasters to society as they pose hazards to humans such as high winds, heavy rain, storm surge, powerful waves, potential tornadoes, coastal flooding, landslides, etc. These societal impacts are often recorded in historical written records after the beginning of literal history. Documentary records of tropical cyclones are sometimes archived in official histories, gazettes, newspapers, and civilian writings such as travel logbooks, diaries, poems, etc. (Fan and Liu 2008). Since 2008, few studies have been published that utilize historical documentary records. However, in 2016, Trouet et al. used documented Spanish shipwrecks to look at tropical cyclone variability in the Caribbean during the Maunder Minimum (MM; 1645–1715 CE), a period defined by the most severe reduction in solar irradiance in documented history (1610–present). This research utilizes a combined documentary time series of Spanish shipwrecks in the Caribbean (1495–1825 CE) and a tree-growth suppression chronology from the Florida Keys (1707–2009 CE). Trouet et al. (2016) found a 75 % reduction in decadal-scale Caribbean tropical cyclone activity during the MM that also correlates with cool North Atlantic SSTs, El Niño-like conditions, and a negative phase of the North Atlantic Oscillation (NAO). It is suggested that these conditions are primarily modulated by reduced solar irradiance during the MM time period. The study also highlights the need for a better understanding of oceanic and atmospheric responses to radiative forcing in order to improve our future tropical cyclone projection skills.

In 2014 Bossak et al. undertook a study of historic Georgia tropical cyclones. They analyzed the frequency trends, intensity over time, seasonality, zone of formation, time from formation to landfall, and spatial distribution for Georgia's 14 recorded tropical cyclone landfalls in HURDAT2. They noted a declining number

of tropical cyclones, both in Georgia and immediately neighboring coasts, since 1851. In each successive 50-year interval, the frequency of tropical cyclones that make landfall in Northeast Florida, Georgia, and South Carolina has decreased. As of 2017, Welford et al. (this volume, Chap. 2) extended this Georgia record through the examination of temporal and spatial tropical cyclone landfall trends along the Georgia coast from 1750 to 2012. Since 1750, 18 of the 24 recorded tropical cyclones that made landfall along the Georgia coast occurred between 1801 and 1900, yet the tropical cyclone intensities have declined since 1851. This study also demonstrates that the mean location of landfall along the Georgia coast has shifted 60 km north and hence closer to Savannah. Whether this change represents a movement due to anthropogenically enhanced global radiative forcing and Atlantic SSTs or a change in tracks due to NAO forcing or a statistical anomaly is impossible to establish. Certainly, $+$NAO or $-$NAO indices affect the location of the subtropical high and the resultant track of tropical cyclones around the periphery of the high pressure (Welford et al. this volume, Chap. 2).

2.2 Speleothem, Coral-, and Tree-Ring Archives

2.2.1 Speleothems

Tropical cyclones produce large amounts of precipitation with distinctly lower $\delta^{18}O$ values than typical low-latitude thunderstorms. This isotopic signal of tropical cyclones can thus be incorporated into the calcium carbonate of stalagmites in limestone caves, in tropical cyclone prone regions.

In 2008, Frappier published a four-step screening method used to select stalagmites with the goal of developing a proxy record of individual tropical cyclone rainfall events (Frappier 2008). Field and laboratory criteria were combined to develop a process for pre-screening speleothem samples to screen out candidate stalagmites whose characteristics indicated lower sensitivity to storm–water infiltration. The approach was designed to increase the likelihood that selected stalagmites would increase the signal to noise ratio of the target phenomenon in the resulting proxy records. Hallmarks of this approach include (1) establishing a priori scientific targets, (2) applying sample criteria in the form of contraindicators, and (3) organizing the sample screening protocol into a series of practical stages. The overall approach to stalagmite selection presented here supports cave conservation and can be adapted readily by others in support of different scientific goals.

In 2014, Haig et al. published research that used a new tropical cyclone activity index (CAI) which is the average accumulated energy expended over the tropical cyclone season within range of the site, accounting for the number of days since genesis and the intensity and size of the storm relative to its distance from the site at each point along its track. The CAI allows for a direct comparison between the modern instrumental record and long-term paleotempestology (prehistoric tropical cyclone) records derived from the $\delta^{18}O$ of seasonally accreting carbonate layers

of actively growing stalagmites. The CAI showed that the low levels of storm activity which have occurred on the mid west and northeast coasts of Australia are unprecedented over the past 550–1500 years (Fig. 1.1). Their results also revealed a repeated multi-centennial cycle of tropical cyclone activity, the most recent of which commenced around AD 1700. The present cycle includes a sharp decrease in activity after 1960 in Western Australia. This is in contrast to the increasing frequency and destructiveness of Northern Hemisphere tropical cyclones since 1970 in the North Atlantic Ocean and the western North Pacific Ocean (e.g., Emanuel 2005).

2.2.2 Corals

Corals in stormwash deposits have previously been used as an indicator of tropical cyclone activity (Fan and Liu 2008); however, new research is being conducted to determine if corals themselves may be used as a direct proxy. Corals are sensitive to, and can record, the $\delta^{18}O$ values of the waters in which they grow and should thus be able to record the changes in precipitation associated with a tropical cyclone.

In 2011, Kilbourne et al. published a study that investigated the usefulness of coral skeletal $\delta^{18}O$ as a means of reconstructing past tropical cyclone events. Isotopic modeling of rainfall mixing with seawater shows that detecting an isotopic signal from a tropical cyclone in a coral requires a salinity of $\sim$33 psu at the time of coral growth, but this threshold is dependent on the isotopic composition of both fresh and saline end-members. Unfortunately, a comparison between coral $\delta^{18}O$ and historical records of tropical cyclone activity, river discharge, and precipitation from multiple sites in Puerto Rico showed that tropical cyclones are not distinguishable in the coral record from normal rainfall using this approach at these sites.

In 2008, Hetzinger et al. presented a $\delta^{18}O$ record from a brain coral situated in the Atlantic tropical cyclone domain. This record showed equal sensitivity to SST and seawater $\delta^{18}O$ variations, with the latter being strongly linked to precipitation. The authors demonstrate that this coral-based proxy record ($\delta^{18}O$) captures the multidecadal variations associated with the Atlantic Multidecadal Oscillation (AMO) and the tropical cyclone activity (Fig. 1.2) that interestingly exhibits a long-term increase over the last century. This study raises new possibilities in extending the limited AMO observational record using corals and therefore the ability to gain new insights into the mechanisms underlying the AMO and its effects on long-term tropical cyclone variations.

2.2.3 Tree Rings

Tropical cyclones impact trees in a variety of ways, which can then be measured through an analysis of the annual growth bands, $\delta^{18}O$ and $\delta^{13}C$ values within the α-cellulose, and even statistical correlations between the rings and isotopic values. The recognition of tree rings as a valuable proxy for tropical cyclones has increased the need for refinement of the methodologies by which tree cores are extracted and the data are analyzed.
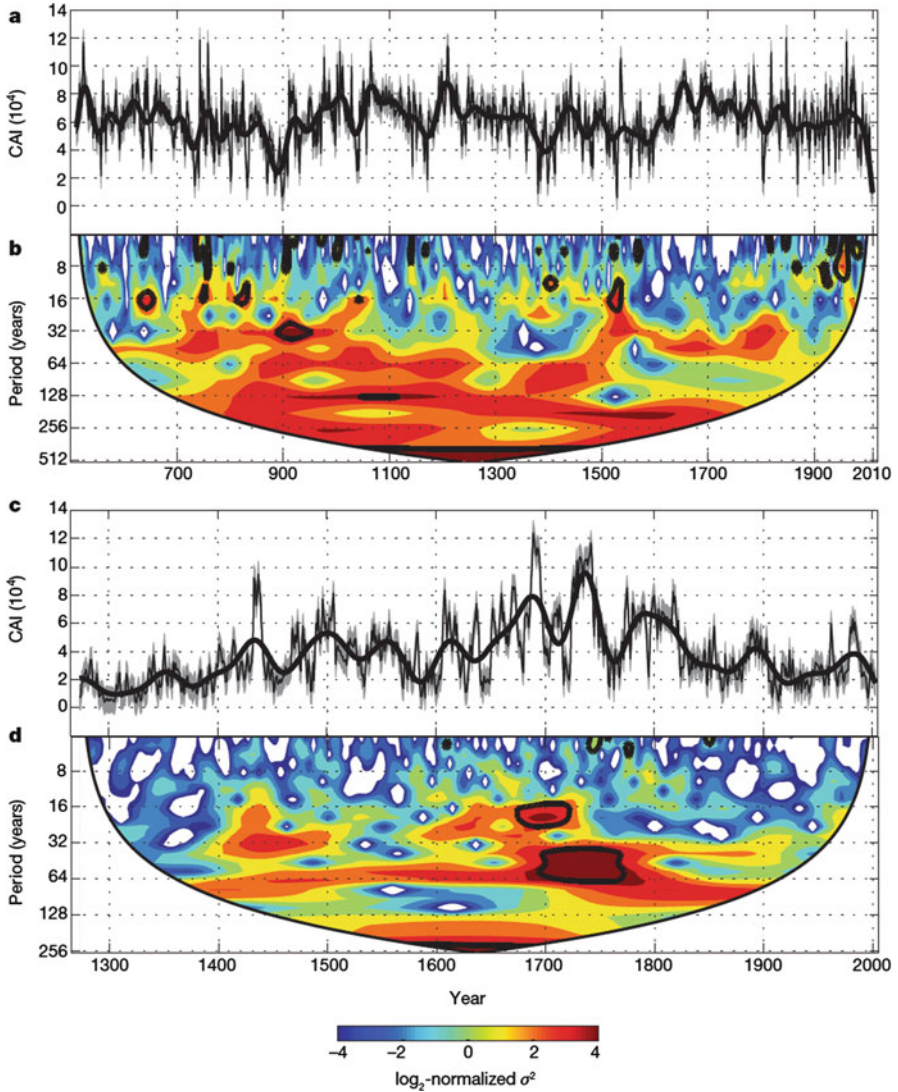
Fig. 1.1 Cyclone activity index (CAI) over the last 1500 and 700 years (Modified from ref. Haig et al. 2014). **a**, **c**, Cape Range (**a**) and Chillagoe (**c**); *black line* indicates smoothing of the series (smoothed data were not used in the statistical analysis). *Gray shading* indicates the r.m.s.e. of the model. **b**, **d**, Wavelet power spectra (Morlet wavelet) of Cape Range (**b**) and Chillagoe (**d**). Power increases from *blue* to *red*, *black* contours indicate regions above the 1 % significance level, and the *white* areas are regions subject to edge effects. The spectra have lag-autocorrelation coefficients of 0.75 (Cape Range) and 0.78 (Chillagoe) (Software provided by C. Torrence and G. Compo (http://atoc.colorado.edu/research/wavelets/))
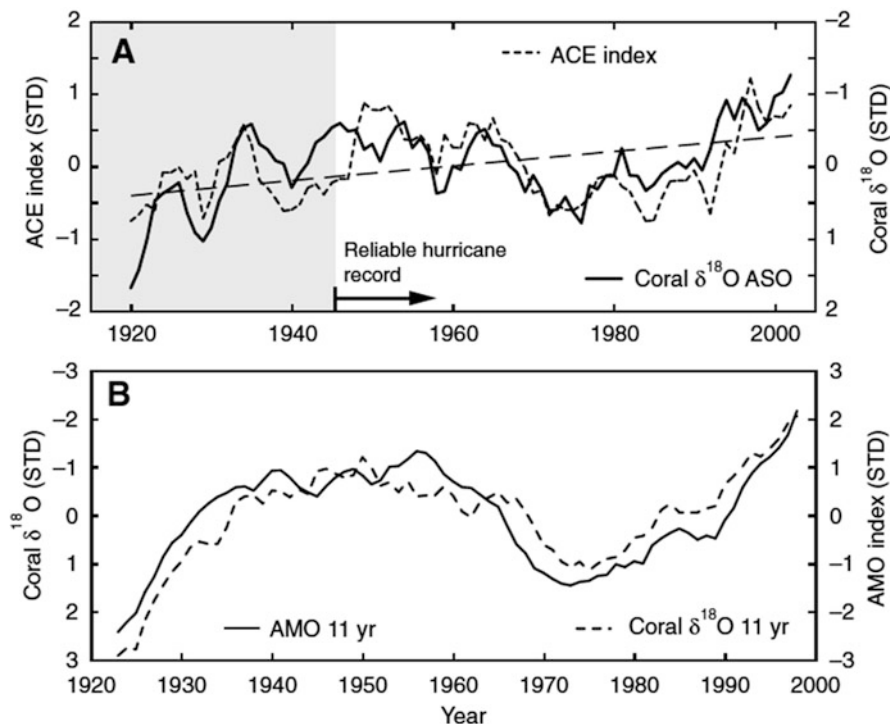
Fig. 1.2 (**a**) Comparison between coral δ^{18}O and the index of accumulated cyclone energy (ACE) for the North Atlantic (Modified from ref. Hetzinger et al. 2008). Data shown are for the peak months of the Atlantic tropical cyclone season, August-September-October (ASO), and were averaged using a 5-year running filter. The correlation is high ($r = -0.66$) and significant at the 1% level, assuming 14 degrees of freedom (1920–2002); $r = -0.52$ for unsmoothed ASO data (not shown), 1918–2004. The correlation is also stable for detrended values ($r = -0.50$ for unsmoothed ASO data and $r = -0.67$ for 5 years means, the same time intervals as above). *Dashed line* represents the upward trend seen in coral δ^{18}O over the 1920–2002 time period. The trend is statistically significant at the 0.1% level, assuming 9 degrees of freedom. (**b**) Comparison between coral δ^{18}O and the AMO index (North Atlantic SST averaged between 0 and 70°N; Enfield et al. 2001). Seasonal mean values were removed from the monthly data before averaging to annual resolution. Then an 11-year running filter was applied. The correlation is high ($r = -0.86$) and statistically significant at the 5% level, even with only four effective degrees of freedom. *AMO* Atlantic Multidecadal Oscillation, *ASO* August-September-October, *STD* standard deviation

Both Li et al. (2011) and Kagawa et al. (2015) have determined ways by which the process of extracting α-cellulose can be hastened without losing, if not gaining, accuracy in the stable isotope analysis. Li et al. (2011) took advantage of the unique ability of tree rings, among other paleotempestite archives, to retain intra-annual climate signals by extracting the α-cellulose directly from the whole wood spline and foregoing both the peeling and grinding methods. Kagawa et al. (2015) increased the versatility of single-batch processing of tree rings through the creation and evaluation of the "cross-section method" whereby they created a prototype

polytetrafluoroethylene (PTFE) case, choosing PTFE due to its nonreactive nature, which could entirely house the tree-ring lath throughout the chemical and drying processes. Freeze-drying the α-cellulose laths showed to be the optimal method of drying with minimum splitting and shrinkage of the α-cellulose and left minimal contamination, and the process then follows standard methods. Both processes provide statistically similar measures in $\delta^{13}C$ and $\delta^{18}O$ integrity; however, the new process presented by Li et al. (2011) and expanded upon by Kagawa et al. (2015) is quicker and more cost-effective which allows for the processing of more samples.

Because dendrochronology relies upon the way that trees respond to their environment, different environments and tree species may pose different kinds of problems when interpreting tree-ring patterns. In 2011, Lewis et al. utilized a multi-tree approach to interpreting tree-ring response to a known climatic driver within a Texas preserve. Through a composite analysis of the $\delta^{18}O$ values, they discovered that sometimes individual trees within a stand would record false positives whereas other times they would not record the storm event at all. By comparing the tree-ring $\delta^{18}O$ values within this study to known climatic trends, Lewis et al. were able to determine that climatic trends such as seasonally uncharacteristic high or low precipitation, drought, and a strong El Niño event could lead to either of these issues. In extending the range of dendrochronological studies, Harley et al. (2011) determined that the South Florida slash pine, the pine species with the southernmost range, is a suitable candidate for tree-ring dating. As a tree species that reliably produces only one growth band per year in a subtropical environment and is most heavily influenced through rainwater, the South Florida slash pine can be used to determine tropical cyclone activity as far south as the Florida Keys. In 2012, Knapp and Hadley also addressed the issue of expanding dendrochronological research but in the Pacific Northwest portion of the United States where high wind events were correlated with extratropical and tropical cyclones. Through this study, Knapp and Hadley were able to provide a 300-year analysis of windstorms within the Pacific Northwest, spanning the time frame between the Little Ice Age and the current climate regime while also identifying the major correlation between the high wind events within the context of the ENSO and non-ENSO phases and the Pacific Decadal Oscillation.

2.3   Beach Ridges

Beach ridges are parallel ridges that form on sandy coastlines and largely consist of coarse sand and shell fragments. Nott and other researchers have found that the cliffy coarse-grained beach ridges in Northeastern, Northern, and Western Australia have been deposited by the wave action usually associated with intense tropical cyclones (Rhodes et al. 1980; Nott et al. 2009; Forsyth et al. 2010; Nott 2011a; Nott and Forsyth 2012). Each ridge in the plain is initially deposited at the rear of the beach. Over time a sequence of ridges develops to form a plain of between 10 and 30 shore parallel ridges. The addition of each new ridge causes the plain to prograde seaward.

The developing ridge at the rear of the beach increases in elevation over time with successive tropical cyclone-generated marine inundation events. Progressively higher marine inundations are required to continue depositing sediment onto the sand ridge as it increases in height (Nott and Forsyth 2012). The ridges generally attain a maximum elevation of 4–6 m above mean sea level. Therefore only the largest marine inundations can deposit sediment onto the crests of ridges at this height; hence, the final sedimentary unit on each ridge crest registers the largest marine inundation responsible for depositing the ridge (Nott and Forsyth 2012). The geology has been supported by meteorological and oceanographic models to determine the origin of a sequence of 29 shore parallel sand beach ridges in Northeastern Australia (Nott et al. 2009). The results suggest that the ridges were constructed by waves and that the final form or height of the ridges is a function of high-energy tropical cyclone-generated waves plus storm tides (Nott and Forsyth 2012).

The beach ridges of sand, shell, and a mixture of sand and shell in Australia show a variable tropical cyclone history throughout the late Holocene. Forsyth et al. (2010) identified two periods of tropical cyclone inactivity between 3380 and 2480 years and between 1440 and 440 CE in a coarse-grained beach ridge sequence near Tully Heads in North Queensland. They also identified periods of activity here between 5000 and 4500 CE and a very active period between 4100 and 3400 CE. At Wonga Beach, several hundred kilometers to the north, Forsyth et al. (2010) recognized a 1200-year period of heightened tropical cyclone activity between 2100 and 900 CE, while prior to this a 1700-year period of tropical cyclone inactivity occurred between 3800 and 2100 CE (Fig. 1.3). Nott (2011a) also identified a 1700-year period of tropical cyclone inactivity between 5400 and 3700 CE from a pure shell beach ridge record at Shark Bay, Western Australia. Nott et al. (2009) identified a 1000-year period of tropical cyclone inactivity between 1820 and 850 years in a sand beach ridge sequence south of Cairns, North Queensland (Fig. 1.3). Nott et al.'s 6000 year-long record of intense tropical cyclones (Nott et al. 2009) implies that extreme tropical cyclones occurred considerably more frequently than that suggested by the short historical record for this region (Fig. 1.3).

On a sidenote, in 2009, Donnelly et al. published an article that addressed the use of beach ridges in sea-level reconstructions. Some authors have argued that the beach ridges along the Gulf of Mexico represent sea-level highstands in the past. They argue that beach ridges cannot be built by storms because storms are typically erosional and the rate of beach ridge formation is considerably slower than the recurrence rate of storms at any one location (Tanner 1995; Morton et al. 2000). This is obviously not the case for beach ridges formed along the NE Australian coast, as discussed by Nott and Forsyth above (Nott and Forsyth 2012). Furthermore, Donnelly argues that for every direct strike many more tropical cyclones would traverse the Gulf of Mexico, significantly increasing the overall wave climate during tropical cyclone seasons and potentially leading to an increase in the frequency of constructional swells (Otvos 1995, 2000). Increases in "fair-weather" swell frequency and height during periods of more tropical cyclone activity in the Gulf of Mexico may provide an alternative explanation for beach ridges developing a few meters above their contemporaneous sea level.
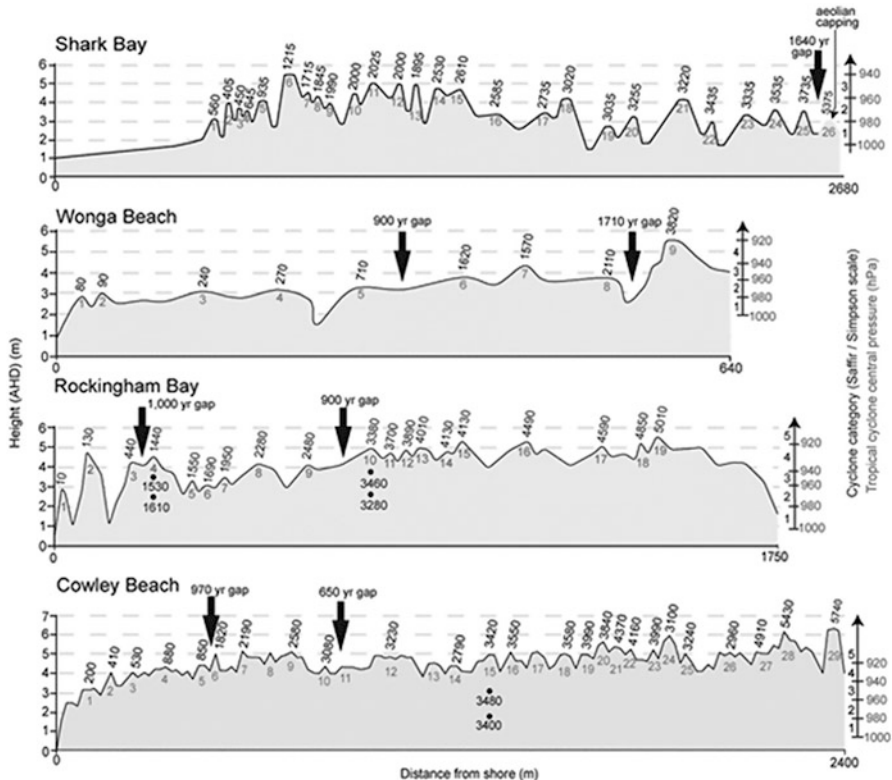
Fig. 1.3 Beach ridge cross-sections and chronologies (Shark Bay is dated using radiocarbon, and remainder using OSL) (Modified from ref. Nott and Forsyth 2012)

2.4 Coastal Lacustrine, Lagoon, and Marsh Overwash Deposits

Most long-term paleotempestological records are created using preserved tropical cyclone overwash signatures. As a tropical cyclone nears the coast, it produces strong winds and storm surge. The storm surge will often breach the barrier island and/or dune system, depositing foreshore, offshore, and dune sediments into back-barrier lagoons, coastal lakes, or marshes. Due to close coastal proximity and their significantly different geomorphological and sedimentological depositional characteristics, coastal lacustrine, lagoon, and marsh deposits are ideal locations for recording high-energy storm surge associated with tropical cyclone events. In this case, tropical cyclone-deposited marine sediments differ from back-barrier lagoon or lake sediments in a number of ways, such as grain size, diatom faunal and foraminifera composition, and percent $CaCO_3$ and organics. By obtaining radiometrically determined age-control points throughout a core and using the

abovementioned proxies to analyze overwash layers, it is possible to generate a much longer tropical cyclone record than the short-term instrumental/historical record. In recent years, a number of paleotempestology studies have been published that utilize coastal lacustrine and lagoonal deposits. These studies can largely be divided up into short-term (or modern) records and longer-term records.

2.4.1   Modern Records

Before 2008 few studies have assessed the sedimentary mechanism or distribution pattern of storm deposits in back-barrier lakes, lagoons, and marshes attributed to the overwash processes of recent known tropical cyclones. In recent years, Williams (2009, 2010, 2011a, b, 2012) has published multiple studies that focus on the better understanding of modern overwash deposits. Both Williams (2009) and Williams and Flanagan (2009) studied overwash deposits associated with Hurricane Rita along the southwest Louisiana coast. Rita's storm surge and accompanying waves transported sand and mud into woodland and freshwater marsh environments leaving a sedimentary deposit that is up to 0.5 m thick and extends at least 500 m inland. Analysis suggests two distinct phases of deposition: a thin layer of finer sand and mud and an overlying thicker layer of coarser sand. These findings suggest deposition from suspension of offshore sand and mud in an early stage of storm surge inundation. This layer is overlain by coarser sand with an abrupt termination 100–150 m inland that was likely deposited as a traction load, formed at a later stage of storm surge inundation. Williams (2010) documents similar storm surge sedimentation for Hurricane Ike on the McFaddin National Wildlife Refuge. Again two distinct styles of sedimentation are found: a thick, sandy washover fan, extending about 150 m inland, deposited as traction load, and an underlying thinner, finer, more organic-rich blanket of sediments extending more than 2.7 km inland, deposited from suspension. This specific study also shows that storm surge sedimentation can extend a considerable distance inland, with the implication that paleotempestology studies could potentially be conducted farther inland. Williams also studied shell bed tempestites in part of southwest Louisiana's Chenier Plain (2011a). The shell bed tempestites are predominantly composed of disarticulated bivalves, probably reworked and transported landward from skeletal remains offshore. The shell bed has an erosional base, is bioclast supported, normally graded, and has common mud rip-up clasts. Williams demonstrates that the Hurricane Ike shell bed is a valuable analog for older palaeotempestological investigations and that tropical cyclones have likely contributed to the construction of both modern berm ridges and paleo-beach ridges on this Louisiana coastal plain. Another study from the southwest Louisiana Chenier Plain (Williams 2013) denotes overwash layers as storm-surge-deposited sand enclosed by marsh sediments. The sand layers have sharp basal contacts, extend hundreds of meters into the marsh, and contrast in lithology and microfossil assemblages with enclosing marsh deposits (Fig. 1.4). Based on the modern analogs of Hurricanes Audrey (1957), Rita (2005) and Ike (2008), and consideration of nearby landfalling tropical cyclones in the
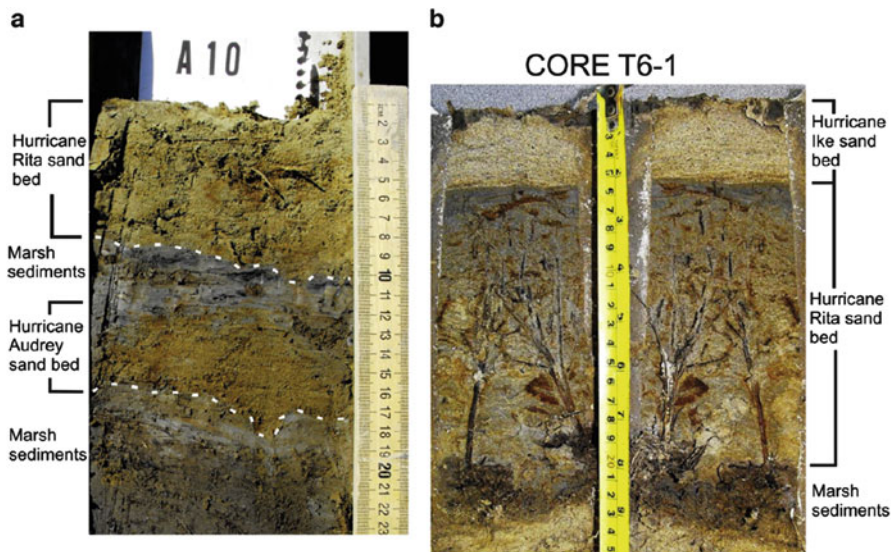
Fig. 1.4 (**a**) Wedge core A10 showing sand beds of Hurricanes Audrey and Rita, separated by a few centimeters of muddy organic-rich marsh sediment (Modified from ref. Williams 2013). *Dashed lines* indicate sharp basal contact of each Sand Bed. (**b**) Core T6-1 showing the sharp contact between sand beds of Hurricanes Ike and Rita. Marsh plants, in growth position and rooted in the buried marsh surface, are encased in Tropical Cyclone Rita's sand bed. Photograph taken approximately 8 months after landfall of Hurricane Ike; by 20 months after landfall, Hurricane Ike's deposit was no longer recognizable having been obscured by bioturbation

historical record, it was determined that the storm intensity threshold of the study site is equivalent to a category 3 hurricane. In many of these studies, Williams (2009, 2010, 2011a, b, 2012) shows that the characteristics of the storm surge deposits, including texture, thickness, inland penetration, and preservation, reflect the intensity and proximity of the landfalling tropical cyclones.

Liu et al. (2011) investigated the patterns and processes of recent storm deposition in coastal lakes by conducting sediment coring, coupled with hydrodynamic measurements, before and after Hurricane Gustav and Ike in Bay Champagne, Lafourche Parish, LA. Two-bottom-mounted conductivity, temperature, and depth sensors (CTDs) deployed on August 29, 2008, 3 days before Hurricane Gustav's landfall, recorded a maximum storm surge of ~2.7 m. A segment of loose sediment, occurring in the middle of this storm deposit, was probably formed by the reworking of the upper part of the Gustav storm deposit by Hurricane Ike, 12 days later. In 2014, Naquin et al. also published a study that looked at geological processes induced by tropical cyclones in Bay Champagne. Within each marine incursion layer, terrestrial elemental concentrations, as determined by XRF, display large depletions. Grain size analysis of a portion of the core (30–86 cm) indicates the presence of two series of sequential high-energy storm deposits followed by intense fluvial flooding within Bay Champagne. These events are attributed to Hurricane

Katrina/Rita in 2005 and Gustav/Ike in 2008. The studies of Liu et al. (2011) and Naquin et al. (2014) highlight the difficulty in differentiating overwash deposits laid down in the same year. This impacts the field of paleotempestology, where, for example, going back through time two overwash layers may be interpreted as one thick overwash layer.

Horton et al. (2009) also studied Hurricane Katrina and Rita's overwash layers in Mississippi and Alabama salt marshes. Horton et al. noted a three-dimensional sediment distribution of tropical cyclone-induced storm surge deposits that tapered landward, overlying salt marsh sediment. A sharp erosional boundary between the pre-storm surge and storm surge sedimentary units was observed by a change in color and lithology. The overlying storm surge sediment unit was coarser than the pre-storm surge unit with a lower organic content. Foraminiferal analyses revealed a virtual absence of tests within the storm surge sediments, whereas abundant agglutinated foraminifera were found in the underlying salt marsh deposits.

2.4.2 Difficulties in Using Tropical Cyclone Overwash Records

As demonstrated above, by better understanding the depositional characteristics of the modern-day tropical cyclone record, in different geographical regions, researchers can progress the field of paleotempestology. However, the study of the modern-day record has also identified potential weaknesses in the research field, and paleotempestology has become more contentious in recent years because the exact nature of storm deposition and preservation is somewhat unclear. The general consensus is that overwash sand layers occurring in coastal lakes and marshes are a reliable proxy for major tropical cyclones, rather than minor tropical cyclones or winter storms (Liu and Fearn 1993, 2000; Liu 2004; Liu et al. 2008; Donnelly et al. 2001a, b, 2004; Donnelly and Webb 2004; Scileppi and Donnelly 2007; Donnelly 2005; Donnelly and Woodruff 2007). There are a number of factors that contribute to the deposition and preservation of overwash archives. In general, overwash is an artifact of storm surge, and storm surge varies with tropical cyclone intensity (decreasing tropical cyclone central pressure), speed of forward storm movement, radius of maximum winds, bathymetry, and coastal configuration. In addition, one must consider the site and its preservational integrity, including overwash sediment source; postdepositional erosion; postdepositional lagoonal productivity, including bioturbation and sediment reworking; and lagoonal sediment accumulation rates. Finally, the physical characteristics and geomorphology of the lagoonal barrier and its vulnerability to being breached by storm surge must be considered. Many of the below studies find that at certain geographic locations, not all tropical cyclones are recorded in the geologic record. Why certain storm events are recorded, and others are not, is generally a combination of the above factors.

Using Hurricane Ivan as a modern analog, Liu et al. (2011) demonstrate that the storm surge associated with this category 3 hurricane caused sand deposition in the southern basins of Little Lake and Middle Lake but not in the center of the

larger Lake Shelby site (Bianchette 2007) confirming that the proxy record from the center of Lake Shelby is sensitive to direct hits by catastrophic hurricanes of categories 4 and 5 only. This research has been advanced by modeling efforts such as those of Elsner et al. (2008) who developed a statistical model that quantitatively links the tropical cyclone return period (frequency) with the tropical cyclone return levels (intensities) for the Lake Shelby area using information derived from both the historical record (AD 1851–2005) and the proxy record. Their study also confirmed that it takes landfalling intense tropical cyclones with wind speeds of at least 64 m s[1] (i.e., middle of the category 4 range) to deposit an overwash sand layer in the center of this particular site. Another modeling study by Woodruff et al. (2008) applied a simple advective-settling model to constrain the coastal flooding intensities required to transport clastic overwash deposits to various distances behind the barrier. They found that the topmost overwash deposits in the core could be attributed to four or five most intense tropical cyclones that have struck Puerto Rico since ca. AD 1820.

In 2011, Hippensteel pointed out inconsistencies in overwash signatures from the back-Folly Island barrier marshes in South Carolina. Sedimentological and micropaleontological analysis of 15 gouge-auger cores revealed a lack of spatio-lateral continuity for paleotempestology deposits. The offshore-indicative calcareous microfossil content of some storm deposits was taphonomically altered or destroyed, and in many cases cores taken 10 m apart provided significantly different storm records. Hippensteel cautions that the combination of bioturbation, erosion, and taphonomic degradation of the foraminifera and sedimentary signatures leaves the comprehensive and complete character of the storm record from the Southeastern Atlantic in doubt. In 2011, Otvos also pointed out some of the same inconsistencies in paleotempestology records where the diversity of topographic, hydrodynamic, and sedimentological settings and factors as well as postdepositional settings account for major difficulties in correlating individual sand layers with specific prehistoric tropical cyclone events. This complicated or prevented identification of discrete tropical cyclones, their velocity categories, calculations of recurrence interval probabilities, and accurate risk assessment. Otvos (2011) recommended that the stable isotope method be used in organic-enriched limnic and brackish muds of paralic basins; which may further refine, detail, quantify, and supplement sand layer-based storm proxy signals for improved storm archiving and correlation on the interregional-to-hemispheric scale. Numerous researchers have embarked on a scrutiny of carefully collected detailed data from several worldwide localities. In time, these studies will elucidate the highly variable prehistoric record of tropical cyclone intensities and frequencies on a global scale.

2.4.3   Long-Term Records

Most of the recent long-term lacustrine, lagoon, and marsh overwash studies are constrained to sites along the North Atlantic Basin coastlines, with a few studies from the Western Pacific margins.

Along the western Caribbean coastline, McCloskey and Keller (2009) proposed that a combination of short- and long-term atmospheric oscillations has resulted in latitudinal movement of the tropical cyclone zone and location of landfall through the Holocene. McCloskey and Keller (2009) support this theory with a 5,000-year-old paleotempestology record from the coast of Belize. They calculate that on average major hurricanes make landfall along the coast of Belize once every decade, over the past 500 years. A temporal clustering of tropical cyclones suggests two periods of hyperactivity between ∼4500 and 2500 BP, which supports a regional model of latitudinal migration of tropical cyclone strike zones. McCloskey and Knowles (2009) support the paleotempestology reconstruction with a GIS-based approach to demonstrate that currently intensity changes of the Bermuda High result in a large latitudinal spread of tropical cyclone track and landfall location across the western North Atlantic, while a literature-based examination of paleoclimatic evidence supports the view that long-term changes in the pole-equator temperature gradient have resulted in significant latitudinal migration of the general North Atlantic atmospheric system throughout the Holocene, with a heightened (reduced) gradient moving the entire system southward (northward). McCloskey and Knowles' model suggests that the location of tropical cyclone landfall since the mid Holocene is controlled by a millennial-scale migration of the tropical cyclone zone (paralleling latitudinal movement of the entire system), complicated by the superimposition of a higher frequency variation in track location (controlled by intensity oscillations).

Along the eastern Gulf of Mexico coastline, Ercolani et al. (2015) used sediment cores from a back-barrier lagoon in Naples, FL to demonstrate the potential importance of MDR SSTs in driving tropical cyclone landfalls. The authors noted an active period of tropical cyclone overwash from 1000 to 500 years BP and an inactive period from 500 to 150 years BP. Ercolani et al. observed an increased number of paleotempestites when MDR SSTs are warmer, coinciding with the Medieval Warm Period, and very few paleotempestites when MDR SSTs are cooler, coinciding with the Little Ice Age. Results from Ercolani et al. are correlated with other Gulf of Mexico paleotempestology studies such as Lane et al. (2011) and Denomee et al. (2014) (both discussed below in "Coastal karst basins") that indicate that MDR SSTs have been a key long-term climate driver of tropical cyclone strikes (Fig. 1.5). This topic was addressed by Mann et al. in 2009 and is expanded on below in Sect. 4.

Several recent studies have been published from sites along the western North Atlantic coastline, more specifically Massachusetts. Besonen et al. (2008) examined annual terrestrially deposited varves spanning the last 1000 years in a lake near Boston, MA. The varves are millimeter-scale siliciclastic/biogenic sedimentary couplets that reflect the seasonal cycle of sedimentation in the lake. Each couplet is deposited annually, but throughout the sequence, there are unusually thick layers of graded sediments (coarser grained at base and fining toward the top of each layer). These thicker beds are composed of terrestrial and organic detritus which correspond in nearly all cases to the passage of a category 2–3 hurricane (Saffir–Simpson scale) close to the catchment. Besonen et al. (2008) found that there
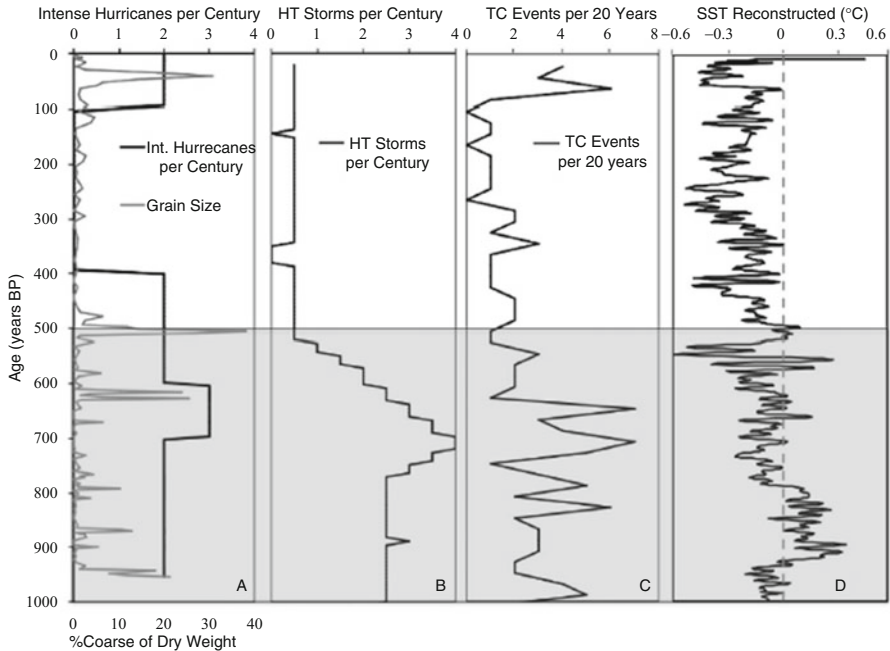
Fig. 1.5 Comparison to other paleotempestology and climate records (Modified from ref. Ercolani et al. 2015). (**a**) Southwest Florida (**b**) Lane et al. (2011), northern Florida (**c**) Denommee et al. (2014), Belize (**d**) Mann et al. (2009) SST reconstruction MDR North Atlantic. HT refers to "high threshold" meaning those storms that generated a deposit at least as coarse as the strongest historic storm to hit the field site. Tropical cyclone events include tropical storms to major hurricanes, not exclusively intense tropical cyclones. The *gray* box identifies similarities among the records

was centennial variation in the record, the twelfth to sixteenth centuries had a significantly higher level of tropical cyclone activity (up to eight extreme events occurring per century) compared to the eleventh and seventeenth to nineteenth centuries when only two to three per century was the norm. They attributed the more active periods to warmer tropical Atlantic SSTs such as occurs in La Niña conditions and the inactive centuries to cooler tropical Atlantic SSTs. Boldt et al. (2010) presented another paleotempestology overwash study from a coastal marsh in Massachusetts (Mattapoisett Marsh). Event layers deposited during historic time match well with known severe tropical cyclone strikes. The fifteenth and sixteenth centuries are among the most active of the last 2000 years with seven events occurring over that time, with some overlap in elevated tropical cyclone activity seen by Besonen et al. (2008) in the twelfth to sixteenth centuries. The authors pointed out that significant variation in the number of intense tropical cyclones is seen, but there is relatively constant tropical cyclone frequency over the last 2000 years.

In 2015 Donnelly et al. published a long, well-resolved 2000-year-old overwash record from Salt Pond, MA (Fig. 1.6). A total of 35 event layers were deposited over the last 2000 years with the highest frequencies found between 1420–1675 CE and 150–1150 CE. This study indicates considerable changes in the frequency of overwash deposits over the last 2000 years, with historically unprecedented intervals of event-bed deposition. Donnelly et al. (2015) demonstrated that there are several intervals in the fourth to seventh centuries, eleventh century, and fifteenth to early seventeenth centuries which exceed that of the calculated centennial frequency of landfalling tropical cyclones in this region (0.9 events per century) derived from the 162-year NOAA best-track dataset. Hence, compared to modern event frequencies in the region, significant portions of the 2000-year Salt Pond record exceed what would be expected based on random event occurrence alone.

Along the western Atlantic margin, Toomey et al. (2013a) reported on a new type of tropical cyclone overwash history developed from 7000 years of coarse-grained deposits in sediment cores taken from the leeward margin of the Great Bahama Bank. At this site, storms are thought to be an important mechanism for transporting coarse sediment from shallow carbonate platforms to the deep-sea and bank-edge sediments. The results from this study agree with previous studies which have emphasized the role of ENSO and the West African Monsoon in controlling late Holocene tropical cyclone frequency and indicate that insolation may be important in the forcing mechanism of the North Atlantic storm intensity on millennial timescales. Indeed, the low frequency of storm events near the Bahamas during the mid-Holocene indicates that increased Northern Hemisphere insolation and a related northward shift of the intertropical convergence zone (ITCZ) may have worked to decrease major North Atlantic hurricane development.

In the North Western Pacific, Woodruff et al. (2009) published sediment core results from two coastal lakes located on the island of Kamikoshiki in Southwestern Japan (Lake Namakoike and Lake Kaiike) that provide evidence for the response of a back-barrier beach system to episodic coastal inundation over the last 6400 years. Periods of barrier breaching are concurrent with an increase in ENSO frequency, indicating that ENSO has potentially played a key role in governing typhoon variability during the mid-to-late Holocene. An inverse correlation is observed between tropical cyclone reconstructions from the western North Atlantic and the Kamikoshiki site, which may indicate an oscillating pattern in tropical cyclone activity between the western Northern Atlantic and the western North Pacific, or at least between the western Northern Atlantic and regions encompassing Southern Japan. The two kamikaze typhoons which contributed to the failed Mongol invasions of Japan in 1274 AD and 1281 AD occur during a period with more frequent marine-sourced deposition at the site, suggesting that the events took place during a period of greater regional typhoon activity. In 2015, Woodruff et al. presented another Japanese coastal lake record that extends back 2000 years. The complete reconstruction indicates periods of greater flood activity relative to the modern beginning ca. 250 CE and extending past the timing of the kamikaze events to 1600 CE. Similar to Woodruff et al. (2009), they interpret the greater regional typhoon activity to greater El Niño activity relative to the modern and the preferential
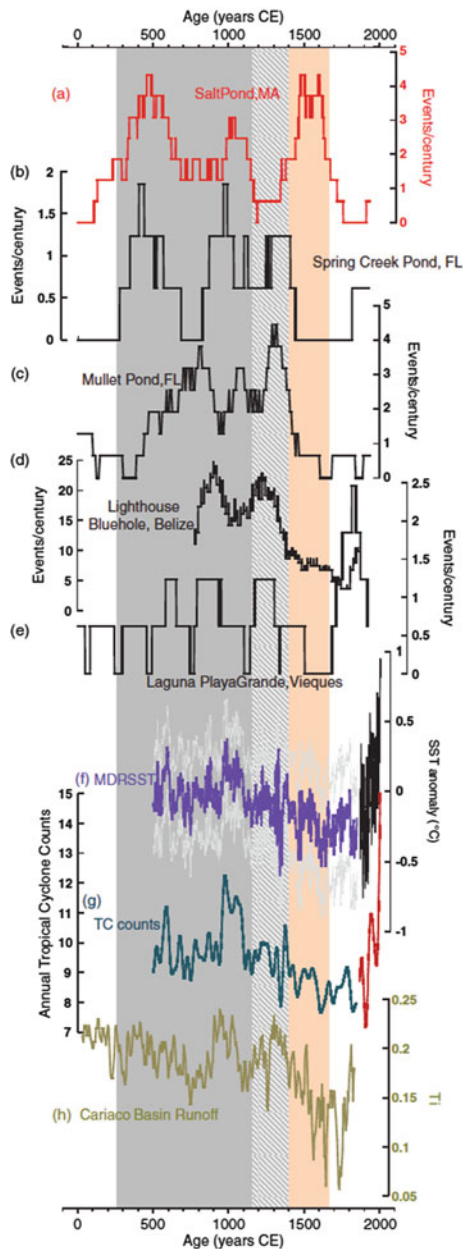
Fig. 1.6 Comparison of Salt Pond reconstruction with Caribbean and Gulf of Mexico tropical cyclone proxy records, reconstructed MDR SST, modeled tropical cyclone activity, and Cariaco Basin runoff (Modified from ref. Donnelly et al. 2015) (**a**) Event-bed frequency at Salt Pond, MA. (**b**) Intense tropical cyclone event-bed frequency from Spring Creek Pond, FL (Brandon et al. 2013). (**c**) Intense tropical cyclone event-bed frequency from Mullet Pond, FL (Lane et al. 2011). (**d**) Event-bed frequency from Lighthouse Blue Hole, Belize (Denommee et al. 2014).

steering of storms toward Japan. In addition, they also note the paired kamikaze typhoons in their sedimentary record and support accounts of them playing an important role in preventing the conquering of Japan by Mongol fleets.

Also in the western North Pacific, Williams et al. (2016) presented typhoon overwash results from coastal marshes, ponds, and swales along the Gulf of Thailand. In this first paleotempestology study in Thailand, cores from two low-energy settings on the Gulf of Thailand coast – a coastal marsh near Cha-am and beach ridge plain swales near Kui Buri – reveal geologic evidence of up to 19 typhoon strikes within the last 8000 years. The sand layers have sharp upper and lower contacts with finer sediments located below and above the sand layers. Possible explanations for this variability in the typhoon record are that typhoons were more frequent and/or more intense in Southeast Asia in the mid-Holocene because of climatic changes associated with the Mid-Holocene Warm Period or that the record reflects site sensitivity changes resulting from a mid-Holocene sea-level highstand.

In the Central South Pacific (Tahaa, French Polynesia), a 5000-year record of overwash deposition from Toomey et al. (2013b) shows strong coherence between recent coarse-grained deposits and observed cyclone events. The long-term reconstructions highlight a period of higher coarse overwash flux between approximately 2900 and 500 year BP, compared with the modern, and an earlier active period between 5,000 and 3800 years BP. Over the later interval (2900–500 years BP), higher than background storm activity is observed near the Bahamas, while a general decrease in storm activity near Japan is observed. Central South Pacific and North Atlantic tropical cyclone activities are different during the earlier active interval (5000–3800 years BP), possibly driven by orbital changes in storm season insolation. These relationships are unexpected given modern observations that indicate tropical cyclone activity in the North Atlantic and central South Pacific increase during opposite ENSO phases. The Tahaa cyclone reconstruction also highlights a period of relative quiescence around French Polynesia today and likewise the potential risk in the future should levels of activity increase to those observed prior to 500 years BP.

Fig. 1.6 (continued) (**e**) Event-bed frequency at Laguna Playa Grande, Vieques (Donnelly and Woodruff 2007). (**f**) MDR SST anomaly reconstruction (*purple*) with 95 % uncertainty envelope (*gray*) (Mann et al. 2009). NOAA ERSST MDR SST data for 1870–2006 (*black*) (Mann et al. 2009). (**g**) Smoothed modern annual Atlantic tropical cyclone counts (*red*) and statistical model estimates of basin-wide tropical cyclone counts from 500 to 1850 CE (*blue*) (Mann et al. 2009). (**h**) Ti record from Cariaco Basin sediments thought to reflect changes in terrestrial runoff and the position of the ITCZ (Haug et al. 2001). *Gray shading* is interval between 250 and 1150 CE when all sites have heightened intense-hurricane-related event beds. *Diagonal gray shading* is interval between 1150 and 1400 CE when Caribbean and Gulf of Mexico sites have heightened intense-hurricane-related event beds and the North American east coast is inactive. *Beige shading* is interval between 1400 and 1675 CE when only the North American east coast is active

2.5 Coastal Karst Basins

Coastal karst basins (CKBs), which are features such as sinkholes, blue holes, and underwater caves, provide alternative paleotempestology archives on carbonate landscapes. Continual dissolution and modification of carbonate terrain over quaternary timescales create a variety of basin-like features in limestone bedrock (van Hengstrum and Scott 2011; van Hengstrum et al. 2015b). These features are able to record the signature of tropical cyclones going back thousands of years.

A number of paleotempestology studies have been published from Apalachee Bay, North Florida, along the Gulf of Mexico. Lane et al. (2011) reported on Mullet Pond, a 4500-year subaerial sinkhole record of tropical cyclone activity located within Apalachee Bay. Approximately 3.9 storms per century occur in this paleorecord, this number being greater than that of previously published paleotempestology records from the region. Intervals of both anomalously high and low storm frequency were identified; however, the rate at which smaller layers were deposited is interpreted to be relatively constant over the last five millennia. Lane et al. suggest that significant variability in tropical cyclone frequency may only have occurred for the highest magnitude events. The frequency of high magnitude events peaked near six storms per century between 2800 and 2300 years ago. These events were relatively rare with about 0–3 storms per century occurring between 1900 and 1600 years ago and between 400 and 150 years ago (Fig. 1.5). A marked decline in the number of large storm deposits, which began around 600 years ago, persisted through present with below average frequency over the last 150 years when compared to the preceding five millennia. This was backed up by a hydrodynamic modeling study that demonstrated that Apalachee Bay is far more susceptible to tropical cyclone surge than historically observed (Lin et al. 2014). Climatological-hydrodynamic modeling (including a method to account for storm size uncertainty), historical observations, and paleotempestology records were combined to investigate local surge risk. The mean return period of the extreme events with estimated surge levels above 5 m is about 40 years, whereas it is about 400 years according to the recent historical storm database (Lin et al. 2014).

Approximately 20 km north of Mullet Pond lies Spring Creek Pond, a coastal sinkhole that contains a 2500-year record of tropical cyclone activity (Brandon et al. 2013). The authors identified and dated 34 storms layers, and an inverse modeling technique is developed to constrain the landfall wind speed of the storms from the grain size of their resultant deposits. The authors show that (1) applying the inverse model to the sediment deposits from the historic (post-1851 CE) record results in landfall wind speeds that are consistent with storms reported in the best-track dataset, (2) all deposits throughout the 2500-year record are capable of being produced by tropical cyclones, including a seemingly anomalous layer dated to 600 years BP, and (3) the Spring Creek Pond record of intense tropical cyclone occurrence is consistent with the above-described reconstruction from Mullet Pond (Lane et al. 2011) with both records indicating a period of increased intense tropical cyclone frequency between 1700 and 600 years ago and decreased intense storm

frequency from 2500 to 1700 and 600 years ago to the present. The variation in intense tropical cyclone strike frequency, particularly the drop in activity at 600 years BP, is potentially the result of inferred shifts in Loop Current penetration into the Gulf of Mexico.

van Hengstum et al. (2015a) presented records of late Holocene storminess and coastal temperature change from a Bermudian submarine cave that is hydrographically circulated with the coastal ocean (Fig. 1.7). Erosion of terrestrial sediment into the submarine cave provides a "storminess signal" that provides evidence for increased storm activity during the Little Ice Age (150–600 calibrated years (cal. years) BP) and centered at 1700 and 3000 cal. years BP. van Hengstum et al. (2015a) noted that understanding the driver of this storminess signal will require higher-resolution storm records to disentangle the contribution of tropical versus extratropical cyclones and a better understanding of tropical cyclone activity during hemispheric cooling periods. Most importantly, however, the signal in Bermuda appears more closely correlated with proxy-based evidence for subtle Atlantic Meridional Overturning Circulation (AMOC) reductions than with NAO phasing.

Gischler et al. (2008) reported on a hurricane-induced overwash record from a blue hole in Belize. The blue hole record consisted of undisturbed, annually layered biogenic carbonate muds and silts with intercalated coarser-grained storm beds. Storm event beds are most common during AD 650–850, around AD 1000, during AD 1200–1300, and AD 1450–1550. Major storm beds are rare during the past 500 years BP. Denommee et al. (2014) also presented a highly detailed sedimentary proxy record of paleotropical cyclone strikes from the blue hole of Lighthouse Reef, Belize. Denomee et al. demonstrated that active tropical cyclone regimes have occurred when both MDR SSTs and NAO mode are high, while inactive tropical cyclone regimes correlate with low MDR SSTs and NAO mode (Fig. 1.5).
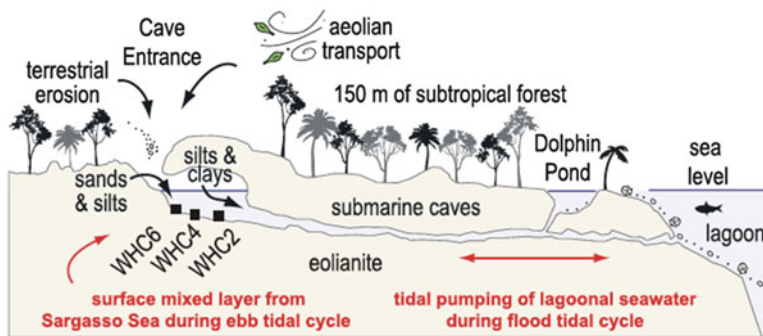

Fig. 1.7 A conceptual model illustrating the point source effect in Walsingham Cavern, where terrestrial sediment enters the subaerial fissure-collapse entrance in the subtropical forest (Idwals Nature Preserve) and is laterally transported into the cave (Modified from ref. van Hengstum et al. 2015a). Temperature monitoring in Walsingham Cavern from 2010 to 2011 indicates that tidal pumping causes seawater to primarily enter the submarine cave from the adjacent lagoon (Castle Harbour). Some seawater, however, is advecting into the submarine cave through the karst that is derived from the upper 75 m of the Sargasso Sea

van Hengstum et al. (2014) presented an overwash record from a blue hole on Great Abaco Island, the Bahamas. The authors found that overall tropical cyclone activity, including all intensities of events, has been variable over the last millennium. A noteworthy quiescent interval occurs from 1150 AD to 1300 AD, coincident with increased El Niño activity and a weakened African easterly jet. Based on SSTs, the African easterly jet, and ENSO activity alone, the climate system at 1350 AD appears to begin creating favorable conditions for tropical cyclone activity in the North Atlantic. By 1500 AD, tropical cyclone activity was encouraged by elevated SSTs, invigorated West African Monsoon, and decreased El Niño events. After 1600 AD, the climate system was likely beginning to hamper cyclogenesis by decreasing SSTs and the African easterly jet, although depressed El Niño activity also persisted. Tropical cyclone activity recorded at this site (Northwest Caribbean, 26°N) compared to that at Mullet Pond (Gulf of Mexico, 29°N) (Lane et al. 2011) appeared antiphased over the last millennium, yet these sites reside at similar latitudes. This may indicate that regional ocean-atmospheric dynamics in different North Atlantic Ocean sub-basins may be playing a larger role modulating regional paleotropical cyclone activity than previously considered.

3 Paleotempestology-Generated Landfall Frequencies and Return Periods

Forecasting future tropical cyclone impacts requires sophisticated modeling, predicated on accurate initialization data. The official NOAA database of historical tropical cyclone tracks (HURDAT) along the Florida coast, for example, only extends back in time to 1851. However, this data is used for purposes along a spectrum from statistically estimating annual expected return frequencies to modeling the impacts of global climate change and sea-level rise on shoreline change; hence, a longer and more complete dataset would result in greater accuracy at initialization. More recently the field of paleotempestology has been working to generate tropical landfall frequencies and return periods that extend back much further in time (thousands of years) for specific geographical regions.

Along the eastern Australian coastline, Nott and Jagger (2013) used a generalized extreme value distribution and Bayesian analysis of a beach ridge plain record of extreme tropical cyclone-generated marine inundations to calculate return rates. Using this approach, the return period of the marine inundation generated by Cyclone Yasi was determined. Cyclone Yasi, which occurred on 3 February 2011, had a central pressure of 929 hPa at landfall near Mission Beach approximately 150 km south of Cairns, Northeast Australia. Nott and Jagger (2013) find that the beach ridge calculated return periods for Cyclone Yasi type storms appear to differ considerably from estimates determined using a probability-based approach (which extrapolates from the short historical record).

For Apalachee Bay, FL, Lin et al. (2014) found that the mean return period for extreme tropical cyclones, with estimated surge levels above 5 m, is approximately 40 years in both climatological-hydrodynamic modeling and the paleotempestology record, whereas it is about 400 years according to the historical storm database. Therefore, both the climatological-hydrodynamic modeling and the overwash-deposit-based long-term reconstructions indicate that Apalachee Bay is far more susceptible to tropical cyclone surge than historically observed. Thus Lin et al. found that due to its limitation and biases, relying on the historical storm record may greatly underestimate the risk of extremes for Apalachee Bay. Donnelly et al. (2015) came to a similar conclusion by correlating five previously published paleotempestology records from multiple sites along the east coast of North America, the Bahamas, and Puerto Rico. Donnelly et al. found that periods of frequent intense tropical cyclone landfalls exceeded historical levels at all five sites over the last 2000 years. Like Lin et al., this study also found that the historical storm record from these geographical regions may be underestimating the risk of tropical cyclones across these locations.

Elsner et al. (2008) quantitatively compared estimated return periods using the historical record and the paleotempestology record from Lake Shelby, Alabama. In the paleotempestology record, the minimum return level of overwash events recorded in sediment cores was estimated using a modern analog (Hurricane Ivan of 2004) to be 54 ms^{-1} (105 kt) for a return period of 318 years, based on 11 events over 3500 years. The expected return level of rare hurricanes in the historical record (1851–2005) at this location and for this return period is estimated using a parametric statistical model and a maximum likelihood procedure to be 73 ms^{-1} (141 kt), with a lower bound on the 95 % confidence interval of 64 ms^{-1} (124 kt). The results between the paleotempestology record and the historical record are not significantly different. Therefore the estimated sensitivity of Lake Shelby to overwash events is consistent with the historical record, given the model. These recent studies highlight the potential importance of verifying return periods derived from the historical record with return periods derived from the paleotempestology record for different geographical locations.

4 Advances in the Understanding of Climate Change-Driven Tropical Cyclone Dynamics

Including recent research outlined in this book chapter and previously published research, numerous paleotempestology records exist for the Western Atlantic Ocean, Gulf of Mexico, Caribbean Sea, South Pacific Ocean, and fewer records from the Northwest Pacific and Indian Oceans (Nott 2011b). In recent years the field of paleotempestology has significantly progressed the understanding of long-term tropical cyclone dynamics and the possible climate drivers associated with long-term tropical cyclone trends.

In the South Pacific Ocean, Haig et al. (2014), Nott (2010), and Forsyth et al. (2010) among others identified millennial-scale variability in tropical cyclone activities over the last 6000 years. Haig et al. (2014) used speleothem records to demonstrate that the low levels of storm activity, which have occurred on the mid west and northeast coasts of Australia, are unprecedented over the past 550–1500 years. Their results also revealed a repeated multi-centennial cycle of tropical cyclone activity, the most recent of which commenced around AD 1700. The present cycle includes a sharp decrease in activity after 1960 in Western Australia. This is in contrast to the increasing frequency and destructiveness of Northern Hemisphere tropical cyclones since 1970 in the Atlantic Ocean and the western North Pacific Ocean. Nott (2004, 2011a) and Nott et al. (2009) also noted millennial-scale variability in tropical cyclones along the Australian coastline. Like Haig, Nott also noted that the long-term trends associated with the Australian paleotempestology records indicate that the frequency of intense tropical cyclones has decreased into the modern day. And in 2012 Nott and Forsyth pointed out the presence of substantial gaps in ridge plain formation over the late Holocene along the NE Australian coast. These gaps are most likely due to periods when fewer high intensity tropical cyclones made landfall (Nott and Forsyth 2012). They noted that some of the overwash sedimentary records from the North Atlantic Basin also have major gaps suggestive of periods of tropical cyclone inactivity. Periods of inactivity in the North Atlantic Basin have been previously related to time periods dominated by El Niño (Donnelly and Woodruff 2007). Comparisons with paleo-ENSO records from Ecuador (Moy et al. 2002) suggested the same may be true of the NE Australian sites (Fig. 1.8) between approximately 3500 and 2500 cal. years BP. However a later phase of tropical cyclone inactivity along the NE Australian coastline (∼1800 to ∼900 years BP) does not correlate well with a higher ENSO index (Fig. 1.8). In addition, there is not a clear coincidence between the major periods of El Niño suggested by the paleo-ENSO record and all of the periods of lower tropical cyclone activity in the North Atlantic and Southwest Pacific, or the periods of heightened tropical cyclone activity in the Northwest Pacific and east Indian Oceans and the Gulf of Carpentaria (Nott and Forsyth 2012, Fig. 1.8).

In the Southwest Pacific, along the Gulf of Thailand, Williams et al. (2016) used a sediment overwash record to show that the frequency of tropical cyclone strikes was two to five times greater from 3900 to 7800 cal. years BP compared to 0–3900 cal. years BP. They interpret this increase in more frequent and/or more intense tropical cyclones as either a response to an increase in mid-Holocene SSTs or that the record reflects site sensitivity changes due to a mid-Holocene sea-level highstand. The possible link to SSTs and a greater frequency of intense tropical cyclone strikes could have important societal implications, given possible consequences of ongoing global warming.

Many more records have become available for the North Atlantic Basin (Western Atlantic Ocean, Gulf of Mexico, and Caribbean Sea) than that of the Pacific. A number of these studies show a clear relationship between tropical cyclones and SSTs (Besonen et al. 2008; Denommee et al. 2014; Ercolani et al. 2015; Hetzinger et al. 2008; Trouet et al. 2016), where higher/lower SSTs in the MDR result in
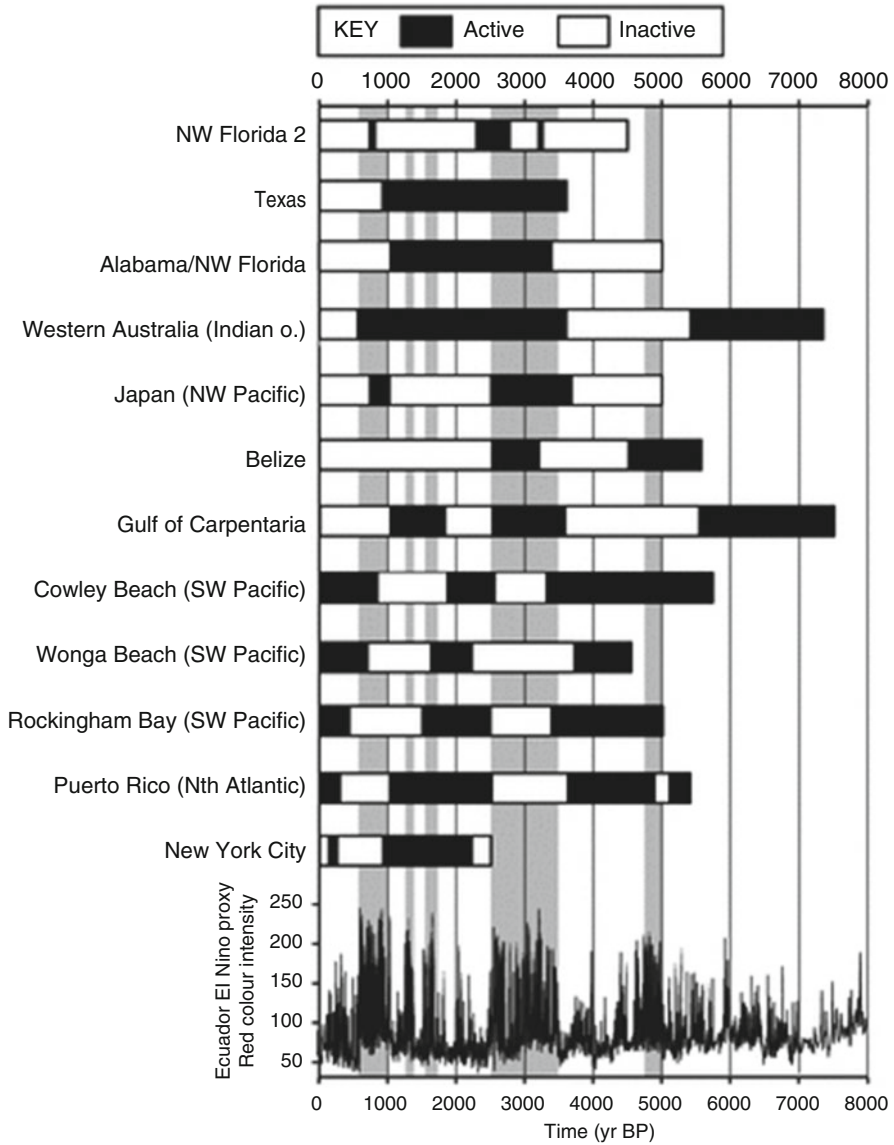
Fig. 1.8 Global phases of tropical cyclone activity and inactivity over past 5000–7000 years (Modified from ref. Nott and Forsyth 2012)

relatively higher/lower tropical cyclone activity. Many of these studies also point to the NAO as a key climate driver of tropical cyclone activity (Denommee et al. 2014; Hetzinger et al. 2008; Trouet et al. 2016), where a more positive phase of NAO results in higher tropical cyclone activity in the North Atlantic Basin.

The importance of SSTs and the NAO was also proposed by Mann et al. (2009) (Fig. 1.9), where authors gathered previously published paleotempestology data from five sites along the North Atlantic Basin that covered the past 1500 years (US Atlantic coast and Puerto Rico). In addition to the paleorecords, a previously published statistical model of the climatic conditions, principally the NAO, SSTs, and ENSO, over the past 1500 years was presented. Both approaches suggest greater regional tropical cyclone activity, or at least as great as the recent (post mid-1990s) increase in activity, occurred during the Medieval Warm Period between AD 900 and 1100. Since this time, regional tropical cyclone activity has decreased until the recent increase. They attribute the heightened medieval tropical cyclone activity to La Niña-like conditions and relatively warm tropical Atlantic SSTs.

Liu and Fearn (1993, 2000) were the first to propose the long-term position of the Bermuda High as an important driver of North Atlantic Basin tropical cyclone landfall position. They proposed that shifts in the position of the Bermuda High were responsible for millennial-scale oscillations in the cycle of North Atlantic tropical cyclone activity. This work has been expanded on by a number of recent works (McCloskey and Keller 2009; Malaizé et al. 2011; McCloskey and Liu 2012; van Hengstum et al. 2016). In 2009, McCloskey and Knowles noted that a
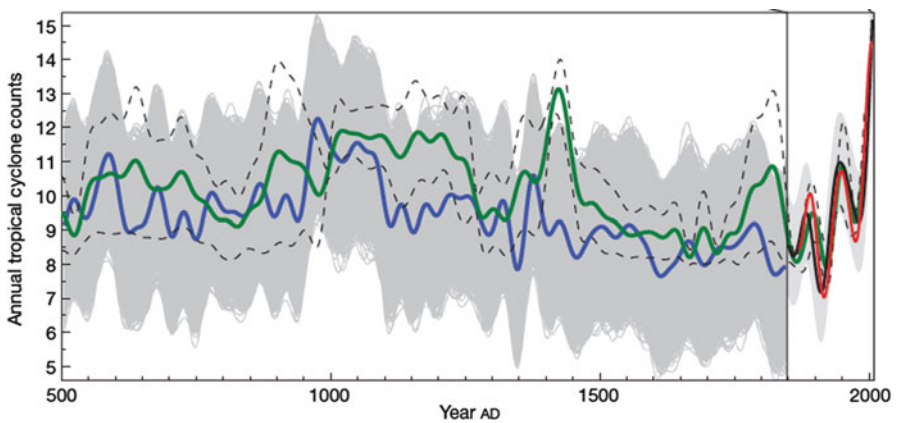

Fig. 1.9 Modern Atlantic tropical cyclone counts (*red*) compared both with statistical model estimates of tropical cyclone activity based on modern instrumental (AD 1851–2006; *black*) and proxy-reconstructed (AD 500–1850; *blue*) climate indices and an estimate of basin-wide land-falling North Atlantic tropical cyclone activity (AD 500–1991) derived from regional composites of overwash sediments (*green*) (Modified from ref. Mann et al. 2009). All series were smoothed at multidecadal (40-year) timescales. The sediment composite record was standardized to have the same mean and multidecadal variance as the statistical model estimates. Uncertainties for the statistical model estimates (*gray shading*, indicating 95 % confidence intervals) take into account the uncertainty in the statistical model itself (*gray shading*) and – in the case of the proxy-reconstructed indices (*gray shading*) – the additional uncertainty due to the uncertainties in the proxy-reconstructed climate indices. Uncertainties for the sediment composite record (*thin dashed black curves* indicating upper and lower limits of the 95 % confidence interval) are derived from jackknifing of the full composite with respect to each of the five contributing regional estimates

strong north or south migration of the ITCZ would be accompanied by similar, if not precisely simultaneous, movements of the Bermuda High and the tropical cyclone zone (McCloskey and Knowles 2009). McCloskey and Keller showed two periods of increased tropical cyclone activity from 5500 to 2500 cal. years BP along the coast of Belize corresponding to an investigation from St. Martin in the French West Indies (Bertran et al. 2004) that noted an increase in tropical cyclone activity between 4900 and 2600 cal. years BP. Both sites are at the same latitude (18°N), thereby supporting the hypothesis of latitudinally coherent periods of increased tropical cyclone activity (McCloskey and Keller 2009). Furthermore, this period correlated to a period of generally southern ITCZ migration, while the period of hyperactivity observed by Liu and Fearn (2000) on the Gulf Coast roughly correlated to a northern ITCZ movement (Haug et al. 2001). Therefore McCloskey proposed a climatically controlled zone of tropical cyclone landfall slowly migrating north and south across the Caribbean. van Hengstum et al. (2016) invoke a similar hypothesis using a 3000-year-old Northern Bahamas (Abaco Island) sinkhole record to demonstrate that the ITCZ has likely helped modulate intense tropical cyclone strikes on the western North Atlantic margin on millennial to centennial scales. The paleotempestology reconstruction closely matches a previous reconstruction from Puerto Rico (Donnelly and Woodruff 2007) and documents a period of elevated intense tropical cyclone activity on the western North Atlantic margin between 2500 and 1000 years BP that coincides with a more northerly ITCZ position. van Hengstum et al. (2016) stipulated that it is the Atlantic Meridional Mode (AMM) that is associated with an anomalous meridional SST gradient across the mean ITCZ latitude and a cross-gradient atmospheric boundary layer flow, which shifts the ITCZ toward the warmer hemisphere. A positive phase of the AMM is associated with a strong meridional SST gradient, a northward shift in the ITCZ, and decreased vertical wind shear in the tropical Atlantic.

In 2014 Wallace et al. used multiple published records from the Gulf of Mexico, Caribbean Sea, and western North Atlantic Ocean coastlines to better understand various climatic modes of variability. Wallace et al. noted that during the mid-Holocene, tropical cyclone activity appears to have been dominated by Northern Hemisphere insolation and a northward shift of the ITCZ toward the warmer hemisphere (Toomey et al. 2013a), as rapid atmospheric temperature shifts that occur during ENSO activity could potentially drive tropical cyclones. This was supported by a climate model (Korty et al. 2012). Donnelly et al. (2015) furthered the understanding of these long-term climate drivers by correlating five previously published paleotempestology records with a new well-resolved paleotempestology record from Salt Pond, Massachusetts. The study revealed that periods of frequent intense tropical cyclone landfalls, that exceeded historical levels, occurred at all sites over the last 2000 years (Fig. 1.6). Many prehistoric tropical cyclone event beds contained more coarse sediment than historical events, which may suggest that prehistoric events achieved greater intensity relative to historical tropical cyclones. The study demonstrated that centennial-scale shifts in MDR SST and associated ITCZ migration played an important role in driving basin-wide changes in intense tropical cyclone activity. Persistently warm MDR SST's drove heightened levels of

intense tropical cyclone activity across much of the western North Atlantic between ca. 250 and 1400 CE; however, activity along the east coast was suppressed between 1150 and 1400 CE. A shift in intense tropical cyclone activity from the Caribbean and Gulf of Mexico to the east coast occurred at the onset of the Little Ice Age (ca. 1400 CE). At this time, many Caribbean and Gulf of Mexico paleotempestology reconstructions observed less tropical cyclone activity, which has mostly been explained by relatively cooler MDR SSTs and a southward shift of the ITCZ (Fig. 1.6). The ensuing interval of heightened intense tropical cyclone activity confined to the east coast between about 1400 and 1675 CE may have been driven by a combination of increased tropical transition cyclogenesis and elevated SSTs off the east coast. Multiple authors (Donnelly et al. 2015; McCloskey et al. 2013; van Hengstum et al. 2016; among others) pointed out the potential importance of SST and ITCZ position because future anthropogenic warming focused in the Northern Hemisphere will likely favor a more northerly ITCZ position, which may in turn return the western North Atlantic margins to an active tropical cyclone period.

5 Conclusions

The most evident characteristic of the above-paleotempestology records is that the majority reveal alternating periods of either greater or lesser tropical cyclone activity over time periods extending back as far as 6000 years. The theme emerging from the recent research is that tropical cyclone behavior, in multiple oceanic basins, is not stochastic over the long term and it appears that periods of greater or lesser tropical cyclone activity have been due to variations in climatic conditions, rather than just random variability over a consistent climatic regime. It has also been shown in multiple paleotempestology studies that periods of frequent intense tropical cyclone landfalls of the past may have exceeded that of the recent (last ∼200 years) tropical cyclone record. Therefore it becomes extremely important to understand the climatic conditions associated with these "active" time periods.

The studies discussed in this review chapter, along with other studies, indicate the importance of multiple long-term climate drivers. In the Pacific Basin, SSTs and ENSO seem to be important aspects of the climate regime in driving long-term tropical cyclone variability. In the North Atlantic Basin, SSTs, and thus AMO, have been shown to be very important to the frequency and intensity of tropical cyclone activity. In addition, positive (El Niño) and negative (La Niña) phases of ENSO continue to show an important influence on hurricane landfalls along the western Atlantic Ocean margins, where negative ENSO phases promote the development of tropical cyclones in the North Atlantic Basin. More recently researchers have been focused on the importance of the ITCZ position. Research shows that a more northerly position of the ITCZ, coincident with warm SSTs in the MDR, promotes cyclogenesis and potential tropical cyclone intensity in the MDR by increasing low-level vorticity and decreasing vertical wind shear and sea-level pressure. In addition, ITCZ latitudinal position can influence the position of the Bermuda High. It has been

suggested that a more northerly ITCZ position results in a more northerly Bermuda High position, which may in turn steer tropical cyclones to make landfall in different geographical locations. In order to better understand the long-term climate drivers of tropical cyclones, and therefore the future behavior of tropical cyclones, more paleotempestology records are needed. But what is clear now is that any simulations of long-term tropical cyclone behavior need to account for climatic influences such as those discussed above (SSTs, NAO, ENSO, AMM, and AMO).

In the last few decades, we have learned a great deal about long-term tropical cyclone dynamics through the field of paleotempestology. This important field of study allows us to extend the relatively short instrumental record back in time and gather information on the potential climate drivers associated with long-term tropical cyclone dynamics. However it is important to keep in mind that this is not a perfect science. Many paleotempestology studies have shown that overwash sand and/or shell layers occurring in coastal lacustrine, lagoon, and marsh settings do not record all tropical cyclone events and are only a reliable proxy for major hurricanes, rather than minor tropical cyclones or winter storms. In addition, studies have shown that some field sites may lack spatio-lateral continuity, where correlating individual sand and/or shell layers with specific prehistoric tropical cyclone events is impossible. For this reason it is important to continue the study of the modern paleotempestology record and its relationship to known tropical cyclone events (as discussed above in "2.4.1 Modern Records and 2.4.2 Difficulties in using Tropical Cyclone Overwash Records"). Paleotempestology studies using multiple approaches (both archives and proxies) as discussed in this chapter add significant confidence to paleotempestology records through cross validation and the development of new paleotempestology proxies. In addition, new proxy development, such as stable isotopes, to supplement sand/shell layer-based storm proxy signals may further refine the field of paleotempestology.

References

Bertran P, Bonnissent D, Imbert D et al (2004) Paléoclimat des Petites Antilles depuis 4000 ans BP: l'enregistrement de la lagune de Grand-Case à Saint-Martin. Compt Rendus Geosci 336:1501–1510

Besonen MR, Bradley RS, Mudelsee M et al (2008) A 1,000-year, annually-resolved record of hurricane activity from Boston, Massachusetts. Geophys Res Lett. doi:10.1029/2008GL033950

Bianchette T (2007) Using Hurricane Ivan as a modern analog in paleotempestology: Lake sediment studies and environmental analysis in Gulf Shores, Alabama. Faculty of the Louisiana State University and Agricultural and Mechanical College in partial fulfillment of the requirements for the degree of Master of Science in The Department of Geography and Anthropology by Thomas Bianchette BS, Western Michigan University

Boldt KV, Lane P, Woodruff JD, Donnelly JP (2010) Calibrating a sedimentary record of overwash from Southeastern New England using modeled historic hurricane surges. Mar Geol 275:127–139. doi:10.1016/j.margeo.2010.05.002

Bossak BH, Keihany SS, Welford MR, Gibney EJ (2014) Coastal Georgia is not immune: hurricane history, 1851–2012. Southeast Geogr 54:323–333

Brandon CM, Woodruff JD, Lane DP, Donnelly JP (2013) Tropical cyclone wind speed constraints from resultant storm surge deposition: a 2500 year reconstruction of hurricane activity from St. Marks, FL. Geochem Geophys Geosyst 14:2993–3008. doi:10.1002/ggge.20217

Denommee KC, Bentley SJ, Droxler AW (2014) Climatic controls on hurricane patterns: a 1200-y near-annual record from Lighthouse Reef, Belize. Sci Rep 4:1–7. doi:10.1038/srep03876

Donnelly JP (2005) Evidence of past intense tropical cyclones from backbarrier salt pond sediments: a case study from Isla de Culebrita, Puerto Rico, USA. J Coast Res 42:201–210

Donnelly JP, Webb III T (2004) Backbarrier sedimentary records of intense hurricane landfalls in the northeastern United States. In: Murnane RJ, Liu KB (eds) Hurricanes and typhoons: past, present, and future. Columbia University Press, New York, p 58–95

Donnelly JP, Woodruff JD (2007) Intense hurricane activity over the past 5,000 years controlled by El Nino and the West African monsoon. Nature 447:465–468. doi:10.1038/nature05834

Donnelly JP, Bryant SS, Butler J et al (2001a) 700 yr sedimentary record of intense hurricane landfalls in southern New England. Geol Soc Am Bull 113:714–727

Donnelly JP, Roll S, Wengren M et al (2001b) Sedimentary evidence of intense hurricane strikes from New Jersey. Geology 29:615–618

Donnelly JP, Butler J, Roll S et al (2004) A backbarrier overwash record of intense storms from Brigantine, New Jersey. Mar Geol 210:107–121. doi:10.1016/j.margeo.2004.05.005

Donnelly C, Hanson H, Larson M (2009) A numerical model of coastal overwash. Proc ICE Marit Eng 162:105–114. doi:10.1680/maen.2009.162.3.105

Donnelly JP, Hawkes AD, Lane P et al (2015) Climate forcing of unprecedented intense-hurricane activity in the last 2000 years. Earth's Future 3:49–65. doi:10.1002/2014EF000274

Elsner JB, Kara AB (1999) Hurricanes of the North Atlantic: climate and society. Oxford University Press on Demand, New York

Elsner JB, Jagger TH, Liu K (2008) Comparison of hurricane return levels using historical and geological records. J Appl Meteorol Climatol 47:368–374. doi:10.1175/2007JAMC1692.1

Emanuel K (2005) Increasing destructiveness of tropical cyclones over the past 30 years. Nature 436:686–688

Ercolani C, Muller J, Collins J et al (2015) Intense Southwest Florida hurricane landfalls over the past 1000 years. Quat Sci Rev 126:17–25. doi:10.1016/j.quascirev.2015.08.008

Fan D, Liu K (2008) Perspectives on the linkage between typhoon activity and global warming from recent research advances in paleotempestology. Sci Bull 53:2907–2922. doi:10.1007/s11434-008-0341-2

Forsyth AJ, Nott J, Bateman MD (2010) Beach ridge plain evidence of a variable late-Holocene tropical cyclone climate, North Queensland, Australia. Palaeogeogr Palaeoclimatol Palaeoecol 297:707–716. doi:10.1016/j.palaeo.2010.09.024

Frappier AB (2008) A stepwise screening system to select storm-sensitive stalagmites: taking a targeted approach to speleothem sampling methodology. Quatern Int 187:25–39. doi:10.1016/j.quaint.2007.09.042

Gischler E, Shinn EA, Oschmann W et al (2008) A 1500-year holocene Caribbean climate archive from the Blue Hole, Lighthouse Reef, Belize. J Coast Res 24:1495–1505

Gray WM (1990) Strong association between West African rainfall and U.S. landfall of intense hurricanes. Science 249:1251–1256

Haig J, Nott J, Reichart GJ (2014) Australian tropical cyclone activity lower than at any time over the past 550–1,500 years. Nature 505:667–671. doi:10.1038/nature12882

Harley GL, Grissino-Mayer HD, Horn SP (2011) The Dendrochronology of Pinus elliottii in the lower Florida keys: chronology development and climate response. Tree-Ring Res 67:39–50. doi:10.3959/2010-3.1

Haug GH, Hughen KA, Sigman DM et al (2001) Southward migration of the intertropical convergence zone through the holocene. Science 293:1304–1308

Hetzinger S, Pfeiffer M, Dullo W-C et al (2008) Caribbean coral tracks Atlantic Multidecadal Oscillation and past hurricane activity. Geology 36:11–14. doi:10.1130/G24321A.1

Hippensteel SP (2011) Spatio-lateral continuity of hurricane deposits in back-barrier marshes. Geol Soc Am Bull 123:2277–2294. doi:10.1130/B30261.1

Horton BP, Rossi V, Hawkes AD (2009) The sedimentary record of the 2005 hurricane season from the Mississippi and Alabama coastlines. Quatern Int 195:15–30. doi:10.1016/j.quaint.2008.03.004

Kagawa A, Sano M, Nakatsuka T et al (2015) An optimized method for stable isotope analysis of tree rings by extracting cellulose directly from cross-sectional laths. Chem Geol 393–394:16–25. doi:10.1016/j.chemgeo.2014.11.019

Kilbourne KH, Moyer RP, Quinn TM, Grottoli AG (2011) Testing coral-based tropical cyclone reconstructions: an example from Puerto Rico. Palaeogeogr Palaeoclimatol Palaeoecol 307:90–97. doi:10.1016/j.palaeo.2011.04.027

Knapp PA, Hadley KS (2012) A 300-year history of Pacific Northwest windstorms inferred from tree rings. Glob Planet Chang 92–93:257–266. doi:10.1016/j.gloplacha.2012.06.002

Korty RL, Camargo SJ, Galewsky J (2012) Variations in tropical cyclone genesis factors in simulations of the Holocene epoch. J Clim 25:8196–8211. doi:10.1175/JCLI-D-12-00033.1

Landsea CW, Nicholls N, Gray WM, Avila LA (1996) Downward trends in the frequency of intense Atlantic hurricanes during the past five decades. Geophys Res Lett 23:1697–1700

Landsea CW, Feuer S, Hagen A et al (2012) A reanalysis of the 1921–30 Atlantic hurricane database. J Clim 25:865–885. doi:10.1175/JCLI-D-11-00026.1

Lane P, Donnelly JP, Woodruff JD, Hawkes AD (2011) A decadally-resolved paleohurricane record archived in the late Holocene sediments of a Florida sinkhole. Mar Geol 287:14–30. doi:10.1016/j.margeo.2011.07.001

Lewis DB, Finkelstein DB, Grissino-Mayer HD et al (2011) A multitree perspective of the tree ring tropical cyclone record from longleaf pine (*Pinus palustris* Mill.), Big Thicket National Preserve, Texas, United States. J Geophys Res. doi:10.1029/2009JG001194

Li Z-H, Labbé N, Driese SG, Grissino-Mayer HD (2011) Micro-scale analysis of tree-ring δ18O and δ13C on α-cellulose spline reveals high-resolution intra-annual climate variability and tropical cyclone activity. Chem Geol 284:138–147. doi:10.1016/j.chemgeo.2011.02.015

Lin N, Lane P, Emanuel KA et al (2014) Heightened hurricane surge risk in northwest Florida revealed from climatological-hydrodynamic modeling and paleorecord reconstruction. J Geophys Res Atmos 119:8606–8623. doi:10.1002/2014JD021584

Liu KB (2004) Paleotempestology: geographic solutions to hurricane hazard assessment and risk prediction. In: Janelle DG, Warf B, Hansen K (eds) WorldMinds: geographical perspectives on 100 problems: commemorating the 100th Anniversary of the Association of American Geographers 1904–2004. Springer Netherlands, Dordrecht, pp 443–448

Liu KB, Fearn ML (1993) Lake sediment record of late Holocene hurricane activities from coastal Alabama. Geology 21:793–796

Liu KB, Fearn ML (2000) Holocene history of catastrophic hurricane landfalls along the Gulf of Mexico coast reconstructed from coastal lake and marsh sediments. In: Ning Z, Abdollahi KK (eds) Current stresses and potential vulnerabilities: implications of global climatic change for the Gulf of Mexico Region of the United States. Franklin Press, Baton Rouge, pp 38–47

Liu KB, Lu H, Shen C (2008) A 1200-year proxy record of hurricanes and fires from the Gulf of Mexico coast: testing the hypothesis of hurricane–fire interactions. Quatern Res 69:29–41. doi:10.1016/j.yqres.2007.10.011

Liu KB, Li C, Bianchette TA et al (2011) Storm deposition in a coastal backbarrier lake in Louisiana caused by Hurricanes Gustav and Ike. J Coast Res 64:1866

Malaize B, Bertran P, Carbonel P et al (2011) Hurricanes and climate in the Caribbean during the past 3700 years BP. The Holocene 21:911–924. doi:10.1177/0959683611400198

Mann ME, Woodruff JD, Donnelly JP, Zhang Z (2009) Atlantic hurricanes and climate over the past 1,500 years. Nature 460:880–883. doi:10.1038/nature08219

McCloskey TA, Keller G (2009) 5000 year sedimentary record of hurricane strikes on the central coast of Belize. Quatern Int 195:53–68. doi:10.1016/j.quaint.2008.03.003

McCloskey TA, Knowles JT (2009) Migration of the tropical cyclone zone throughout the holocene. In: Elsner BJ, Jagger HT (eds) Hurricanes and climate change. Springer US, Boston, pp 169–187

McCloskey TA, Liu K (2012) A 7000 year record of paleohurricane activity from a coastal wetland in Belize. The Holocene 1–14. doi: 10.1177/0959683612460782

McCloskey TA, Bianchette TA, Liu KB (2013) Track patterns of landfalling and coastal tropical cyclones in the Atlantic basin, their relationship with the North Atlantic Oscillation (NAO), and the potential effect of global warming. Am J Clim Chang 2:12–22. doi:10.4236/ajcc.2013.23A002

Morton RA, Paine JG, Blum MD (2000) Responses of stable bay-margin and barrier-island systems to Holocene sea-level highstands, western Gulf of Mexico. J Sediment Res 70:478–490. doi:10.1306/2DC40921-0E47-11D7-8643000102C1865D

Moy CM, Seltzer GO, Rodbell DT, Anderson DM (2002) Variability of El Nino/Southern Oscillation activity at millennial timescales during the Holocene epoch. Nature 420:162–165. doi:10.1038/nature01194

Naquin JD, Liu K, McCloskey TA, Bianchette TA (2014) Storm deposition induced by hurricanes in a rapidly subsiding coastal zone. J Coast Res 308–313. doi: 10.2112/SI70-052.1

Nott J (2004) Palaeotempestology: the study of prehistoric tropical cyclones—a review and implications for hazard assessment. Environ Int 30:433–447. doi:10.1016/j.envint.2003.09.010

Nott J (2010) A theory (involving tropical cyclones) on the formation of coarse-grained sand beach ridges in NE Australia. Geol Soc Lond, Spec Publ 346:7–22. doi:10.1144/SP346.2

Nott J (2011a) A 6000 year tropical cyclone record from Western Australia. Quatern Sci Rev 30:713–722. doi:10.1016/j.quascirev.2010.12.004

Nott J (2011b) Tropical cyclones, global climate change and the role of Quaternary studies. J Quatern Sci 26:468–473. doi:10.1002/jqs.1524

Nott J, Forsyth A (2012) Punctuated global tropical cyclone activity over the past 5,000 years. Geophys Res Lett. doi:10.1029/2012GL052236

Nott J, Jagger T (2013) Deriving robust return periods for tropical cyclone inundations from sediments. Geophys Res Lett 40:370–373. doi:10.1029/2012GL054455

Nott J, Smithers S, Walsh K, Rhodes E (2009) Sand beach ridges record 6000 year history of extreme tropical cyclone activity in northeastern Australia. Quatern Sci Rev 28:1511–1520. doi:10.1016/j.quascirev.2009.02.014

Otvos EG (1995) Multiple pliocene-quaternary marine highstands, northeast Gulf Coastal plain: fallacies and facts. J Coast Res 11:984–1002

Otvos EG (2000) Beach ridges—definitions and significance. Geomorphology 32:83–108. doi:10.1016/S0169-555X(99)00075-6

Otvos EG (2011) Hurricane signatures and landforms—toward improved interpretations and global storm climate chronology. Sediment Geol 239:10–22. doi:10.1016/j.sedgeo.2011.04.014

Rhodes EG, Polach HA, Thom BG, Wilson SR (1980) Age structure of Holocene coastal sediments; Gulf of Carpentaria, Australia. Radiocarbon 22:718–727

Scileppi E, Donnelly JP (2007) Sedimentary evidence of hurricane strikes in western Long Island, New York. Geochem Geophys Geosyst. doi:10.1029/2006GC001463

Tanner WF (1995) Origin of beach ridges and swales. Mar Geol 129:149–161

Toomey MR, Curry WB, Donnelly JP, van Hengstum PJ (2013a) Reconstructing 7000 years of North Atlantic hurricane variability using deep-sea sediment cores from the western Great Bahama Bank. Paleoceanography 28:31–41. doi:10.1002/palo.20012

Toomey MR, Donnelly JP, Woodruff JD (2013b) Reconstructing mid-late Holocene cyclone variability in the Central Pacific using sedimentary records from Tahaa, French Polynesia. Quatern Sci Rev 77:181–189. doi:10.1016/j.quascirev.2013.07.019

Trouet V, Harley GL, Domínguez-Delmás M (2016) Shipwreck rates reveal Caribbean tropical cyclone response to past radiative forcing. Proc Natl Acad Sci 113:3169–3174. doi:10.1073/pnas.1519566113

van Hengstum PJ, Scott DB (2011) Ecology of foraminifera and habitat variability in an underwater cave: distinguishing anchialine versus submarine cave environments. J Foram Res 41:201–229. doi:10.2113/gsjfr.41.3.201

van Hengstum PJ, Donnelly JP, Toomey MR et al (2014) Heightened hurricane activity on the Little Bahama Bank from 1350 to 1650 AD. Cont Shelf Res 86:103–115. doi:10.1016/j.csr.2013.04.032

van Hengstum PJ, Donnelly JP, Kingston AW et al (2015a) Low-frequency storminess signal at Bermuda linked to cooling events in the North Atlantic region, West Sussex. Paleoceanography, 30:52–76. doi:10.1002/2014PA002662

van Hengstum PJ, Richards DA, Onac BP, Dorale JA (2015b) Coastal caves and sinkholes. In: Shennan I, Long AJ, Horton BP (eds) Handbook of sea-level research. Wiley, pp 83–103

van Hengstum PJ, Donnelly JP, Fall PL et al (2016) The intertropical convergence zone modulates intense hurricane strikes on the western North Atlantic margin. Sci Rep 6:21728. doi:10.1038/srep21728

Wallace DJ, Woodruff JD, Anderson JB, Donnelly JP (2014) Palaeohurricane reconstructions from sedimentary archives along the Gulf of Mexico, Caribbean Sea and western North Atlantic Ocean margins. Geol Soc Lond, Spec Publ 388:481–501. doi:10.1144/SP388.12

Welford MR, Bossak BH, Gibney EJ, et al (2017) Archival evidence of secular changes in Georgia hurricanes: 1750–2012. In: Collins JC, Walsh K (eds) Hurricanes and climate change. Springer

Williams HFL (2009) Stratigraphy, sedimentology, and microfossil content of Hurricane Rita storm surge deposits in southwest Louisiana. J Coast Res 25:1041–1051. doi:10.2112/08-1038.1

Williams HFL (2010) Storm surge deposition by Hurricane Ike on the Mcfaddin National Wildlife Refuge, Texas: implications for paleotempestology studies. J Foram Res 40:210–219. doi:10.2113/gsjfr.40.3.210

Williams HFL (2011a) Stratigraphic record of hurricanes Audrey, Rita and Ike in the Chenier plain of southwest Louisiana. J Coast Res Spec Issue 64:1921–1926

Williams HFL (2011b) Shell bed tempestites in the Chenier Plain of Louisiana: late holocene example and modern analogue. J Quatern Sci 26:199–206. doi:10.1002/jqs.1444

Williams HFL (2012) Magnitude of Hurricane Ike storm surge sedimentation: implications for coastal marsh aggradation. Earth Surf Process Landf 37:901–906. doi:10.1002/esp.3252

Williams HFL (2013) 600-year sedimentary archive of hurricane strikes in a prograding beach ridge plain, southwestern Louisiana. Mar Geol 336:170–183. doi:10.1016/j.margeo.2012.12.005

Williams HFL, Flanagan WM (2009) Contribution of Hurricane Rita storm surge deposition to long-term sedimentation in Louisiana coastal Woodlands and marshes. J Coast Res Spec Issue 56:1671–1675

Williams HFL, Choowong M, Phantuwongraj S et al (2016) Geologic records of holocene typhoon strikes on the Gulf of Thailand coast. Mar Geol 372:66–78. doi:10.1016/j.margeo.2015.12.014

Woodruff JD, Donnelly JP, Mohrig D, Geyer WR (2008) Reconstructing relative flooding intensities responsible for hurricane-induced deposits from Laguna Playa Grande, Vieques, Puerto Rico. Geology 36:391–394. doi:10.1130/G24731A.1

Woodruff JD, Donnelly JP, Okusu A (2009) Exploring typhoon variability over the mid-to-late Holocene: evidence of extreme coastal flooding from Kamikoshiki, Japan. Quatern Sci Rev 28:1774–1785. doi:10.1016/j.quascirev.2009.02.005

Woodruff JD, Kanamaru K, Kundu S, Cook TL (2015) Depositional evidence for the Kamikaze typhoons and links to changes in typhoon climatology. Geology 43:91–94. doi:10.1130/G36209.1

Chapter 2
Archival Evidence of Secular Changes in Georgia Hurricanes: 1750–2012

Mark R. Welford, Brian H. Bossak, and Ethan J. Gibney

Abstract North Atlantic hurricanes present the greatest recurring meteorological hazard along the southern and eastern shores of the USA. Since the late 1800s, in contrast to much of the Southeastern USA, the Georgia coast has experienced infrequent hurricane landfalls, particularly in recent decades. As a result, coastal storm preparedness complacency appears to be rampant along the Georgia coastline. Both local and state governments were unprepared for shadow evacuation during Hurricane Floyd in 1999. The study described here includes an examination of temporal and spatial trends in hurricane landfall along the Georgia coast from 1750 to 2012. Since 1750, 18 of the 24 recorded hurricanes that made landfall along the Georgia coast occurred between 1801 and 1900, yet the hurricane intensities have declined since 1851. Most critically our data establishes that the mean location of landfall along the Georgia coast has shifted 60 km north and hence closer to Savannah. Future efforts to re-characterize hurricane surge zones and improve evacuation infrastructure along the Georgia coast must reevaluate this threat.

M.R. Welford (✉)
Department of Geology and Geography, Georgia Southern University, Statesboro, GA 30460, USA

B.H. Bossak
Department of Health and Human Performance, College of Charleston, Charleston, SC, USA
e-mail: brian.bossak@gmail.com

E.J. Gibney
NOAA National Weather Service Forecast Office, San Diego, CA 92127, USA
e-mail: ethan.gibney@noaa.gov

North Atlantic hurricanes present the greatest recurring meteorological hazard along the southern and eastern shores of the USA. The most significant magnitude of such storms is experienced at the location(s) where landfall occurs, although significant impacts from wind and rain accompany hurricanes (and their weaker constituents as tropical storms and tropical depressions) as they move inland or tangent to a shoreline. While storm surges, especially to the northeast of the location of hurricane landfall, can and are very destructive, more recent tropical cyclones have been associated with effects from high winds and inland flooding. Since the late 1800s, in contrast to much of the Southeastern USA, the coastline of Georgia has experienced infrequent hurricane landfalls, particularly in recent decades. This study includes an examination of temporal and spatial trends in hurricane landfall along the Georgia coast from 1750 to 2012.

The North Atlantic hurricane database (HURDAT2) contains data on tropical cyclones occurring in the North Atlantic basin as far back as the year 1851. Analysis of tropical cyclone activity across the time series contained in HURDAT2 suggests large temporal and spatial variability in hurricane landfalls. This variability in tropical cyclones combined with an influx of people moving to coastal zones within the state of Georgia since the most recent hurricane landfall is potentially associated with coastal storm preparedness complacency that appears to be rampant along the Georgia and Northern Florida coasts (Kaiser 2014; Wang and Kapucu 2007). According to the US Census, since 1980, the population of Georgia has increased by nearly 5 million with more than 200,000 more people living permanently in the coastal counties of Chatham (where Savannah is located adjacent to South Carolina), Bryan, Liberty, McIntosh, Glynn, and Camden (located adjacent to Florida) (Table 2.1; US Census 1995, 2000, 2015). Many of the new residents along Georgia's coastal zones may not have experience with hurricanes and therefore potentially underestimate the possibility of hurricane destructiveness (Gladwin and Peacock 1997). In addition, while many new coastal residents may underestimate hurricane destructiveness, many other newcomers might overestimate risk, leading to potentially dangerous shadow evacuation events, whereby people leave potential landfall sites when they were not required to and thus exacerbate the hazard potential

Table 2.1 Georgia and Georgia's coastal counties populations from 1960 to 2014

Year	2014 est.	2010	2000	1990	1980	1970	1960
Georgia	10097343	9687653	8186453	6478216	5463105	4589575	3943116
Chatham	283379	265128	232048	216935	202226	187767	188299
Bryan	33906	30233	23417	15438	10175	6539	6226
Liberty	65198	63453	61610	52745	37583	17569	14487
McIntosh	14214	14333	7144	8634	8046	7371	6364
Glynn	82175	79626	67568	62496	54981	50528	41954
Camden	52027	50513	43664	30167	13371	11334	9975
Totals	530899	503286	435451	386415	326382	281108	267305

of coastal storms (Gladwin and Peacock 1997). For example, in 1999 a shadow evacuation occurred as Hurricane Floyd was projected to potentially track onshore in Northern Florida and Georgia. The resulting shadow evacuation along the Georgia coast overwhelmed the north and east lanes of I-95 and I-16, respectively, near Savannah (Dash and Gladwin 2007). This particular shadow evacuation event was part of one of the largest hurricane evacuations and traffic jams in US history, with estimates of more than 2.5 million people in Florida, Georgia, South Carolina, North Carolina, and Virginia leaving their homes to escape the potential landfall of Hurricane Floyd (Baker 2000). In South Carolina, 25 % of households took two or more cars compounding the traffic congestion along the evacuation routes (Wolshon et al. 2001; Dow and Cutter 2002). Many of those fleeing the approaching storm were trapped along the established evacuation routes, with many divided highways becoming unidirectional – which still did little to relieve the tremendous amount of traffic at standstill. If the storm had made landfall in locations where multitudes were essentially stuck on evacuation routes, the risk of significant harm could have been greatly magnified.

The most recent hurricane landfall along the Georgia coastline was Hurricane David (Saffir-Simpson Hurricane Wind Scale (SSHWS) Category 2) in 1979, and, as previously mentioned, the last major evacuation occurred during Hurricane Floyd (SSHWS Category 2) in 1999. The "Sea Islands" hurricane of August 27, 1893 (SSHWS Category 3, 16 ft surge) that killed between 1000 and 2000 people and left upward of 30,000 people homeless is ranked among the five deadliest US hurricanes to impact the country in recorded history (Fraser 2006; HVRI 2014). In fact, it is quite likely that this storm killed many more people than is currently estimated in historical accounts, but estimates of those killed were mostly restricted to white, landowning Americans (Fraser 2006; HVRI 2014). Just 12 years prior, the sixth deadliest hurricane in US history, the Savannah hurricane of August 27, 1881 (SSHWS Category 2), caused 335 deaths in Savannah (Fraser 2006). Historical records indicate that although Georgia has avoided significant hurricane landfalls in the last couple of decades, the coastline of Georgia itself is not immune to destructive, deadly hurricanes.

Researchers (e.g., LaVoie 2011) have stressed the importance of identifying historical, pre-HURDAT2 tropical cyclones in order to understand long-term trends in tropical cyclone activity, especially in light of a possible association between the frequency and intensity of tropical cyclones and anthropogenic climate change (Webster et al. 2005; Maue 2009, 2011). In order to better characterize the risk of hurricane landfall over time, we utilized historical records and HURDAT2 data to examine hurricane impacts along Georgia's coastal counties to develop a long-term dataset (1750–2012) of coastal Georgia hurricanes. Given our temporal constraints, we did not model synthetic tropical cyclone tracks, although such efforts have proved useful over longer time scales (e.g., Elsner et al. 2008; Woodruff et al. 2008). We generated track maps of hurricanes present in our records using ArcGIS. Utilizing this reconstructed data, we estimated return intervals for all intense (or major) hurricanes in the area of study (SSHWS 3 or higher). Our goal was to

improve and enhance the existing knowledge of the long-term record of severe coastal storms and improve the risk characterization of hurricane impacts along Georgia's coastal counties.

1   Description of Data and Methods

North Atlantic hurricanes have been historically documented for hundreds of years; however, few regional chronologies exist that include tropical cyclone activity prior to 1851. These works include Poey (1855), Tannehill (1938), Ludlum (1963), Dunn and Miller (1960), Millas (1968), Fernandez-Partagas and Diaz (1996), Fraser (2006), Chenoweth (2006), Chenoweth and Divine (2008), Mock (2008), Mock et al. (2010), LaVoie (2011), Chenoweth and Mock (2013), and Chenoweth (2014). In previous work, we noted a decreasing trend in coastal Georgia hurricane frequency in the period from 1851 to 2012 (Bossak et al. 2014). This trend appears to mirror regional decreases in hurricane activity along the eastern shore of the USA (Keim et al. 2007; Zandbergen 2009; Maue 2011). Thus, extending coastal Georgia's hurricane record back in time to 1750 by utilizing documentary records, such as diaries, newspapers, ship logs, military records, and weather records, is another critical step toward evaluating the significance of our prior findings and better understanding of long-term hurricane activity along Georgia's coastline. Estimated storm tracks were developed from the historical data and observations and then compared and contrasted with Chenoweth's (2006) proposed storm tracks. Although quantitative meteorological data is scarce prior to 1851, qualitative data from historical archives are plentiful even for Georgia, which contained a somewhat more sparsely populated coastal region compared with states such as South Carolina or Massachusetts. Although geological proxies, such as tree-ring isotope records (e.g., Miller et al. 2005) and sediment records (e.g., Liu and Fearn 2000; Elsner et al. 2008; Ercolani et al. 2015), in coastal barrier island cores are useful for detecting prehistoric overwash patterns with characteristics of strong hurricane landfalls, they are not used for our analysis due to spatial, temporal, and intensity issues that have yet to be resolved with high confidence. For example, in one study, ten barrier island core samples along the Gulf of Mexico were analyzed for overwash evidence of Hurricane Opal of 1995, a Category 4 hurricane; however, only one of the ten cores contained an overwash sand layer (Elsner et al. 2008).

An extensive inventory of documentary information located in state, federal, personal, and business websites including all the websites listing historic newspapers from Florida, Georgia, and South Carolina and NOAA's compilation by Sandrik and Landsea (2003) was conducted as part of this research project. All hurricane and tropical storms that possibly impacted the Georgia coast identified in academic journal articles, books, professional papers, and monologues were tabulated. Extensive use was made of Fraser (2006) as a reference volume because it provides an in-depth chronology of historical hurricanes affecting South Carolina and coastal Georgia from the late 1600s to 2004. Data from these sources generated

a potential tropical cyclone candidate list of 61 hurricanes and/or tropical storms that impacted the Georgia coast from 1750 to 1850. Primary sources (newspapers, diaries, ship logs/weather records) were then used to evaluate each individual storm and narrow the candidate list further.

2 Newspapers

Newspapers from the period prior to 1851 occasionally contained detailed weather descriptions of Georgia tropical cyclones dating as far back as the late eighteenth century. These descriptions sometimes included details of the storm including the estimated time frame of storm impact, wind direction, wind intensity, rainfall, storm surge, and damage to buildings and trees and specific details about the geographic extent of damage, ship wrecks, and deaths (Ludlum 1963; Mock 2004; Chenoweth 2006). Historically, Savannah served as the state's primary site of maritime, urban, and economic activity; as a result many newspapers within the research period relevant to this study (1751–1850) were printed in the surrounding area. Specifically, 13 newspapers from Savannah provide some details about tropical cyclones that impacted Georgia. Relevant newspapers that were examined for hurricane-related information included the *Columbian Museum* (1796–1799), *Gazette of the State of Georgia* (1783), *Georgia Gazette* (1763–1802), *Royal Georgia Gazette* (1781), *Savannah Republic* (1802–1903), *Georgia Republican and State Intelligencer* (1802–1808), *Savannah Evening Ledger* (1808–1815), *Savannah Daily Republic* (1820), *Savannah Republican* (1816–1855), *Savannah Mercury* (1828–1829), *Savannah Gazette* (1817), *Daily Republican* (1839–1840), and *The Savannah Museum* (1822).

Milledgeville, which is currently a small-sized city in central Georgia, served as the state's capital from 1804 to 1868. As a result, numerous influential newspapers were printed in the city during this period of time. These papers regularly reported on regional stories and reprinted news accounts from other regional or state newspapers. We examined eight newspapers published in Milledgeville for hurricane-related information, including *Federal Union* (1830–1872), *Georgia Argus* (1810–1815), *Milledgeville Intelligencer* (1808), *Reflector* (1817–1819), *Georgia Journal* (1809–1847), *Southern Recorder* (1820–1872), *Southern* (1828), and the *Standard of Union* (1836–1841). The following excerpt from the *Georgia Journal* provides an example of a Milledgeville newspaper report on what was later determined to be the strongest tropical cyclone to impact Savannah during the nineteenth century (1824):

> *Georgia Journal*, Tuesday, September 28: "HURRICANE-After some days of heavy threatening weather, with profuse showers of rain, the wind commenced blowing on Tuesday afternoon about 5 o'clock, from the N.E. accompanied with rain, from which time it continued increasing until 2 o'clock the following morning during which it blew a complete hurricane. Shortly after 2 o'clock the wind suddenly changed to the S. E. where it continued about an hour and a half, and then gradually abated. Our city has not experienced anything of a like nature that will bear a comparison with it, since the dreadful storm of 1804."

In addition, 11 newspapers from other areas in the state were reviewed for hurricane information including the *Albany Patriot* (1845–1866), *Athenian* (1827–1832), *Cherokee Phoenix* (1828–1834), *Columbus Enquirer* (1828–1890), *Columbus Sun* (1828–1890), *Georgia Messenger* (1823–1847), *Macon Telegraph* (1826–1908), *Upper Georgia Whig* (1847), *Southern Banner* (1833–1837), *Southern Miscellany* (1842–1849), and the *Southern Whig* (1838–1850).

Prior to the mid-1830s, most newspapers in the state were published on a weekly basis and were biased toward news associated with the date of publication. Thus, weaker storms, or storms that impacted areas with sparse populations during a period of several days prior to print, were not necessarily considered newsworthy enough to warrant inclusion. In general and as would be expected, newspaper reports contained more extensive information concerning stronger storms and their impacts. An exception to the emphasis on the most recent storms occurred when documentary letters or contributed articles from other regional newspapers were reprinted several weeks after the occurrence of a particular storm.

The newspapers that were utilized for the historical (pre-1851) portion of this research project are archived in a variety of sources, including The Digital Library of Georgia, the Library of Congress, the University System of Georgia's Interlibrary Loan, Georgia Historical Society, and various websites. A total of 40 newspapers were examined for this historical hurricane research. In addition, the research team visited the Georgia Historical Society's Savannah location on several different occasions in person to scan the newspaper archives and peruse the microfiche newspapers on file.

3 Diaries/Letters

Private diaries, journals, and letters provide useful documentation of the impact of tropical cyclones at, and immediately after, landfall. These documents often contain large amounts of weather-related information such as daily weather activity and have proven useful for tropical cyclone reconstruction (Sullivan 1986). Many documents contained valuable information on weak tropical cyclones that would not have warranted inclusion in newspapers. The following excerpt is an account by Aaron Burr, Vice President of the United States of America, who was visiting John Couper in St. Simons when a hurricane passed directly over St. Simons Island and the city of Darien, Georgia:

> Wednesday, September 12, 1804.
>
> On Friday last, hearing that Mr. Couper had returned and was very seriously ill, I took a small canoe with two boys, and went to see him. He lay in a high fever. When about to return in the evening, the wind had risen so that, after an ineffectual attempt, I was obliged to give it up, and remain at Mr. C.'s. In the morning the wind was still higher. It continued to rise, and by noon blew a gale from the north, which, together with the swelling of the water, became alarming. From twelve to three, several of the out-houses had been destroyed; most of the trees about the house were blown down. The house in which we were shook and rocked so much that Mr. C. began to express his apprehensions for our safety. Before three, part of the

piazza was carried away; two or three of the windows bursted in. The house was inundated with water, and presently one of the chimneys fell. Mr. C. then commanded a retreat to a storehouse about fifty yards off, and we decamped, men, women, and children. You may imagine, in this scene of confusion and dismay, a good many incidents to amuse one if one had dared to be amused in a moment of much anxiety. The house, however, did not blow down. The storm continued till four, and then very suddenly abated, and in ten minutes it was almost a calm. I seized the moment to return home. Before I had got quite over, the gale rose from the southeast and threatened new destruction. It lasted great part of the night, but did not attain the violence of that from the north; yet it contributed to raise still higher the water, which was the principal instrument of devastation. The flood was about seven feet above the height of an ordinary high tide. This has been sufficient to inundate great part of the coast; to destroy all the rice; to carry off most of the buildings which were on low lands, and to destroy the lives of many blacks. The roads are rendered impassable, and scarcely a boat has been preserved. Thus all intercourse is suspended. The mail-boat, which ought to have passed northward last Saturday, and by which it was intended to forward this letter, has not been heard of. This will go by a man who will attempt to get from Darien to Savannah on foot, being sent express by the manager of Major Butler; but how, or whether it will go on from Savannah, is not imagined.

Major Butler has lost nineteen negroes (drowned), and I fear his whole crop of rice, being about two hundred and sixty acres. Mr. Brailsford, of Charleston, who cultivates in rice an island at the mouth of the Alatamaha, has lost, reports say, seventy-four blacks. The banks and the buildings on the low lands are greatly injured. We have heard nothing from the southward, nor farther than from Darien northward.

Davis, Matthew L. (1837). *Memoirs of Aaron Burr*. New York: Harper & Brothers.

4   Ship Logs

Although ship logbooks can provide detailed climatological information, there are limitations when searching for data specific to hurricanes. Little information is provided on the landfall location of hurricanes. Also, logbook entries may be scarce during hurricane season due to ships seeking refuge of harbors. Despite these limitations, ship log databases were explored as part of this study. Here are two examples from the Navy Department Library:

Gun Boat #164 sank in a squall at St. Mary's Georgia. 20 drowned. 16 Sep. 1813.

From the same storm, a letter by Commodore Hugh Campbell to the Secretary of the Navy:

The Saucy Jack privateer, of Charleston, lying ready to sail, is now lying high and dry on a marsh that must be at least 5 feet above the level of low tide. She draws 14 feet, seven feet being the common rise.

5   Meteorological Records

Early instrumental data and meteorological records occasionally included observations of temperature, precipitation, wind speed, wind strength, cloudiness, and barometric pressure. The Live Oak Public Libraries and the Fort Pulaski National

Monument were contacted to obtain any meteorological records available from 1750 to 1850. Unfortunately, neither the Live Oak Public Libraries nor the Fort Pulaski National Monument had any such records to provide for this study. The *meteorological register* (1831–1842) was also examined, which included monthly weather records from Oglethorpe Barracks in Savannah and Ft. Marion in St. Augustine, but neither of these yielded viable data suggestive of hurricane activity. However, several residents of early Savannah owned barometers and recorded barometric pressure readings. Barometric pressure readings below 29 in Hg are generally considered to be consistent with the presence of hurricanes or strong tropical storms, and the magnitude of the reading itself provides information on extrapolated storm intensity. But reliable barometric readings indicative of hurricanes were not found among the weather diaries analyzed at the Georgia Historical Society.

The Georgia Historical Society in Savannah, GA, possesses original meteorological observations for Savannah (listed in the Society's index under "Savannah Meteorological Tables, MS 700"). The observations available were from January 1828 through December 1828 and January 1836 through December 1836. These observations were limited and did not identify any possible hurricanes.

Intensities (weak vs. strong) of historical hurricanes (1750–1850) were determined by using estimates of the Saffir-Simpson Hurricane Potential Damage Scale as a foundation. Death toll, storm surge, and reported damage to crops, infrastructure, and ships were examined for each hurricane candidate in-line with methodologies noted by Chenoweth and Mock (2013); however, we did not feel sure enough of our ability to replicate their methodology as described, nor our limited data sets to estimate hurricane intensities as other than either weak or strong.

6 Creation of Hurricane Trajectories

Michael Chenoweth (2006) describes the reanalysis of Poey's previously published chronology of Atlantic basin tropical cyclones using 5606 newspapers and 456 logbooks from numerous archives. Our tracks were constructed using methods similar to those employed in Scheitlin et al. (2010). We initially utilize explicit latitude/longitude (lat/lon) pairs provided in Chenoweth's analysis. These pairs represent the known or estimated location of the center of a tropical cyclone based on ship records, personal accounts, and newspapers. In cases where there are at least two lat/lon pairs given for a storm, the points are plotted as x and y values using ESRI's ArcGIS. A line is then drawn connecting the two points. If there are additional points, lines are drawn connecting these subsequent points. Next, to show how storms may have moved between oft-distant points, the tracks are adjusted (i.e., bent) based on information gathered from the historical literature. Finally, the tracks were smoothed using a Bezier interpolation smoothing algorithm. For storms not appearing in Chenoweth's analysis, we estimated storm paths from information determined through the historical literature. Based on this collated information, rough tracks are again drawn in ArcGIS and then smoothed as described earlier.

A sum total of 40 newspaper periodicals (including all publications available from 1750 to 1850), 22 journals/diaries, 9 ship log/weather record databases, 10 hurricane chronologies, 31 books, and 62 websites (including descriptions and articles) were utilized to develop the historical hurricane candidate list. Upon further analysis, we concluded that ten hurricanes impacted coastal Georgia between 1750 and 1850 (eight direct impacts and two indirect impacts). To increase confidence in our storm counts, each storm that was considered a hurricane in the final database contained at least three separate primary evidentiary sources (Table 2.2).

Table 2.2 Hurricanes that directly impacted Georgia's coastline: 1750–2012: A total of 24 hurricanes occurred during the period of study

Date	Name	Intensity Peak	Intensity At landfall	County
Sept 8–16, 1752	–	–	Strong	
Sept 3–12, 1804	–	–	Strong	McIntosh/C
Oct 4–5, 1811	–	–	Weak	St. Marys/S
Sept 16–17, 1813	–	–	Strong	St. Marys/S
Aug 1–9, 1817	–	–	Weak	St. Marys/S
Sept 7–15, 1824	–	–	Strong	McIntosh/C
Aug 11–19, 1830	–	–	Weak	Chatham/N
Aug 1–7, 1837	–	–	Weak	Duval, Fl/S
Sept 30-Oct 10, 1842	–	–	Weak	Glynn/C-S
Oct 5–13, 1846	–	–	Weak	Levy, Fl/S
Oct 19–22, 1853	–	SSHWS 2	SSHWS 1	Offshore
Sept 7–12, 1854	–	SSHWS 3	SSHWS 3	Chatham/N
Sept 1–13, 1878	–	SSHWS 2	SSHWS 1	Offshore
Aug 21–29, 1881	–	SSHWS 2	SSHWS 2	Liberty
Aug 21–27, 1885	–	SSHWS 3	–	SC/N GA
Aug 15–30, 1893	–	SSHWS 3	SSHWS 3	Chatham/N
Sept 22–30, 1896	–	SSHWS 3	SSHWS 2	Inland
Aug 30-Sept 1, 1898	–	SSHWS 1	–	SC/N GA
Sept 25-Oct 6, 1898	–	SSHWS 4	SSHWS 4	Camden/S
Aug 23–30, 1911	–	SSHWS 2	SSHWS 1	SC/N GA
Sept 6–19, 1928	–	SSHWS 5	SSHWS 1	Offshore
Aug 5–14, 1940	–	SSHWS 1	SSHWS 1	SC/N
Oct 9–16, 1947	–	SSHWS 1	SSHWS 2	Chatham/N
Aug 25-Sept 6, 1979	David	SSHWS 5	SSHWS 2	McIntosh/C

*S = Southern GA coastline
C = Central GA coastline
N = Northern GA coastline
SSHWS = Saffir-Simpson Hurricane Wind Scale Category (1, 2, 3, 4 or 5)
WEAK = SSHWS Category 1 or 2 (estimated)
STRONG = SSHWS Category 3, 4 or 5 (estimated)

7   HURDAT2

This study also assessed the 14 hurricanes in the HURDAT2 database that made direct landfall along coastal Georgia during the period 1851–2012. Note that HURDAT2 includes a state designation where a hurricane makes direct impact along a coastal region (i.e., hurricane force winds are experienced and/or the center of the storm crosses the coast), and thus our definition of landfalls is synonymous with HURDAT2 state designations. Figure 2.1 illustrates the tracks of all coastal Georgia landfalls since 1751, including the HURDAT2 data.

8   Results

Our data identify five characteristics associated with the time series of Georgia hurricanes. First, 75 % (18/24) of all coastal Georgia hurricanes since 1750 occurred between 1801 and 1900 (Table 2.2 and Fig. 2.2). Second, there is no significant difference in the proportion of Category 1 hurricanes in comparison to the proportion of Category 2, 3, and 4 hurricanes between 1850 and 2012 (Table 2.2 and Fig. 2.3).
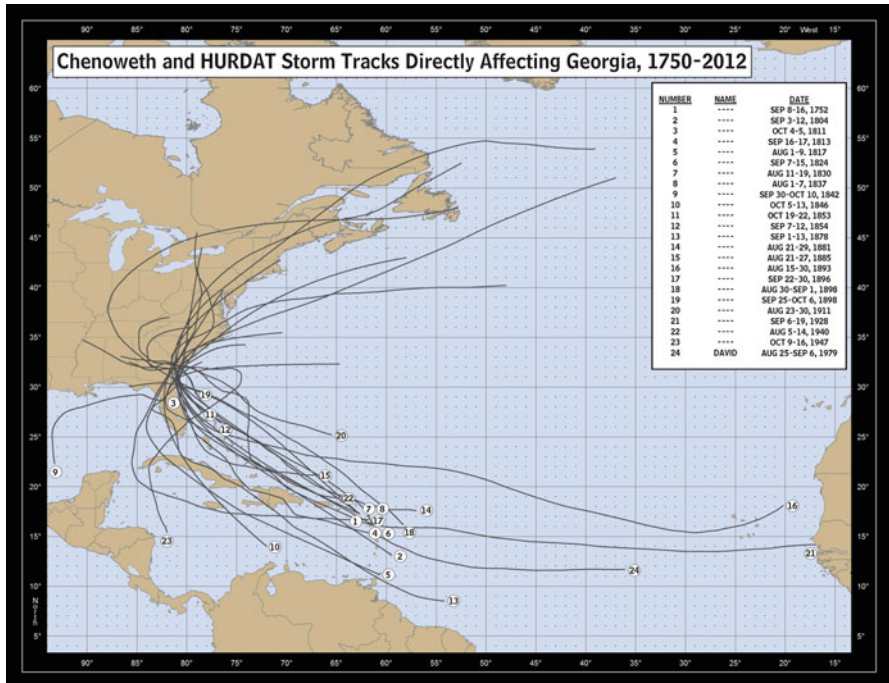
Fig. 2.1 Track maps of hurricanes making landfall along coastal Georgia between 1750 and 2012
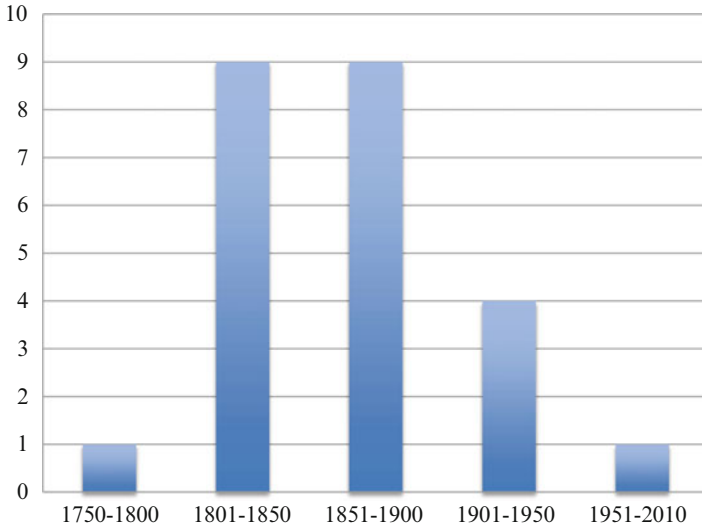
Fig. 2.2 Frequency of Hurricanes Striking Coastal Georgia: 1750–2012. Only the 24 hurricanes known to have made landfall or strongly impacted the Georgia coastline are included in this graph
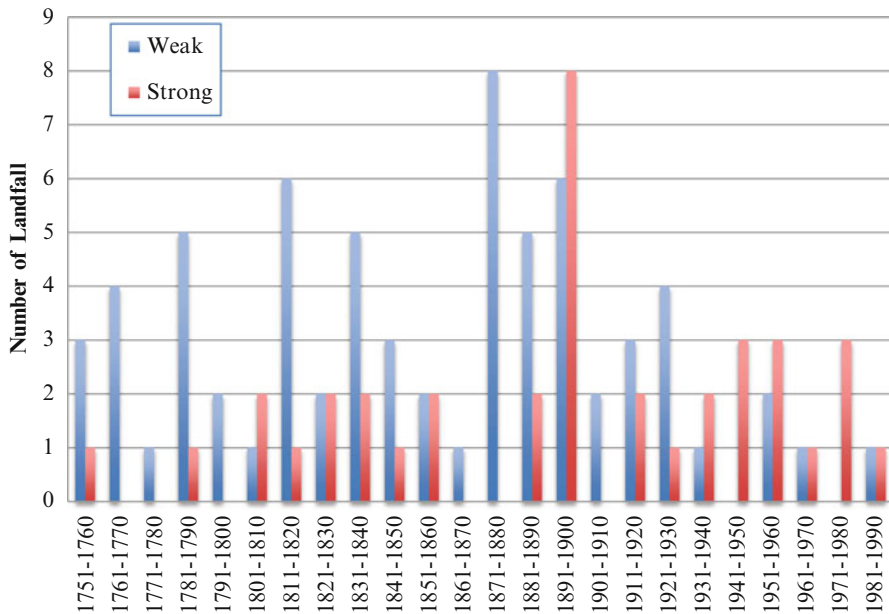

Fig. 2.3 Number of hurricanes affecting Georgia coast – 1751-1990 (weak is Category 1; strong is Categories 2, 3, 4). These include all those hurricanes that made the candidate list from 1751 to 1850 but excluding tropical storms and all those HURDAT2 storms that affected but not necessarily made landfall along the Georgia coast since 1851
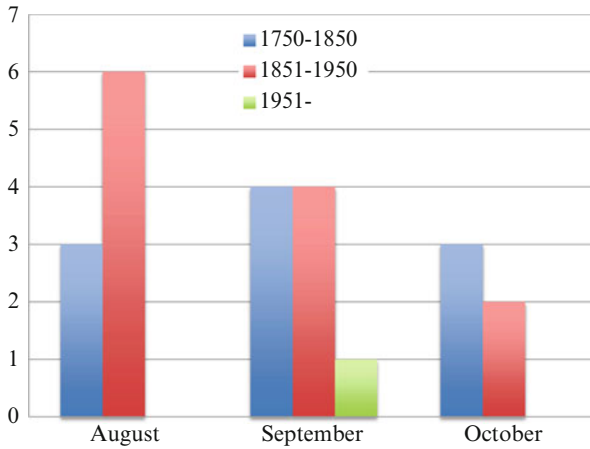
Fig. 2.4 Coastal Georgia Seasonality of Landfall from 1750 to 2012: Number of hurricane landfalls during hurricane season (June 1-November 30), by coastal region, from 1750 to 2012. There is no record of a Georgia hurricane landfall in the months of June, July, or November, with a peak landfall month of August. Data is from the North Atlantic Hurricane Database (HURDAT2) and historic records pre-1850

Third, on average, estimated intensities for the landfalling hurricanes recorded along coastal Georgia and neighboring regions (NE Florida and South Carolina) have decreased since 1851 (Table 2.2 and Fig. 2.3; Bossak et al. 2014, Fig. 2.3) with storm intensity peaking between 1880 and 1900. Fourth, our data indicates that more hurricanes, recorded along the Georgia coast, are occurring early in August since 1851 (HURDAT2) (Fig. 2.4). Lastly, the mean location of hurricane landfall along the Georgia coast, based on the estimated storm tracks assembled from the candidate list of historical hurricanes, has moved northward along the coast by approximately 60 km (Fig. 2.5).

9   Discussion

After careful review of the data, several questions surround the pattern of landfalls observed, particularly in light of recent climate change scenarios and their impact on tropical cyclone frequency and intensity. For example, why did nine strong hurricanes strike Georgia in the late 1800s, but only one made landfall in the late 1900s (Figs. 2.2 and 2.3)? What is the long-term nominal risk for hurricane landfall along the Georgia coast: is it more or less common for Georgia to experience so many (or so few) landfalls within a 100-year interval during the nineteenth (twentieth) century (Figs. 2.2 and 2.3)? The paucity of Atlantic sea surface temperature (SST) data prior to the operation of weather satellites in the 1960s hinders developing an adequate explanation for this temporal variability
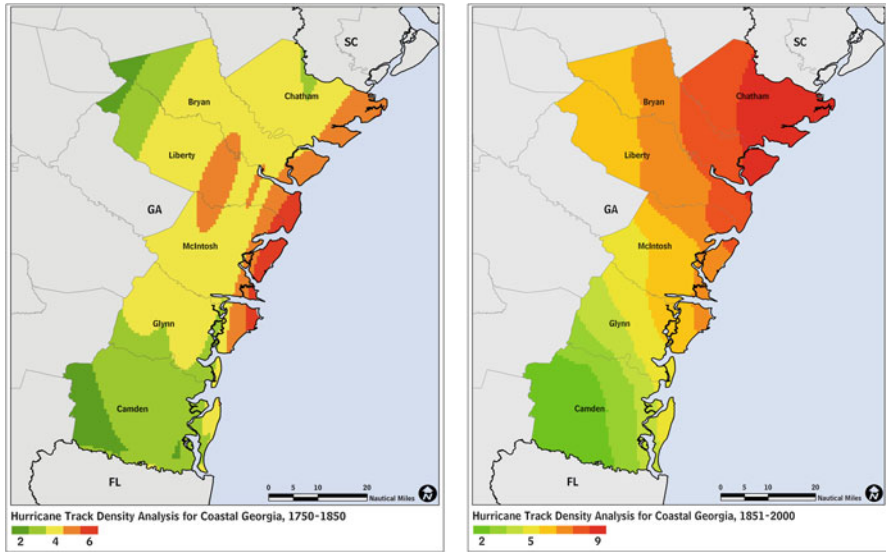
Fig. 2.5 Spatial Distribution of hurricanes based on line density analysis along coastal Georgia counties between 1750–1850 and 1851–2012

in hurricane impacts along the Georgia coast. Nevertheless, decadal variations in Atlantic SST (Atlantic Multidecadal Oscillation (AMO)), seasonal and temporal variations in Western Sahel rainfall, spatial-temporal variations in North Atlantic Oscillation (NAO), and fluctuations in El Niño-Southern Oscillation (ENSO) all play a role, along with a number of other climatologic factors, in either suppressing or enhancing Atlantic hurricane activity. The following is a speculative discussion of the possible role Atlantic SST, AMO, NAO, and ENSO might have played in the changes in hurricane frequency observed along the Georgia coast since 1751.

Decadal variations in hurricane activity have been tied to changes in Atlantic SST structure (Gray 1990). Variability in Western Sahel rainfall that affects North Atlantic hurricane formation (Gray 1990) appears related to fluctuations in the intensity of the thermohaline circulation (THC) in the North Atlantic (Gray et al. 1997). The NAO affects the position of the North Atlantic subtropical high cell and sea-level pressure patterns, with a resultant impact on the tracks of Atlantic basin tropical cyclones. When the NAO index is positive and the subtropical high is located more to the north and east, the East Coast of the United States is at higher risk for hurricane landfalls, and in contrast, when the NAO index is negative and the subtropical high is located more to the south and west, the Gulf Coast has a greater risk of hurricane landfalls (Elsner et al. 2000). The NAO also appears tied to decadal variations in the formation of deep water off Iceland (Kushnir 1994). In fact, in coupled atmospheric-ocean models, a positive NAO appears to increase THC and meridional heat transport in the North Atlantic (Hakkinen 1999). In the

1950s, the NAO index was positive, the Atlantic SSTs were relatively warm, and six hurricanes hit the East Coast, while just one hit the Gulf Coast region. In the 1960s, the NAO index was negative, the Atlantic SSTs were relatively cool, and six hurricanes made landfall along the Gulf Coast with none making landfall along the East Coast (Elsner et al. 2000). Elsner et al. (2000) infer that the NAO was mostly positive during the period from 1851 to 1951 suggesting that the large incidence of Georgia hurricane landfalls, especially in the 1880s and 1890s, was possibly associated with a subtropical high located more to the north and east, relatively warm Atlantic SSTs, a strong THC, and a positive AMO (Klotzbach et al. 2015). The high incidence of hurricane landfalls along the Georgia coast in the later 1800s (1881, 1885, 1893, 1896, Aug 1898, Sept 1898; Table 2.2 and Figs. 2.2 and 2.3) appears associated with a positive AMO (Klotzbach et al. 2015) but is split by one known period of high ENSO activity in 1890 (Garcia-Herrera et al. 2007).

ENSO events can suppress the formation of North Atlantic hurricanes (Goldenberg et al. 2001; Collins and Roche 2010); for instance, between 1991 and 1994, there were few Atlantic hurricanes (Landsea et al. 1996) due in part to a long-lasting El Niño event from 1991 to 1995 (Trenberth and Hoar 1996). La Niña, the cold phase of ENSO, promotes weak vertical shear in upper-level winds across the Atlantic and above-normal Western Sahel rainfall (Elsner et al. 2000). These works suggest that ENSO events might suppress, for a short period, physical processes controlled by a positive NAO, THC, and wet Western Sahels that determine decadal-long forcing of hurricane formation. Therefore the 8-year break between 1885 and 1893 might be a possible function of the 1890 ENSO event.

The proportion of weak and strong hurricanes from 1751 to 2012 appears to have held steady, but the number of both weak and strong hurricanes affecting Georgia's coast, including those that make landfall, has declined since 1851, particularly since the two-decade landfall activity peak of 1880–1900 (Fig. 2.3; Bossak et al. 2014).

What impacts will future global climatic change have on the seasonality, location of landfalls, and changes in hurricane intensity along the Georgia coastline? The temporal variability in historic and HURDAT2 data, the seasonal change in hurricane landfall, the migration north of the mean location of hurricane landfall along the Georgia coast, and even the reduction in frequency of hurricane landfalls in coastal Georgia are observations that may or may not be associated with long-term climate trends. Global climatic change driven by increased CO_2 levels is leading to increased variability, number, and intensity of both hurricanes (Webster et al. 2005; Knutson et al. 2010) and tornadoes (Trapp et al. 2007; Diffenbaugh et al. 2013) and increases in the number of warmer ocean temperature anomalies (Elsner et al. 2000; Virmani and Weisberg 2006).

Modeling suggests that anthropogenically enhanced global radiative forcing will lead to a 6–34 % decrease in hurricane frequency but an increase in hurricane intensity of 2–11 % by 2100 (Knutson et al. 2010). Our data might illustrate the early beginning of this shift in frequency (see Bossak et al. 2014) or suggest that hurricane trajectories since 1751 have shifted northward in possible response to enhanced global radiative forcing, with the end result that Georgia has experienced a

reduction in landfalls over the last 100 years (Table 2.2 and Fig. 2.3). Our data could also be anomalous given that anthropogenically enhanced global radiative forcing may increase Atlantic SSTs, which in turn may lead to increased Western Sahel rainfall that has been robustly associated with an increase in number and intensity of Atlantic hurricanes in prior research (Gray 1990).

Data suggest that the peak in hurricane landfalls along the Georgia coast has shifted from September during the period 1750–1850 to August during the period 1851–2010 (Fig. 2.4). Elsner et al. (2000) found that since 1801, the average landfall for East Coast hurricanes is September 6. However, data paucity hinders making a robust, defendable statement that Georgia landfalls represent a new trend in the seasonality of East Coast hurricanes. One question which needs further research is whether the hurricane season is increasing in duration with hurricanes occurring both earlier (e.g., 2005 hurricane season, Virmani and Weisberg 2006) and later in the traditional season (e.g., Hurricane Sandy). Our data suggests an increase in hurricanes occurring in August since 1851, which is earlier than the seasonal peak described in Elsner et al. (2000).

A line density analysis of hurricane tracks illustrates that between 1750 and 1850 and from 1851 to 2012, the mean location of hurricane landfall along the Georgia coast moved north by approximately 60 km (Fig. 2.5). Liberty and McIntosh counties (among the least densely populated Georgia coastal counties) experienced the highest frequency of hurricanes in coastal Georgia between 1750 and 1850, whereas the highest frequency of hurricanes occurred near Chatham County between 1851 and 2012 (Fig. 2.5). Whether this change represents a movement due to anthropogenically enhanced global radiative forcing and Atlantic SSTs or a change in tracks due to NAO forcing or a statistical anomaly is impossible to establish. Certainly, +NOA or −NOA indices affect the location of the subtropical high and the resultant track of hurricanes around the periphery of the high pressure. If this change is sustained in the future, the potential financial and human toll along coastal Georgia may return to the very high levels experienced in the late 1800s. The locus of hurricane landfall between 1851 and 2012 is Chatham County, where Savannah is located. This is troubling because since 1960, Chatham County and Savannah have seen a significant increase in human population (Table 2.1) and a related increase in infrastructure and are the most populated of coastal counties in Georgia (Table 2.1). Between 1960 and 2010, Chatham County's permanent population increased by 99,000 people, 80,000 of which have been added to Chatham County since 1980. Thus the largest growth in Chatham's population has occurred since the last hurricane landfall that of Hurricane David in 1979. These data mirror the storm preparedness complacency along the Georgia coast noted in prior research (Kaiser 2014; Wang and Kapucu 2007). Since the early historical period of 1750–1850, the locus of hurricane landfall has moved away from the least populated coastal county of McIntosh (with only 14,214 current residents) to the most populated: Chatham County with 283,379 residents (US Census 1995, 2000, 2015). Moreover, the 1999 Hurricane Floyd evacuation overwhelmed Chatham County's three evacuation routes of I-16, I-95, and US 80 (Dash and Gladwin 2007). Yet the only response in the intervening years has been to set up a protocol to open

eastbound lanes on I-16 to westbound traffic during hurricane evacuations from
Savannah (Chatham County Emergency Management 2012).

10 Strengths and Weaknesses

A study focusing solely on coastal Georgia's present and historical hurricane record
is novel. Our methodology suggests that historical data analysis can be used to fill
in potential gaps in the near-term landfall record based on geological proxy data (Lu
and Liu 2003). Georgia was established as a colony in 1732, and the first Georgia
newspaper published was the *Georgia Gazette* in 1763; therefore, historical records
before 1800 are limited. Because of this limitation, it is possible that undocumented
hurricanes made landfall along Georgia's coast prior to 1800. Moreover, we were
unable to conclusively identify a number of other hurricanes or tropical storms that
might have made landfall or tracked along the Georgia coast (Table 2.3). This list
represents storms that only have one or two documents supporting their existence.

A small sample size will typically yield insignificant statistical results. Due to
a lack of sufficient wind speed and barometric pressure records prior to 1851,
historical documents were heavily relied upon to determine whether winds were
at hurricane force and, if so, whether the storm was weak (Cat 1, 2) or strong (Cat
3, 4, 5).

Table 2.3 Other possible hurricanes that either made landfall or tracked along the Georgia coast
between 1750 and 1850

Date	Type	Location	C4	C5	C6	C7
Oct 22, 1780	Hurricane	Moved from NW Florida over Georgia, made ocean nr Valdosta		Yes		Yes
Oct 7 1783	Hurricane	Grazed Georgia coast:	Yes	Yes		
Aug 23–28, 1787	Hurricane	Grazed Georgia coast, landed SC		Yes		
Sept 19, 1787	Hurricane	Storm surge killed 23 along SC & GA coasts: Jordan 'History of Storms'	Yes	Yes		
Sept 8–9, 1811	Hurricane	Hurricane very close to GA shore	Yes	Yes		
late Aug 1819	TS	Possible TS landfall Darien	Yes		Yes	
Sept 27-28, 1822	Hurricane	Brushed Savannah, severe SC, 25 ships washed ashore, 200 drowned	Yes	Yes		
June 2–3, 1825	TS	Landfall St Augustine, moved back out to see, hit Tybee hard	Yes	Yes	Yes	
12–13 Oct 1848	TS	Hurricane force winds from St Marys to Savannah but offshore	Yes	Yes	Yes	

C4 Fraser 2006
C5 Chenowth 2006
C6 Sandrik & Landsea 2003
C7 LaVoie 2011

11 Conclusions

Georgia's coastal population has increased despite the underlying threat of a destructive hurricane in any given year (Fraser 2006). According to US Census Bureau (2010, 2015) data, 283,379 people reside in Chatham County, which encompasses metropolitan Savannah. This represents an 18 % increase from the 2000 population, which was recorded 1 year after the Hurricane Floyd evacuation along the southeastern US seaboard (US Census Bureau 2015) and a 29 % increase from the 1990 population recorded 1 year after Hurricane David hit just south of Savannah (US Census Bureau 1995, 2015). This growth is occurring faster than proportional increases in transportation infrastructure, such as Highway 80, which still serves as the only evacuation route for the entire population of Tybee Island (population of 3054, US Census Bureau 2015), as well as I-95 (N/S) and I-16 (E/W) that serve as primary evacuation routes along Georgia's coast. Given the potential for destructive hurricanes (nine between 1800 and 1850) to make landfall in this region, an evacuation-related disaster remains a high risk.

Significant numbers of tourists frequent the coastal counties of Georgia; in particular, Savannah attracted in 2014 13.4 million visitors, of which 7.6 million were overnight visitors spending over $2.5 billion and generating $20.7 million in hotel/motel tax revenue (Savannah Chamber of Commerce 2015). In excess of 90 % of the overnight visitors were involved in leisure travel and hence were tourists (Savannah Chamber of Commerce 2015). Although April, May, and June are the busiest months, there is little variation around the mean suggesting that each month Savannah attracts nearly a million visitors. Savannah's principal attraction is the city's historic architecture that although located high above any hurricane storm surge (Chatham Emergency Management 2015) is susceptible to wind damage. The Savannah hurricane of August 27, 1881 (SSHWS Category 2), caused 335 deaths in Savannah, yet the population was only 30,709 (Fraser 2006; US Census Bureau 2000). Today a similar-sized hurricane, if it had an orientation of between 65 and 90° to the coast, could inflict significant damage and potentially impact local residents and visitors. However, the Savannah hurricane of August 27, 1881, was only 1 of 24 hurricanes in this study that hit Savannah, therefore suggesting the likelihood of just such a reoccurrence is very small indeed.

At the same time that the population of Chatham and other coastal Georgia counties is increasing, FEMA released new proposed flood maps in 2015 for Georgia coastal counties that will allow the property elevation covered by FEMA to drop as flood elevations will drop between 1 and 3 ft (Glynn County FIRM maps 2015). This will mean many V-designated insurance zones will move to an A zone (V or velocity zones are the most flood prone and subject to both mandatory and the highest flood insurance rates). Zone Vs are subject to inundation by a 1 % annual chance flood event (FEMA 2015). Zone As are located landward of Zone V and occur where breaking wave heights occur between 1.5 and 3 ft during storm surges (FEMA 2015). For households moving from Zone V to Zone A, this will represent a significant reduction in insurance costs:

"My understanding is that Glynn County has fared extremely well," Hardman said. "FEMA has been very kind."

"We have no history of flooding, no history of hurricanes (in 40 years) and I think that's been accurately reflected by the new FEMA maps," Hardman said. "It's nice to be able to accurately portray the historical picture in future estimates." Jack Hardman, a Nationwide Insurance agent. (Hobbs 2015)

Given the spatiotemporal variability of hurricane landfalls that this research identifies between 1750 and 2010, the changes proposed by FEMA and statements by insurance agents and the rapid explanation of Chatham county and Savannah are deeply worrying. Even more worrying is that research by Webster et al. (2005) and Knutson et al. (2010) clearly suggests that anthropogenically enhanced global radiative forcing will lead to an increase in hurricane intensity of 2–11 % by 2100.

References

Baker EJ (2000) Southeast U.S. hurricane evacuation traffic study behavioral analysis. Hazards Management Group, Tallahassee

Bossak BH, Keihany S, Mullis D, Gibnery E, Welford MR (2014) Coastal Georgia is not immune: hurricane history, 1851–2012. Southeast Geogr 54(3):323–333

Chatham County Emergency Management (2012) Evacuation information. http://www.chathamemergency.org/evacuation-information/find-your-evacuation-zone.php. Accessed 13 Jan 2016

Chenoweth M (2006) A reassessment of historical Atlantic basin tropical cyclone activity, 1700–1855. Climate Change 76:169–240

Chenoweth M (2014) A new compilation of North Atlantic tropical cyclones, 1851–98. J Clim 27(23):8674–8685

Chenoweth M, Divine D (2008) A document-based 318-year record of tropical cyclones in the Lesser Antilles, 1690–2007. Geochem Geophys Geosyst 9(8), Q08013. doi:10.1029/2008GC002066

Chenoweth M, Mock CJ (2013) Hurricane "Amanda": rediscovery of a forgotten U.S. Civil War Florida Hurricane. Bull Am Meteorol Soc 94:1735–1742

Collins JM, Roache DR (2010) The inactive 2009 hurricane season in the North Atlantic Basin: an analysis of environmental conditions. Nat Weather Dig 34(2):117–128

Dash N, Gladwin H (2007) Evacuation decision making and behavioral responses: individual and household. Nat Hazards Rev 8(3):69–77

Diffenbaugh NS, Scherer M, Trapp RJ (2013) Robust increases in severe thunderstorm environments in response to greenhouse forcing. PNAS 110(41):16361–16366

Dow K, Cutter S (2002) Emerging hurricane evacuation issues: Hurricane Floyd and South Carolina. Nat Hazards Rev 3(1):12–18

Dunn GE, Miller BI (1960) Atlantic hurricanes. Louisiana State University Press, Baton Rouge

Elsner JB, Liu K-B, Kocher B (2000) Spatial variation in major U.S. hurricane activity: statistics and a physical mechanism. J Clim 13:2293–2305

Elsner JB, Jagger TH, K-b L (2008) Comparison of hurricane return levels using historical and geological records. J Appl Meteorol Climatol 7:368–374

Ercolani C, Muller J, Collins J, Saverese M, Squiccimara L (2015) Intense Southwest Florida hurricane landfalls over the past 1,000 years. Quatern Sci Rev 126:17–25

FEMA (2015) http://www.fema.gov/media-library/assets/documents/7273. Accessed 13 Jan 2016

Fernandez-Partagas J, Diaz HF (1996) Atlantic hurricanes in the second half of the nineteenth century. Bull Am Meteorol Soc 77:2899–2906

Fraser WJ Jr (2006) Low country hurricanes. The University of Athens Press, Athens

Garcia-Herrera R, Diaz HF, Garcia RR, Prieto MR, Barriopedro D, Moyano R, Hernandez E (2007) A chronology of El Nino events from primary documentary sources in Northern Peru. J Clim 21:1948–1962

Gladwin H, Peacock WG (1997) Warning and evacuation: a night for hard houses. In: Morrow BH, Gladwin H (eds) Hurricane Andrew: gender, ethnicity and the sociology of disasters. Routledge, New York, pp 52–74

Glynn County (2015) 2015 Draft FIRM Maps – working set. http://glynncounty.org/index.aspx?NID=1775. Accessed 13 Jan 2016

Goldenberg SB, Landsea CW, Mestas-Nunez AM, Gray WM (2001) The recent increase in Atlantic Hurricane activity: causes and implication. Science 293:474–479

Gray WM (1990) Strong association between West African Rainfall and U.S. landfall of intense hurricanes. Science 249(4974):1251–1256

Gray WM, Sheaffer JD, Landsea CW (1997) Climate trends associated with multi-decadal variability of Atlantic hurricane activity. In: Diaz HF, Pulwarty RS (eds) Hurricanes, climate and socioeconomic impacts. Springer, Berlin, pp 15–53

Hakkinen S (1999) Variability of the simulated meridional heat transport in the North Atlantic for the period 1951–1993. J Geophys Res 104:10991–11007

Hobbs L (2015) History on homeowners' side with new FEMA flood map in Georgia. The Brunswick News. September 2, 2015. http://www.emergencymgmt.com/disaster/History-on-Homeowners-Side-Wth-New-FEMA-Flood-Map.html. Accessed 13 Jan 2016

HVRI (2014) Hazards and Vulnerability Research Institute http://webra.cas.sc.edu/hvri/feature/aug2013_dom.aspx. Accessed 20 Aug 2015

Kaiser C (2014) Are you complacent about Hurricane preparedness? Disaster Planning Blog http://www.p.firestorm.com/Blog/are-floridians-getting-complacent-about-hurricane-preparedness.html. Accessed 13 Jan 2016

K-b L, Fearn ML (2000) Reconstruction of prehistoric landfall frequencies of catastrophic hurricanes in Northwestern Florida from lake sediment records. Quatern Res 54(2):238–245

Keim BD, Muller RA, Stone GW (2007) Spatiotemporal patterns and return periods of tropical storm and hurricane strikes from Texas to Maine. J Clim 20:3498–3509

Klotzbach P, Gray W, Fogarty C (2015) Active hurricanes era at its end? Nat Geosci 8:737–738

Knutson TR, McBride JL, Chan J, Emanuel K, Holland G, Landsea C, Held I, Kossin JP, Srivastava AK, Sugi M (2010) Tropical cyclones and climate change. Nat Geosci. doi:10.1038/ngeo779

Kushnir Y (1994) Interdecadal variations in North Atlantic sea surface temperature and associated atmospheric conditions. J Clim 7:141–157

Landsea CW, Nicholls N, Gray WM, Avilia LA (1996) Quiet early 1990s continues trend of fewer intense Atlantic hurricanes. Geophys Res Lett 23:1697–1700

LaVoie S (2011) An analysis of Atlantic hurricane seasons in the Pre-HURDAT Era (1751–1850). In: Abstracts of the 91st annual general meeting of American Meteorological Society

Lu H, Liu K (2003) Phytoliths of common grasses in the coastal environments of southeastern USA. Estuar Coast Shelf Sci 58:587–600

Ludlum DM (1963) Early American hurricanes, 1492–1870. American Meteorological Society, Boston

Maue RN (2009) Northern hemisphere tropical cyclone activity. Geophys Res Lett 36, L05805. doi:10.1029/2008GL035946

Maue RN (2011) Recent historically low global tropical cyclone activity. Geophys Res Lett 38, L14803. doi:10.1029/2011GL047711

Millas JC (1968) Hurricanes of the Caribbean and adjacent regions, 1492–1800. Academy of the Arts and Sciences of the Americas, Miami

Miller DL, Mora CI, Grissino-Mayer HD, Mock CJ, Uhle ME, Sharp Z (2005) Tree-ring isotope records of tropical cyclone activity. PNAS 103(39):14294–14297

Mock CJ (2004) Tropical cyclone reconstructions from documentary records: examples for South Caroline, United States. In: Murname RJ, Liu K (eds) Hurricanes and typhoons: past, present and future. Columbia University Press, New York, pp 121–147

Mock CJ (2008) Tropical cyclone variations in Louisiana, U.S.A., since the late eighteenth century. Geochem Geophys Geosyst 9(5):Q05V02. doi:10.1029/2007GC001846

Mock CJ, Chenoweth M, Altamirano I, Rodgers MD, García-Herrera R (2010) The Great New Orleans Hurricane of 1812. Bull Am Meteorol Soc 91:1653–1663

Poey A (1855) A chronological table comprising 400 cyclonic hurricanes which have occurred in the West Indies and in the North Atlantic within 362 years, from 1493–1855. J R Geogr Soc 25:291–328

Sandrik A, Landsea CW (2003) Chronological listing of tropical cyclones affecting North Florida and Coastal Georgia 1565–1899. http://www.aoml.noaa.gov/hrd/Landsea/history/index.html. Accessed 13 Jan 2016

Savannah Chamber of Commerce (2015) http://www.savannahchamber.com/economic-development/tourism. Accessed 13 Jan 2016

Scheitlin KN, Elsner JB, Malmstadt JC, Hodges RE, Jagger TH (2010) Toward increased utilization of historical hurricane chronologies. J Geophys Res 115:1–10

Sullivan CL (1986) Hurricanes of the Mississippi Gulf Coast. Gulf, Biloxi

Tannehill IR (1938) Hurricanes, their nature and history. Princeton University Press, Princeton

Trapp RJ, Diffenbaugh NS, Brooks HE, Baldwin ME, Robinson ED, Pal JS (2007) Changes in severe thunderstorms during the 21st century caused by anthropogenically enhanced global radiative forcing. PNAS 104(50):19719–19723

Trenberth KE, Hoar TJ (1996) The 1990–1995 El Niño-Southern Oscillation event: longest on record. Geophys Res Lett 23(1):57–60

U.S. Census Bureau (1995) Population of counties by decennial census: 1900 to 1990. http://www.census.gov/population/cencounts/ga190090.txt. Accessed 13 Jan 2016

U.S. Census Bureau (2000) Summary File 1 (SF 1) 100-percent data. http://factfinder.census.gov/faces/tableservices/jsf/pages/productview.xhtml?src=bkmk. Accessed 13 Jan 2016

U.S. Census Bureau (2015) State & county quickfacts http://quickfacts.census.gov/qfd/states/13000.html. Accessed 13 Jan 2016

Virmani JI, Weisberg RH (2006) The 2005 hurricane season: an echo of the past or a harbinger of the future? Geophys Res Lett 33, L05707. doi:10.1029/2005GL025517

Wang X, Kapucu N (2007) Public complacency under repeated emergency threats: some empirical evidence. J Public Admin Res Theory 18:57–78. doi:10.1093/jopart/mum001

Webster P, Holland G, Curry J, Chang H (2005) Changes in tropical cyclone number, duration, and intensity in a warming environment. Science 309(5742):1844–1846

Wolshon B, Urbina E, Levitan M (2001) National review of hurricane evacuation plans and policies. LSU Hurricane Center Report, www.hurricane.lsu.edu. Accessed 13 Jan 2016

Woodruff JD, Donnelly JP, Emanuel K, Lane P (2008) Assessing sedimentary records of paleohurricane activity using modeled hurricane climatology. Geochem Geophys Geosyst 9:Q09V10. doi:10.1029/2008GC002043

Zandbergen PA (2009) Exposure of US counties to Atlantic tropical storms and hurricanes, 1851–2003. Nat Hazards 48:83–99

Chapter 3
Near-Time Sea Surface Temperature and Tropical Cyclone Intensity in the Eastern North Pacific Basin

Jerry Y. Jien, William A. Gough, Ken Butler, Vincent Cheng, and George Arhonditsis

Abstract Although a significant relationship between near-time sea surface temperature (SST) and tropical cyclone (TC) intensity has been found for many major TC basins, this topic has not been explored in the eastern North Pacific (ENP) basin. When the main development region of the (ENP) Ocean is subdivided into eastern (EDR) and western (WDR) development regions, SSTs show a weak, yet significant, positive relationship with intensities of the six-hourly TC observations and storms' maximum strengths only in the WDR. This SST-storm intensity relationship is most apparent for the maximum lifetime TC intensity of WDR major hurricanes. The maximum strength of major hurricanes in the ENP basin is more clearly established in the WDR where SST is at least 25 °C, well below the minimum SST value that is observed in the North Atlantic basin.

When intensity observations are binned into SST intervals, the upper bound value of TC intensity is found to increase with SST. Compared to the previous TC climatological analysis (Whitney and Hobgood (1997) J Clim 10(11):2921–2930), the maximum relative wind speed has increased for SST bins of 27 °C (>26.5 °C and <27.5 °C) or higher. While a linear function was determined previously as the best empirical fit for the ENP maximum potential intensity (ENPMPI) for each SST bin (Whitney and Hobgood (1997) J Clim 10(11):2921–2930), other means of curve fitting such as the exponential decay (increase form) function also show skill at representing the SST-dependent ENPMPI in the WDR. When storm observations are regionally stratified, the rate of increasing maximum potential intensity with SST flattens out towards the highest SST category. Under the ambient condition in which

J.Y. Jien (✉) • W.A. Gough • V. Cheng • G. Arhonditsis
Department of Physical and Environmental Sciences, University of Toronto Scarborough, 1265 Military Trail, Scarborough, Ontario M1C 1A4, Canada
e-mail: jerry.jien@mail.utoronto.ca; gough@utsc.utoronto.ca; vi.cheng@utoronto.ca; georgea@utsc.utoronto.ca

K. Butler
Department of Computer and Mathematical Sciences, University of Toronto Scarborough, 1265 Military Trail, Scarborough, Ontario M1C 1A4, Canada
e-mail: butler@utsc.utoronto.ca

the theoretical MPI is assumed along ENP storm tracks, the updated relationship of the outflow temperature with SST resembles an inverse (negative) sigmoid curve.

1   Introduction

Sea surface temperatures (SSTs) have been long thought to be one of the major determining factors in limiting the structure and development of tropical cyclones (Miller 1958; Gray 1968; Merrill 1988; Evans 1993; DeMaria and Kaplan 1994; Whitney and Hobgood 1997; Saunders and Lea 2008). Spatial differences of SST anomalies have also been associated with the interannual variability of the El Niño–Southern Oscillation (ENSO) signal to influence regional tropical cyclone (TC) activity (Chu 2004; Diamond et al. 2013; Wood and Ritchie 2013; Patricola et al. 2014; Zhang and Wang 2015; Boucharel et al. 2016) and landfall impacts (Landsea et al. 1998; Goldenberg et al. 2001; Raga et al. 2013; Martinez-Sanchez and Cavazos 2014) due to changes in TC strength. However, recent research indicates that the development of TCs depends on more than just the absolute value of SST. As confirmed in the data-sparse eastern North Atlantic basin (Wu et al. 2010), Vecchi and Soden (2007), for example, noted that local differences in SST from the zonal or all-tropical mean provided a more effective metric to account for TC intensification than local SST itself. Such derivation of "relative SST" has shown a significant relationship to the storm intensity index (Zhang and Wang 2015) and some practicality in the field of seasonal TC forecast (Caron et al. 2015) in the eastern North Pacific (ENP) basin, where TCs are most active on a per unit area and time (Collins and Roache 2011). Despite this remote/regional control of the local TC intensity, the near-time SST remains one of the primary indicators in regulating the upper boundary of storm intensity and its lifetime maximum wind speed.

Miller (1958) proposed a direct relationship between SST and the minimum sea-level pressure in the surrounding air below the storm eye. Within the context of future climate change scenarios, Emanuel (1987) pointed out that the maximum reduction in sea-level pressure experienced through SST warming pertains only to the reduction of the lowest sustainable pressure achieved by the most intense TC. While a range of environmental conditions could influence the lifetime storm intensity (Gray 1968), SST has been acknowledged to influence a storm's maximum lifetime intensity. However, this direct relationship appears to be less important at explaining TC intensity above a certain SST value (Evans 1993; Michaels et al. 2006). For example, because dynamic forcings such as vertical wind shear are found to be key in determining the intensities of North Atlantic storms (Gray 1984;

Saunders and Lea 2008), it appears TC intensity could be more sensitive to other factors such as atmospheric dynamical influences rather than a single thermodynamic limit alone (Michaels et al. 2006).

SSTs have been found to act as a cap to limit TC intensity at a global scale (Merrill 1988), while outflow temperature at the upper troposphere is critical at determining its maximum potential intensity (MPI; Bister and Emanuel 1998). Using the most reliable storm observations for each TC development basin, intensity data were binned according to the corresponding SST groups to derive empirical relationships of SSTs and their maximum sustained TC winds for the North Atlantic Ocean (DeMaria and Kaplan 1994), Northwestern Pacific Ocean (Zeng et al. 2007) and ENP Ocean (Whitney and Hobgood 1997) and, most recently, Bay of Bengal (Kotal et al. 2009), part of the North Indian basin. While the extent of the relationship of SST-TC intensity varies among basins, a positive correlation between the maximum TC intensity and SST is generally agreed for all TC areas. However, the fact that most TCs do not achieve their SST-bounded MPI suggests other mechanisms are at play.

Instead of assigning each TC observation according to the SST group that it was detected, maximum sustained winds of all TC tracks were directly linked to SST values (Evans 1993; Michaels et al. 2006). However, results of correlating SST values with TC intensities of multiple basins also caution against the overreliance of a single SST predictor at explaining the sustained maximum TC winds (Evans 1993; Henderson-Sellers et al. 1998; Goldenberg et al. 2001). Such an attempt to determine the nature of the SST-TC relationship is further complicated by a storm's self-inflicted SST cooling along its tracks (Mei and Pasquero 2013). Using a relatively higher-resolution SST dataset, Michaels et al. (2006) shared a similar concern in addressing TC intensification by using SSTs alone. Although an SST threshold of 28.25 °C had been determined for North Atlantic TCs to reach major hurricane strength (50 m s^{-1} or greater), further SST warming does not substantially contribute to the rise of maximum TC wind speeds (Michaels et al. 2006).

Observations of TC intensity have been linked to climatological SSTs in multiple basins (Evans 1993) and updated for the North Atlantic TCs (Michaels et al. 2006). However, such research for the ENP basin has been only presented in Whitney and Hobgood (1997) but has not yet been evaluated statistically. Though it had been determined that ENP storm intensities respond to SST change as found in other basins (Evans 1993; Michaels et al. 2006), there may be differences in which ENP storm intensity shows its SST dependence. For instance, ENP storm intensity may be more responsive to thermodynamic limitation when ocean heat sources from both the sea surface and thermocline are considered (Balaguru et al. 2013; Jin et al. 2014). In addition, spatial pattern of SST anomalies may be expressed through ENSO in contrasting storm strength and impacts between local hurricane seasons (Raga et al. 2013; Wood and Ritchie 2013; Martinez-Sanchez and Cavazos 2014). Nevertheless, a direct attribution of near-time SST values to TC winds would also be an improvement over previous basin-wide studies (Emanuel 2005; Webster et al. 2005) and reveal how contemporaneous SST would facilitate the ultimate TC intensity at different levels of storm strength.

The effect of SST on maximum ENP storm intensity was better understood by attributing the SST category as a determining factor on the upper bound of MPI. Based on the exponential function in fitting the maximum TC intensity using SST in the North Atlantic basin (DeMaria and Kaplan 1994), a linear function has been extended for ENP storms (Whitney and Hobgood 1997). After all storms' translational speeds have been removed from the six-hourly observations of sustained winds, the eastern Pacific MPI (EPMPI; m s^{-1}) is developed as such:

$$\text{EPMPI} = C_0 + C_1 \, (\text{SST}), \tag{3.1}$$

whereas SST (°C) is associated with a slope (parameter estimate) of $C_1 = 79.17262$ m s^{-1} and a y-intercept (constant) of $C_0 = 5.361814$ m s^{-1} °C^{-1}. However, it has been nearly two decades since this empirical relationship on the effect of SST on maximum ENP storm intensity was first documented (Whitney and Hobgood 1997). Due to the SST warming observed worldwide (Xie et al. 2010) and locally (Ralph and Gough 2009), we hypothesize that the upper bound of maximum ENP storm intensity should have also shifted. If this direct relationship holds, then EPMPI pertaining to each SST group is expected to increase as well. As such, the SST-dependent theory of MPI can be refined using the most recent (1982–2013) SST climatological dataset which has a higher temporal-spatial resolution.

The objective of this study is to quantify and update the relationship between TC intensity and its underlying SSTs for ENP storms. Though there is more than one convention (Collins and Mason 2000; Ralph and Gough 2009) to derive the longitudinal boundary as to how the main development region of the ENP basin should be subdivided, to better understand its relationship with its environment, there is a general agreement that the local storm activity should be longitudinally stratified into eastern (EDR; 10–20°N and 85–112°W) and western (WDR; 10–20°N and 112–140°W) development regions. Hence, regional differences of how TC intensity responds to SST fluctuation will be investigated. Given the previous understanding of the regional sensitivity to environmental influences (Collins and Mason 2000; Ralph and Gough 2009; Jien et al. 2015), it is expected that intensities of all WDR storm observations and their lifetime maxima would be more sensitive to SST changes.

Section 2 describes details of the TC and SST datasets and methods used to analyze them. Section 3 provides one rationale for dividing the ENP basin longitudinally when examining possible environmental linkages. In Sect. 4 we explore the spatial misalignment of the warmest SST and maximum storm intensity. Section 5 explores the impact of SST on the maximum lifetime intensity. Section 6 updates the empirical functions by incorporating SST as the dependent variable using the most recent TC climatology. As an update from the work of Whitney and Hobgood (1997), Sect. 7 relates to the update of the outflow temperature at the top of storm clouds (assuming ambient MPI is attained), followed by conclusion in Sect. 8.

2 Data and Methods

Storm track data from the Central Pacific region and eastern North Pacific basins are retrieved from the best track HURDAT2 (Landsea and Franklin 2013) of the National Hurricane Center. This dataset records TC characteristics such as a storm's 1-min maximum sustained wind speed and its geographic positions at six-hourly intervals. Although non-developing tropical depressions are better integrated in the current storm dataset, the possible incompleteness of the early record led to our exclusion of storm data during the pre-satellite era. Due to uncertainty in wind speed estimation below the tropical storm designation, all non-developing tropical depressions are excluded in our analysis.

Modifications from the previous HURDAT (Davis et al. 1984) version include the maximum radii distances of 34 kt (18 m s^{-1}), 50 kt (26 m s^{-1}) and 60 kt (31 m s^{-1}) at all four quadrants of cardinal directions. In addition, reports of storm track positions other than the synoptic (00, 06, 12 and 18 Z) timeframes, when locations of intensity maxima and landfalls are detected, were recently added to the storm dataset after 2012. Because the goal of the study is to refine the analysis of the relationship of SST and TC intensity from Whitney and Hobgood (1997), the consideration of TC climatology in the study coincides with the data availability of the daily SST dataset, covering the period of 1982–2013.

Since only storm data within the ENP boundary, as defined in this study, are of interest for this work, a total of 1445 six-hourly TC observations that lie west of 140°W were eliminated. During the 32-year span, a total of 496 ENP storms were associated with 12,657 six-hourly TC observations, approximately 25.5 six-hourly observations per TC. In comparison, an average of 24.1 six-hourly observations are associated with each storm during the 1963–1993 period from Whitney and Hobgood (1997), a slightly shorter storm duration per TC than the analysis period of the study. Of the 1445 ENP storm observations eliminated beyond 140°W, 84 of them had continued to track further westward, past the International Date Line.

Daily mean SST values are retrieved from Optimum Interpolation SST dataset from the National Oceanic and Atmospheric Administration/National Climatic Data Center (NOAA/NCDC) with a spatial resolution of 0.25° by 0.25°.[1] This refined spatial-temporal resolution of SST record had been applied to investigate the TC-induced SST response (Hart et al. 2007; Dare and McBride 2011a) but has not been applied to update the relationship of ENP TC intensity with SST. Of the 12,657 six-hourly observations, 188 were observed over land. Hence, SST values over 12,469 TC observations from 1982 to 2013 are matched and extracted based on the linear interpolation of nearby SST grids. Because TCs had been shown to reduce local SST, averages of SST values 1 week prior to and after each storm passage at each TC

---

[1]*NOAA High-Resolution SST data provided by the NOAA/OAR/ESRL PSD, Boulder, Colorado, USA, from their Web site at* http://www.esrl.noaa.gov/psd/.

position are also included to monitor the progression of SST-dependent TC intensity. In total, a time series of 15 days of SSTs are obtained in association with each TC position.

The SST control of the maximum TC intensity has been established by a clear statistical linkage when SST is treated as a continuous variable. However, because there remain uncertainties in the measurement of storm wind speed at the tropical depression stage, records with wind speed below 18 m s^{-1} are often considered unreliable (Collins 2010). While the SST effect at various TC stages is of inherent interest, only maximum wind speeds for named storms (NS, sustained wind speed between 18 and 32 m s^{-1}), hurricanes (H, sustained wind speed between 33 and 50 m s^{-1}) and major hurricanes (MH, sustained wind speed greater than 50 m s^{-1}) are quantitatively related to the underlying seawater temperature. Any TC observation over land is of necessity associated with missing SST data. Consequently, a total of 188 observations and 2 storms that had their maximum lifetime intensities detected onshore are removed from the correlation analysis.

To update the previous Eastern Pacific Maximum Potential Intensity developed over the 1963–1993 period (Whitney and Hobgood 1997), all TC tracks are binned into a total of 13 SST groups from 19 to 31 °C, each with a 1 °C range. As an alternative way to demonstrate the impact of SST on TC intensity, daily SSTs 7 days prior to storm arrivals were averaged and rounded to the nearest whole number. As evidence of local SST warming, additional storm intensity data at the 30 °C and 31 °C SST categories are included in our analysis and added from a range of 19 to 29 °C groups (at the 1 °C SST interval) during the 1963–1993 TC climatological record (Whitney and Hobgood 1997). The maximum intensity values at each SST group are extracted to develop an empirical function that best fit these data points. Results were repeated for each of the ENP Main Development Region (MDR) subdivisions. Due to a lack of data for SST groups below 19 °C (23 °C), 27 (16) observations were removed from WDR (EDR).

To further understand the longitudinal variation of ENP storm activity and how TC intensity would respond to SST differences, the TC track record is longitudinally binned into subdivisions of the MDR: EDR and WDR (Fig. 3.1). The regional
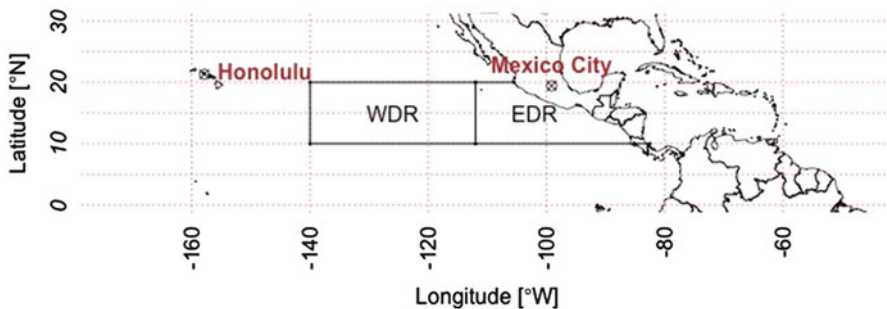

Fig. 3.1 The subdivision of the ENP Main Development Region (MDR) into the EDR and WDR

affiliation of each storm is directly linked to the region where a storm's maximum intensity is achieved (Collins and Roache 2011). For example, if a storm is formed in EDR but attained its maximum intensity in WDR, it is considered as a WDR storm. Additionally, for Sects. 5, 6 and 7, storm observations are partitioned into EDR or WDR according to their six-hourly positions, and their intensities are directly related to the underlying SST measurements. To compare with previous analysis performed by Whitney and Hobgood (1997), the relative velocity of storm track is compiled and calculated by subtracting its translation speed from the maximum wind speed. Translation speed is calculated by dividing the total distance travelled 6 h before and after the storm's current position, except at the initiation and dissipation points where six-hourly movements between the first two points and last two points are computed respectively (DeMaria and Kaplan 1994; Whitney and Hobgood 1997; Mei et al. 2012). The average translation speed for 12,657 tracks is about 4.4 m s^{-1}, comparable to the value of 4.7 m s^{-1}, noted in Whitney and Hobgood (1997).

3 Longitudinal Division of ENP Basin

Of the 496 ENP storms identified, many did not remain within the region where they first formed. Table 3.1 shows that if storms are regionally separated based on locations where they were originally detected, more than three quarters of seasonal storm counts were derived from EDR. However, many had achieved their maximum winds and spent the majority of their lifespan after entering the WDR. During this type of transition, others have suggested that these EDR-originated systems should be designated as WDR storms (Collins and Mason 2000; Collins and Roache 2011). As such, there tends to be a greater number of WDR storms produced during any storm season within a given annual cycle. Of the total 496 ENP storms between 1982 and 2013, the EDR-to-WDR storm ratio is approximately 3:4. In other words, a net movement of EDR-originated storms into WDR occurs every season. Although it

Table 3.1 Annual/seasonal numbers of storm genesis in terms of named/tropical storms (NS), hurricanes (H) and major hurricanes (MH) are stratified between EDR and WDR averaged from 1982 to 2013 based on the location where the peak intensity is established. Total storm count is also sorted according to where storms were initially detected

	EDR	WDR
Initial	11.8	3.8
NS	6.7	8.8
H	3.6	5.0
MH	3.0	5.6

is much more common for WDR storms to originate from the EDR, Rosa (1994) is the only exception where its region of translocation is reversed. Rosa (1994) originated in the WDR and unconventionally migrated to the EDR, where it peaked as a Category 2 (wind speed greater than 42.7 m s^{-1}) storm prior to dissipation over Mexico.

When the six-hourly TC observations are regionally assigned to where each of the 496 ENP storms attained its maximum lifetime intensity, TCs that tracked beyond 140°W are also included. Of all six-hourly track records associated with WDR storms, only 19 out of 8679 WDR storm tracks are recorded to have reached land. In comparison, a greater proportion (170 out of 5425) of EDR storm track points made landfall. While WDR storms are generally expected to travel westward, sometimes passing over Hawaii, only one had crossed Hawaii. This is due to a combination of the fact that Hawaii has a smaller land surface and that most of WDR storm landfalls on the North American continent require westerly winds to induce strong TC recurvature. Interestingly, when comparing the average translational speed between EDR and WDR landfalling storms, significant differences were detected. The average translation speed (15.3 m s^{-1}) associated with these EDR landfalling storm records is almost twice as large as the average (7.4 m s^{-1}) of all landfalling WDR storm tracks. Part of the difference is due to an overall more rapid recurvature of EDR storms when making landfalls.

During the period of 1982–2013, the annual average number of ENP storm count has been decreasing. This is mostly attributed to a below-normal number of WDR storms. On the other hand, the number of EDR storms stays relatively the same. Using the Theil-Sen slope estimator, a reduction of 0.17 WDR storms per year (5.3 storms over 32 years) is observed to be statistically significant at the 5 % significance level (Fig. 3.2). This value is large considering the seasonal average of storm count is 8.8 storms in the region. Since WDR storm activity represents a significant proportion of ENP storm activity, this reduction of WDR storm count is a major contributor to a decreasing trend (significant at $p < 0.05$, not shown) of total ENP storms during the same time period.

During an average hurricane season, more than half of the total ENP storm count (15.5) became WDR storms. However, the most recent (1981–2013) TC climatology indicates that the number of EDR-originated WDR storms has diminished. Trend analysis shows the annual proportion of these transitioning WDR storms to the total ENP storm count has decreased significantly ($p < 0.05$) averaging to a reduction of 5.1 WDR storms over the time period (Fig. 3.3). In addition, the reduced WDR storms match well with the diminishing number of EDR-to-WDR storms. As such, this downward trend implies seasonal WDR storm frequency is becoming less reliant on EDR for storm initiations, leading to further storm growth and development in the WDR.

While a reduced number of WDR storms may seem that WDR storm seasons are progressively less active, it should be interpreted more carefully. Most of the downward trend of total WDR storm (Fig. 3.2) is explained by the lack of transfer
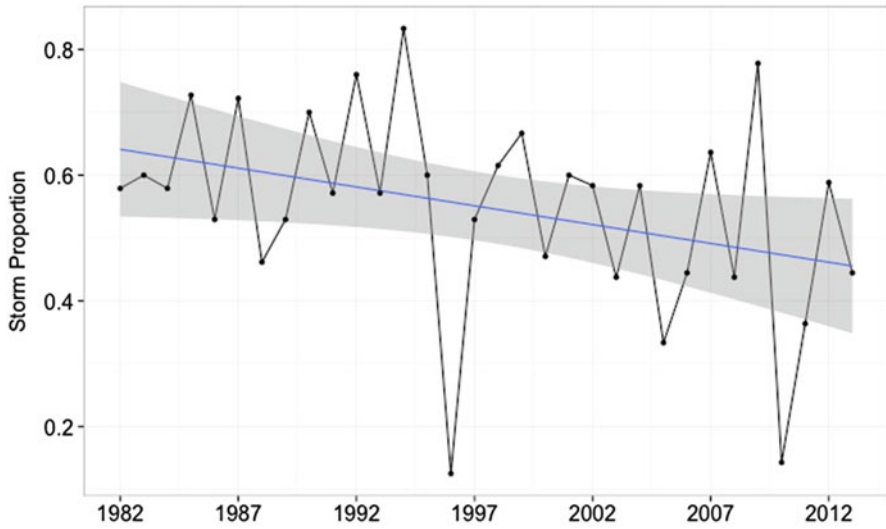
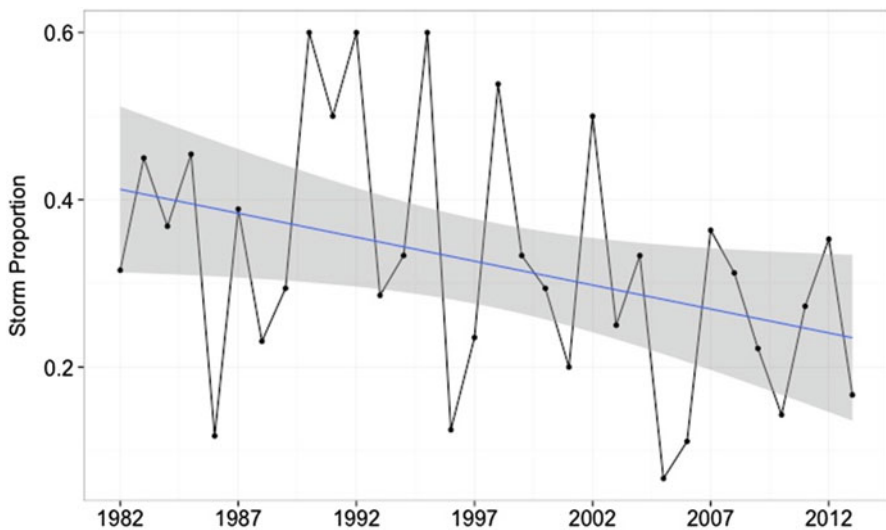**Fig. 3.2** Annual proportions of WDR storms to all ENP storms from 1982 to 2013

Fig. 3.3 Annual proportions of EDR-derived WDR storms to the total WDR storm count from 1982 to 2013

of storms from the EDR to WDR (Fig. 3.3). At the same time, the number of WDR storms that originated within the WDR boundary has remained stable. In fact, numbers of WDR hurricanes and major hurricanes have both increased significantly (Collins and Mason 2000).

4 Displacements of Maximum TC Intensity and Maximum SST and Initial Genesis Point

Under the influence of tropical easterly flow, ENP storms predominantly track westward and gradually divert poleward, over cooler tropical water prior to dissipation. Many of them can be traced as far upstream as African easterly waves that only intensify to TC strength after crossing the North Atlantic, the Caribbean Sea and the Gulf of Mexico (Molinari et al. 1997; Thorncroft and Hodges 2001). While most storms form close to the North American coast, these storms typically undergo intensification and obtain their maximum lifetime intensity distant from the coast. Figures 3.4a, b show the northwest tendency for storms before gaining peak intensity. On average, it requires a storm to shift 3.7° northward and 9.6° westward of its original identification point to achieve its maximum lifetime wind speed.
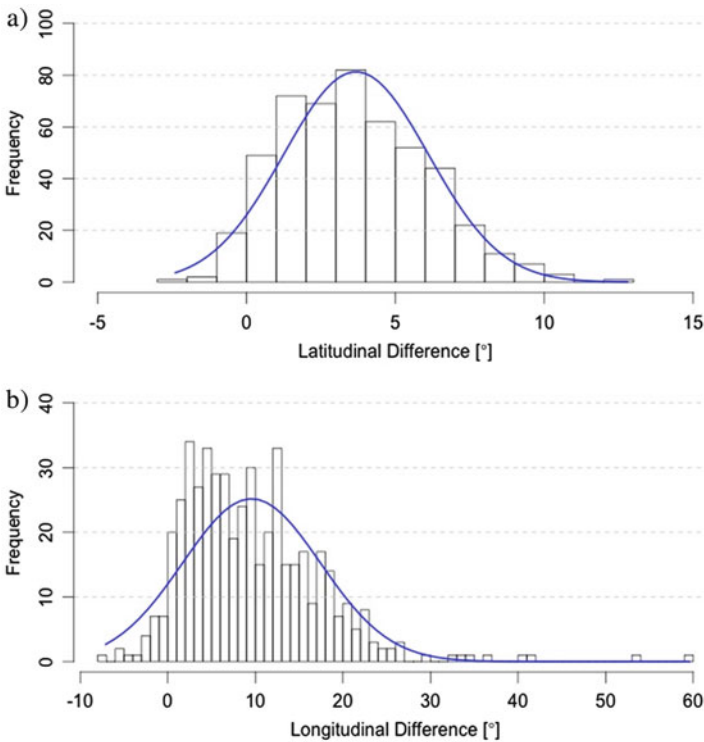
Fig. 3.4 (**a**) Distribution of latitudinal differences between the locations of storm genesis and maximum lifetime intensity for all ENP storms from 1982 to 2013 and (**b**) same as (**a**), but for longitudinal differences. Each histogram is outlined with a normal curve (in *blue*)
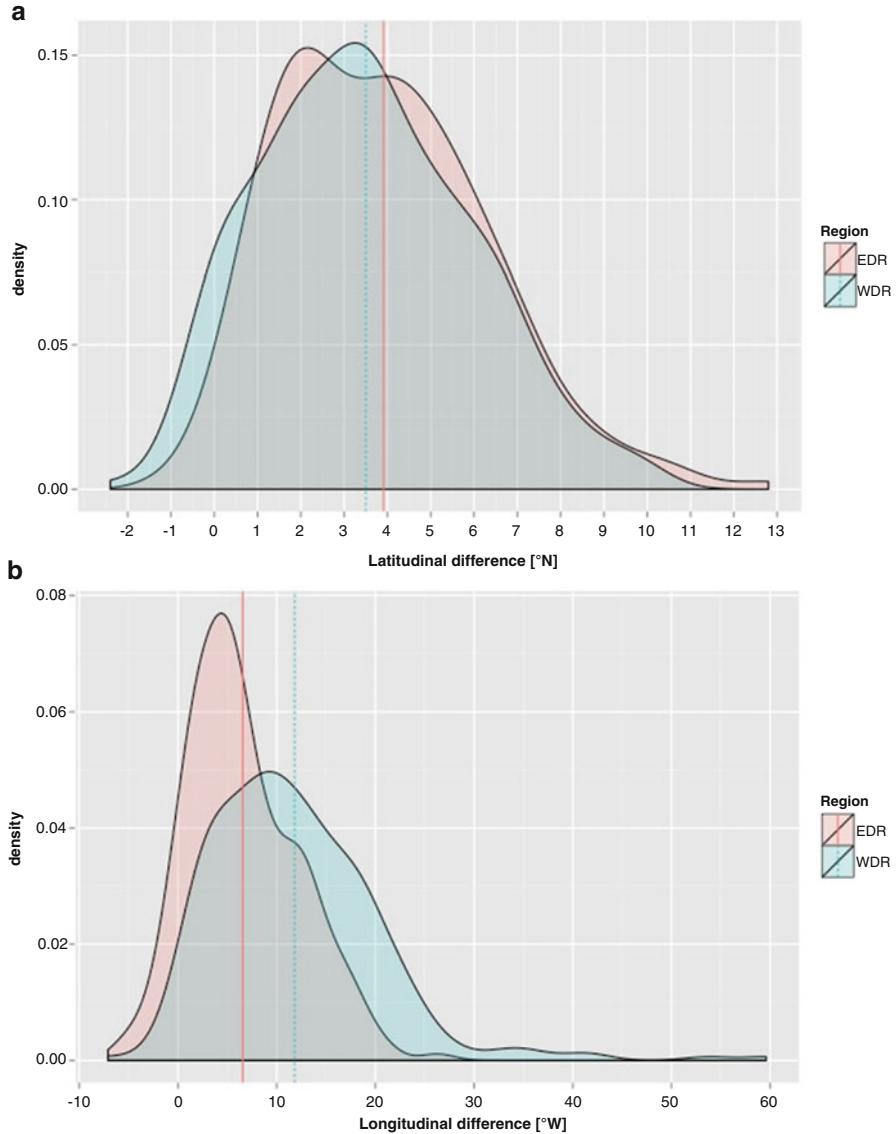
Fig. 3.5 (**a**) Distribution of latitudinal differences of locations between storm genesis and maximum lifetime intensity for EDR and WDR storms from 1982 to 2013 and (**b**) same as (**a**), but for longitudinal differences

When storms are separated into EDR and WDR subregions, regional variations of latitudinal (Fig. 3.5a) and longitudinal (Fig. 3.5b) differences are observed despite the average locations of their maximum lifetime intensities being found northwest of their initial detections. While the mean latitudinal difference between the initial storm detection and its maximum intensity of EDR storms is only 0.4° northward

of WDR storms, WDR storms' mean longitudinal difference is 5.3° westward of EDR storms. Although a greater longitudinal shift is detected for WDR storms, it is mostly attributed to the fact that 58 % of WDR storms were initiated in the EDR and experienced longer periods of intensification than those WDR storms that were originated within WDR. However, even if WDR storms that originated from EDR are removed, WDR's mean longitudinal difference is still maintained at 2.4° greater, significant at the 5 % confidence interval, than that of EDR storm's average longitudinal shift. The ability for WDR storms to track over a greater distance before achieving maximum intensity is linked to a longer longitudinal shift. This is supported by a clear right-tailed distribution for longitudinal differences, mainly attributed to WDR storms (Fig. 3.5b).

Although ocean temperature tends to be higher where storms initially formed, their genesis locations are not necessarily the highest SST experienced during a storm's lifecycle. The higher SST tends to provide the most optimum condition for TC development. However, its maximum lifetime intensity is rarely achieved where the highest SST is encountered. On average, the maximum intensity is located north-west of where the highest weekly SST is found a week prior to the storm passage. The resulting latitudinal (Fig. 3.6a) and longitudinal (Fig. 3.6b) differences are more evenly distributed compared to displacements between maximum intensity and initial storm genesis location (Fig. 3.4a, b). Such a comparison also demonstrates that the highest SSTs are experienced closer to maximum lifetime intensities than initial genesis locations of ENP storms. An average delay of 1.7 days is observed for a storm to establish peak intensity after experiencing its warmest seawater versus approximately 3 days after a storm was first generated. This coincidence where the highest storm intensity is matched with the highest SST was found for only 18 storms, representing less than 4 % of the total storm count.

The spatial misalignment of maximum SST and maximum intensity is generally displayed by North Atlantic storms though the extent of displacement differs compared to ENP storms. While two-thirds of North Atlantic storms met their maximum SSTs within 5° latitude of maximum lifetime intensity (Michaels et al. 2006), 83 % of ENP storms had done so. Overall, this latitudinal displacement for ENP storms' maximum intensity is 2.2° northward of where maximum SST is achieved, only half of North Atlantic storms' displacement (Michaels et al. 2006). These comparisons relative to North Atlantic storms signify ENP storms' stronger linkage to areas with the highest SST in acquiring maximum intensity.

For storms that took an eastward recurvature or landfall, the highest SSTs are often found near shore when their strengths are diminishing, possibly in conjunction with extratropical transitioning. Interestingly, peak intensities for these storms took less time to establish than those that experience warmest SST at their earliest stage of development. As contrasting environmental conditions near shore and in the open water could dictate a difference of TC development, the WDR reveals a strong longitudinal displacement (Fig. 3.7b) between locations of the warmest SST and maximum lifetime intensity (Fig. 3.7a). Although this could also be attributed to WDR storms that have encountered the maximum SST while they were still in the EDR, 137 (or 40 %) of WDR storms match this criterion. This is lower than
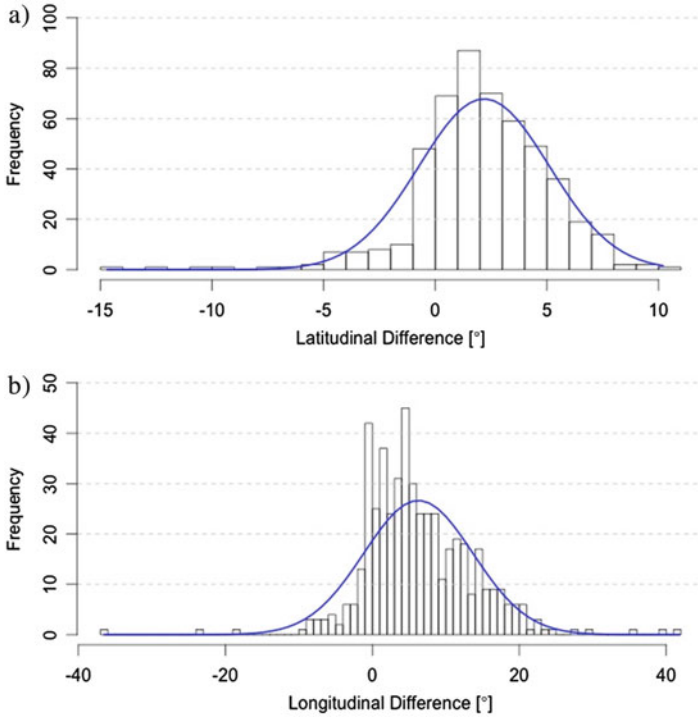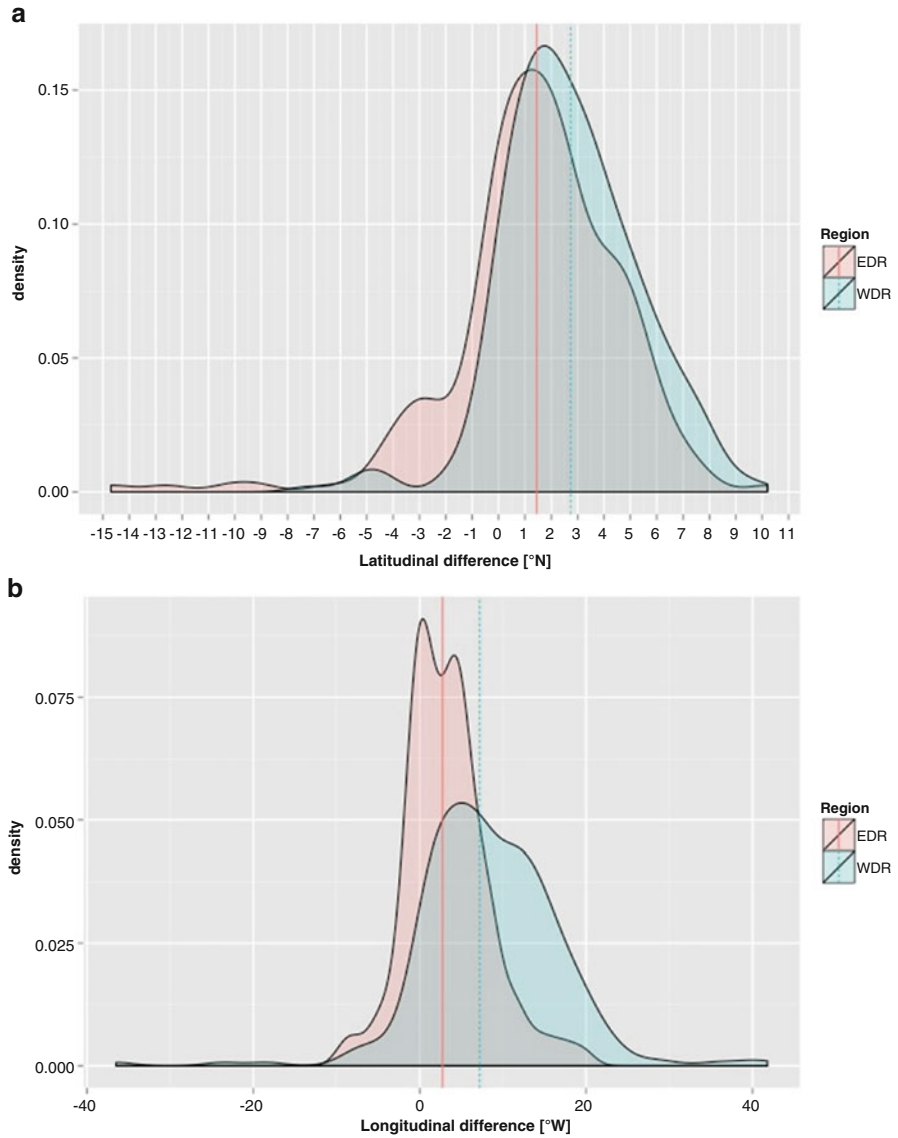
Fig. 3.6 (**a**) Distribution of latitudinal differences between the locations of maximum SST and maximum lifetime intensity for all ENP storms from 1982 to 2013 and (**b**) same as (**a**), but for longitudinal differences. Each histogram is outlined with a normal curve (in *blue*)

those storms (58 %) that formed in EDR but achieved maximum lifetime intensities in WDR. Even when these storms are excluded, storms that attained maximum intensity and maximum SST in the WDR still maintain a 2° westward bias over EDR storms.

5 Correlation Between SST and TC Intensity

5.1 All Observations

Since the onset of a storm induces a cold wake (due to turbulence-induced entrainment below surface waters) and thus obscures the SST-TC intensity relationship, a 7-day SST average prior to the storm arrival was used to correlate with the intensity observations. Possibly due to a large sample size ($n = 12{,}469$), Fig. 3.8 shows the linear regression fit is significant ($p < 0.001$) despite a slope of 0.889 and R^2 value of 0.020 for storm track positions observed prior to crossing the westernmost boundary

a

b

Fig. 3.7 (**a**) Distribution of latitudinal differences between locations of maximum SST and maximum lifetime intensity for EDR and WDR storms from 1982 to 2013 and (**b**) same as (**a**), but for longitudinal differences

division at 140°W. Such a low value for the coefficient of determination implies that SST is a rather weak predictor for storm intensity.

Though the explained variance is small, yet significant, it is higher than a similar correlation analysis performed in the North Atlantic basin (Michaels et al. 2006).
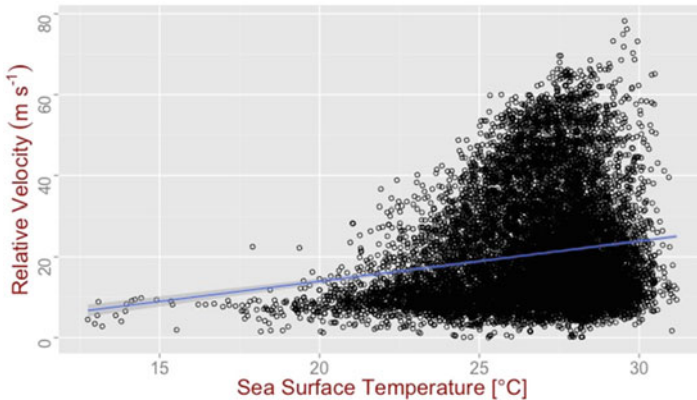
Fig. 3.8 Scatterplot and regression fit for all observations of TC intensity against the weekly SSTs averaged over 7 days prior to storm passage

If storm tracks that traversed west of the ENP boundary are also included (not shown), the linear regression is still significant. Such a significant linkage between SST and TC intensity is consistent with that of Ralph and Gough (2009), which considered the correlation of TC activity of all storm strengths and basin-wide SSTs at a monthly scale. Although our analysis shows that the explained variance is small, this association of near-time SSTs and TC wind speeds is consistent with Michaels et al. (2006). Though SST certainly provides a certain degree of influence on the upper bound of TC intensity, SST is clearly far from being the sole control of TC intensity. Even when elevated SSTs are observed, other atmospheric factors such as wind shear diminish TC strength (Landsea et al. 1998; Maue 2009). The fact that the R^2 in the present study is higher than a similar analysis conducted for North Atlantic storms (Michaels et al. 2006) may indicate greater SST influences on ENP storm intensities.

Upon investigating how TC intensity is related to SST at a daily scale, the temperature measurement at the ocean surface demonstrates a two-way, SST-TC relationship. Though it is shown in Fig. 3.8 that SST directly contributes to TC intensification, storm passage is capable of cooling the ocean surface at least a week prior to its arrival. The strength of SST reduction depends on storm translation speed and its intensity (Cione and Uhlhorn 2003; Mei and Pasquero 2013). For instance, a slow-moving storm with high winds would likely enhance the process of vertical mixing by drawing cold water underneath. The result of this cold wake left behind a TC may impede its own development and impose a negative impact on the formation and development of potential storms nearby (Bender and Ginis 2000).

Figure 3.9 shows the SST averages 7 days before and after (total of 15 days) for locations of all 12,469 storm tracks. Generally, this cooling remained for at least 1 week since the storm has departed, with the greatest SST reduction experienced during the period between 1 day before onset until the day of storm arrival. Such a sharp drop in the ocean surface temperature is likely the result of a greater
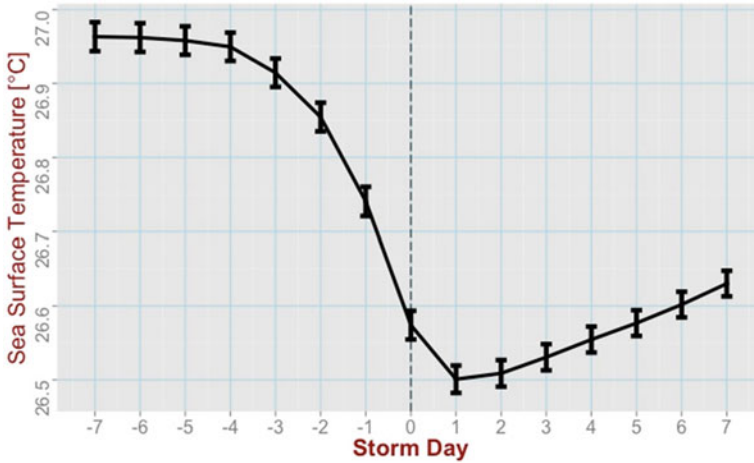
Fig. 3.9 Daily SST response (with standard error) to the influence of storm passage over a 15-day time series

vertical mixing due to a close proximity to the radius of maximum winds and storm movement, which entrains cooler waters beneath the sea surface. Such a cooling effect lasts longer and is more pronounced for locations that experience storms with lower translation speeds and higher storm intensities (Dare and McBride 2011a). Compared to the North Atlantic TCs, since the average translation speed is higher in that basin, SST reduction associated with a slower storm movement is generally greater in the ENP basin.

When all 12,469 observations of storm intensity are correlated with their same-day SSTs (i.e. Day 0), a weak relationship is found (slope $= 0.63078$ and $R^2 = 0.01094$). Although the result of a linear least-squares fit maintains its statistical significance ($p < 0.001$), the fact that the greatest SST decrease occurs during the day prior to storm arrival weakens the near-time SST-TC intensity relationship. The effect of SST cooling on the SST-TC intensity relationship is likely to be most important when storms are undergoing rapid intensification, particular during September, the peak month of the ENP hurricane season (Kaplan et al. 2010). Once the TC-induced rate of SST cooling diminishes, storms are found to intensify at a faster rate (Cione and Uhlhorn 2003).

While the choice of daily SST at least a week before storm arrival does not dramatically change the explained variance for the linear fit with TC intensity (Table 3.2), the use of the weekly SST dataset (Michaels et al. 2006) may not be as closely aligned to the initial storm detection as the daily time interval data. For instance, when a storm has just formed, the SSTs averaged during the past week may be more critical at determining storm genesis than TC intensification. Figure 3.10 compares a 15-day time series of SST averages centred at the genesis stage and the time when a storm's peak intensity is observed. From the day before until the day after the detection of maximum lifetime intensity, the most dramatic SST decline

Table 3.2 Regression analysis of storm intensity of all EDR and WDR observations with daily SST at 7 days prior to storm passage with Day 0 being the arrival day of storm passage

Region/days before	EDR		WDR	
	Slope	R^2	Slope	R^2
7	−0.79	0.01	1.55	0.06
6	−0.81	0.01	1.56	0.06
5	−0.72	0.00	1.60	0.06
4	−0.67	0.00	1.61	0.06
3	−0.69	0.00	1.60	0.06
2	−0.67	0.00	1.62	0.06
1	−0.63	0.00	1.59	0.06
0	−1.43	0.02	1.32	0.04
7-day average	−0.79	0.00	1.64	0.06
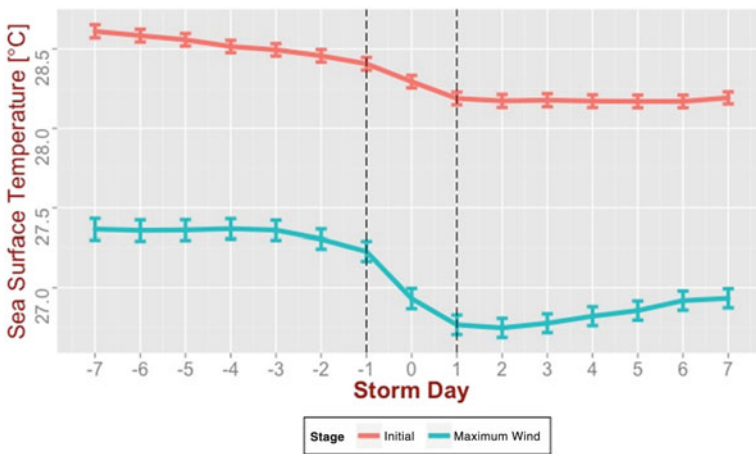
Fig. 3.10 Same as in Fig. 3.9, but the 15-day SST is centred around the storm genesis and maximum lifetime TC intensity. *Dashed lines* represent the daily range of the highest rate of SST reduction

can be discerned. This is mostly likely due to a combination of a slower translation speed and a strong TC wind speed in churning up colder water from below (Mei and Pasquero 2013). Since weak TC winds are associated with fast-moving, decaying storms, virtually little to no SST recovery is observed past the storm genesis stage. In contrast, the average SST recovery at only those locations that just experienced peak storm intensities is 0.06 °C higher than the average of all TC observations.

5.2   MDR Subdivisions

When TC observations are subdivided and binned into EDR and WDR, the sensitivity of TC intensity to SST is regionally distinct. With the addition of a
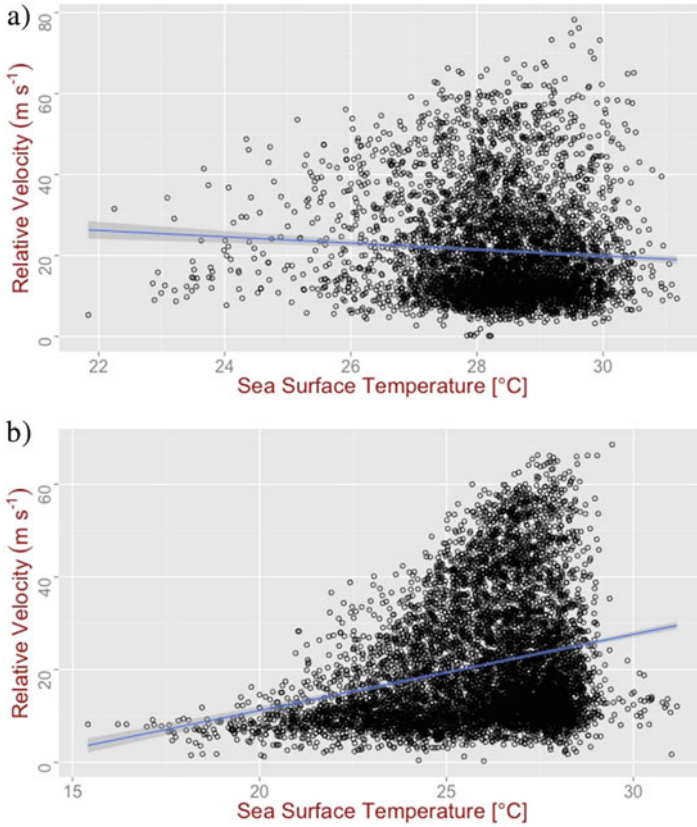
Fig. 3.11 (**a**) Relative wind speeds for all EDR storm observations and (**b**) same as (**a**) but for all WDR storm observations

linear regression of least-squares fit, Fig. 3.11a, b shows a scatterplot of EDR (WDR) storm intensity and SST averaged over a 7-day period prior to TC detection. Compared to EDR, despite a rather low explained variance, WDR storm intensities are more responsive to SST differences. In fact, the slope is nearly twice as large for MDR storms during any day of the week prior to the TC arrival. From Table 3.2, the worst fit is found at Day 0, when the negative (positive) slope is strongest (weakest) at EDR (WDR). In the EDR, this corresponds to the time when the greatest rate of SST reduction due to storm influences is observed (Fig. 3.12). This SST reduction in EDR continues until a local minimum is observed 2 days after the storm appearance. While the temperature of the ocean surface is noted to reduce at a slower pace a week prior until the day before EDR storms arrive, SST is observed to start cooling only 4 days prior to TC arrival until the local minimum appears the day after the WDR storm passage.
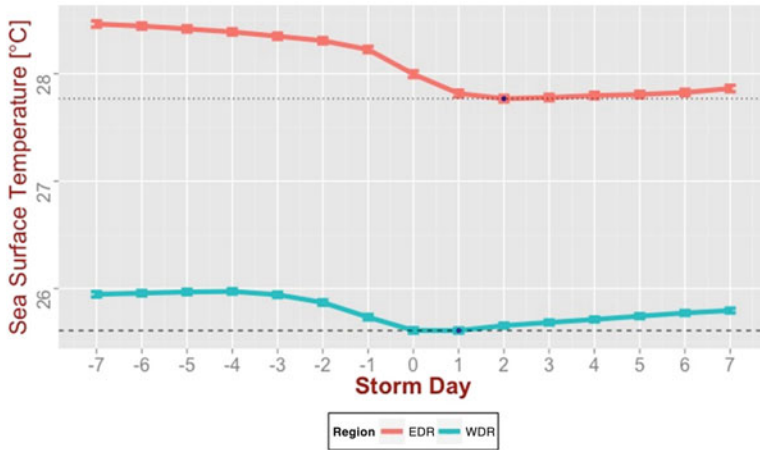
Fig. 3.12 Same as Fig. 3.9, but separated for storm passages of EDR and WDR observations. *Dashed lines* represent the reference SSTs of local minima over for EDR and WDR

Subdividing ENP storm observations into EDR and WDR sectors is also critically important to the understanding of the regional difference in which TC wind speed responds to SSTs at different storm development stages. In particular, the relationship of WDR storm intensity with the underlying SST shows a greater significance when the maximum lifetime intensity is examined. Such a finding of SST control over the maximum lifetime TC intensity would not have been possible if the ENP basin had not been subdivided. Similar to the above result, little association with SST is detected on the day when maximum relative wind is detected. On average, the greatest correlations are observed 2 days before TC arrivals when the impact of TCs on ocean temperature is less pronounced. This observation has been previously hypothesized but not proven until the use of the daily SST dataset. In terms of ocean surface cooling, EDR storm observations generate greater SST reductions at least a week prior to storm geneses and the attainment of maximum intensities; however, TC passages at both regions display little evidence of SST recoveries (Figs. 3.13a, b). However, dramatic differences of SST responses between EDR and WDR are noticed for locations that experience passages of maximum lifetime intensities (Fig. 3.13b). EDR storm records tend to be accompanied by greater SST reduction than WDRs.

Regional sensitivity for the maximum lifetime intensity to SSTs is found to differ between EDR and WDR storms. Figure 3.14a, b depicts the scatterplots of maximum lifetime intensity of relative winds with average weekly SSTs, 7 days prior to TC arrival for all 283 (213) WDR (EDR) storms. Comparatively, the SST range when WDR major hurricanes (Fig. 3.14a) have established peak intensities is shorter, and on average colder, than that of EDR major hurricanes (Fig. 3.14b). Specifically, this study found the importance of an SST of 25 °C (24 °C), above which all but one major hurricane (hurricanes) has established peak intensities in
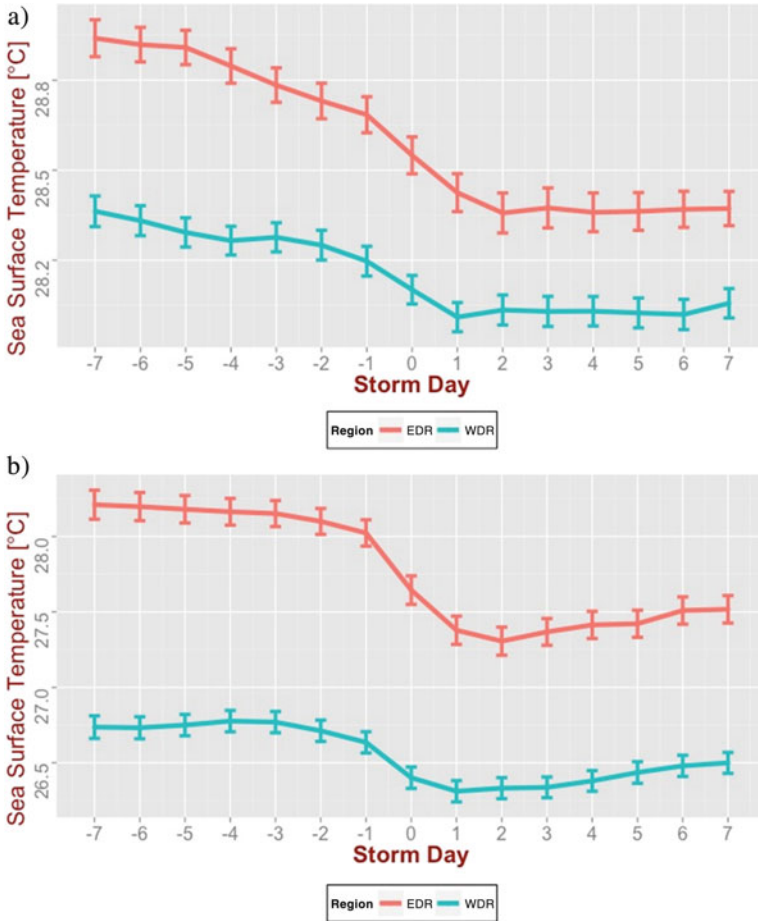
Fig. 3.13 (**a**) Same as Fig. 3.12, but for the average SST conditions during storm genesis and (**b**) same as (**a**) but during the maximum lifetime intensity

WDR. Meanwhile, such SST limitation is less clear in EDR, with most of its major hurricanes established at SSTs higher than 27 °C. Compared to the maximum SST level of 28.25 °C that is required to attain the maximum lifetime intensity of North Atlantic major hurricanes (Michaels et al. 2006), this SST requirement in WDR is dramatically lower. Comparison studies within and between major TC development basins suggest the SST requirement to sustain major hurricanes is not uniform.

Although an SST threshold of 28.25 °C is identified for North Atlantic storms to achieve maximum strengths of major hurricane status, Michaels et al. (2006) show North Atlantic TC winds that achieved maximum intensities past this SST requirement have little to no relationship with corresponding SSTs. Even if only the intensities of major hurricanes were investigated, SST does not seem to be the
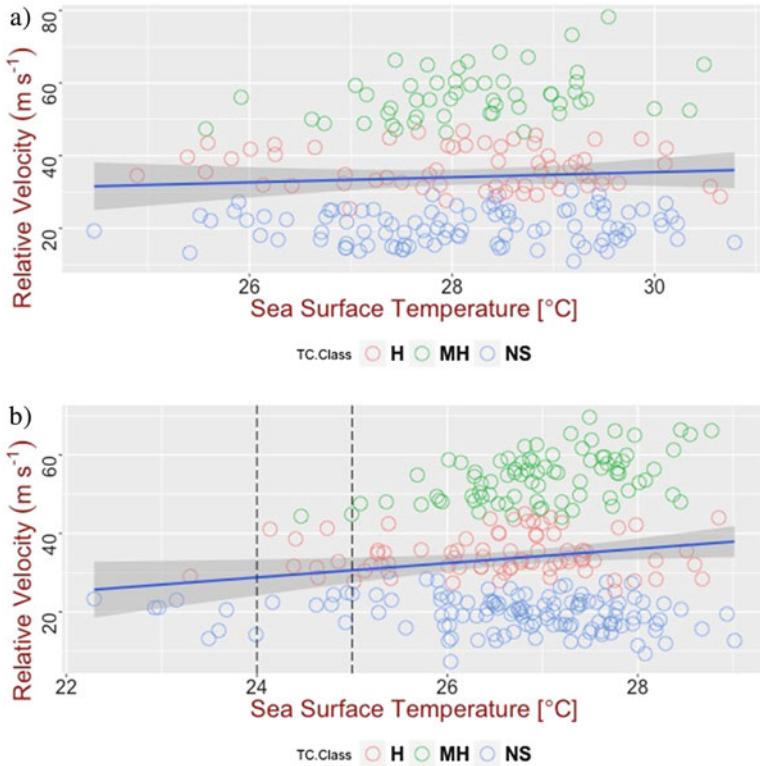
Fig. 3.14 (**a**) Scatterplot and linear regression of maximum lifetime intensity of relative velocity for EDR storms ($N = 213$) and daily SSTs averaged a week prior to maximum storm strength and (**b**) same as (**a**) but for WDR storms ($N = 283$). The *dashed lines* with cooler (warmer) SST indicates the requirement for hurricane (major hurricane) genesis

overriding factor in determining the maximum TC winds. However, in the ENP basin, the maximum intensity of WDR major hurricanes demonstrates significant relationship with daily SSTs. Figure 3.15 shows the SST and TC intensity for WDR major hurricanes 3 days before relative winds are achieved. A linear regression analysis on this day has the highest slope and explained variance. To compare with the previous result shown in the North Atlantic basin (Michaels et al. 2006), this correlation test was also replicated using maximum winds (relative velocity + translation speed); and, the result also shows similar statistical significance at $p < 0.01$. Though maximum intensities of WDR major hurricanes are critically dependent on SST conditions, many WDR storms remain weakly developed despite encountering favourable SST conditions that are well above the minimum requirement (25 °C) to attain the maximum strength of major hurricanes. In contrast, while maximum lifetime TC intensity for all EDR storms is not found to positively correlate with ocean surface temperature, a weak, but positive, relationship was found for maximum winds of EDR major hurricanes and their underlying SSTs.
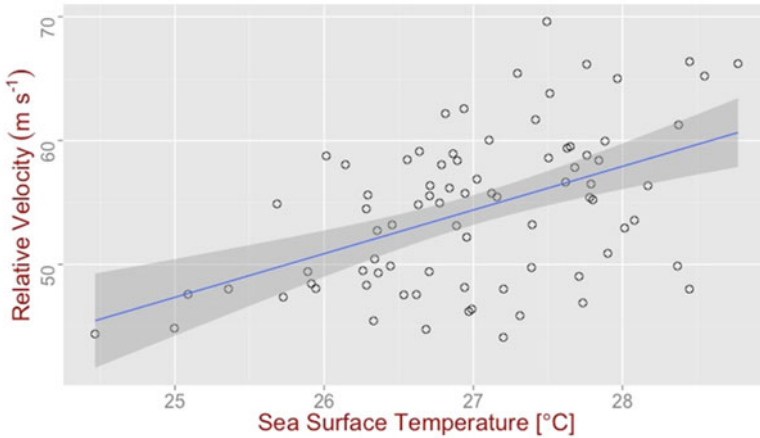
Fig. 3.15 Scatterplot and linear regression of maximum lifetime intensity of relative velocity for WDR storms that reached major hurricane strength with SST 3 days before maximum storm strength

6 Upper Bound of TC Intensity by SST Groups

In addition to statistically linking SSTs to observations of TC winds, the impact of increasing SST on the maximum sustained winds can also be explored by stratifying records of TC wind speed into SST groups based on the work of DeMaria and Kaplan (1994). By rounding average SST values a week prior to TC arrival to the nearest integer, TC winds have generally maintained the same relationship with increasing SSTs as found by Whitney and Hobgood (1997). Overall, warmer SSTs are able to sustain a higher maximum TC intensity. Compared with Whitney and Hobgood (1997), an update to the current TC record shows that the maximum intensities at some of the highest SST categories are increasing.

Table 3.3 summarizes the 1982–2013 storm intensities in each SST bin, updated from 1963 to 1993 climatology (Whitney and Hobgood 1997). Two extra (30 °C and 31 °C) SST bins are now required, though it has been noted that there were few storm observations from 1963 to 1993 climatology that encounter SSTs greater than 29.5 °C. Similar proportions (77 %) of the total TC intensity observations were found in the 26 °C or higher SST bins, though the highest average TC intensity has shifted from 26 °C (Whitney and Hobgood 1997) to 27 °C bin (Table 3.3). A gradual decrease in the average TC intensity with increasing SST is partly due to degrading storms recurring over shallow and warm water prior to dissipation at landfall. It could be also attributed to a tendency for storms to form and develop over the highest SSTs and slowly decay while passing over cooler water (Whitney and Hobgood 1997).

Though the total number of analysis years is 1 year more than that of Whitney and Hobgood (1997), there are an additional 1595 SST observations associated

Table 3.3 Summary of TC intensity records stratified into SST bins

SST (°C)	Sample size	Average intensity (m s^{-1})	Maximum intensity (m s^{-1})
19.0	34	7.4	12.2
20.0	74	8.5	16.2
21.0	148	10.2	28.3
22.0	280	12.2	38.8
23.0	475	13.8	40.1
24.0	714	16.4	48.7
25.0	952	21.6	55.7
26.0	1,386	24.4	60.0
27.0	2,367	24.4	66.3
28.0	3,304	21.4	68.5
29.0	1,966	20.4	74.9
30.0	708	20.1	78.2
31.0	34	18.6	50.4
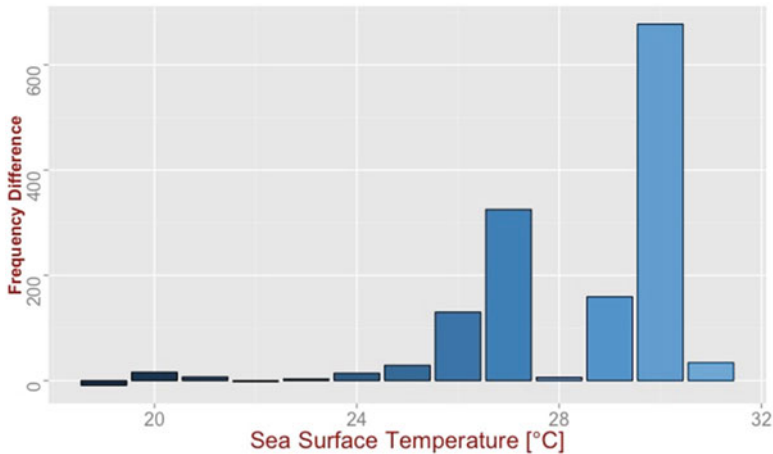
Fig. 3.16 Anomaly of TC observations in each SST bin during 1982–2013 compared to 1963–1993

with the TC record. This value is large considering that the average number of the SST-TC record between 1963 and 1993 per year is 356.8, roughly averaging 36 more observations/year during the 1982–2013 period. Although it is difficult to attribute the recent spurt of TC activity to climate change due to an inconsistent monitoring of TC tracks when compared with data prior to the 1970s, the recent SST warming has shifted the corresponding surge of TC observations towards the distribution with higher SST values. Figure 3.16 shows that most of the surge in TC detection associated with SST warming occurs preferentially in the higher SST bins. Likewise, less of an increase in TC observations are observed to be distributed

Table 3.4 Details on storms that attained the highest relative winds at each SST bin

SST (°C)	Year	Name	Latitude (°N)	Longitude (°W)	Maximum winds (m s^{-1})	Strength	Relative winds (m s^{-1})	Region
19.0	2001	NARDA	16.3	139.6	15.4	TD	12.2	WDR
20.0	2005	KENNETH	16.5	139.4	23.1	NS	16.2	WDR
21.0	2013	GIL	13.7	138.2	33.4	H	28.3	WDR
22.0	2004	ISIS	16.3	135.7	43.7	H	38.8	WDR
23.0	2008	CRISTINA	14.1	133.7	46.3	H	40.1	WDR
24.0	1995	ADOLPH	17.8	108.8	51.4	MH	48.7	EDR
25.0	2006	EMILIA	30.8	125.2	59.2	MH	55.7	WDR
26.0	1988	CARLOTTA	21.7	123.7	64.3	MH	60.0	WDR
27.0	1984	NORBERT	19.4	116.3	72.0	MH	66.3	WDR
28.0	1998	KENNA	18.3	108.3	74.6	MH	68.5	EDR
29.0	1997	LINDA	17.7	110.3	79.7	MH	74.9	EDR
30.0	1997	LINDA	17.1	109.6	82.3	MH	78.2	EDR
31.0	2009	JIMENA	15.7	105.5	54.0	MH	50.4	EDR
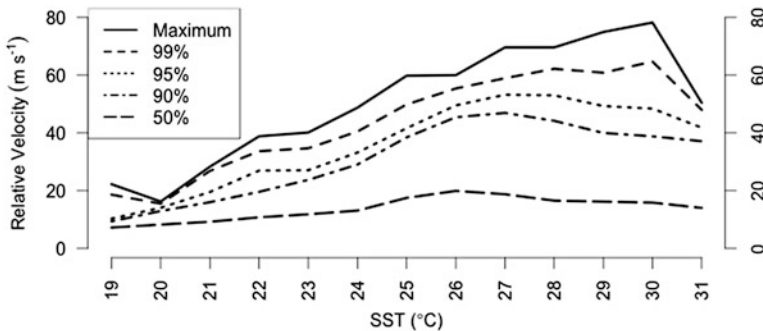
Fig. 3.17 Storm relative winds at the maximum intensity and 99th, 95th, 90th and 50th intensity percentiles at all SST bins after translation speeds have been accounted

at lower SST values. Thus, this improvement of thermodynamic condition is able to allow storms to extract energy to reach higher maximum TC intensities. Consequently, storms (in Table 3.4) that are responsible for achieving the highest maximum intensity in each SST bin differ from those found in Table 3.2 of Whitney and Hobgood (1997). TCs Linda (1997), Kenna (2002) and Rick (2009) had all exceeded the maximum strength of Trudy (1990), which was found to be the most intense storm from an earlier 1963 to 1993 period (Whitney and Hobgood 1997).

Since it is of interest to understand the effect of SSTs on storm intensity, only the maximum, 99th, 95th, 90th and 50th, percentiles of TC winds are plotted in Fig. 3.17. Initial linear increases are noted for 90th percentiles or above though the rate of increase flattens, or even decreases, as bins of higher SSTs are approached. Only the maximum intensity values maintained a linear growth rate with increasing
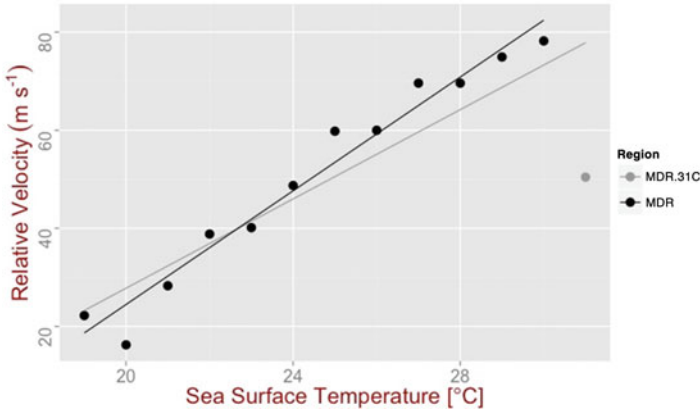
Fig. 3.18 Scatterplot and regression line drawn for the maximum storm intensity attained by each SST bin with and without the maximum intensity at the 31 °C bin

SSTs. Because Fig. 3.18 shows that the maximum intensity dips dramatically at the 31 °C bin, its value is not included in the empirical derivation of MPI (Eq. 3.2), possibly due to a lack of observation in the highest SST category. Using a locally weighted scatterplots smoothing known as LOWESS (not shown), the fit is best described as a linear relationship. The updated (1982–2013) relationship between empirical MPI and SST in the ENP basin has an equation of the form

$$\text{ENPMPI} = A\,(\text{SST}) + B, \tag{3.2}$$

where ENPMPI (m s^{-1}) represents the revised ENP maximum potential intensity, with a constant of $B = -91.4863$ m s^{-1} and a slope of $A = 5.7975$ m s^{-1} °C^{-1}. Overall, 96 % of total data variance is explained by ENPMPI. Compared to Whitney and Hobgood (1997), this updated ENPMPI sees an increase in slope showing the linear fit is stronger than the past TC climatology (Fig. 3.18).

When the ENP MDR is subdivided, it is evident that there are regional differences in the distribution and magnitude of TC intensities among the SST bins. A warmer (colder) SST condition is experienced in the EDR (WDR), where 16 (slightly over a thousand) TC track records are associated with SST bins lower than the 23 °C category (Tables 3.5 and 3.6). Towards the upper bound of TC intensity distribution, over 95 % of EDR storm observations (Table 3.5) are in the 26 °C category or greater, while only 64 % for the WDR (Table 3.6). When the maximum intensity is regionally compared for each SST bin, maximum intensities observed in the WDR are higher at SST categories of 25 °C and 27 °C (Table 3.6), while the highest attained TC intensities at other SST bins are higher in the EDR (Table 3.5). Although maximum TC intensity is not unanimously favoured within a particular ENP MDR subdivision, the average storm intensity at each SST bin is consistently stronger in the EDR (Table 3.5).

Table 3.5 Same as in Table 3.3 but for six-hourly TC observations in EDR

SST (°C) bin	Sample size	Average intensity (m s^{-1})	Maximum intensity (m s^{-1})
<23.5	16	20.9	45.3
24	33	23.6	52.2
25	48	29.1	48.7
26	178	30.2	60.3
27	597	27.8	62.7
28	1,728	22.3	73.3
29	1,714	18.1	78.2
30	685	16.7	62.2
31	27	13.3	33.1

Table 3.6 Same as in Table 3.3 but for six-hourly TC observations in WDR

SST (°C) bin	Sample size	Average intensity (m s^{-1})	Maximum intensity (m s^{-1})
<18.5	27	6.9	11.8
19	34	7.4	12.2
20	74	8.5	16.2
21	148	10.2	28.3
22	278	12.1	38.8
23	461	13.8	40.1
24	681	16.1	45.2
25	904	21.4	55.7
26	1,208	23.2	60.0
27	1,770	24.6	66.5
28	1,576	24.3	66.2
29	252	21.2	68.7
30	23	12.0	21.9
31	7	10.7	13.7

When maximum, 99th, 95th, 90th and 50th, percentiles of TC intensity are plotted for the EDR (Fig. 3.19a) and WDR (Fig. 3.19b), regionally specific positive relationships are observed for TC intensities. In the EDR, a smoother increase in the maximum TC intensity (1.7 m s^{-1} per °C) is observed while the average WDR intensity experiences a steeper (5.6 m s^{-1} per °C) increase. At TC intensities of lower percentiles, this increase is slower towards the higher SST categories for both regions. When the average intensity within each SST bin is compared between regions, observations from both regions show less sensitivity to higher SST conditions than the maximum intensity. Differences between the two regions are dramatically different for TC winds at the higher percentiles. WDR storm intensities greater than the 90th percentile of each SST bin are more dependent on SSTs than for EDR storms.

Since the ENP basin exhibits longitudinally different SST conditions for TC development, ENPMPI derived above might not best represent the upper limit of
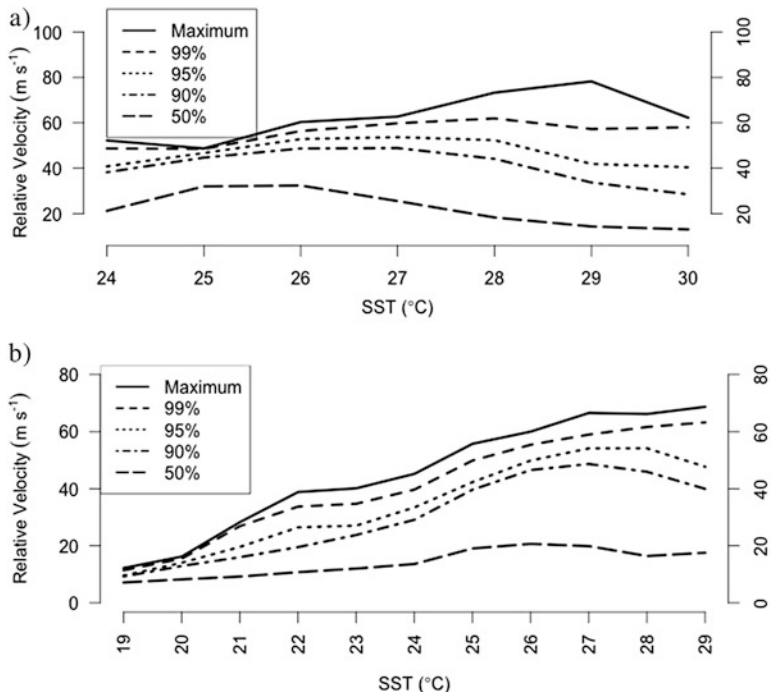
Fig. 3.19 (**a**) Same as Fig. 3.17, but only for EDR storm observations and (**b**) same as Fig. 3.17, but only for WDR storm observations

maximum intensity as a function of SST category when local storms are regionally divided. Based on the above findings, the MPI in the EDR (ENPMPI$_e$) and the WDR (ENPMPI$_w$) may require different empirical models than that performed for the entire basin. Due to a limited record of maximum TC intensity associated with each SST bin (Table 3.5), only data from 24 to 30 °C bins are used for ENPMPI$_e$. By examining the LOWESS curve (Fig. 3.20), it appears a linear function is still the most suitable function in describing the data distribution (up to 29 °C) for ENPMPI$_e$, with an equation of

$$ENPMPI_e = A_e \, (SST_e) + B_e, \tag{3.3}$$

where ENPMPI$_e$ (m s^{-1}) has a constant of $B_e = -35.756$ m s^{-1} and $A_e = 3.64$ m s^{-1} °C^{-1}. However, compared with ENPMPI, ENPMPI$_e$'s residual standard error has grown to 7.637 m s^{-1}. An ANOVA was attempted to compare the difference in residual error between a linear and a curve (polynomial) fit. Though a curve fit leads to a smaller error (3.73 m s^{-1}), it is not statistically different from the error associated with a linear function fit ($p > 0.05$).

For WDR observations, while the distribution of maximum TC intensity is observed to shift towards higher SST bins, the LOWESS curve indicates the growth
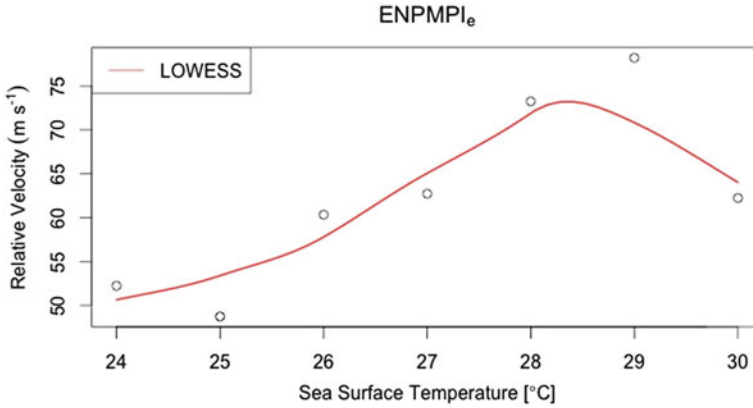
Fig. 3.20 Scatterplot for maximum storm intensity attained by each SST bin of all EDR observations. A locally weighted scatterplot smoothing (LOWESS) is applied

rate of maximum TC intensity starts to slow at the 26 °C SST bin. Interestingly, this is also generally observed as the minimum SST requirement for TC genesis and development (Palmén 1948; Dare and McBride 2011b). This flattening of growing maximum TC intensity appears to initiate at even cooler SST bins for the lower percentile curves (Fig. 3.19b). As such, even with a higher SST, other environmental influences may be more important in determining the ultimate maximum TC intensity. When linear and quadratic (curve) functions are compared for data fitting, both functions had parameter estimates that are found to be highly statistically significant. Overall, the ANOVA results indicate that the reduced predicted error of a quadratic fit is significantly lower than that of a linear function ($p < 0.01$). Thus, a linear function is deemed inadequate to represent ENPMPI$_w$. Instead, an exponential decay (increase form) function is found to be more suitable with the following equation:

$$\mathrm{ENPMPI}_w = C_w + B_w e^{-Aw(\mathrm{SST}-\mathrm{To})}, \tag{3.4}$$

where T_o (°C) is specified as the reference temperature and A_w, B_w and C_w are constants of the parameter estimates. With $T_o = 29$ as the highest SST bin, using a non-linear least-squares fit, $A_w = 100.40171$, $B_w = -29.90966$ and $C_w = 0.11039$. Figure 3.21 shows the data and the fitted function for ENPMPI$_w$, with a residual standard error of 2.764 m s^{-1}. Comparatively, a linear regression fit generated an error of 4.192 m s^{-1}. The choice of the exponential decay function in the form of (3.4) is indicative of the flattening of the fitted curve, starting at the 26 °C SST bin. Though it was not taken into consideration for the function fit, the reduced slope is also evident for North Atlantic storms at SST bins above 28 °C (DeMaria and Kaplan 1994). In our case, due to data limitations, there remains some uncertainty for the reduced growth to continue beyond the 29 °C bin, the reference SST bin below which ENPMPI$_w$ applies.
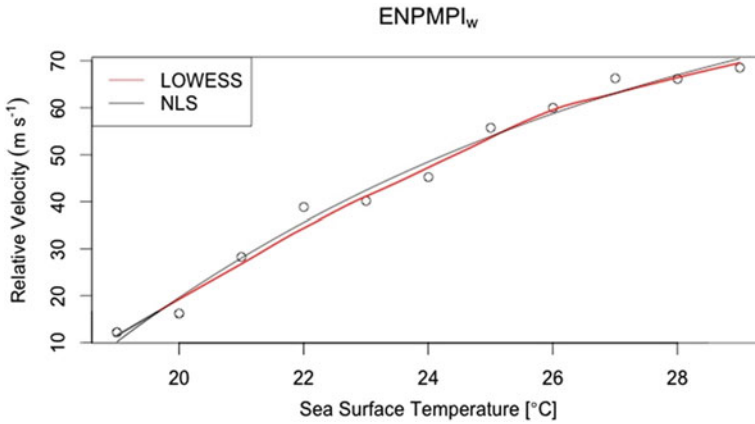
Fig. 3.21 Non-linear least-squares (NLS) fitting of maximum storm intensities bounded by SST bins at WDR, with the LOWESS curve added

7 Outflow Temperature

In addition to SST, TC maximum potential intensity is also limited by the outflow temperature near the tropopause for various TC basins (Wing et al. 2015). A cooler outflow temperature provides a more efficient mechanism at raising MPI through the effective removal of energy at the storm top. The calculation of the outflow temperature relies on surface conditions of SST and sea-level pressure, as well as temperature, pressure and relative humidity at various tropospheric levels (Bister and Emanuel 1998). Data used to construct an environmental sounding in the spatial-temporal overlap of the six-hourly ENP storm tracks are obtained from the NCEP North American Regional Analysis (Mesinger et al. 2006).

Through studies using reanalyzed atmospheric data (Wing et al. 2007, 2015; Emanuel et al. 2013) and idealized experiments in modelling the storm's environment (Ramsay 2013; Wang et al. 2014), it has been shown that maximum TC winds (minimum sea-level pressure) have noticeably increased (reduced) with decreasing outflow temperature. In contrast to the upper-tropospheric condition, the slowly increasing North Atlantic SST demonstrates the cooling of the outflow temperature is relatively more important in contributing to the recent increase in the potential intensity of North Atlantic storms (Emanuel et al. 2013). However, the consistency of the rising North Atlantic potential intensity derived from the NCEP-reanalyzed data has been challenged when data from other reanalysis products were compared (Vecchi et al. 2013).

To compare the regional difference of outflow temperature in the ENP basin, Fig. 3.22 shows the recent trend of the outflow temperature at two central locations that were arbitrarily selected to represent the EDR, at 10°N 105°W, and WDR, at 10°N 125°W. Overall, the WDR representation demonstrates a significant cooling of nearly 6 °C between 1982 and 2015, while the EDR representation has only

Fig. 3.22 The outflow temperatures (1982–2015) required to achieve theoretical maximum potential intensity at 10°N 105°W and 10°N 125°W are plotted to represent locations in EDR and WDR respectively
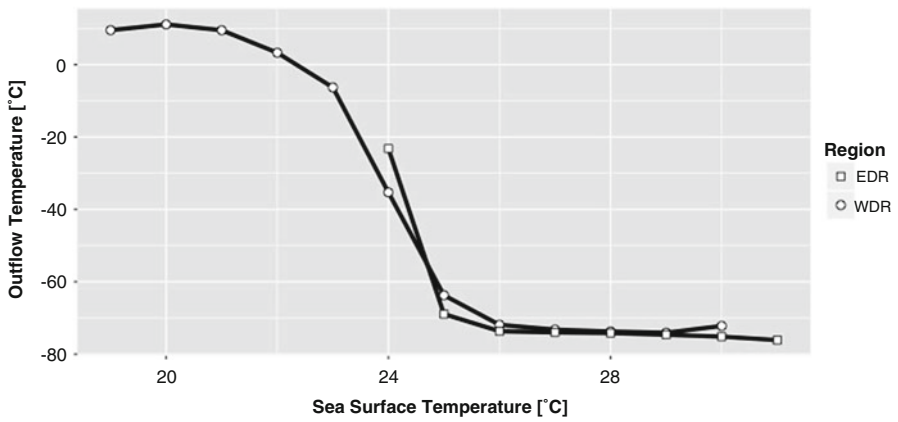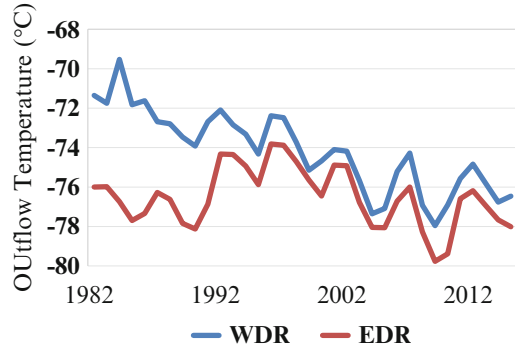
Fig. 3.23 The relationship of outflow temperatures vs. SSTs that is required to reach maximum potential intensity for EDR and WDR storm observations (1982–2013)

experienced one-fourth of the WDR's cooling rate during the same period. A greater rate of cooling in the outflow temperature reveals the overall WDR has become less stabilized, supporting a more favourable upper-atmospheric environment for storm development, as reflected in the growing number of ENP major hurricanes towards the end of the twentieth century (Collins and Mason 2000). This cooling trend lends support to the earlier analysis in which the recent increase in the maximum storm intensity is attained at each SST category in the WDR. Although Fig. 3.22 does not reflect the outflow temperatures required to establish MPI along existing storm tracks, such regional difference in the upper-tropospheric temperature offers support for the relative difference of storm intensities between EDR and WDR.

To test if the outflow temperature that is required to achieve theoretical MPI varies within the ENP basin, Fig. 3.23 plots the outflow temperatures of EDR and WDR storm observations against SSTs. During the 1982–2013 period, the averaged outflow temperature as a function of SST category reflects a slightly

cooler outflow temperature at the 25–30 °C SST interval in the EDR, where stronger maximum surface wind speed and lower minimum sea-level pressure were empirically determined. When data of both regions are combined, the shape of data distribution is similar to WDR and resembles a reversed (negative) sigmoid curve, which does not entirely resemble the SST-outflow temperature relationship from Whitney and Hobgood (1997). In particular, our analysis shows the out-flow temperatures of WDR storms associated with SSTs below the 24 °C bin exhibit a warmer atmosphere near the cloud top. This is reflected by a rapid decrease of the upper-tropospheric temperature within a SST range between 23.5 and 25.5 °C. The slow-cooling outflow regions, corresponding to SSTs higher than 25.5 °C, is reflected by a slower increase in the maximum WDR storm winds (Fig. 3.21). As such, this empirically calculated MPI at the highest SST condition is rarely obtained through real-time storm observations and could also vary due to storm track variability (Wing et al. 2007, 2015; Kossin and Camargo 2009).

8 Conclusions

For TC development basins worldwide, SSTs have been recognized, directly (Evans 1993) and indirectly through ENSO influences (Chu 2004), as the major thermodynamic limit of maximum TC intensity. While local SST increase tends in general to elevate storm intensity, remote SST changes (Vecchi and Soden 2007) and upper-tropospheric temperatures (Bister and Emanuel 1998) could enforce significant impacts on the upper limit of TC intensity. As the long-term conditions of the ocean surface shift to a warmer condition, TC intensities are expected to strengthen with SST increase. Although the spatial-temporal resolution of SST data has remained a challenge in pinpointing the SST condition underlying storm tracks, near-time (daily) SST data with a spatial resolution of 0.25° by 0.25° are employed to document its extent of impact on ENP storm winds. Due to the spatial sensitivity of ENP storm intensity to environmental conditions, the limiting effect of SST on ENP storm strength is demonstrated to vary within this region. Because the inhibiting effect of the rate of SST decrease is stronger (weaker) during EDR (WDR) storm passage, the SST impact on TC intensity is greater for WDR storm observations and their maximum lifetime intensities.

Two ways of exploring the SST-TC intensity relationship are presented in the study: (1) correlating SST values with TC intensity and (2) stratifying TC observations into SST bins of 1 °C interval and then relating TC intensities of all TC data points with SST category. Although the direct SST measurement is not the only factor contributing to TC intensity, this association for ENP storms is stronger than that of North Atlantic storms. Using the linear least-squares regression, the results of the study indicate a statistically significant relationship exists between SST and TC intensity. Alternatively, though SST anomalies calculated by subtracting local SST from the ENP Main Development Region (MDR) SST average have been recently

demonstrated to have a greater association with local storm count and intensity (Zhang and Wang 2015), the effect of relative SST as an anomaly from the zonal-mean SST and its impact on the regional sensitivity of ENP storm intensities are still unknown. Further investigation of the maximum lifetime intensity of major hurricanes shows the SST influence on TC intensity is greatest for the most intense storms. Stratification of TC winds according to near-time SST bins supports the previous finding of the SST-dependent MPI in the ENP basin, indicating a stronger relationship when the most recent TC climatology is compared to the past.

Under a regional difference in SST conditions, ENP storms are longitudinally divided to understand regional sensitivity of storm intensity to an SST limit. Compared to the EDR, intensities for WDR storm observations are more responsive to SST fluctuations. When the maximum winds of WDR storms are considered and categorized into different levels of TC intensity, major hurricanes display a stronger association with contemporaneous SST values. In contrast to the North Atlantic region where an absence of such a relationship was found (Michaels et al. 2006), subdividing MDR has facilitated a regional variation in which the maximum TC intensity is correlated with SST. An examination of minimum SST requirements to achieve certain TC strengths also reveals regionally distinct SST ranges to achieve peak intensities for hurricanes and major hurricanes. Compared to the SST limit (28.25 °C) for attaining major hurricanes in the North Atlantic basin, lower SST values are observed where most of the EDR (27 °C) and WDR (25 °C) major hurricanes are established in the ENP.

In contrast to Whitney and Hobgood (1997), an updated ENP storm climatology reveals that the relationship between the outflow temperature and corresponding SST required to attain theoretical MPI is non-linear even when storm groups are longitudinally divided. While the association between maximum storm intensity with SST has increased with a changing climate, when the ENP MDR is subdivided, such linkage is stronger for WDR storm observations until a certain SST limit is approached. Part of this observed relationship may be attributed to a less potent SST reduction inflicted by WDR storm passages. However, such a contrast in the regional TC intensity can also be steered by the outflow temperature near cloud tops. Past the 25 °C SST bin, where the maximum storm intensities of most WDR major hurricanes would have already been sustained, the decay in the growth rate of MPI is marked by a slower reduction of the outflow temperature in the upper troposphere.

Despite a downward trend experienced in the transport of EDR-originated WDR storms, SST warming supports the strengthening of the strongest storms. However, WDR storms indicate such a response becomes non-linear with a slower rate of increase as warmer SSTs are approached. In addition, the association of TC intensity to SST is further challenged by observations of relatively weak intensity over warm SSTs before progressing and intensifying over cooler waters. As such, future studies involving the thermodynamic limit of TC intensity may need to incorporate the ocean heat content by taking into account of not only SST but also energy generated across the entire thermocline depth (Balaguru et al. 2013; Jin et al. 2014). The incorporation of the total ocean heat content may reveal a latitudinal, as opposed to longitudinal, contrast in the relationship of SST-TC

intensity (Balaguru et al. 2013). Although other atmospheric factors could also have an important role in modifying TC intensity, the application of near-time SST greatly contributes to the understanding that, in addition to the regional difference of SST requirement for genesis and intensification of major hurricanes, the eventual intensity of major hurricanes in the WDR are greatly limited by SST conditions encountered prior to the peak of its lifetime intensity.

With the realization of higher maximum lifetime intensity and MPI under the future scenario of continuous SST warming, future increase of ocean temperatures may raise the intensity of damaging storm winds. Since stronger storms tend to be sustained over longer distances, SST warming may also lengthen TC influence for a greater spatial extent. Upon landfall, storm tracks may extend further inland, posing a direct threat to coastal safety. From a forecasting point of view, the possibility of an extended TC influence upon landfalling TCs may result in the broadening of uncertainties associated with near-time projection of storm path. Consider as the strongest TC to exist in the western hemisphere since the satellite era, Hurricane Patricia (2015), as well as other potent storms, had reinvigorated efforts at further investigating the ENP storm outlook under a continuously evolving climate.

References

Balaguru K, Leung LR, Yoon J-H (2013) Oceanic control of northeast Pacific hurricane activity at interannual timescales. Environ Res Lett 8:4009. doi:10.1088/1748-9326/8/4/044009

Bender MA, Ginis I (2000) Real-case simulations of hurricane–ocean interaction using a high-resolution coupled model: effects on hurricane intensity. Mon Weather Rev 128:917–946

Bister M, Emanuel KA (1998) Dissipative heating and hurricane intensity. Meteorol Atmos Phys 65:233–240

Boucharel J, Jin F-F, Lin II, Huang H-C, England MH (2016) Different controls of tropical cyclone activity in the Eastern Pacific for two types of El Niño. Geophys Res Lett. doi:10.1002/2016GL067728

Caron L-P, Boudreault M, Camargo SJ (2015) On the variability and predictability of eastern north Pacific tropical cyclone activity. J Climate 28:9678–9696

Chu P-S (2004) ENSO and tropical cyclone activity. In: Murnane RJ, Liu KB (eds) Hurricanes and typhoons: past, present, and potential. Columbia University Press, New York, pp 297–332

Cione JJ, Uhlhorn EW (2003) Sea surface temperature variability in hurricanes: implications with respect to intensity change. Mon Weather Rev 131:1783–1796

Collins J (2010) Contrasting high North-East Pacific tropical cyclone activity with low North Atlantic activity. Southeast Geogr 50:83–98

Collins JM, Mason IM (2000) Local environmental conditions related to seasonal tropical cyclone activity in the Northeast Pacific basin. Geophys Res Lett 27:3881–3884

Collins JM, Roache DR (2011) The 2009 hurricane season in the eastern North Pacific basin: an analysis of environmental conditions. Mon Weather Rev 139(6):1673–1681

Dare RA, Mcbride JL (2011a) Sea surface temperature response to tropical cyclones. Mon Weather Rev 139(12):3798–3808

Dare RA, Mcbride JL (2011b) The threshold sea surface temperature condition for tropical cyclogenesis. J Climate 24(17):4570–4576

Davis MAS, Brown GM, Leftwich P (1984) A tropical cyclone data tape for the eastern and Central North pacific basins, 1949–1983: contents, limitations, and uses. NOAA Technical Memorandum NWS NHC 25, http://www.nhc.noaa.gov/pdf/NWS-NHC-1984-25.pdf

DeMaria M, Kaplan J (1994) Sea surface temperature and the maximum intensity of Atlantic tropical cyclones. J Climate 7:1325–1334

Diamond HJ, Lorrey AM, Renwick JA (2013) A southwest Pacific tropical cyclone climatology and linkages to the El Niño–Southern Oscillation. J Climate 26:3–25

Emanuel KA (1987) The dependence of hurricane intensity on climate. Nature 326(6112):483–485

Emanuel KA (2005) Increasing destructiveness of tropical cyclones over the past 30 years. Nature 436:686–688

Emanuel K, Solomon S, Folini D, Davis S, Cagnazzo C (2013) Influence of tropical tropopause layer cooling on Atlantic hurricane activity. J Climate 26:2288–2301

Evans JE (1993) Sensitivity of tropical cyclone intensity to sea surface temperature. J Climate 6:1133–1140

Goldenberg SB, Landsea CW, Mestas-Nuñez AM, Gray WM (2001) The recent increase in Atlantic hurricane activity: causes and implications. Science 293:474–479

Gray WM (1968) A global view of the origin of tropical disturbances and storms. Mon Weather Rev 96:669–700

Gray WM (1984) Atlantic seasonal hurricane frequency: part I. El Nino and 30 mb quasi-biennial oscillation influences. Mon Weather Rev 112:1649–1668

Hart RE, Maue RN, Watson MC (2007) Estimating local memory of tropical cyclones through MPI anomaly evolution. Mon Weather Rev 135(12):3990–4005

Henderson-Sellers A et al (1998) Tropical cyclones and global climate change: a post-IPCC assessment. Bull Am Meteorol Soc 79:19–38

Jien J, Gough WA, Butler K (2015) The influence of El Niño-Southern Oscillation on tropical cyclone activity in the eastern North Pacific basin. J Climate 28(16):2459–2474

Jin F-F, Boucharel J, Lin II (2014) Eastern Pacific tropical cyclones intensified by El Niño delivery of subsurface ocean heat. Nature 516:82–85

Kaplan J, DeMaria M, Knaff JA (2010) A revised tropical cyclone rapid intensification index for the Atlantic and eastern north Pacific basins. Weather Forecast 25(1):220–241

Kossin JP, Camargo SJ (2009) Hurricane track variability and secular potential intensity trends. Clim Change 9:329–337

Kotal SD, Kundu PK, Bhowmik SKR (2009) An analysis of sea surface temperature and maximum potential intensity of tropical cyclones over the Bay of Bengal between 1981 and 2000. Meteorol Appl 16(2):169–177

Landsea CW, Franklin JL (2013) Atlantic hurricane database uncertainty and presentation of a new database format. Mon Weather Rev 141(10):3576–3592

Landsea CW, Bell GD, Gray WM, Goldenberg SB (1998) The extremely active 1995 atlantic hurricane season: environmental conditions and verification of seasonal forecasts. Mon Weather Rev 126(5):1174–1193

Martinez-Sanchez JN, Cavazos T (2014) Eastern tropical Pacific hurricane variability and landfalls on Mexican coasts. Climate Res 58(3):221–234

Maue RN (2009) Northern hemisphere tropical cyclone activity. Geophys Res Lett 36(5):L05805. doi:10.1029/2008GL035946

Mei W, Pasquero C (2013) Spatial and temporal characterization of sea surface temperature response to tropical cyclones. J Climate 26(11):3745–3765

Mei W, Pasquero C, Primeau F (2012) The effect of translation speed upon the intensity of tropical cyclones over the tropical ocean. Geophys Res Lett 39:L07801. doi:10.1029/2011GL050765

Merrill RT (1988) Environmental influences on hurricane intensification. J Atmos Sci 45:1678–1687

Mesinger F et al (2006) North American regional reanalysis. Bull Am Meteorol Soc 87(3):343–360

Michaels PJ, Knappenberger PC, Davis RE (2006) Sea-surface temperatures and tropical cyclones in the Atlantic basin. Geophys Res Lett 33(9):L09708. doi:10.1029/2006GL025757

Miller BI (1958) On the maximum intensity of hurricanes. J Meteor 15:184–195

Molinari J, Knight D, Dickenson M, Vollaro D, Skubis S (1997) Potential vorticity, easterly waves and eastern Pacific intensification. Mon Weather Rev 125:2699–2708

Palmén E (1948) On the formation and structure of tropical hurricanes. Geophysica 3:26–38

Patricola C, Saravanan R, Chang P (2014) The impact of the El Niño–Southern Oscillation and Atlantic meridional mode on seasonal Atlantic tropical cyclone activity. J Climate 27:5311–5328

Raga GB, Bracamontes-Ceballos B, Farfán LM, Romero-Centeno R (2013) Landfalling tropical cyclones on the Pacific coast of Mexico: 1850–2010. Atmosfera 26(2):209–220

Ralph TU, Gough WA (2009) The influence of sea-surface temperatures on eastern North Pacific tropical cyclone activity. Theor Appl Climatol 95:257–264

Ramsay HA (2013) The effects of imposed stratospheric cooling on the maximum intensity of tropical cyclones in axisymmetric radiative–convective equilibrium. J Climate 26:9977–9985

Saunders MA, Lea AS (2008) Large contribution of sea surface warming to recent increase in Atlantic hurricane activity. Nature 451(7178):557–560

Thorncroft C, Hodges K (2001) African easterly wave variability and its relationship to Atlantic tropical cyclone activity. J Climate 14:1166–1179

Vecchi GA, Soden BJ (2007) Effect of remote sea surface temperature change on tropical cyclone potential intensity. Nature 450(7172):1066–1070

Vecchi GA, Fueglistaler S, Held IM, Knutson TR, Zhao M (2013) Impacts of atmospheric temperature changes on tropical cyclone activity. J Climate 26:3877–3891

Wang S, Camargo SJ, Sobel AH, Polvani LM (2014) Impact of the tropopause temperature on the intensity of tropical cyclones – an idealized study using a mesoscale model. J Atmos Sci 71:4333–4348

Webster PJ, Holland GJ, Curry JA, Chang H-R (2005) Changes in tropical cyclone number, duration, and intensity in a warming environment. Science 309:1844–1846

Whitney LD, Hobgood JS (1997) The relationship between sea surface temperatures and maximum intensities of tropical cyclones in the eastern north Pacific Ocean. J Climate 10(11):2921–2930

Wing AA, Sobel AH, Camargo SJ (2007) The relationship between the potential and actual intensities of tropical cyclones on interannual time scales. Geophys Res Lett 34:L08810. doi:10.1029/2006GL028581

Wing AA, Emanuel K, Solomon S (2015) On the factors affecting trends and variability in tropical cyclone potential intensity. Geophys Res Lett 42:8669–8677. doi:10.1002/2015GL066145

Wood KM, Ritchie EA (2013) An updated climatology of tropical cyclone impacts on the southwestern United States. Mon Weather Rev 141:4322–4336

Wu L, Tao L, Ding Q (2010) Influence of sea surface warming on environmental factors affecting long-term changes of Atlantic tropical cyclone formation. J Climate 23(22):5978–5989

Xie S-P, Deser C, Vecchi GA, Ma J, Teng H, Wittenberg AT (2010) Global warming pattern formation: sea surface temperature and rainfall. J Climate 23(4):966–986

Zeng Z, Wang Y, Wu C-C (2007) Environmental dynamical control of tropical cyclone intensity – an observational study. Mon Weather Rev 135(1):38–59

Zhang G, Wang Z (2015) Interannual variability of tropical cyclone activity and regional Hadley circulation over the northeastern Pacific. Geophys Res Lett 42:2473–2481

Chapter 4
Modern Tropical Cyclone Wind Observation and Analysis

Christopher C. Hennon and Ethan E. Wright

Abstract Direct observation of the maximum wind in tropical cyclones is extremely rare because of the violence of the environment, the paucity of ocean-borne observing stations, and the remoteness and size of the storms. Besides raising confidence in historical tropical cyclone climate records – which are currently inadequate for climate studies – accurate measurements of the tropical cyclone wind structure and other characteristics are particularly important to more accurately forecast storms, thus mitigating economic and human loss. Large amounts of resources have been devoted to develop innovative methods to adequately observe these systems. This chapter will present an overview of the observing systems and instruments that are used to observe tropical cyclone winds in the early twenty-first century, including in situ and remote sensing approaches. Techniques used to determine the maximum wind speed in the frequent absence of more direct observations are also discussed.

1 Introduction

Tropical cyclones (TCs) develop and spend most of their life cycle over oceans, creating difficulties in measuring their properties and making accurate predictions about how they will evolve. There are many ways of defining the intensity of a TC, including minimum pressure, size, and several different characteristics of the wind field. Typically the maximum sustained wind (MSW), or the strongest wind speed measured over a certain averaging period, is the most desired property used to determine TC intensity. There are several good reasons for this. In operations, storms are categorized by MSW according to the Saffir-Simpson scale (Schott et al. 2012),

C.C. Hennon (✉) • E.E. Wright
Department of Atmospheric Sciences, University of North Carolina at Asheville, Asheville, NC, USA
e-mail: chennon@unca.edu; ewright1@unca.edu

which remains the most publicly visible classification of TC intensity today. Also, TC wind directly impacts coastal residents through wind damage and drives storm surge – a devastating advance of water that destroys coastal structures and poses a large risk for human life. Finally, MSW historically is the most pervasive variable recorded in forecast agency TC data records, called "best-track" (BT) data. BT data are post-storm analyses predominantly composed of quality-controlled observations and estimates of wind where observations are scarce.

A consistent, accurate diagnosis of the MSW and associated wind field in a TC is critical for the computer models that are used to predict where a storm moves and how strong it will be when it arrives. It is also vitally important for understanding how the nature of TCs may be changing through time (i.e., as a response to climate change). Despite the demonstrated importance of TC wind data, accurate measurements of TC wind fields rarely occur, especially outside of the North Atlantic basin because:

1. The nature and location of TCs make direct observation logistically difficult.
2. Observation platforms that can accurately measure winds in these extreme environments (aircraft, buoys) are expensive to deploy and maintain, limiting their scope.
3. Satellites can capture nearly all TCs but the quality of the wind data and inherent limitations of space observation limit accurate MSW estimates.
4. Even in well-observed storms, only a relatively small portion of the storm is observed at any given time – the "true" wind field remains elusive (Nolan et al. 2014).

The uncertainties in the TC wind field inherent during the observation phase and inconsistencies in how global agencies handle the MSW lead to problems with post-storm wind data. For example, the averaging period for the MSW varies across global forecast agencies. The World Meteorological Organization (WMO) standard is a 10-min average, which is followed by the Japan Meteorological Agency (JMA). However, the US National Hurricane Center (NHC) and the US Joint Typhoon Warning Center (JTWC) use a 1-min average. Changing technology and procedures at various agencies has also led to an increase in uncertainty in TC wind records through time. This divergence of standard procedures arises from a vacuum of quality observations since TCs form, develop, and typically decay over areas of ocean basins where direct observation of their characteristics is rare. It is no surprise then that the historical TC record contains errors and inconsistencies that frustrate researchers and generate ambiguity about TC responses to climate change.

It is important then to review and understand the strengths, weaknesses, and general characteristics of the tools and procedures that are used to measure and diagnose TC wind. This chapter will examine the instruments and techniques of modern day (early twenty-first century) TC wind observation in the context of operational applications. The following section details the instruments and means of measuring TCs from inside the storm. This will be followed by a brief overview of the satellite systems that are employed in the TC forecasting and analysis processes. Finally, applied techniques for determining the MSW and the nature of the full TC

wind field will be discussed. Unless otherwise stated, all references to MSW in this chapter correspond to the US definition of MSW, which is the 1-min average wind speed at a 10-m neutral height above the surface.

2 In Situ Observation

Direct observation of TCs is rare, even in modern times. Rappaport et al. (2009) note that aircraft reconnaissance, the most desirable method for obtaining quality measurements of TC wind, occurs in only about 30 % of the total life cycle of TCs in the North Atlantic. Outside of the North Atlantic, where more than 85 % of all TC activity occurs, there have been no regular reconnaissance missions since 1987. In this section we introduce and briefly examine the methods and instruments that are commonly used to directly measure the TC MSW. Some of the instruments described below (stepped frequency microwave radiometer, Doppler radar) are remotely sensed data, but we include them in this section since they are measured from within the TC.

(a) *Aircraft reconnaissance*

TC observations from aircraft are generally regarded as the best method to obtain high-resolution wind (and other meteorological) data for several reasons. Missions, especially those with more than one aircraft, can cover a wide area of the storm in a short time (several hours). The data collected on those missions are transmitted back to the operational forecast center almost instantaneously and can be made available to forecasters soon after. Recent technological developments with onboard instrumentation, specifically the adoption of the stepped frequency microwave radiometer (SFMR) and Global Positioning Satellite (GPS) dropwindsondes (both discussed below), have dramatically increased the value of aircraft missions. However, the high cost of transforming and maintaining aircraft for safely flying into the violent cores of TCs has prevented every country but the USA from regularly flying operational missions, leaving less than 5 % of all global TC synoptic times (00, 06, 12, 18 Coordinated Universal Time, or UTC) influenced by this high-quality data. It should be noted that as of this writing, Japan is planning to restart active aircraft reconnaissance in the western Pacific in 2016 for at least a 5-year period.

Reade (2014) describes the interesting history of TC aircraft reconnaissance, which began with several informal flights during the mid-1940s. Both the US Navy (USN) and Air Force (USAF) began regular missions in the western Pacific in 1944; the USAF also began missions in the North Atlantic the same year. The 53rd USAF Weather Reconnaissance Squadron, now commonly known as the "Hurricane Hunters," was first activated around this time and continues to fly missions today, primarily in the North Atlantic. Collins and Flaherty (2014) provide a comprehensive overview of the Hurricane Hunters, including their history, aircraft, and instrumentation used. Before the regular

satellite observation of ocean basins began in the 1960s, many planes were flown with the purpose of finding storms. Once storms were found or otherwise reported by island residents or shipping interests, subsequent aircraft missions estimated the wind speed through visual inspection of the ocean surface. Additionally, pressure readings were made and then used to estimate the MSW based on established pressure-wind relationships.

Eventually, instrumentation was developed to accurately measure the relative wind speed at the aircraft flight level. Flight-level winds are still recorded by every reconnaissance mission today and have served as a valuable source of data when more desirable surface measurements of wind speed, through the SFMR or GPS dropwindsonde, were not available. To translate the flight-level wind to the MSW, a reduction is typically employed to account for the higher frictional effects in the boundary layer. Powell et al. (1996) discuss the issues with reducing flight-level winds to surface winds and have found that flight-level winds are typically within 20 % of the true surface wind.

Accurate reductions of flight-level wind are highly dependent on the vertical profile structure of TCs, which until recently has been difficult to measure due to obvious logistical challenges and safety concerns. However, the development of GPS dropwindsondes has provided forecasters and analysts with an expanded picture of the TC environment. Work with GPS dropwindsonde data in TC cores has led to changes in the flight-level wind reduction algorithms, which now reduce winds to 90 % of the 700-mb flight-level wind (e.g., Landsea et al. 2004).

(b) *GPS dropwindsondes*

A dropwindsonde is a package of instruments contained in a cylindrical copper case that is ejected from the bottom of an aircraft. As the dropwindsonde falls toward the ocean surface, it records and transmits measurements of temperature, humidity, pressure, and wind at a very high frequency (2 Hz) back to the aircraft. From typical launch altitudes ($\sim$700 mb, or 6 km above sea level), dropwindsondes typically provide 7 min of data before splashing into the ocean, falling under parachute at a velocity of 10–16 m s^{-1}. At those vertical velocities, GPS dropwindsondes measure atmospheric parameters approximately every 5 m.

Dropwindsondes were originally tracked via a network of Omega navigational stations (see Govind (1975) for information on these early versions of the modern dropwindsonde). After extensive use in measuring the tropical atmosphere during the Global Atmospheric Research Program Atlantic Tropical Experiment (GATE) program (1974), Omega dropwindsondes were first deployed in the environmental wind field of a TC during Hurricane Debby (1982) by National Oceanic and Atmospheric Administration (NOAA) WP-3D (P3) aircraft (Burpee et al. 1984). The potential improvement of TC forecasts was recognized early on, and deployment of Omega dropwindsondes continued through 1993 in both the North Atlantic and eastern Pacific. For example, Burpee et al. (1984) demonstrated that computer model TC track forecasts improved 16–30 % when dropwindsonde data was included in the model analysis field.

Even with the newly found success of incorporating Omega dropwindsonde observations into numerical forecast models, there were still challenges to the system of using Omega signals to derive wind speeds. On occasion, thunderstorm activity decreased the signal strength of Omega transmissions and reduced the reliability of the wind speed data retrieved from the instruments (Smalley 1979). There were also large data losses in the low levels of the troposphere due to Omega signal propagation (Hock and Franklin 1999). In the mid-1990s budget constraints were also threatening the continued operation of the worldwide Omega network (Rappaport et al. 2009).

The latest generation of dropwindsonde instruments overcame these challenges by incorporating GPS technology into dropwindsondes. Led by the US National Center for Atmospheric Research (NCAR) and the German Aerospace Research Establishment (DLR), development of the GPS dropwindsonde was completed in 1996 and boasted numerous advantages over the Omega systems – including higher wind speed accuracy and sampling rates, which increased the vertical resolution of wind speed measurements (Hock and Franklin 1999). In addition, GPS dropwindsondes are also able to measure winds in the lowest portions of the atmosphere, providing forecasters with a true in situ 10-m wind speed.

Improvements in track and intensity forecasts of TCs continued to be realized with the regular use of GPS dropwindsondes – first from drops in the TC environment and then in the inner core of TCs themselves. Aberson and Franklin (1999) document significant forecast improvements in track (32 %) and intensity (20 %) of the Geophysical Fluid Dynamics Laboratory (GFDL) hurricane model when GPS dropwindsonde vertical profiles from the outer TC environments were included in the model run. On 3 August 1997, NOAA P3 aircraft measured the first vertical profiles in a hurricane eyewall when dropwindsondes were deployed into Hurricane Guillermo. By the very next season, the USAF Hurricane Hunters regularly included GPS dropwindsondes in all of their operational missions.

Winds measured by GPS dropwindsondes are considered to be the gold standard; however, some care must be taken when interpreting the data. Franklin et al. (2003) collected approximately 600 soundings from inside or close to the eyewalls of 17 hurricanes in part to describe the vertical profile of wind speed. They suggested that single observations of wind speed by dropwindsondes should not be considered representative as a sustained wind speed, since the sonde responds almost immediately to any high-frequency variation in the wind field (i.e., turbulence); rather, estimates of surface MSW should be obtained through a longer averaging period. This requires either averaging the wind speed as the dropwindsonde falls through the boundary layer (500 m to the surface) and then decreasing the value by 20 % to account for frictional effects near the surface or averaging just the lowest 150 m and then adjusting to the surface using a mean dropwindsonde-based eyewall profile. In either case, Franklin et al. (2003) demonstrate that GPS dropwindsonde data have proven extremely valuable in understanding the nature of the TC wind field.

(c) *Stepped frequency microwave radiometer (SFMR)*

One of the biggest weaknesses of GPS dropwindsondes is the low areal coverage of the instrument. On typical reconnaissance missions, there are a limited number of dropwindsondes that provide only point measurements of wind. The development and operational use of the SFMR on board Hurricane Hunter and NOAA P3 aircraft provides a highly accurate estimate of the MSW over a much larger area. The SFMR is an instrument that determines the MSW by directly measuring the radiative emission of the sea surface, expressed as a brightness temperature (e.g., Uhlhorn and Black 2003). The nature of the sea state has a strong relationship to brightness temperature, as wind creates increased surface roughness, breaking waves, and seafoam (Jones et al. 1981). For example, Barrick and Swift (1980) demonstrated that the percentage of foam coverage due to wave breaking increases monotonically with wind speed.

Uhlhorn and Black (2003) provide a good description of the modern SFMR instrument and its use in hurricanes. The SFMR contains a downward-pointing antenna that passively reads nadir (orthogonal to the surface) brightness temperatures at six different frequencies ranging from 4.55 to 7.22 GHz (C-band); the diversity of frequencies allows for estimation of both surface wind speed and rainfall. Wind speeds are estimated through the application of a geophysical model function (GMF) that relates the surface emissivity to wind. The emissivity is a function of surface foam from wave breaking – which is strongly correlated with the local wind speed – and a contribution from the atmosphere, which is accounted for in a forward radiative transfer model (Ulaby et al. 1981). Originally conceived and developed in the late 1970s and first flown into Hurricane Allen (1980), the SFMR and its GMF have undergone a number of improvements during the 1980s and 1990s. By 2008, the SFMR was installed on all USAF and NOAA reconnaissance aircraft, supplementing the wind data provided by GPS dropwindsondes. SFMR data are even more critical when dropwindsondes stop transmitting wind data close to the ocean surface, a frequent occurrence in strong TCs.

SFMR wind speeds have been carefully validated against GPS dropwindsonde data that have been adjusted to account for time averaging and the standard 10-m measuring height (Uhlhorn and Black 2003; Uhlhorn et al. 2007). Uhlhorn and Black (2003) compared 249 paired samples of SFMR measurements from 1998, 1999, and 2001 with GPS dropwindsonde data. Figure 4.1 shows the scatterplot comparison of all points. Note the positive bias ($+2.33$ m s^{-1}) in the SFMR data and the RMSE value of 3.31 m s^{-1}. Uhlhorn and Black attribute some of the errors to the generation of foam on the ocean surface from something other than local wind, such as the known dependence of the retrieval on wind fetch. An analysis of SFMR wind errors based on storm quadrant (different quadrants have different wave generating properties) supports this idea. Subsequent work (Uhlhorn et al.
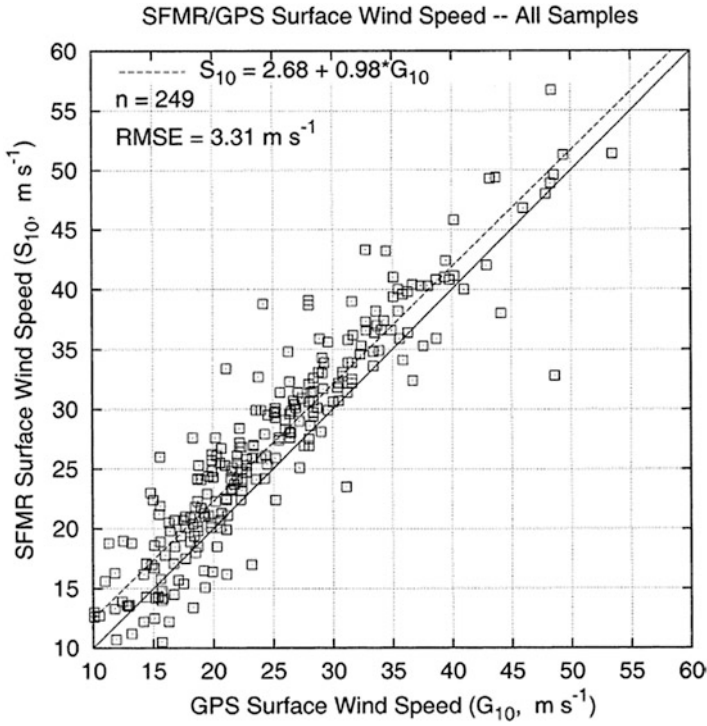
Fig. 4.1 SFMR-GPS surface wind speed comparisons from Uhlhorn and Black (2003). The *solid line* indicates perfect correlation, and the *dashed line* indicates the best fit (© American Meteorological Society. Used with permission)

2007) led to the development of an updated SFMR algorithm that corrected this high bias and made extreme wind speed retrievals (>60 m s^{-1}) more accurate.

(d) *Buoys*

Ocean buoys have traditionally provided the most accurate measurement of near-surface TC winds – but of course only when the storm passed near enough to the instrument. There are essentially two types of buoys: moored and free floating ("drifters"). There are over 1000 active drifters at any time worldwide, but most do not have wind sensors and thus do not regularly contribute to TC wind measurement. However, there have been some targeted experiments where wind-equipped drifters have been dropped ahead of approaching TCs in the Atlantic and Pacific basins (Niiler et al. 2003).

The accuracy of buoy wind measurements is perceived to be very high (e.g., Gilhousen 1987) – so high that almost all of the remotely sensed wind data discussed later uses buoy data for validation. However, there are still concerns that must be considered when measuring high winds with

buoys. Buoys employing mechanical anemometers risk failure when wind speeds exceed 25 m s^{-1}, and there may be a low bias introduced due to wave sheltering effects during large swells generated in TCs. Howden et al. (2008) performed an analysis of buoy-measured winds by a sonic anemometer (a design less susceptible to failure) during a close passage of Hurricane Katrina (2005). Their results suggested that many buoy measurements in TCs may be further biased low because of a failure to account for buoy pitch and roll, which exposes the anemometer to the wind at an angle.

(e) *Ship and surface stations*

Of course the biggest disadvantage to using buoy wind data both operationally and in research is the scarcity of TC overpasses. Most moored buoys are stationed near coastal areas, and a measurement of the area where the TC MSW may occur happens infrequently. A similar challenge is encountered with using ship-mounted anemometers to measure TC winds – ships typically avoid TCs – so wind observations in the strongest parts of the storm are rare. Approximately 4000 ocean-going vessels currently participate in the WMO's Voluntary Observing Ship (VOS) program, in an effort to alleviate the dearth of surface ocean observations. Accurate wind observations from ships, even those with anemometers, are difficult in high winds. Wave activity pitches and rolls the ship, causing artificial variance in observations. Furthermore, wind shielding from high swells, as with buoy data, is also a concern.

Surface-based observations of wind only occur when a TC is in close proximity to a coastline or offshore platform. The US National Data Buoy Center (NBDC) established the Coastal-Marine Automated Network (C-MAN) in the early 1980s in an effort to formally maintain meteorological observation in US coastal areas. These stations have been installed on lighthouses, beaches, offshore platforms, and near-shore islands. Because of the diversity of wind exposure through the C-MAN network, the wind data can exhibit significant variability across short distances. Stations constructed in areas where land-induced friction plays a significant role typically record lower wind speeds compared to marine-exposed stations as well as ships and buoys (Dunion and Velden 2002). In addition to the C-MAN network, TCs are observed by more regular observation stations near the coast, such as National Weather Service Automated Surface Observing Stations (ASOS).

Similar to mechanical anemometers mounted on buoys, land-based mechanical anemometers are also susceptible to failure at higher wind speeds. It is thus quite rare to find suitable land station wind speed data to verify very strong TC landfalls. Hurricane Andrew (1992) had long been classified a Category 4 hurricane on the Saffir-Simpson scale at landfall in South Florida because the MSW was determined principally by reconnaissance flight-level winds reduced to the surface. Surface anemometers, particularly the C-MAN

station at Fowey Rocks, Florida, failed before measuring the peak winds in the storm's eyewall. A subsequent reanalysis of the storm by Landsea et al. (2004) upgraded Andrew to a Category 5 based primarily on new surface wind reduction factors that were determined from new GPS dropwindsonde data.

(f) *Doppler radar*

Doppler radar can determine local wind velocities by bouncing radiation off of particles (e.g., rain, ice) embedded in the flow. Surface-based Doppler radars have been shown effective at determining horizontal wind speeds in TCs. Tuttle and Gall (1999) modified a method originally conceived by Rinehart and Garvey (1978) to track reflectivity echoes (TREC). They showed that TREC was particularly effective in the lower few km of the storm where vertical wind shear is relatively weak. Radar winds were typically within 10 % of aircraft measurements in the storm and rarely were off by more than 10 kt. Harasti et al. (2004) further investigated the use of TREC and other methods for applying Doppler radar data to TC winds. Modifications were made to TREC and the ground-based velocity track display (GBVTD) algorithm to make them more accurate and operationally friendly; for example, the data were converted to ground-relative wind speeds. Based on test cases in two TCs with reconnaissance data, Harasti et al. (2004) showed that both TREC and GBVTD were able to retrieve the MSW of a TC with an accuracy $\sim 2 \text{ m s}^{-1}$.

Of course, the application of ground-based Doppler radar is limited to times when TCs move near the radar site. Both NOAA and NASA have installed Doppler radar systems on board aircraft to increase the reach of the radar. The Imaging Wind and Rain Airborne Profiler (IWRAP, Fernandez et al. 2005) is a dual-frequency radar that is mounted on the NOAA P3 aircraft, which typically flies at lower altitudes (2–4 km) in TCs. NASA has developed and installed the High-Altitude IWRAP (HIWRAP, Li et al. 2008) on board its Global Hawk unmanned high-altitude (18–20 km) aircraft (Sect. 4c). Wind retrieval algorithms applied to IWRAP and HIWRAP data have shown skill in retrieving the horizontal winds in TCs. For example, Guimond et al. (2014) showed that IWRAP wind retrievals at nadir had errors of $\sim 4.0 \text{ m s}^{-1}$ when compared to flight-level winds in Hurricane Isabel (2003). Although this error is about twice as high as ground-based Doppler winds, it is still quite remarkable given the challenges of accounting for the movement of the aircraft itself.

3 Remote Observation

Although the in situ measurement of TCs is ideal, in reality, such observations are rare. Fortunately, the situation has become progressively better in recent decades as a number of satellite systems have filled in the gaps. This section will examine

three of the more popular systems used to observe TC winds: geostationary orbiting environmental satellite (GOES) cloud track winds, scatterometers, and microwave sounders.

(a) *GOES (cloud-drift winds)*

Understandably there is much focus on determining the MSW, which occurs near the TC core. But the strength and distribution of the wind field around the periphery (∼50–500 km from the center) are also of importance to forecasters and other maritime interests. Typically, reconnaissance aircrafts do not sample that area of the storm, and overpasses over buoys or ships are too infrequent. To fill in this gap of quality surface wind observations, a technique was developed to track cumuliform clouds in 15-min sequences of GOES visible channel images (Velden et al. 1998). An accurate assessment of the cloud level and a reasonable transition to a 10-m wind could provide valuable wind data away from the central core.

Dunion and Velden (2002) verified GOES winds against GPS dropwind-sonde data from three 1998 TCs (Bonnie, Danielle, and Georges) at radii ranging from 400 to 1600 km from the TC centers (500 collocated points total). They found a RMSE of approximately 5 kt for the GOES cloud-drift winds – certainly accurate enough to be used with confidence. Further comparisons of surface-adjusted GOES winds were made with in situ data (ships, buoys, and stations on lighthouses and oil platforms). The RMSE was similar, with an overall value of ∼5.5 kt.

The GOES cloud-drift winds have been successfully incorporated into H*Wind, a TC wind data assimilation and objective analysis system discussed in Sect. 4b. Further research using water vapor and IR channels have led to the creation of a large number of useful products, including wind shear, vorticity, and convergence analyses across any ocean basin. These are accessible in near real time on the Cooperative Institute for Meteorological Satellite Studies website at the University of Wisconsin–Madison (CIMSS 2015).

(b) *Scatterometers*

Scatterometers have proven to be successful at retrieving both surface wind speed and direction in the vicinity of TCs. These active microwave scanners operate by emitting pulses of Ku-band (13.4 GHz) or C-band (5.3 GHz) radiation toward the ocean surface, where the energy interacts with capillary-scale (<1-cm wavelength) waves. The intensity of the backscatter is proportional to the magnitude of the surface wind stress, which is then translated to a wind speed via a GMF. Furthermore, the orientation of the capillary waves provides scatterometers with data to retrieve the wind direction as well. Scatterometers have been observing TCs regularly since the European ERS-1 and ERS-2 missions during the 1990s. The USA joined the scatterometer community when NASA successfully launched the NSCAT instrument in September 1996. NSCAT was shown to be very accurate (Freilich and Dunbar 1999) in retrieving

both wind speed and direction, thus encouraging the subsequent scatterometer missions (SeaWinds) after NSCAT's failure in June 1997.

SeaWinds, on board the QuikSCAT satellite, was launched in 1999 and provided almost continuous coverage of ocean vector winds for 11 years. The instrument was briefly joined by a twin instrument on board the Japanese satellite ADEOS-II in late 2002, providing nearly twice daily global coverage of ocean winds until the failure of ADEOS-II in October 2003. The instruments on SeaWinds were Ku-band scatterometers that provided 25-km resolution data across a nearly 800 km wide swath. The coverage and accuracy of SeaWinds ocean vector winds was a boon to TC forecasters (e.g., Brennan et al. 2009), who could now estimate storm wind radii more accurately and determine the existence of closed surface circulations in immature TCs with more confidence. There were also demonstrated improvements in storm track forecasting when scatterometer data were assimilated into models.

There are several well-known limitations with scatterometer wind retrievals that constrain their application to TCs. Ku-band scatterometers are sensitive to rain. Drops enhance the roughness (and backscatter) at the ocean surface, disassociating the surface roughness with the actual wind speed. Rain also attenuates the signal in the atmosphere, reducing the backscatter received at the satellite. The net effect is a function of the true surface wind speed (often unknown) and the intensity of the rain (also not accurately known). Therefore, surface wind retrievals thought to be contaminated with rain are frequently "flagged" and ignored or used with caution by analysts. In general, it has been shown that rain leads to a high retrieval wind speed bias for TCs at tropical storm wind speeds and below, while there is a progressively low bias in retrieved wind speeds at higher intensities (e.g., Brennan et al. 2009). Furthermore, even in ideal conditions, the wind retrievals will "saturate" or maximize at about 45 m s^{-1}, regardless of the TC intensity. C-band scatterometers, like the European ASCAT, are particularly prone to saturate at higher wind speeds (although they are generally less sensitive to rain). Because of these reasons, it is not possible to use scatterometer winds to estimate the MSW in most TCs, since retrievals in the eyewall region typically contain the highest rain rates and are most likely to saturate the signal. Nevertheless, active scatterometer missions such as ASCAT, OceanSat, and RapidScat (on board the International Space Station) continue to provide valuable wind data for many TCs.

(c) *Advanced Microwave Sounding Unit (AMSU)*

As with scatterometer data, microwave sounding units enjoy the advantage of "seeing through" clouds which frequently obscure the central area of TCs. By measuring the vertical structure of the TC core temperature, microwave sounding data can be converted into a wind field by mapping core temperatures to surface wind speeds when they are known from GPS or SFMR measurements. Microwave sounders were originally conceived and deployed in the 1960s; the deployment of the Microwave Sounding Unit (MSU) aboard the Television and Infrared Observation Satellite (TIROS-N) in 1978 marked the first high-quality

observations of vertical profiles of atmospheric temperature and water vapor content from space. The current generation of microwave sounders is the Advanced Microwave Sounding Unit (AMSU), first launched into orbit in 1998 aboard the NOAA-15 satellite (Goldberg 1999).

The AMSU is a cross-track scanning radiometer that passively measures electromagnetic radiation. A scanning mirror cycles through 30 separate angles – ranging from 1.67 to 48.33° – of the earth's surface every 8 s. With an effective ground resolution of 48 km and a swath width of 2343 km (e.g., Kidder et al. 2000), the AMSU is able to adequately measure most TCs regularly, although the coarse resolution can limit the skill and confidence in measuring the inner core of TCs – which may be much smaller. There are 20 combined frequency channels, subdivided into temperature (AMSU-A) and moisture sounding (AMSU-B) groups.

The vertical profile of atmospheric temperature is determined by measuring the brightness temperature at a number of levels. As mentioned previously, the MSW can then be estimated either by correlating the strength of the TC warm core to more well-known estimates of MSW or through employing pressure-wind relationships. Kidder et al. (2000) performed a correlation study between the warm core and the MSW and found that the upper-level warm core anomaly could be used to estimate MSW to an accuracy of 10 m s^{-1}. Demuth et al. (2004) showed even better success by calculating a surface pressure and geopotential height fields through the hydrostatic and gradient wind equations. They analyzed 100 cases during the 1999–2001 seasons and found that the mean absolute error was 5.3 m s^{-1} when compared to BT data, which is comparable to error experienced through the use of the Dvorak technique (Sect. 4a). Another advantage of this method is that wind radii estimates can be easily determined through the application of these balance equations.

The latest generation from the AMSU family is the Advanced Technology Microwave Sounder (ATMS), which combines all of the channels from AMSU-A and AMSU-B into one instrument. ATMS provides a more efficient platform for collecting vertical soundings of temperature and moisture with a wider swath and better horizontal resolution than AMSU (26 km vs. 48 km at nadir). It is one of five instruments on board the Suomi National Polar-orbiting Partnership (S-NPP) satellite, launched in 2011.

Today, the strengths and limitations of the AMSU instrument are well understood. The wind retrievals are one of many sources considered by analysts and forecasters in determining the MSW, although its significance operationally is routinely overshadowed by the use of the Dvorak technique (Sect. 4a), especially when other data sources (e.g., SFMR, GPS dropwindsondes) are absent. AMSU winds also serve as an important source in MSW superensemble techniques currently in development, such as SATCON (Sect. 5c).

4 Applied Techniques

The evolution of scatterometers and microwave sounders into more useful sources of TC wind data continues today. One shortcoming in the operational use of these and other polar-orbiting observing platforms is the irregularity of TC overpasses. In the tropics, gaps between subsequent satellite swaths are at their largest. Even in the most ideal situation, a satellite may observe a TC no more than twice a day. The use of geostationary data (cloud track winds, Sect. 3a), which allows for near-continuous observation of TCs, has limited ability to determine winds anywhere near the TC core. Without an ideal way of measuring the MSW, researchers have developed a number of applied techniques that build upon the strengths of these individual systems. This section will examine two of these: the Dvorak technique and H*Wind.

(a) *Dvorak Technique*

The Dvorak technique (Dvorak 1972, 1975, 1984) is an algorithm developed in the 1970s and improved upon during the 1980s that uses visible and/or infrared geostationary imagery to estimate the MSW. It was the first and still the only reliable method of determining the MSW based on the characteristics of the cloud pattern in a satellite image. In fact, the algorithm has been adopted at every TC forecast agency in the world and remains the most widely used method for determining MSW. Velden et al. (2006) provide an extensive review on the Dvorak technique; here, we will provide a brief description of how the algorithm works and its accuracy.

The technique can be used with visible or IR imagery; however, the IR version (called the enhanced IR or EIR) is generally more accurate and is the least subjective. Figure 4.2 shows an enhanced IR image of Supertyphoon Haiyan (2013), a storm which went on to inflict catastrophic damage to the Philippines. The gray shades are the traditional enhancement used for the Dvorak technique and represent the cloud brightness temperatures. The first step in estimating the MSW is to find the center of the storm, which in this case is relatively easy since Haiyan has a clear "eye." Step 2 is to determine the "cloud pattern," which could be one of four choices: curved band, shear, eye, or embedded center. A curved band pattern will present itself as a comma-type cloud and generally will translate to a weaker system. Embedded center storms are circular in appearance but the center of the storm will be covered with clouds. Shear storms have an exposed circulation center (separate from the main area of convection) and can be difficult to identify in IR imagery. In this case, it is clear that Haiyan is exhibiting an eye pattern.

Once the cloud pattern is identified, a number of pattern-specific features are determined; for example, in eye patterns it is important to identify the cloud color (brightness temperature range) that completely surrounds the eye, how thick it is, and how large of a difference in temperature exists between it and the warmest cloud pixel in the eye. All of these factors have been shown to be related to the strength of the MSW. This process produces what is called a
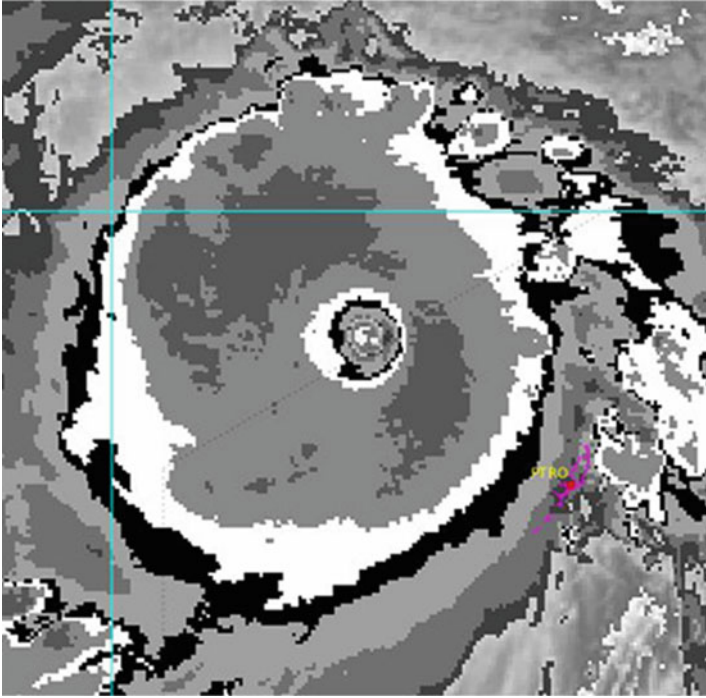
Fig. 4.2 Infrared-enhanced image of Supertyphoon Haiyan (2013) in the western Pacific Ocean. Image courtesy of the Cooperative Institute for Meteorological Satellite Studies (CIMSS), University of Wisconsin-Madison

"Data T" number, which has a value between 1.0 and 8.0 and can be related to MSW through the use of a lookup table (Table 4.1). Next, a number of rules and constraints are applied to limit the effect of transient features in the satellite image that could lead to a false intensity. For example, it has been observed that TCs rarely change intensity by more than 1.0 Data T numbers in a 6-h period. Once the rules are applied, a "current intensity" or CI number is used to determine the MSW through the same lookup table (Table 4.1).

Knaff et al. (2010) performed a verification study of Dvorak estimates. They compared the MSW from the Dvorak estimate to the BT MSW for those times that were influenced by aircraft reconnaissance data (i.e., when there was aircraft data ± 2 h from the BT time). Figure 4.3 shows the bias, mean absolute error (MAE), and root-mean-square error (RMSE) by BT intensity for Dvorak estimates from two different agencies. There is a clear dependence of Dvorak accuracy on storm intensity – errors generally increase at higher intensity, while a high negative bias develops. Knaff et al. attribute this bias to the nature of the cold cloud tops in the North Atlantic basin, which rarely achieve the low temperatures observed in western Pacific storms – the area from which the

Table 4.1 EIR Dvorak T
number conversion to
maximum sustained wind (kt)

T number	Maximum wind (kt)
1.0	25
1.5	25
2.0	30
2.5	35
3.0	45
3.5	55
4.0	65
4.5	77
5.0	90
5.5	102
6.0	115
6.5	127
7.0	140
7.5	155
8.0	170

Dvorak technique was originally developed. In general, the 12-kt RMSE for hurricane-strength storms is quite remarkable given that the MSW estimates originate from only IR images.

Despite its demonstrated successes, MSW estimates from the Dvorak technique are frequently scrutinized because the process is inherently subjective and vulnerable to user error, especially when users are not sufficiently trained. Large differences in Dvorak estimates for the same storm image have been demonstrated (e.g., Nakazawa and Hoshino 2009), leading to many of the heterogeneities in BT data discussed in the opening of this chapter. These differences arise from the uncertainties involved with identifying the proper cloud pattern, the diverse set of rules and constraints that local agencies have developed to "tune" the technique to their area of interest, and limitations in applying the technique in certain situations like "pinhole eyes" (very small eyes barely resolved in satellite imagery) or "midget typhoons" (very small TCs that appear to not obey the normal Dvorak rules). An automated Dvorak technique, now called the Advanced Dvorak Technique (ADT, Olander and Velden 2007), was developed to mitigate many of these challenges in the manual routine. User subjectivity is taken out of the process through the application of automated storm center and pattern determination schemes. Final intensity estimates are corrected through an analysis of North Atlantic and Pacific storms. Presently, the ADT is frequently consulted in operations as another viable estimate of MSW, and improvements to the system are continually made.

In the absence of regular, high-quality observational data, the Dvorak technique continues to overwhelmingly influence global TC MSW estimates. Despite its limitations and the continuing increase in the quantity and quality of wind observations, there is little evidence that the Dvorak technique will fade in importance over the next few decades.
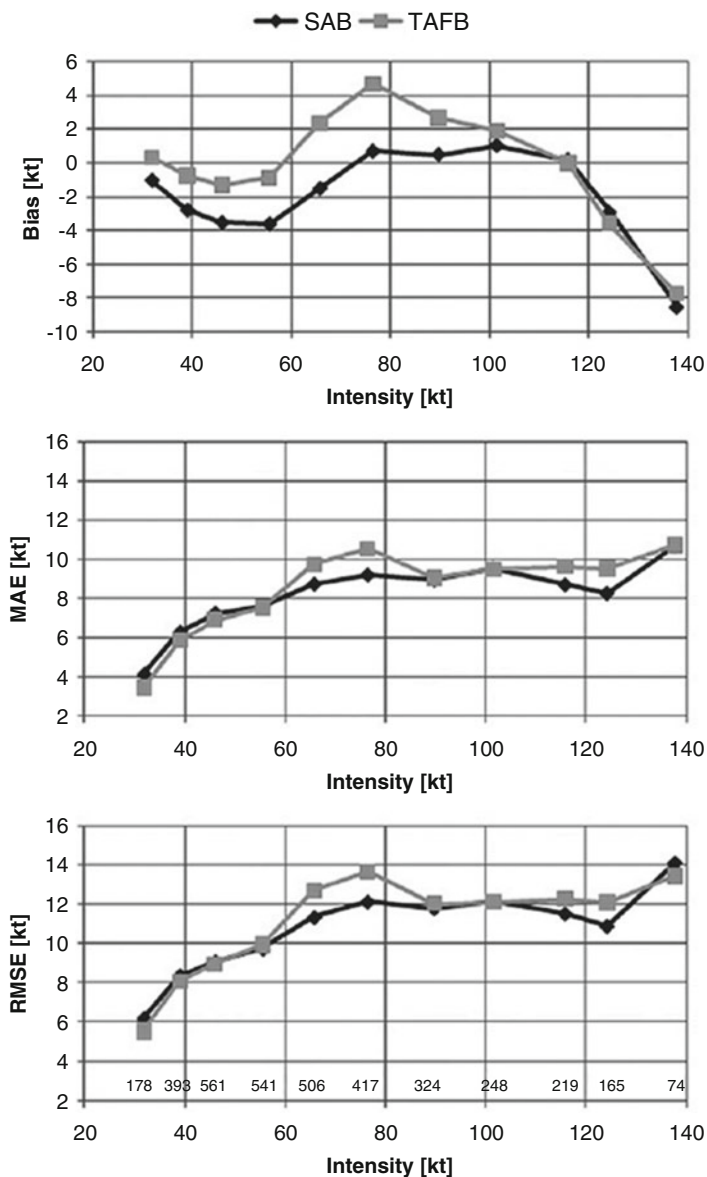
Fig. 4.3 (*Top*) biases, (*middle*) MAEs, and (*bottom*) RMSEs associated with Dvorak tropical cyclone intensity estimates (kt) from the Satellite Analysis Branch (SAB) and the Tropical Analysis and Forecast Branch (TAFB) that were made with ±2 h of an aircraft reconnaissance fix. The verification is based on the BT intensities at those times, and the analysis domain was the Atlantic basin. The number of cases is provided in the *bottom* panel (caption and figure from Knaff et al. (2010), Figure 3) (© American Meteorological Society. Used with permission)

(b) *H*Wind*

Any observations of TC wind are heterogeneous in space and time. Instruments aboard polar-orbiting satellites, such as scatterometers and microwave sounders, will fly over a TC at different times of day. Buoy, ship, and surface station measurements are sporadic at best. Reconnaissance aircrafts are in a storm for a number of hours and will only sample a small portion of the environment. Given this situation, it is difficult for forecasters and analysts to merge the disparate observations into a cohesive evaluation of the storm's intensity. In turn, the assimilation of the TC into numerical model analysis fields will suffer, resulting in inferior forecasts of storm track and intensity. During times of rapid change in the TC structure and/or intensity, the problem is exacerbated.

This issue has long been recognized in the TC community; one popular solution is the data assimilation and analysis system called H*Wind (Powell et al. 1998). H*Wind is composed of a data server that collects wind data from a number of platforms, including aircraft data, scatterometers, surface stations, buoys, GOES cloud-drift winds, Doppler radar, and more. The data are quality controlled and transformed to a storm-relative framework. The H*Wind user can control the time window of observations to consider, the weights applied to each, and even the algorithms used to adjust the data to the standard 10-m, 1-min sustained criteria. The user can also exclude suspicious observations or entire datasets. The H*Wind analysis algorithm is then run, producing a gridded isotach analysis (~2-km resolution) of the mean state of the TC centered around the analysis time.

Figure 4.4 shows an H*Wind analysis of Hurricane Wilma (2304 UTC 21 October 2005) as the storm interacted with the Yucatan Peninsula. The data that were used for the analysis are shown at the top of the image, including the time window for each. Overall the storm, especially outside the inner core, is symmetrical with discontinuities noted at the land/sea interface. This is because the analysis is accounting for the type of exposure (land vs. marine) that the wind is experiencing. This symmetrical pattern is common in H*Wind analyses. It arises when the analysis algorithm experiences sparse observations (common) and tends to smooth out the wind field. The MSW of the storm near this time is shown as a "+" symbol just to the northeast of the center and is probably near a SFMR or GPS dropwindsonde measurement in the eyewall. Without aircraft data, reliable analyses of TCs are not possible as SFMR and GPS dropwindsonde data are generally required to measure the MSW in TCs with some confidence. Below the analysis image, other relevant information that may be useful for assessing the storm impact is given to the user (e.g., storm kinetic energy, wind/wave destructive potential).

H*Wind has served as a valuable tool in TC research, particularly as a validation tool for some remote sensing platforms (e.g., Laupattarakasem et al. 2010). Though never adopted for real-time use because of time constraints in an operational setting, TCs are still actively analyzed, and archived real-time storm analyses are still available through Risk Management Solutions/H*Wind Scientific (RMS 2016).
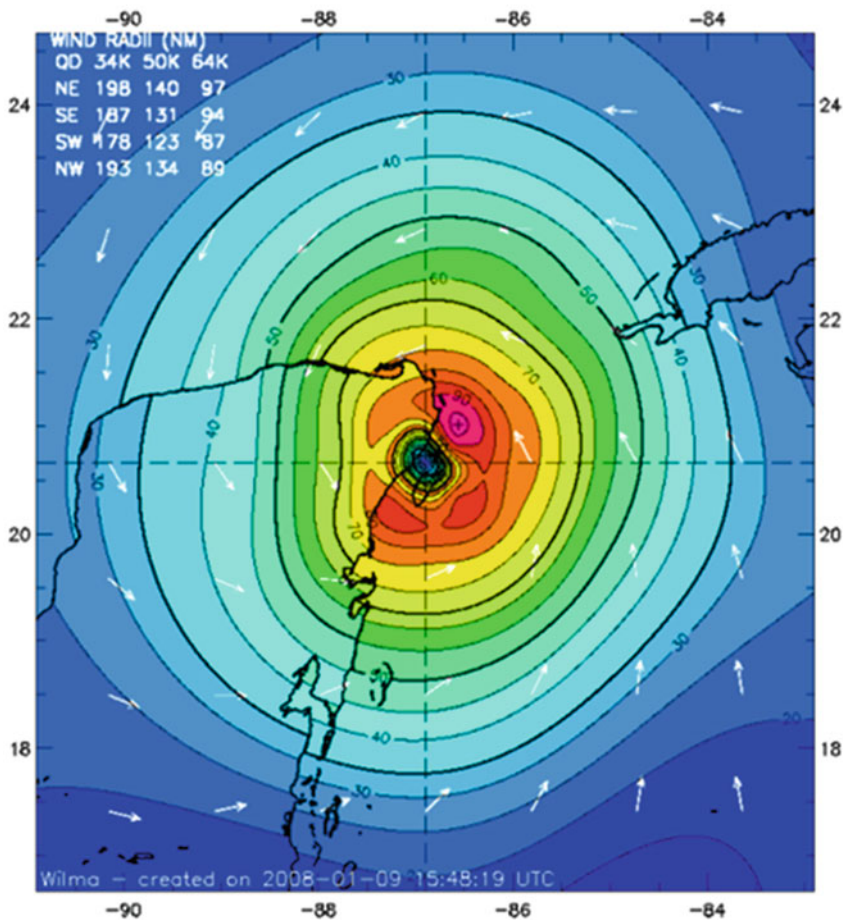
Fig. 4.4 H*Wind isotach analysis of Hurricane Wilma (2005) centered at 2304 UTC 21 October 2005

5 Experimental Approaches

Despite the broad consensus that aircraft reconnaissance is the optimal mode of TC wind observation, there is little evidence to suggest that there will be any significant increase in the frequency of recon missions. Reade (2014) highlights a number of countries that are planning to begin regular missions, but cost and other logistical challenges ensure that TCs will remain poorly sampled for many years to come. Yet there have been several promising developments in data collection and analysis that promise to improve our ability to observe TC winds more accurately and frequently. Although currently experimental, the following all have the potential to move the needle forward, either through increased coverage in space and/or time or better accounting for errors in current wind estimates.

(a) *HIRad*

As discussed earlier, the SFMR is a valuable instrument capable of accurately measuring surface wind in TCs. Perhaps the biggest limitation of the SFMR is that accurate measurements of wind can only be obtained at near nadir, severely limiting the amount of storm coverage. Recent work on off-nadir measurements using the SFMR, called HIRad (Cecil et al. 2015), offer the potential to cover much larger areas of the storm from a single reconnaissance flight. A specialized antenna allows for measurements of surface brightness temperature up to 40° off nadir, allowing for a swath of wind speed and rain rate measurements of more than 50 km from an aircraft flying at 20-km altitude with the application of a specialized GMF. If the data at the edges of the swath can be shown to be accurate, this would be a large step forward in measuring TC winds.

The HIRad instrument has been flown into several TCs for testing, including Hurricanes Earl (2010), Karl (2010), Ingrid (2013), Gonzalo (2014), Joaquin (2015), and Patricia (2015). Figure 4.5 shows the retrieved surface wind speed from a flight through Hurricane Patricia. The data resolution is quite fine (1–3 km), and it is clear that many details of the surface wind near the core of the TC can be resolved, including the calm eye and the intense eyewall. Qualitative comparisons with nearby GPS dropwindsonde measurements show promise; however, the initial passes through all these systems have uncovered large errors, particularly in deciphering between the wind and rain signals in the brightness temperature field. Thus, HIRad remains an experimental platform for now.

(b) *Aerosondes*

In recent years, unmanned aerial vehicles (UAVs), or aerosondes, have been developed for TC reconnaissance. Originally constructed in the early 1990s (Holland et al. 2001), aerosondes contain a number of meteorological instruments that can potentially provide measurements in difficult environments such as TCs. The first successful flight into a mature TC was conducted on 16 September 2005 into Tropical Storm Ophelia. The drone was able to report winds and other data, including sea surface temperature, from the TC boundary layer – a place where safety concerns prohibit the flight of manned aircraft.
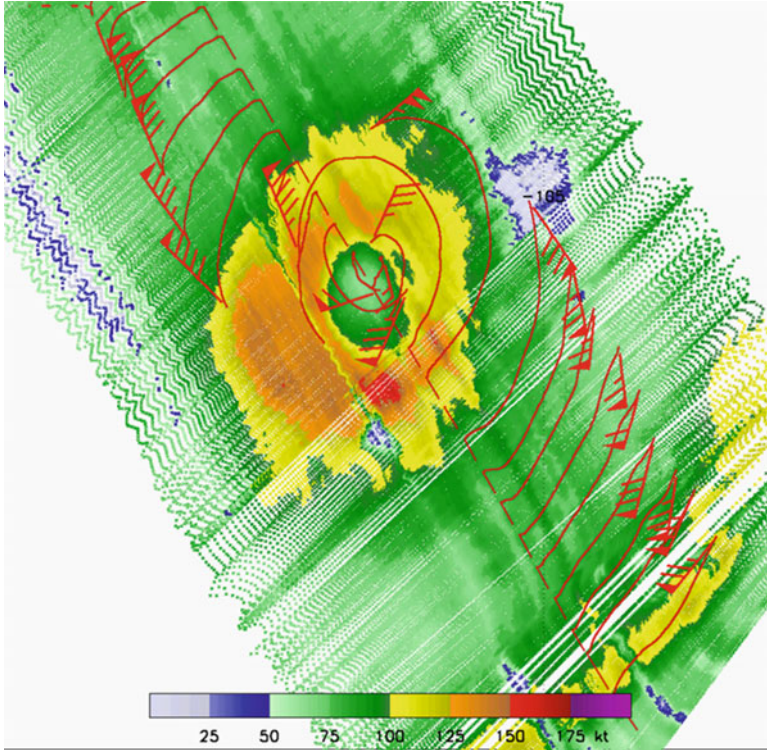
Fig. 4.5 HIRad wind speed retrievals (*colors*, in kt) through Hurricane Patricia (2015) with trajectories and wind barbs from GPS dropwindsondes overlaid (Figure courtesy of Daniel Cecil (NASA))

Reports from the time (e.g., NOAA 2006) were optimistic that a continuing UAV observation program would return big benefits to the TC community and fill in critical thermodynamic and dynamic data near the US coastline. However, there appears to have been little movement toward routine operational deployment of UAVs. In the research arena, NASA uses its Global Hawk aircraft to fly into TCs as part of a number of experiments. Unlike the UAV flown into Ophelia, the Global Hawk aircraft are designed to fly high-altitude missions over a long (∼24 h) duration. In addition to a sounder and lidar that provide high-resolution temperature, humidity, and aerosol data, the Global Hawk has the ability to release dropwindsondes, allowing for the vertical measurement of wind speed. Recently, several flights were made into Hurricane Edouard (2014) as part of the Hurricane Severe Storm Sentinel (HS3) mission, where the Global Hawk dropped dozens of dropwindsondes in or near the eye. The HIWRAP Doppler instrument discussed in Sect. 2f is also flown aboard the Global Hawk aircraft.

(c) *Satellite Consensus Algorithm (SATCON)*

SATCON (Velden and Herndon 2014) is a weighted consensus algorithm that uses MSW evaluations from the ADT (Sect. 3a), two different AMSU sounder algorithms, and a Special Sensor Microwave Imager Sounder (SSMIS). Weights are calculated based on the type of TC cloud scene (determined objectively) being evaluated. For example, errors in the ADT vary depending on whether the TC has an eye, a cloud shield over the center, or some other pattern such as shear. Errors in AMSU sounding MSW estimates, as described above in Sect. 3c, depend on the scan geometry of the sensor relative to the TC eye size and position. SATCON produces estimates of both MSW and minimum sea level pressure using unique weights for each parameter. Recently, a theoretical pressure-wind relationship was employed to create a new input into the consensus – the MSW from the SATCON MSLP.

Figure 4.6 shows a series of SATCON MSW estimates compared to its individual members, the human-based Dvorak technique, and the NHC BT MSW during the intensification phase of Hurricane Patricia (2015) in the eastern Pacific. This is an interesting case because Patricia was the strongest TC ever measured in the western hemisphere; this created challenges in estimating the intensity of Patricia using the Dvorak and ADT techniques, which historically underestimate high-end intensities. An additional unique aspect of this time series is that reconnaissance aircraft did sample the storm near peak intensity,
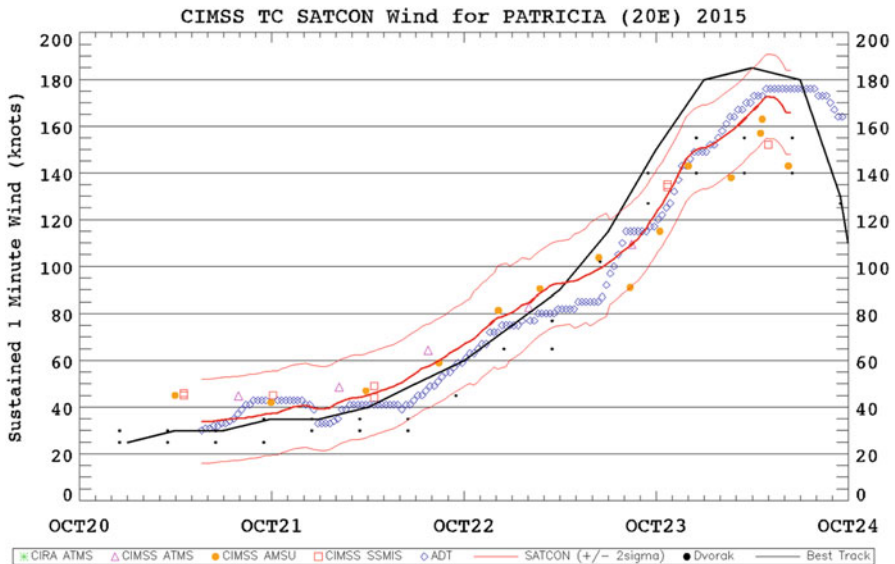
Fig. 4.6 SATCON MSW estimates (*red line*) for the intensification phase of Hurricane Patricia (2015). Shown for comparison are intensity estimates from its microwave ensemble members (shapes), the Dvorak technique (*black dots*), and the BT intensity from the US National Hurricane Center (*black line*) (Figure courtesy of Derrick Herndon (SSEC, University of Wisconsin))

which directly contributed to the higher BT intensities seen on 23 October and increased confidence in their values. SATCON clearly outperformed its members during the first 2 days of the storm but underestimated Patricia at peak intensity (175 kt vs. 185 kt). When evaluated over many storm times that were influenced by reconnaissance data, Velden and Herndon (2014) show that SATCON's average RMSE outperforms the subjective Dvorak estimates by ∼10 %. Work continues on refining and adding inputs into SATCON, including the subjective Dvorak technique.

6   Conclusion

It may now be a little clearer why we began this chapter with words of caution about the quality of historical BT data. The observation platforms and instruments described here rarely if ever measure TCs at the same time. They all have particular strengths and weaknesses that must be accounted for. The "gold standard" for TC wind observation – data from aircraft reconnaissance missions such as SFMR and GPS dropwindsondes – is currently regularly collected for only North Atlantic basin storms. Intensities of TCs outside those directly observed in the North Atlantic are strongly influenced by analyst interpretations of geostationary imagery (Dvorak technique), which can lead to dramatically different conclusions when using BT records for assessing trends. For example, Webster et al. (2005), Wu et al. (2006), and Kossin et al. (2007) found an increase, decrease, and no change, respectively, in the frequency of severe typhoons in the western Pacific between a recent and earlier time period. Webster and Wu used different agency BT records, while Kossin applied an objective intensity algorithm to homogeneous IR satellite data. Kossin et al. (2013) provide a good source for further reading on the differences in global BT data.

Until high temporal and spatial observations of TCs can occur, there will always be a large degree of uncertainty in the MSW value. Nolan et al. (2014) investigated the utopian idea of having a dense network (spaced 11-km apart) of anemometers that measure the eye and eyewall of a TC with no instrument error. Simulations show that this network would still underestimate the MSW in a 60-m s^{-1} hurricane by 5 m s^{-1} through undersampling. Our best chance in the next few decades of achieving or exceeding this benchmark is through the continued development and successful deployment of satellite-based systems that can provide regular, dense coverage of TCs. If we can rely less on interpretation of geostationary imagery for MSW, the more likely a satisfactory BT record will be possible.

measuring tropical cyclone winds from buoys. Derrick Herndon (Space Science and Engineering Center, University of Wisconsin) provided Fig. 4.6 and improved the discussion on SATCON.

References

Aberson SD, Franklin JL (1999) Impact on hurricane track and intensity forecasts of GPS dropwindsonde observations from the first-season flights of the NOAA Gulfstream-IV Jet aircraft. Bull Am Meteorol Soc 80:421–427. doi:10.1175/1520-0477(1999)080<0421:IOHTAI>2.0.CO;2

Barrick DE, Swift CT (1980) The Seasat microwave instruments in historical perspective. IEEE J Oceanic Eng 5:74–79. doi:10.1109/JOE.1980.1145457

Brennan MJ, Hennon CC, Knabb RD (2009) The operational use of QuikSCAT ocean surface vector winds at the National Hurricane Center. Weather Forecast 24:621–645. doi:10.1175/2008WAF2222188.1

Burpee RW, Marks DG, Merrill RT (1984) An assessment of omega dropwindsonde data in track forecasts of Hurricane Debby (1982). Bull Am Meteorol Soc 65:1050–1058. doi:10.1175/1520-0477(1984)065<1050:AAOODD>2.0.CO;2

Cecil DJ, Biswas SK, Jones WL (2015) Hurricane imaging radiometer (HIRAD) [Internet]

CIMSS (2015) CIMSS tropical cyclone intensity consensus for Patricia (20E). http://tropic.ssec.wisc.edu/real-time/satcon/archive/2015/201520E.html. Accessed 24 Jun 2016

Collins J, Flaherty P (2014) The NOAA hurricane hunters: a historical and mission perspective. Fla Geogr 45:14–27

Demuth JL, DeMaria M, Knaff JA, Vonder Haar TH (2004) Evaluation of advanced microwave sounding unit tropical-cyclone intensity and size estimation algorithms. J Appl Meteorol 43:282–296. doi:10.1175/1520-0450(2004)043<0282:EOAMSU>2.0.CO;2

Dunion JP, Velden CS (2002) Application of surface-adjusted GOES low-level cloud-drift winds in the environment of Atlantic tropical cyclones. Part I: Methodology and validation. Mon Weather Rev 130:1333–1346. doi:10.1175/1520-0493(2002)130<1333:AOSAGL>2.0.CO;2

Dvorak VF (1972) A technique for the analysis and forecasting of tropical cyclone intensities from satellite pictures. NESS, Washington, DC

Dvorak VF (1975) Tropical cyclone intensity analysis and forecasting from satellite imagery. Mon Weather Rev 103:420–430. doi:10.1175/1520-0493(1975)103<0420:TCIAAF>2.0.CO;2

Dvorak VF (1984) Tropical cyclone intensity analysis using satellite data. US Department of Commerce, National Oceanic and Atmospheric Administration, National Environmental Satellite, Data, and Information Service, Washington, DC

Fernandez DE, Kerr EM, Castells A et al (2005) IWRAP: the imaging wind and rain airborne profiler for remote sensing of the ocean and the atmospheric boundary layer within tropical cyclones. IEEE Trans Geosci Remote Sens 43:1775–1787. doi:10.1109/TGRS.2005.851640

Franklin JL, Black ML, Valde K (2003) GPS dropwindsonde wind profiles in hurricanes and their operational implications. Weather Forecast 18:32–44. doi:10.1175/1520-0434(2003)018<0032:GDWPIH>2.0.CO;2

Freilich MH, Dunbar RS (1999) The accuracy of the NSCAT 1 vector winds: comparisons with National Data Buoy Center buoys. J Geophys Res Oceans (1978–2012) 104:11231–11246. doi:10.1029/1998JC900091

Gilhousen DB (1987) A field evaluation of NDBC moored buoy winds. J Atmos Ocean Technol 4:94–104. doi:10.1175/1520-0426(1987)004<0094:AFEONM>2.0.CO;2

Goldberg MD (1999) Generation of retrieval products from AMSU-A: methodology and validation. In: Technical Proceedings of the 10th International ATOVS Study Conference. Boulder, pp 215–229

Govind PK (1975) Omega windfinding systems. J Appl Meteorol 14:1503–1511. doi:10.1175/1520-0450(1975)014<1503:OWS>2.0.CO;2

Guimond SR, Tian L, Heymsfield GM, Frasier SJ (2014) Wind retrieval algorithms for the IWRAP and HIWRAP airborne Doppler radars with applications to hurricanes. J Atmos Ocean Technol 31:1189–1215. doi:10.1175/JTECH-D-13-00140.1

Harasti PR, McAdie CJ, Dodge PP et al (2004) Real-time implementation of Single-Doppler Radar analysis methods for tropical cyclones: algorithm improvements and use with WSR-88D display data. Weather Forecast 19:219–239. doi:10.1175/1520-0434(2004)019<0219:RIOSRA>2.0.CO;2

Hock TF, Franklin JL (1999) The NCAR GPS dropwindsonde. Bull Am Meteorol Soc 80:407–420. doi:10.1175/1520-0477(1999)080<0407:TNGD>2.0.CO;2

Holland GJ, Webster PJ, Curry JA et al (2001) The Aerosonde robotic aircraft: a new paradigm for environmental observations. Bull Am Meteorol Soc 82:889–901. doi:10.1175/1520-0477(2001)082<0889:TARAAN>2.3.CO;2

Howden S, Gilhousen D, Guinasso N et al (2008) Hurricane Katrina winds measured by a buoy-mounted sonic anemometer. J Atmos Ocean Technol 25:607–616. doi:10.1175/2007JTE-CHO518.1

Jones WL, Swift CT, Black PG, Delnore VE (1981) Airborne microwave remote-sensing measurements of hurricane allen. Science 214:274–280. doi:10.1126/science.214.4518.274

Kidder SQ, Goldberg MD, Zehr RM et al (2000) Satellite analysis of tropical cyclones using the Advanced Microwave Sounding Unit (AMSU). Bull Am Meteorol Soc 81:1241–1259. doi:10.1175/1520-0477(2000)081<1241:SAOTCU>2.3.CO;2

Knaff JA, Brown DP, Courtney J et al (2010) An evaluation of Dvorak technique–based tropical cyclone intensity estimates. Weather Forecast 25:1362–1379. doi:10.1175/2010WAF2222375.1

Kossin JP, Knapp KR, Vimont DJ et al (2007) A globally consistent reanalysis of hurricane variability and trends. Geophys Res Lett. doi:10.1029/2006GL028836

Kossin JP, Olander TL, Knapp KR (2013) Trend analysis with a new global record of tropical cyclone intensity. J Clim 26:9960–9976. doi:10.1175/JCLI-D-13-00262.1

Landsea CW, Franklin JL, McAdie CJ et al (2004) A reanalysis of hurricane Andrew's intensity. Bull Am Meteorol Soc 85:1699–1712. doi:10.1175/BAMS-85-11-1699

Laupattarakasem P, Jones WL, Hennon CC et al (2010) Improved hurricane ocean vector winds using SeaWinds active/passive retrievals. IEEE Trans Geosci Remote Sens 48:2909–2923. doi:10.1109/TGRS.2010.2043110

Li L, Heymsfield G, Carswell J, et al (2008) High-altitude imaging wind and rain airborne radar (HIWRAP). In: IGARSS 2008–2008 IEEE International Geoscience and Remote Sensing Symposium. IEEE, Boston, pp 354–357

Nakazawa T, Hoshino S (2009) Intercomparison of Dvorak parameters in the tropical cyclone datasets over the Western North Pacific. SOLA 5:33–36. doi:10.2151/sola.2009-009

Niiler P, Lumpkin R, Centurioni L (2003) Operational deployments of drifting buoys into targeted tropical cyclones. ftp://ftp.wmo.int/Documents/PublicWeb/amp/mmop/documents/dbcp/Dbcp34/presentations/03_Niiler_Hurricane.pdf. Accessed 24 Jun 2016

NOAA (2006) Final Report: first-ever successful UAS mission into a tropical storm (Ophelia - 2005). https://uas.noaa.gov/projects/demos/aerosonde/Ophelia_final.html. Accessed 24 Jun 2016

Nolan DS, Zhang JA, Uhlhorn EW (2014) On the limits of estimating the maximum wind speeds in hurricanes. Mon Weather Rev 142:2814–2837. doi:10.1175/MWR-D-13-00337.1

Olander TL, Velden CS (2007) The advanced Dvorak technique: continued development of an objective scheme to estimate tropical cyclone intensity using geostationary infrared satellite imagery. Weather Forecast 22:287–298. doi:10.1175/WAF975.1

Powell MD, Houston SH, Reinhold TA (1996) Hurricane Andrew's landfall in south Florida. Part I: Standardizing measurements for documentation of surface wind fields. Weather Forecast 11:304–328. doi:10.1175/1520-0434(1996)011<0304:HALISF>2.0.CO;2

Powell MD, Houston SH, Amat LR, Morisseau-Leroy N (1998) The HRD real-time hurricane wind analysis system. J Wind Eng Ind Aerodyn 77 & 78:53–64. doi:10.1016/S0167-6105(98)00131-7

Rappaport EN, Franklin JL, Avila LA et al (2009) Advances and challenges at the National Hurricane Center. Weather Forecast 24:395–419. doi:10.1175/2008WAF2222128.1

Reade D (2014) The resurgence of tropical cyclone reconnaissance aircraft in the far East and Western Pacific. http://www.p-3publications.com/PDF/ResurgenceofTropicalCycloneReconnaissanceAircraft.pdf. Accessed 24 Jun 2016

Rinehart RE, Garvey ET (1978) Three-dimensional storm motion detection by conventional weather radar. Nature 273:287–289. doi:10.1038/273287a0

RMS real-time hurricane impact data. http://www.hwind.co/legacy_data/. Accessed 24 Jun 2016

Schott T, Landsea C, Hafele G, et al (2012) The Saffir-Simpson hurricane wind scale. [Internet]. Available from: http://www.nhc.noaa.gov/pdf/sshws.pdf. Accessed 2016

Smalley JH (1979) The dropwindsonde system. Atmos Technol 10:24–28

Tuttle J, Gall R (1999) A single-radar technique for estimating the winds in tropical cyclones. Bull Am Meteorol Soc 80:653–668. doi:10.1175/1520-0477(1999)080<0653:ASRTFE>2.0.CO;2

Uhlhorn EW, Black PG (2003) Verification of remotely sensed Sea surface winds in hurricanes. J Atmos Ocean Technol 20:99–116. doi:10.1175/1520-0426(2003)020<0099:VORSSS>2.0.CO;2

Uhlhorn EW, Black PG, Franklin JL et al (2007) Hurricane surface wind measurements from an operational stepped frequency microwave radiometer. Mon Weather Rev 135:3070–3085. doi:10.1175/MWR3454.1

Ulaby FT, Moore RK, Fung AK (1981) Microwave remote sensing: active and passive, vol 1, Microwave remote sensing fundamentals and radiometry. Addison-Wesley Publishing Co., Kansas University, Lawrence

Velden CS, Herndon D (2014) Update on the SATellite CONsensus (SATCON) algorithm for estimating TC intensity. In: Poster session I. San Diego

Velden CS, Olander TL, Wanzong S (1998) The impact of multispectral GOES-8 wind information on Atlantic tropical cyclone track forecasts in 1995. Part I: Dataset methodology, description, and case analysis. Mon Weather Rev 126:1202–1218. doi:10.1175/1520-0493(1998)126<1219:TIOMGW>2.0.CO;2

Velden C, Harper B, Wells F et al (2006) The Dvorak tropical cyclone intensity estimation technique: a satellite-based method that has endured for over 30 years. Bull Am Meteorol Soc 87:1195–1210. doi:10.1175/BAMS-87-9-1195

Webster PJ, Holland GJ, Curry JA, Chang H-R (2005) Changes in tropical cyclone number, duration, and intensity in a warming environment. Science 309:1844–1846. doi:10.1126/science.1116448

Wu M-C, Yeung K-H, Chang W-L (2006) Trends in western North Pacific tropical cyclone intensity. Eos Trans Amer Geophys Union 87:537–538. doi:10.1029/eost2006EO48

Chapter 5
Inland Tropical Cyclones and the "Brown Ocean" Concept

Theresa Andersen and Marshall Shepherd

Abstract In several regions of the world, tropical cyclones have been known to maintain or increase strength after landfall without transitioning to extratropical systems. It is hypothesized that these inland areas help sustain tropical cyclones when there has been plentiful rainfall, leading to unusually wet soil and strong latent heat release. Additionally, given the symmetric structure of warm-core cyclones, the atmosphere should tend toward barotropic conditions that mimic an ocean environment. Observational and modeling studies support this "brown ocean" concept, providing a global climatology of inland tropical cyclones, pinpointing regions that are more favorable for re-intensification, and analyzing individual cyclones to better understand the associated land-atmosphere feedbacks.

1 Introduction

Broadly defined, a tropical cyclone (TC) is a center of low pressure that develops over the oceans within tropical and subtropical latitudes. Such latitudes provide adequate Coriolis force and warm sea surface temperatures to sustain the storm (Frank 1977). A critical component of TCs (hereafter referring to tropical storms, hurricanes, typhoons, and cyclones) is the latent heat flux associated with evaporation

---

T. Andersen (✉)
Research Square, Durham, NC 27701, USA
e-mail: tkande@gmail.com

M. Shepherd
Department of Geography, University of Georgia, Athens, GA 30602, USA
e-mail: marshgeo@uga.edu

from the ocean surface. Such storms transfer heat from the ocean surface to the atmosphere through condensation. This energy transfer is the fuel supply for the TC.

Most TCs weaken after landfall because the ocean-based moisture supply is removed. The lack of adequate latent heat flux coupled with increased friction, increased wind shear, and larger temperature gradients is not conducive to maintaining a warm-core structure and tropical characteristics. However, scholars have recently identified several cases where TCs maintain their strength or even intensify overland (see Andersen and Shepherd 2013).

A common way that this phenomenon occurs is through the process of extratropical transition (ET). When a TC transitions, the temperature field becomes increasingly asymmetric, and the storm becomes a cold-core structure (i.e., the geostrophic winds increase with height because of the increasingly baroclinic atmosphere or the presence of temperature/density gradients). Roughly 46 % of Atlantic tropical cyclones undergo extratropical transition according to Hart and Evans (2001). Hurricane Sandy (Shepherd 2012) is a well-known example of an ET that caused significant damage in the densely populated Northeast USA. In the western North Pacific, three types of ET have been characterized by Klein et al. (2000). Complex ET is described as a preexisting front interacting with a TC to generate a new ET cyclone. Compound ET occurs when a mid-latitude cyclonic storm and a TC merge to produce a new ET cyclone. The third type is a dissipating TC that demonstrates recurvature (Klein et al. 2000).

However, some TCs have been observed to maintain their strength (and tropical characteristic) or even intensify overland without ET. Tropical Storm Erin intensified overland in Texas and Oklahoma in 2007. Doppler radar measurements detected an "eye" over central Oklahoma (Fig. 5.1). Arndt et al. (2009), Evans et al. (2011), and Kellner et al. (2012) suggested that latent heat fluxes from antecedent rainfall and anomalously moist soils over Texas and Oklahoma may have contributed to the intensification. Our analysis of satellite-derived rainfall in the region leading up to the event supports that finding (Fig. 5.2).

Using a mesoscale model, Chang et al. (2009) found that monsoonal depressions remain intense overland when a significant rainfall preceded landfall. Emanuel et al. (2008) also noticed that vertical heat fluxes from wet, hot sandy regions of northern Australia may have been playing a role in the intensification of cyclones. The authors noted that antecedent moisture or precipitation from the TC itself could be the source of this particular land-atmosphere feedback. Both Kishtawal et al. (2012) and Chen (2012) have also discussed the role of inland characteristics (soil heat flux and/or friction) on TC intensity or life cycles in India and China, respectively. In 2015, Tropical Storm Bill lingered for days after making landfall in Texas. Later in the chapter, a more detailed analysis of Tropical Storm Bill is presented.

A series of seminal papers (Andersen and Shepherd 2013; Andersen et al. 2013) has advanced the "Brown Ocean" theory. This theory is based on the "Green Ocean" analogy that has been put forth to describe the contributions of the Amazon forest to the regional hydroclimate regime (Wang et al. 2000). The Brown Ocean concept refers to tropical cyclones that maintain or increase strength after landfall. This work was possibly the first comprehensive and global assessment of the concept of tropical cyclone maintenance or intensification (hereafter referred to as TCMI).
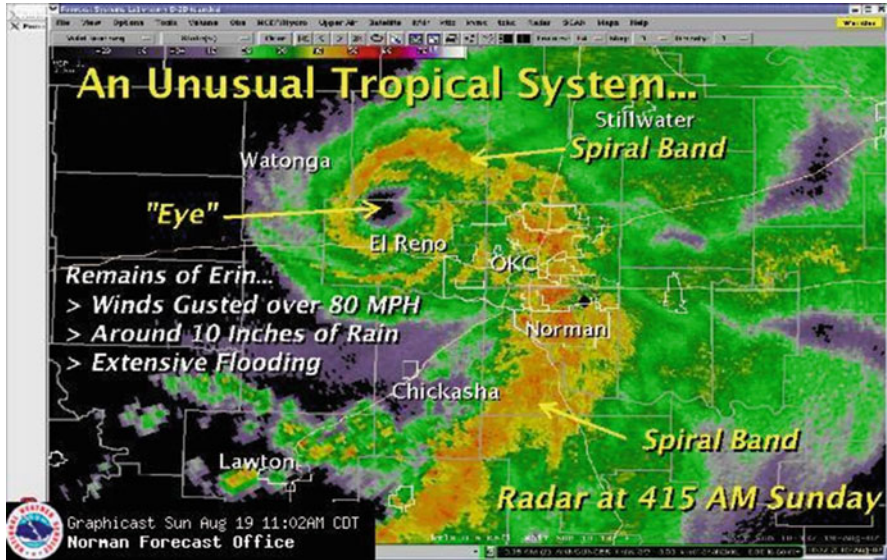
Fig. 5.1 Remains of Tropical Storm Erin (2007) over Oklahoma with an "eye" (Figure provided by National Weather Service (NWS) Norman Forecast Office)

Beyond scientific curiosity, there are societally relevant reasons why the study of TCMIs warrants attention. TCs account for more than 15,000 deaths annually and over $1.5 billion in damage (Rakhecha and Singh 2009). The National Hurricane Center also noted that inland flooding causes 59 % of the fatalities from landfalling hurricanes (Rappaport 2014). Shepherd et al. (2007) showed that rainfall is a significant hazard of landfalling hurricanes but can also be critical for regional water supplies and drought mitigation. Climate change may also impact the intensity and frequency of TCs (Shepherd and Knutson 2007). Though initially controversial, most literature suggests that climate change will likely lead to more intense and perhaps longer-lived TCs, with a reduction in the overall frequency (Bender et al. 2010; Hill and Lackmann 2011; Murakami et al. 2012). Kossin et al. (2014) also noted that the latitude at which hurricanes experience maximum intensification may be migrating poleward.

Although scientific studies highlight the hazards of TCs and even the potential risk from inland storms, there is still more focus on the storms prior to landfall. Post-landfall warnings or classifications are given little consideration. The well-known Saffir-Simpson scale is largely based on wind speed, and it does not always quantify the post-landfall damage potential, which is largely rainfall-driven (Senkbeil and Sheridan 2006; Kantha 2010). Senkbeil and Sheridan (2006) offered a classification system for post-landfall TCs in the USA that better quantified the risks to urban areas and populated coastal regions. The classification system included maximum sustained winds, gustiness, rainfall, pressure, storm surge, and duration. At a minimum, it is increasingly necessary to better represent the rainfall and flood risks associated with landfalling TCs and TCMIs.
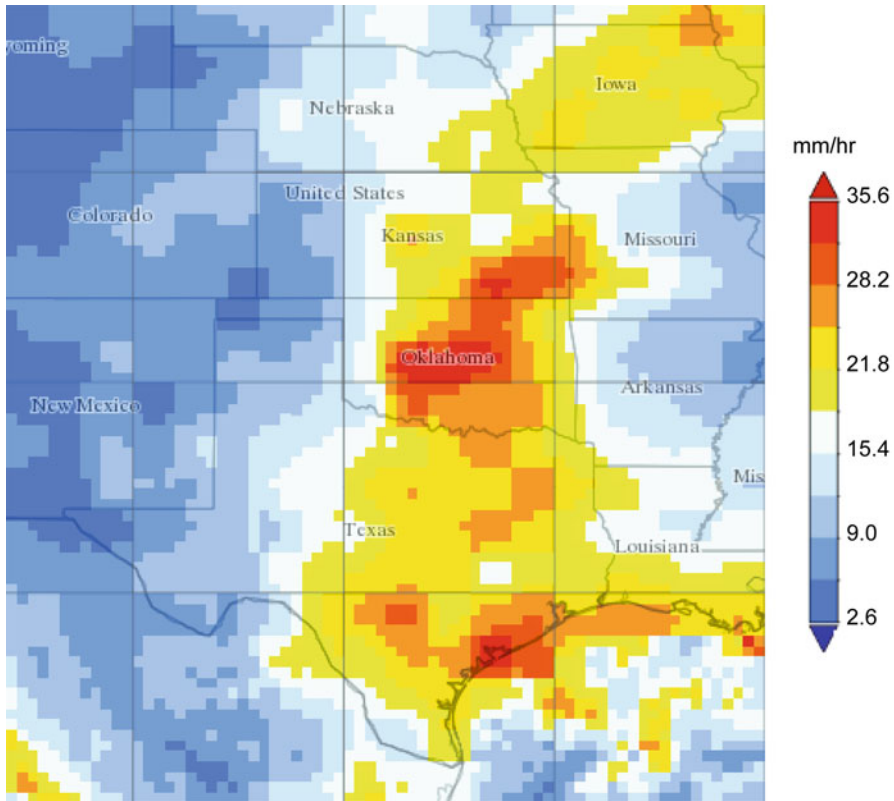
Fig. 5.2 TRMM 3B43 monthly average three-hourly precipitation rate (mm/h) for Tropical Storm Erin (May–August 2007) (Source: NASA Giovanni website)

2 TCMI: Background, Climatology, and Physical Processes

Andersen and Shepherd (2013) set out to create a global climatology of TCMIs to better understand spatial and temporal patterns of the events. The tropical cyclone data were obtained from the International Best Track Archive for Climate Stewardship (IBTrACS, http://www.ncdc.noaa.gov/oa/ibtracs/ Knapp et al. 2010) during the satellite era (1979–2008). They incorporated atmospheric and environmental data relevant to the TC events from NASA's Modern-Era Retrospective Analysis for Research and Applications (MERRA, http://gmao.gsfc.nasa.gov/research/merra/intro.php). The compelling results are summarized in Fig. 5.3.

The TCs were first classified according to their track and strength (i.e., whether the storm tracked inland and, if so, was it still intact?). Over the 30-year period, 227 TCs tracked inland after making landfall (ITCs). Of the ITCs, 45 maintained or increased strength inland (MIs) based on the maximum sustained wind speed and central pressure. Seventeen of those underwent extratropical transition, mainly over North America. Sixteen of the MIs continued as warm-core structures (TCMIs);
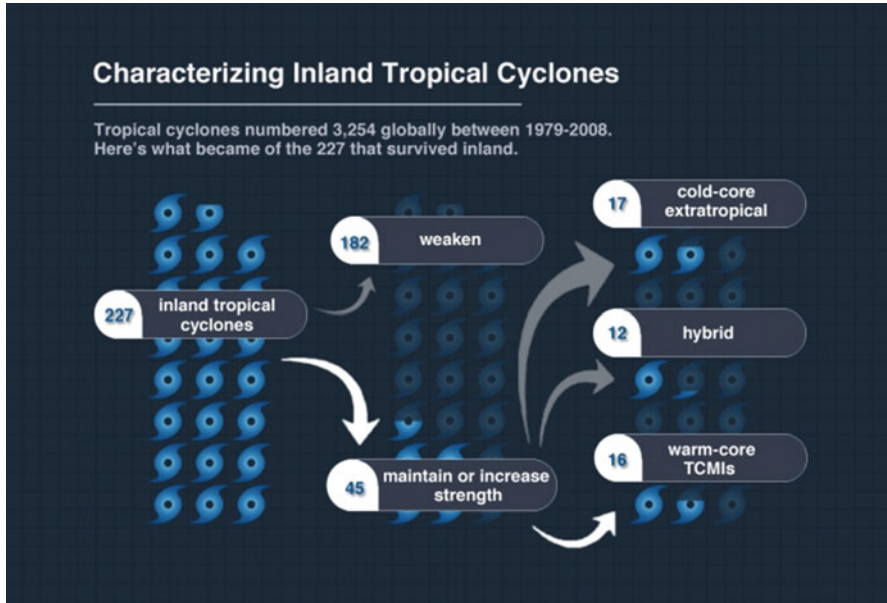
Fig. 5.3 Tropical cyclones that exhibited maintenance or intensification overland from 1979 to 2008 globally (Figure courtesy of NASA/Kathryn Hansen)

these primarily occurred over Australia. The remaining 12 MIs were found to be hybrid storms, not distinctly warm- or cold-core; these occurred over the USA, India, and China. Although China and the USA experience the most tropical cyclone landfalls, Australia sees the most TCMI cases (Fig. 5.4). Northern Australian soil is sandy and may have relatively high sensible and latent heat fluxes during the hurricane season that contribute to the intensification phenomenon. This finding is consistent with Emanuel et al. (2008).

The TCMI climatology suggests that these systems thrive in inland environments that mimic tropical conditions. TCMIs prefer quasi-barotropic environments and generally do not encounter strong temperature gradients post landfall. Low-level temperature gradients at the time of intensification indicate that TCMIs are associated with significantly smaller 850-hPa temperature ranges compared with ETs.

Tropical cyclones derive their energy from ocean surface evaporation and latent heat release. Therefore, to remain warm-core structures overland, a moisture-rich environment may need to exist. According to the data, soil moisture gradients existed in the vicinity of the intensification regions, consistent with the Brown Ocean concept. Over north-central Australia, three strong intensification events occurred consecutively: Sam in December 2000, Wylva in February of 2001, and Abigail in March 2001. In this region, TCs themselves are a primary source of precipitation and may provide the soil moisture needed to force subsequent TCMI events.
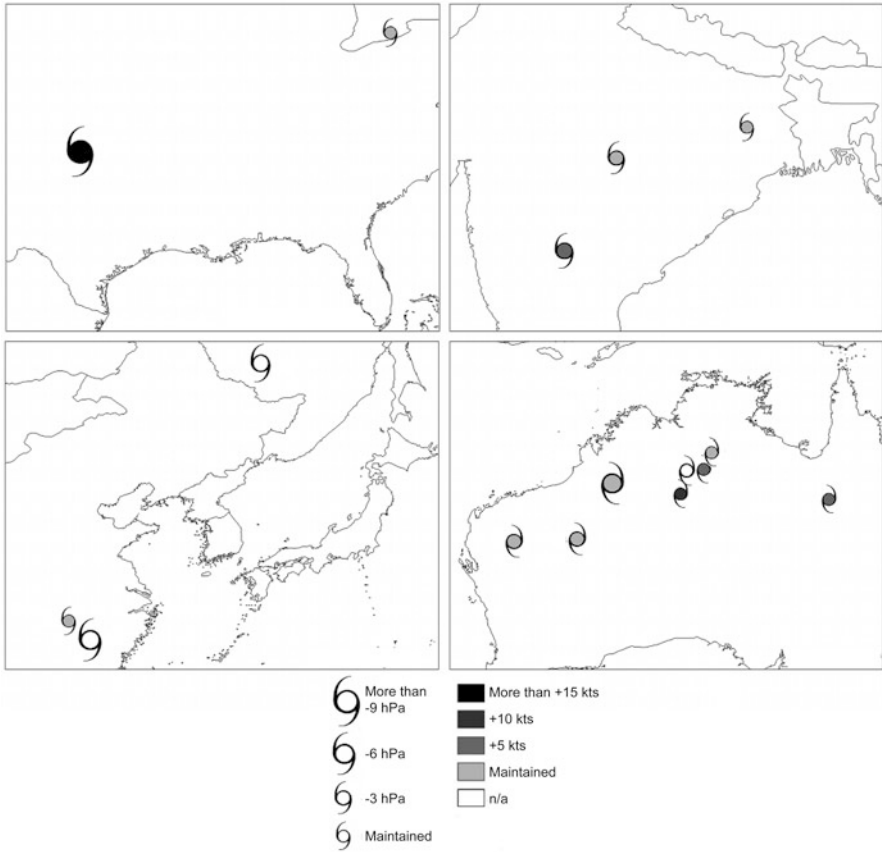
Fig. 5.4 Historical TCMI events by region. The hurricane symbol represents the location at time of inland maintenance or intensification. The symbol size represents the central pressure fall (0–9 hPa), and tone represents the sustained maximum wind speed increase (0–15+ knots) since landfall or previous maximum overland (Image credit: Andersen and Shepherd (2013))

An analysis of the surface energy fluxes indicates that tropical cyclones were sustained following high latent heat fluxes (LHFs) and rainfall events near the peak of the hurricane season. The area-mean LHF leading up to the TCMI events averaged 70 W m^{-2}, the LHF threshold for TCMI occurrence for this dataset (Andersen and Shepherd 2013).

Wetter soils tend to absorb more radiation compared with dry soils due to the high heat capacity of water (Radcliffe and Šimůnek 2010). These wet soils increase evaporation to produce a moist, unstable boundary layer (Clark and Arritt 1995; Bosilovich and Sun 1999; Lynn et al. 1998). Strengthened moisture transport, rainfall reinforcement, and an associated latent heat trigger are important factors for inland-tracking storm intensity (Dong et al. 2010; Kishtawal et al. 2012). Emanuel et al. (2008) performed simulations using a TC model coupled to a one-dimensional

soil model to determine the role of large vertical heat fluxes from recently moistened soil in cyclone redevelopment in Australia. The results indicated that warm, wet soils may help to maintain or energize landfalling TCs through surface heat transfer. In Asia, freshwater bodies and wetlands are hypothesized to supply energy to typhoons (Chen 2012) and Shen et al. (2002) found that a 0.5 m layer of water is sufficient to reduce landfall decay.

2.1 One-Dimensional Model Studies

Previous work has suggested that TCMIs are unique to Australia because of the ability of sandy soil to rapidly release huge amounts of energy when moistened (Emanuel et al. 2008). Andersen et al. (2013), however, sought to simulate the soil profiles of four major TC intensification regions. Energy flux values leading up to four TCMI events, one in each region, were generated to assess the feasibility of the Brown Ocean concept. The analysis was performed using the HYDRUS-1D numerical water and heat flow model and MERRA atmospheric data. Andersen et al. (2013) determined the trends and magnitudes of the surface energy fluxes before a cyclone entered the intensification region and compared the simulated energy flux values to observed values over the tropical ocean. In their analysis, the soil temperature and heat fluxes from the model runs were used to assess the surface conditions prior to the tropical cyclone. In southeastern China, northern Australia, and central India, the temperatures decreased slightly with time, while soil temperatures in the south-central USA increased. The USA and Australia had the greatest diurnal fluctuations and highest maximum temperatures, possibly due to high solar radiation during the day and radiational cooling at night.

In the regions where intensification was to occur, the LHF was highest in the afternoons/evenings and lowest in the mornings. As solar radiation warmed the boundary layer throughout the day, evaporation increased along with the LHF. The LHF values were consistently higher in China and India. In the USA and Australia, the LHF trend closely followed the precipitation trend due to the overall drier conditions. The daily maximums for all regions often reach 200 W m^{-2}. The soil texture did not appear to have a significant effect on the LHF magnitudes across regions; however, the diurnal changes were sharper over Australia (Andersen and Shepherd 2013; Andersen et al. 2013).

LHFs within TCs are not precisely known due to the lack of accurate observations. However, remote sensing observations and algorithms have been used to calculate reasonable estimates (Guimond et al. 2011). According to Zhang and Rossow (1997), the mean annual LHF peaks around 115–125 W m^{-2} near 15°N/S. Trenberth and Fasullo (2007) estimate that the typical LHF over the tropical ocean is approximately 120 W m^{-2}. Satellite-derived LHF estimates of the pre-TC ocean environment are approximately 100–200 W m^{-2} (Liu et al. 2011). In the western North Pacific, TC LHF maxima have been estimated as 150–190 W m^{-2} (Gao and

Chiu 2010). According to the Andersen et al. (2013) HYDRUS study, daytime LHF values over the study regions of southeastern China, south-central USA, northern Australia, and central India easily exceed these estimates.

Compared with observations, HYDRUS underestimated the pre-storm maximum LHF values (up to 140 W m^{-2} in Australia). Despite this bias, the HYDRUS inland fluxes were remarkably higher than the ocean fluxes (>200 %) in China and India. In the USA and Australia, the land and ocean fluxes were nearly equal. The results indicated that just before the passage of a cyclone, the land surface is capable of producing a daytime LHF magnitude that is comparable to that over the ocean. Because of the area-averaging method used with HYDRUS, the moisture fluxes produced were likely conservative. Considering LHF is a primary contributor to TC formation and intensification, the land surface may play an important role in aiding the maintenance and intensification of TCs when soils are moist.

2.2 Three-Dimensional Model Studies

Numerical weather models are valuable tools for studying the feedbacks between the land surface and landfalling TCs. Evans et al. (2011) utilized the Weather Research and Forecast (WRF) model to simulate the re-intensification of Tropical Storm Erin (2007) over Oklahoma. A control simulation and eight sensitivity simulations were run with varying soil moisture conditions. They found that the final intensity of the vortex was linked to maintenance of planetary boundary layer (PBL) moisture over preexisting wet soil. Lin et al. (2010) studied the landfall of Hurricane Isabel over the complex terrain of the Appalachian Mountains using WRF coupled with the Advanced Circulation Model. The model accurately reproduced orographically enhanced rainfall and the general wind field; however, wind maxima were displaced. Similarly, Xie and Zhang (2012) found that accurate TC track forecasts are essential in determining flood potential in Taiwan due to topographical forcing.

Zhang et al. (2011) used WRF to simulate land surface effects on Typhoon Sepat (2007) in China and found that the model successfully reproduced the typhoon track and rainfall. Sensitivity experiments revealed that sensible heat flux (SHF) and latent heat flux (LHF) maintained the cyclone and spiral structure overland. Moreover, the distribution and intensity of the rain field were dependent on accurate soil moisture content initialization (Zhang et al. 2011). In a sensitivity study of North Atlantic TCs to soil parameters, Kishtawal et al. (2012) revealed that the intensities of hurricanes Rita and Katrina were impacted by changes in surface roughness and soil heat capacity. However, the impacts were limited compared to the observational analysis and suggest a need for improvement in modeled surface feedbacks.

While approaching land, TC wind speed may be reduced as a result of momentum loss due to land surface roughness. However, the radial wind component may increase in the PBL, which produces inflow and enhanced moisture convergence (Au-Yeung and Chan 2010; Zhu 2008). Likewise, higher moisture availability overland can help to sustain TCs by increasing condensation and latent heat supply (Tuleya and Kurihara 1978; Tuleya 1994). Studies have found that moisture

distribution along the coast, land roughness variation, and small-scale surface features are important factors influencing TC intensity and track post landfall (Au-Yeung and Chan 2010; Bozeman et al. 2012; Zhu 2008). Soil heat capacity and conductivity are also important characteristics that influence the surface temperature and cyclone decay process (Tuleya 1994; Kishtawal et al. 2012). Over northern Australia, it has been suggested that large vertical heat fluxes from recently wetted, hot, sandy soil help to intensify inland-moving TCs (Emanuel et al. 2008). In India, overland monsoon depressions have been observed to maintain intensity longer if the area received prior rainfall (Chang et al. 2009).

Building on observational analyses and Andersen et al. (2013), the authors employed WRF to evaluate the sensitivity of Cyclone Abigail (2001) to a range of soil moisture conditions. Northern Australia is particularly unique because its soil characteristics and recent studies confirm that TCMIs are more common in this geographic region of the world (Emanuel et al. 2008).

TC Abigail began as an area of low pressure in the Coral Sea on 22 February 2001. Two pressure centers merged and tracked westward. Just before making landfall in eastern Australia, the system intensified. At 0000 UTC on 24 February, the system made landfall near Cairns and subsequently weakened. The highest recorded wind speed was 65 kts. Abigail redeveloped and intensified overland twice. The first time was around 1 March 0600 UTC when the pressure dropped to 998 hPa. The second intensification occurred around 3 March 0000 UTC at which time the pressure dropped to 992 hPa. The latter time period is the focus of this paper. Thermal wind analysis indicates Abigail maintained a warm core for the duration of both intensification periods (Andersen and Shepherd 2013). The tropical cyclone structure and rainbands are apparent in HURSAT visible satellite imagery (Fig. 5.5). Near Halls Creek, a clear eye formed on 1 March 1700 UTC and was apparent until 3 March 0600 UTC. The six-hourly precipitation peaks at 0.83″ and the wind direction changes around 2 March. The low-pressure center can be seen on the Bureau of Meteorology (BOM) surface analyses.

WRF version 3.5 was configured for a single processor with basic nesting and compiled for a real data simulation. A single simulation domain spanning 275×325 horizontal grid points at 8 km resolution and 34 vertical levels is utilized (Fig. 5.6). The initial and boundary conditions are provided by the National Centers for Environmental Prediction (NCEP) FNL (Final) Operational Global Analysis $1.0° \times 1.0°$ data (NCEP FNL 2000). The product is prepared every 6 h from the Global Data Assimilation System (GDAS). The data are available on the surface and 26 pressure levels between 1000 and 10 hPa. According to Evans et al. (2011), 1° data are useful for mesoscale studies of soil moisture impacts on vortices. Higher-resolution data can introduce unrealistic convective-scale feedbacks. The simulation time begins 2 March 2001 0000 UTC (24 h before intensification) and ends 3 March 2001 0600 UTC. The United States Geological Survey (USGS) land use map of the study area shows that it is dominated by savanna, shrubland, and grassland.

The unified Noah land surface model was used for surface physics (Chen and Dudhia 2001). It includes soil temperature and moisture in four layers, fractional snow cover, and frozen soil physics. The Yonsei University (YSU) scheme is used for PBL physics (Hong et al. 2006). It is a nonlocal-K scheme with an
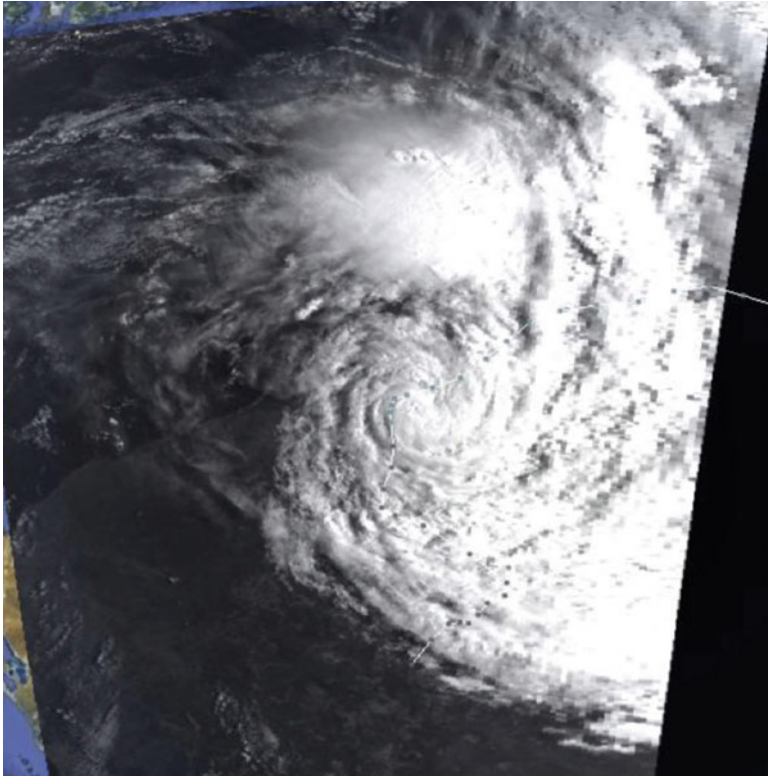
Fig. 5.5 HURSAT visible satellite image of Cyclone Abigail 3 March 2001 0100 UTC. It has a characteristic tropical cyclone structure with a low-pressure center and spiraling rainbands

explicit entrainment layer and parabolic K profile in an unstable mixed layer. The fifth-generation Pennsylvania State University-NCAR Mesoscale Model (MM5) similarity scheme, based on Monin-Obukhov with the Carlson-Boland viscous sublayer, is used for surface layer physics (Skamarock et al. 2008). The KF cumulus option, a deep and shallow convection sub-grid scheme, is utilized (Kain and Fritsch 1990). The KF scheme has been identified as superior to alternative convective schemes for TCs in many studies (Prater and Evans 2002; Ma and Tan 2009; Deshpande et al. 2012). In a study of heavy rainfall events in Korea, activating the cumulus parameterization at intermediate resolutions (e.g., 9 km) improved the simulation results (Lee et al. 2011). A summary of the model configurations is shown in Table 5.1.

For this study, a control run and two sensitivity tests were developed. The control run (CONTROL) was used to verify the model, identify discrepancies with historical records, and represent the actual soil moisture scenario for the case study. Similar to Kellner et al. (2012), the sensitivity tests were a DRY run (50 % reduced soil moisture content) and a WET run (50 % increased soil moisture content) at initialization.
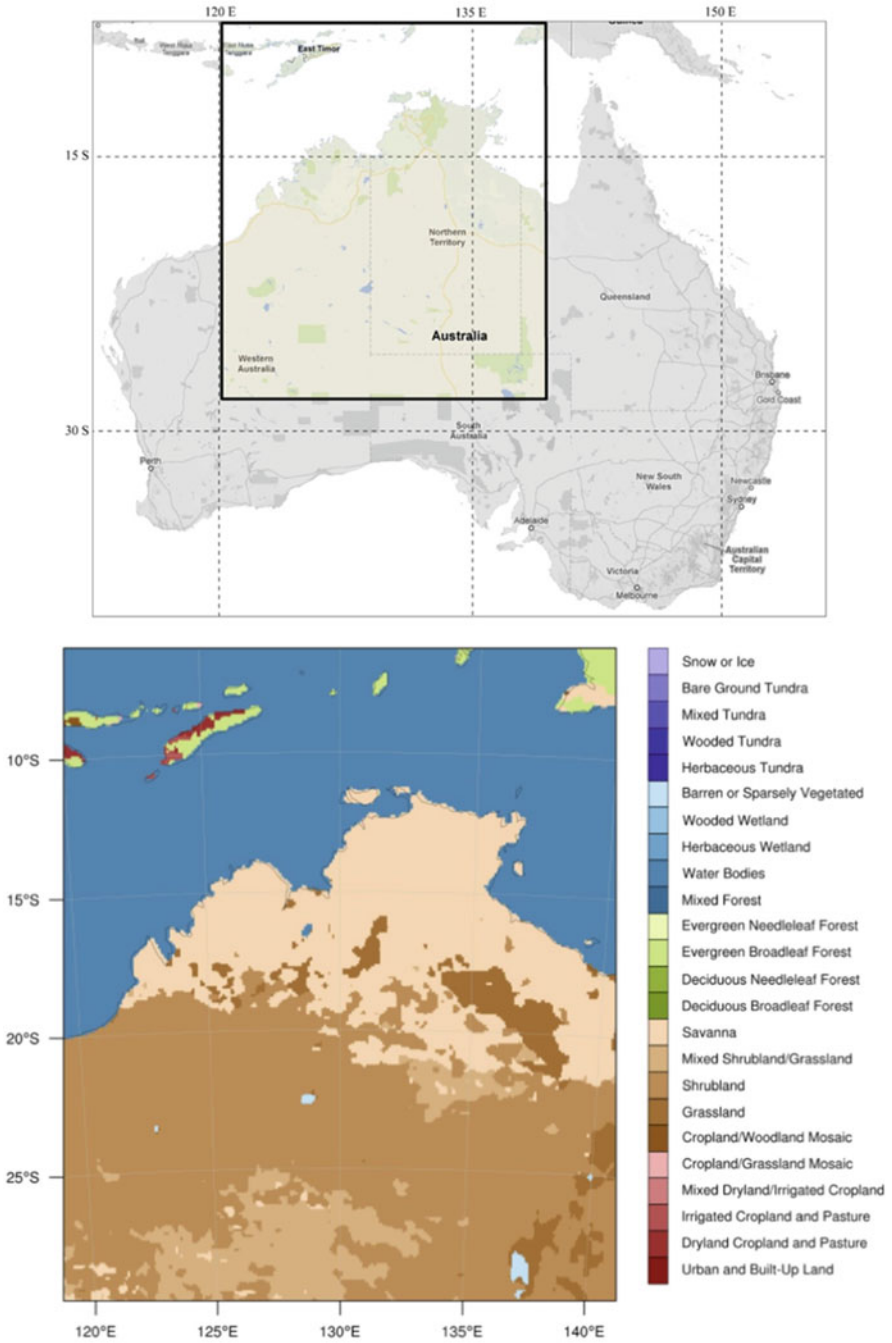
Fig. 5.6 WRF Domain and soil types

Table 5.1 WRF-ARW parameters and configurations

Model parameter	Configuration
Version	WRF-ARW v3.5 (Skamarock et al. 2008)
Domain	$275 \times 325 \times 34$
Horizontal grid spacing	8 km
Duration	30 h, 0000 UTC 2 Mar–0600 UTC 3 Mar 2001
Initial and boundary conditions	6-hourly $1.0° \times 1.0°$ NCEP FNL operational analyses
Microphysical parameterization	Purdue-Lin (Chen and Sun 2002)
Boundary layer parameterization	YSU (Hong et al. 2006)
Surface layer parameterization	MM5 similarity (Skamarock et al. 2008)
Land surface parameterization	Unified Noah land surface model (Chen and Dudhia 2001)
Longwave radiation parameterization	RRTM scheme (Mlawer et al. 1997)
Shortwave radiation parameterization	Dudhia scheme (Dudhia 1989)
Cumulus parameterization	Kain-Fritsch (Kain and Fritsch 1990)

Using a percentage allows for the majority of the gridpoint values to decrease (increase) while still maintaining extremes. To prevent the modified values from exceeding 100 %, a 0.65 threshold was implemented (note: no control values over land masses were excluded as a result because all values were below the threshold). All of the other parameters remain the same for the three cases. The simulations are compared quantitatively and qualitatively in terms of surface LHF, precipitation, total precipitable water (PW), minimum central pressure, wind fields, and convective available potential energy (CAPE).

CONTROL, DRY, and WET simulations were run with parameterizations similar to ocean-based TC studies. The domain and soil types are found in Fig. 5.6. The results indicate that a decrease in the initial soil moisture results in a weaker cyclone with less precipitation, reduced LHF, higher pressure, and weaker winds, whereas the opposite is true when increasing the initial soil moisture (Fig. 5.7). The output from the control run was more similar to the wet run than to the dry run, which highlights the anomalously wet conditions during Cyclone Abigail's intensification. The findings suggest that WRF captures land surface feedbacks related to landfalling tropical systems: specifically, soil moisture content and associated moisture fluxes influence cyclone intensity and structure.

3   2015 Case Study

In 2015, another possible "Brown Ocean" storm affected the central USA. Tropical Storm Bill traversed Texas, Oklahoma, and Arkansas following several weeks of record rainfall (Fig. 5.8). The remnants of Bill lingered for several days, and it was hypothesized that the "Brown Ocean" was partially responsible. Bill maintained its
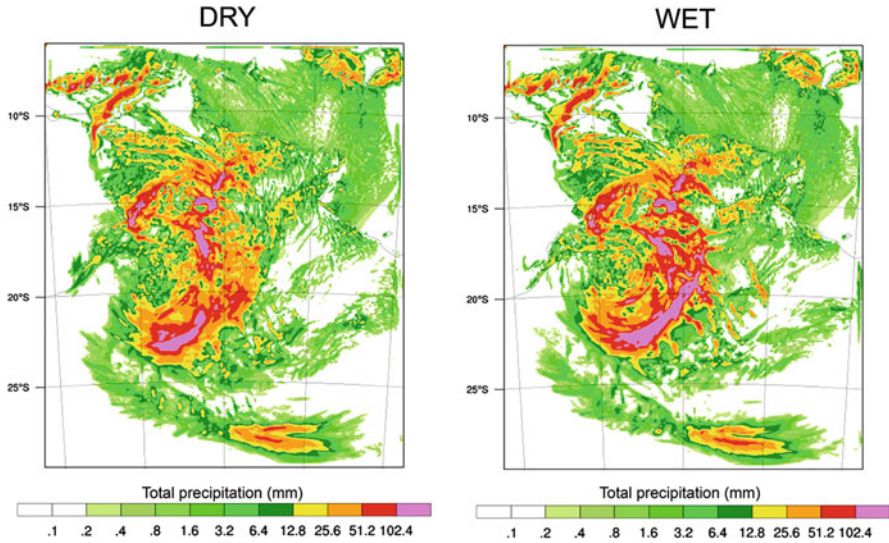
Fig. 5.7 The 6-h precipitation (mm) for DRY (*left*) and WET (*right*) simulations valid 0000 UTC 3 March 2001
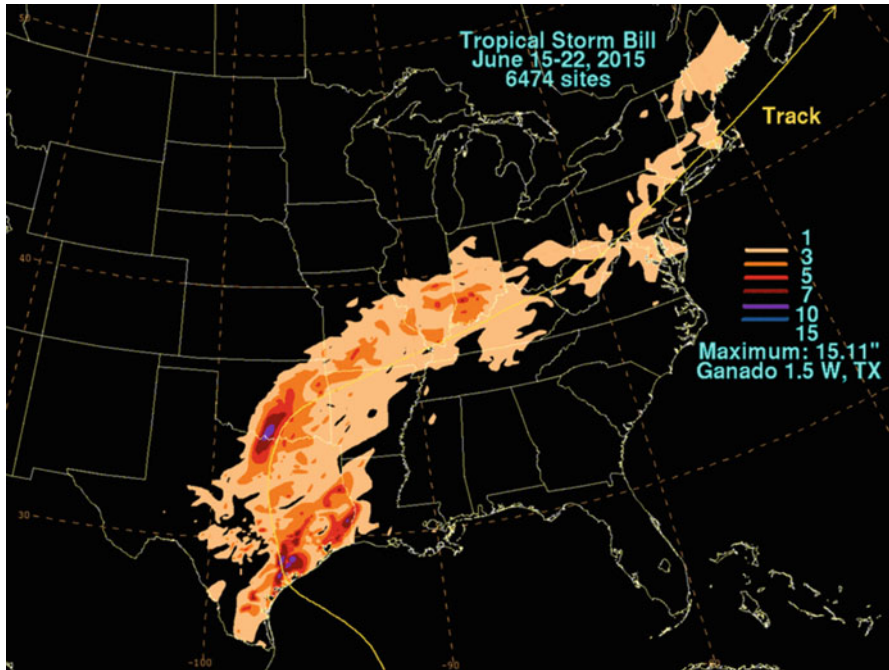
Fig. 5.8 Rainfall (in inches) associated with Tropical Storm Bill (2015). Note: 1 in = 25.4 mm. (Courtesy of NOAA. https://upload.wikimedia.org/wikipedia/commons/thumb/e/e3/Tropical_ Storm_Bill_2015_United_States_rainfall.gif/800px-Tropical_Storm_Bill_2015_United_States_ rainfall.gif)
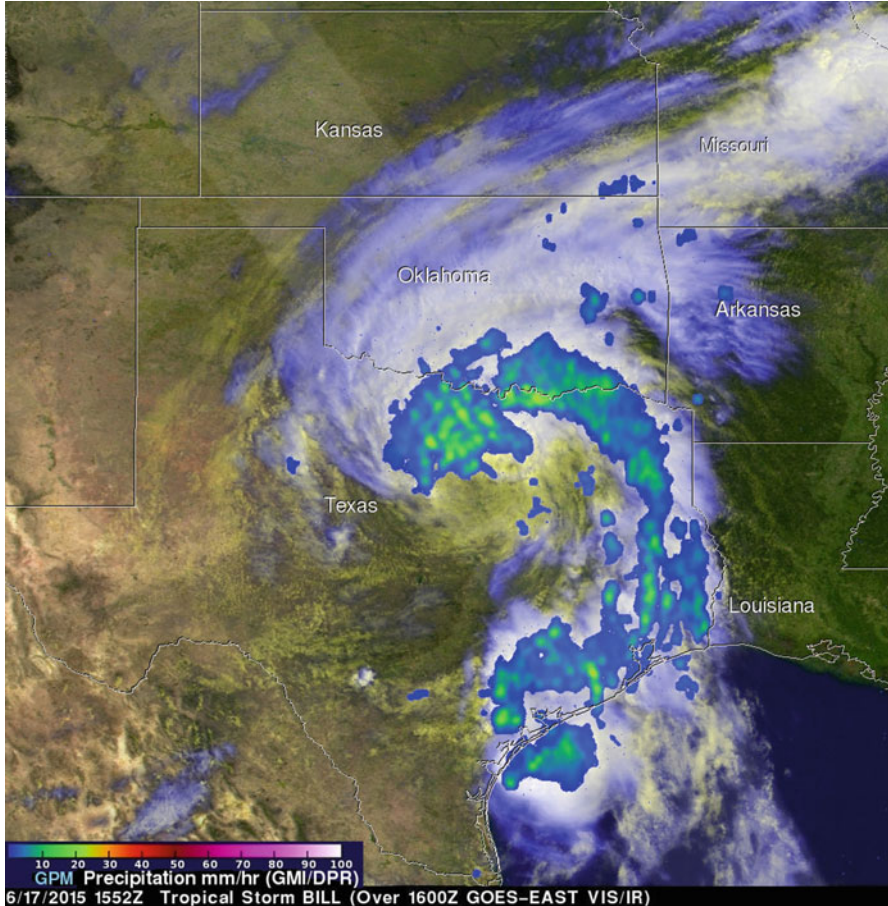
Fig. 5.9 Passive microwave image from the NASA Global Precipitation Measurement mission satellite of the remnants of Tropical Storm Bill over Oklahoma. 17 June 2015 at 1552 UTC (Source: NASA)

tropical characteristics throughout most of the life cycle. On 17 June 2015, Bill was downgraded to a tropical storm after landfall but remained fairly organized. The rainfall totals actually exhibited a secondary maxima near southern Oklahoma with significant inland impacts in Kentucky and Indiana.

Radar data also indicated that Bill maintained a tropical storm-like structure well inland in the same way that Tropical Storm Erin did in 2007. Figure 5.9 shows that spiral banding is quite evident as the storm moved into Oklahoma.

Figure 5.10 shows the antecedent rainfall over the region prior to Bill's landfall. The antecedent rainfall in the 3 months prior to the landfall of Tropical Storm Bill clearly indicated that ample soil moisture would have been present under the track of Bill. This storm offers a nice case study for future scholarly work on the "Brown Ocean" theory.
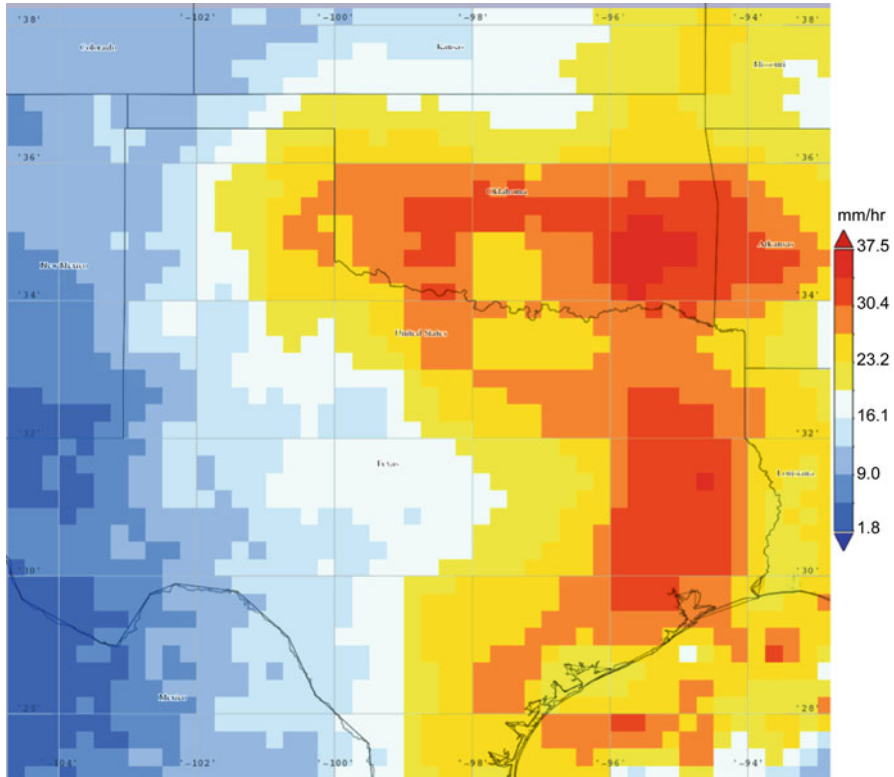
Fig. 5.10 TRMM 3B43 monthly average three-hourly precipitation rate (mm/h) for Tropical Storm Bill (April to June 2015) (Source: NASA Giovanni website)

4 Conclusions

Scholarly literature has continually indicated that tropical cyclones, under certain conditions, can maintain or intensify strength overland. While many of these cases can be explained by synoptic extratropical transitioning, both observational and modeling analyses suggest that a "Brown Ocean" effect is also a factor. The "Brown Ocean" is characterized by three observable conditions: (1) a barotropic lower atmosphere with minimal horizontal temperature variations, (2) sufficient antecedent soil moisture, and (3) latent heat flux values from surface evaporation that reach at least 70 Wm^{-2}.

Future studies will be required to exploit emerging observations and modeling systems, such as the Soil Moisture Active and Passive (SMAP) mission and advanced coupled atmosphere-land modeling systems (e.g., NASA Unified WRF (NU-WRF) and coupled Land Information System (LIS)). Future lines of research must continue to refine our understanding of the roles of soil moisture on inland

TC processes and determine whether assimilating soil moisture into models can improve storm intensity and precipitation forecasts. Ultimately, serious consideration of inland TC classification systems may also be needed.

References

Andersen T, Shepherd JM (2013) A global spatio-temporal analysis of inland tropical cyclone maintenance or intensification. Int J Climatol 34:391–402. doi:10.1002/joc.3693

Andersen T, Radcliffe D, Shepherd JM (2013) Quantifying surface energy fluxes in the vicinity of inland-tracking tropical cyclones. J Appl Meteorol Climatol 52:2797–2808. doi:10.1175/JAM-C-D-13-035

Arndt DS, Basara JB, McPherson RA et al (2009) Observations of the overland reintensification of tropical storm Erin, 2007. Bull Am Meteorol Soc 90:1079–1093. doi:10.1175/2009BAMS2644.1

Au-Yeung AYM, Chan JCL (2010) The effect of a river delta and coastal roughness variation on a landfalling tropical cyclone. J Geophys Res Atmos 115:D19121. doi:10.1029/2009JD013631

Bender MA, Knutson TR, Tuleya RE et al (2010) Modeled impact of anthropogenic warming on the frequency of intense Atlantic hurricanes. Science 327:454–458. doi:10.1126/science.1180568

Bosilovich MG, Sun WY (1999) Numerical simulation of the 1993 midwestern flood: land atmosphere interactions. J Climate 12:1490–1505. doi:10.1175/1520-0442(1999)012<1490:NSOTMF>2.0.CO;2

Bozeman ML, Niyogi D, Gopalakrishnan S et al (2012) An HWRF-based ensemble assessment of the land surface feedback on the post-landfall intensification of tropical storm Fay (2008). Nat Hazards 63:1543–1571. doi:10.1007/s11069-011-9841-5

Chang H, Niyogi D, Kumar A et al (2009) Possible relation between land surface feedback and the post-landfall structure of monsoon depressions. Geophys Res Let 36:1–6. doi:10.1029/2009GL037781

Chen LS (2012) Research progress on the structure and intensity change for the landfalling tropical cyclones. J Trop Meteor 18:113–118. doi:10.3969/j.issn.10068775.2012.02.001

Chen F, Dudhia J (2001) Coupling an advanced land-surface/hydrology model with the Penn State–NCAR MM5 modeling system. Part I: model description and implementation. Mon Weather Rev 129:569–585. doi:10.1175/1520-0493(2001)129<0569:CAALSH>2.0.CO;2

Chen SH, Sun WY (2002) A one-dimensional time dependent cloud model. J Meteorol Soc Jpn 80:99–118. doi:10.2151/jmsj.80.99

Clark CA, Arritt RW (1995) Numerical simulations of the effect of soil moisture and vegetation cover on the development of deep convection. J Appl Meteorol 34:2029–2045. doi:10.1175/1520-0450(1995)034<2029:NSOTEO>2.0.CO;2

Deshpande MS, Pattnaik S, Salvekar PS (2012) Impact of cloud parameterization on the numerical simulation of a super cyclone. Ann Geophys 30:775–795. doi:10.5194/angeo-30-775-2012

Dong M, Chen L, Li Y et al (2010) Rainfall reinforcement associated with landfalling tropical cyclones. J Atmos Sci 67:3541–3558. doi:10.1175/2010JAS3268.1

Dudhia J (1989) Numerical study of convection observed during the winter monsoon experiment using a mesoscale two-dimensional model. J Atmos Sci 46:3077–3107. doi:10.1175/1520-0469(1989)046<3077:NSOCOD>2.0.CO;2

Emanuel K, Callaghan J, Otto P (2008) A hypothesis for the redevelopment of warm-core cyclones over northern Australia. Mon Weather Rev 136:3863–3872. doi:10.1175/2008MWR2409.1

Evans C, Schumacher RS, Galarneau TJ (2011) Sensitivity in the overland reintensification of tropical cyclone Erin (2007) to near-surface soil moisture characteristics. Mon Weather Rev 139:3848–3870. doi:10.1175/2011MWR3593.1

Frank W (1977) The structure and energetics of the tropical cyclone II. Dynamics and energetics. Mon Weather Rev 105:1136–1150. doi:10.1175/15200493(1977)105<1136:TSAEOT>2.0.CO;2

Gao S, Chiu LS (2010) Surface latent heat flux and rainfall associated with rapidly intensifying tropical cyclones over the western North Pacific. Int J Remote Sens 31:4699–4710. doi:10.1080/01431161.2010.485149

Guimond SR, Bourassa MA, Reasor PD (2011) A latent heat retrieval and its effects on the intensity and structure change of hurricane Guillermo (1997). Part I: the algorithm and observations. J Atmos Sci 68:1549–1567. doi:10.1175/2011JAS3700.1

Hart RE, Evans JL (2001) A climatology of the extratropical transition of Atlantic tropical cyclones. J Climate 14:546–564. doi:10.1175/1520-0442(2001)014<0546:ACOTET>2.0.CO;2

Hill KA, Lackmann GM (2011) The impact of future climate change on TC intensity and structure: a downscaling approach. J Climate 24:4644–4661. doi:10.1175/2011JCLI3761.1

Hong SY, Noh Y, Dudhia J (2006) A new vertical diffusion package with an explicit treatment of entrainment processes. Mon Weather Rev 134:318–2341. doi:10.1175/MWR3199.1

Kain JS, Fritsch JM (1990) A one-dimensional entraining/detraining plume model and its application in convective parameterization. J Atmos Sci 47:2784–2802. doi:10.1175/1520-0469(1990)047<2784:AODEPM>2.0.CO;2

Kantha L (2010) Discussion of "A hydrodynamics-based surge scale for hurricanes". Ocean Eng 37:1081–1084. doi:10.1016/j.oceaneng.2010.04.003

Kellner O, Niyogi D, Lei M et al (2012) The role of anomalous soil moisture on the inland reintensification of tropical storm Erin (2007). Nat Hazards 139:1573–1600. doi:10.1007/s11069-011-9966-6

Kishtawal CM, Niyogi D, Kumar A et al (2012) Sensitivity of inland decay of North Atlantic tropical cyclones to soil parameters. Nat Hazards 63:1527–1542. doi:10.1007/s11069-011-0015-2

Klein P, Harr P, Elsberry R (2000) Extratropical transition of western North Pacific tropical cyclones: an overview and conceptual model of the transformation stage. Weather Forecast 15:373–395. doi:10.1175/1520-0434(2000)015<0373:ETOWNP>2.0.CO;2

Knapp KR, Kruk MC, Levinson DH et al (2010) The International Best Track Archive for Climate Stewardship (IBTrACS): unifying tropical cyclone best track data. Bull Am Meteorol Soc 91:363–376. doi:10.1175/2009BAMS2755.1

Kossin JP, Emanuel KA, Vecchi GA (2014) The poleward migration of the location of tropical cyclone maximum intensity. Nature 509:349–352. doi:10.1038/nature13278

Lee SW, Lee DK, Chang DE (2011) Impact of horizontal resolution and cumulus parameterization scheme on the simulation of heavy rainfall events over the Korean Peninsula. Adv Atmos Sci 28:1–15. doi:10.1007/s00376-010-9217-x

Lin N, Smith JA, Villarini G et al (2010) Modeling extreme rainfall, winds, and surge from hurricane Isabel (2003). Weather Forecast 25:1342–1361. doi:10.1175/2010WAF2222349.1

Liu J, Curry JA, Clayson CA et al (2011) High-resolution satellite surface latent heat fluxes in North Atlantic hurricanes. Mon Weather Rev 139:2735–2747. doi:10.1175/2011MWR3548.1

Lynn BH, Tao WK, Wetzel PJ (1998) A study of landscape-generated deep moist convection. Mon Weather Rev 126:928–942. doi:10.1175/1520-0493(1998)126<0928:ASOLGD>2.0.CO;2

Ma LM, Tan ZM (2009) Improving the behavior of the cumulus parameterization for tropical cyclone prediction: convection trigger. Atmos Res 92:190–211. doi:10.1016/j.atmosres.2008.09.022

Mlawer EJ, Taubman SJ, Brown PD et al (1997) Radiative transfer for inhomogeneous atmospheres: RRTM, a validated correlated-k model for the longwave. J Geophys Res Atmos 102:16663–16682. doi:10.1029/97JD00237

Murakami H, Wang Y, Yoshimura H et al (2012) Future changes in tropical cyclone activity projected by the new high-resolution MRI-AGCM. J Climate 25:3237–3260. doi:10.1175/JCLI-D-11-00415.1

National Centers for Environmental Prediction/National Weather Service/NOAA/U.S. Department of Commerce (2000, updated daily) NCEP FNL operational model global tropospheric analy-

ses, continuing from July 1999. Research Data Archive at the National Center for Atmospheric Research, Computational and Information Systems Laboratory. doi:10.5065/D6M043C6

Prater BE, Evans JL (2002) Sensitivity of modeled tropical cyclone track and structure of hurricane Irene (1999) to the convective parameterization scheme. Meteorol Atmos Phys 80:103–115. doi:10.1007/s007030200018

Radcliffe DE, Šimůnek J (2010) Soil physics with HYDRUS: modeling and applications. CRC Press, Boca Raton, p 373

Rakhecha P, Singh VP (2009) Applied hydrometeorology, 1st edn. Springer-Verlag, New York, p 364, LLC

Rappaport EN (2014) Fatalities in the United States from Atlantic tropical cyclones: new data and interpretation. Bull Am Meteorol Soc 95:341–346. doi:10.1175/BAMS-D-12-00074.1

Senkbeil JC, Sheridan SC (2006) A post landfall hurricane classification system for the United States. J Coast Res 22:1025–1034. doi:10.2112/05-0532.1

Shen W, Ginis I, Tuleya R (2002) A numerical investigation of land surface water on landfalling hurricanes. J Atmos Sci 59:789–802. doi:10.1175/1520-0469(2002)059<0789:ANIOLS>2.0.CO;2

Shepherd JM (2012) What we can learn from the satellite-based rainfall footprint of superstorm Sandy: a preliminary synopsis. In: Earthzine. http://www.earthzine.org/2012/12/16/what-we-can-learn-from-the-satellite-based-rainfall-footprint-of-superstorm-sandy-a-preliminary-synopsis/. Accessed 16 Dec 2012

Shepherd JM, Knutson T (2007) The current debate on the linkage between global warming and hurricanes. Geog Compass 1:1–24. doi:10.1111/j.1749-8198.2006.00002.x

Shepherd JM, Grundstein A, Mote TL (2007) Quantifying the contribution of tropical cyclones to extreme rainfall along the coastal southeastern United States. Geophys Res Lett 34:1–5. doi:10.1029/2007GL031694

Skamarock WC, Klemp JB, Dudhia J et al (2008) A description of the advanced research WRF version 3. NCAR Tech. Note NCAR/TN-4751STR, p 125

Trenberth KE, Fasullo J (2007) Water and energy budgets and hurricanes and implications for climate change. J Geophys Res 112:1–10. doi:10.1029/2006JD008304

Tuleya RE (1994) Tropical storm development and decay: sensitivity to surface boundary conditions. Mon Weather Rev 122:291–304. doi:10.1175/1520-0493(1994)122<0291:TSDADS>2.0.CO;2

Tuleya RE, Kurihara Y (1978) A numerical simulation of the landfall of tropical cyclones. J Atmos Sci 35:242–257

Wang JF, Bras RL, Eltahir EAB (2000) The impact of observed deforestation on the mesoscale distribution of rainfall and clouds in Amazonia. J Hydrometeorol 1:267–286. doi:10.1175/1525-7541(2000)001<0267:TIOODO>2.0.CO;2

Xie BG, Zhang FQ (2012) Impacts of typhoon track and island topography on the heavy rainfalls in Taiwan associated with Morakot (2009). Mon Weather Rev 140:3379–3394. doi:10.1175/MWR-D-11-00240.1

Zhang YC, Rossow WB (1997) Estimating meridional energy transports by the atmospheric and oceanic general circulations using boundary fluxes. J Climate 10:2358–2373. doi:10.1175/1520-0442(1997)010<2358:EMETBT>2.0.CO;2

Zhang Y, Cassardo C, Ye CA et al (2011) The role of the land surface processes in the rainfall generated by a landfall typhoon: a simulation of the typhoon Sepat (2007). Asia-Pacific J Atmos Sci 47:63–77. doi:10.1007/s13143-011-1006-7

Zhu P (2008) Impact of land-surface roughness on surface winds during hurricane landfall. Q J R Meteor Soc 134:1051–1057. doi:10.1002/qj.265

Chapter 6
Typhoon/Hurricane Disaster Prediction and Prevention for Coastal, Offshore, and Nuclear Power Plant Infrastructure

Liu Defu, Liu Guilin, Wang Fengqing, and Han Longzhi

Abstract With an increasing tendency of natural hazard frequency and intensity, risk assessment of some design codes for coastal defense infrastructure should be of paramount importance in influencing the economic development and protection of life in China. Comparison between existing extreme statistical models like Gumbel, Weibull, P-III distribution or probable maximum typhoon/hurricane (PMT/PMH), and design basis flood (DBF) with our proposed univariate and multivariate compound extreme value distribution (CEVD and MCEVD) showed that all the planned, designed, and constructed coastal infrastructure for cities and nuclear power plants that use the accepted, traditional safety regulations is menaced by the possibility of future typhoon/hurricane disasters and cannot satisfy the safety requirements that accompany the increasing tendency of extreme natural hazards. The disasters caused by Hurricane Katrina (2005), Rita (2005), and Sandy (2012) have validated the 1982 CEVD and 2006 MCEVD predicted extreme hazards in New Orleans, the Gulf of Mexico, and Philadelphia areas. The 2013 Typhoon Fitow disaster in China also validated the 2006 MCEVD predicted results.

Keywords Typhoon/hurricane disasters prediction and prevention • Compound extreme value distribution (CEVD) • Multivariate CEVD • Poisson-nested logistic trivariate compound extreme value distribution (PNLTCEVD) • Stochastic simulation method – P-ISP • Standard project hurricane (SPH) • Probable maximum hurricane (PMH) • API recommendations • Coastal • Offshore and nuclear power plant • Design code calibration • Joint probability safety assessment

L. Defu • W. Fengqing
Ocean University of China, Qingdao 266003, China
e-mail: liu@ouc.edu.cn; wfq@ouc.edu.cn

L. Guilin (✉) • H. Longzhi
Ocean University of China, Qingdao 266100, China
e-mail: liuguilin73@ouc.edu.cn; hanlongzhi@163.com

1 Introduction

China has a wide continental slope to dissipate tsunami energy. If an M9 earthquake occurs at the Manila trench or Ryukyu trench, the wave height produced by a tsunami at the south and southeast China coast would be no more than 5–6 m (Liu et al. 2007). The World Meteorological Organization estimates that about 90 % of all natural disasters are extreme meteorological hazards like typhoons, hurricanes, and tropical cyclone-triggered disasters in the Pacific, Atlantic, and Indian oceans, the Caribbean Sea, and the Gulf of Mexico areas. In 1972, Typhoon Rita made landfall on the Dalian port in the North Bohai Bay of China, causing severe damage. The severe Typhoon Nina in 1975 induced 1631 mm of rainfall in 3 days. Around Banqiao Dam and downstream 64 reservoir dams collapsed. The flooding resulted in more than 171,000 deaths and affected 12,000,000 people. The Banqiao Dam was designed by a Pearson Type III distribution to withstand a 1000-year flood. Our study found that, using traditional extrapolation (such as a Pearson type III model), it was difficult to determine the design return period for the extreme events induced by typhoons. According to the randomness of annual typhoon occurrence frequency along different sea areas, frequency can be considered as a discrete random variable. Typhoon characteristics or typhoon-induced extreme sea events are continuous random variables based on the order statistics and theory of measure, and using these variables, the compound extreme value distribution (CEVD) can be derived (Liu et al. 2001).

During the past few years, CEVD has been developed into multivariate compound extreme value distribution (MCEVD) and applied to predict and prevent typhoon-induced disasters for coastal areas, offshore structures, and estuarine cities (Defu et al. 2006; Liu et al. 2001, 2006, 2011a, b). Many applications of MCEVD in engineering design and risk analysis show the scientific and practical value of its predicted results in China and abroad (Nafaa et al. 1991; Ochi 1982; Quek and Cheong 1992; Muir and El-Shaarawi 1986; Norwegian Det Norsk Company 1988; KORDI 2004; China Ministry of Transportation 1986). As mentioned in "Summary of Flood Frequency Analysis in the United States" (Kirby and Moss 1987): "The combination of the event-based and joint probability approaches promises to yield significantly improved descriptions of the probability laws of extraordinary floods." MCEVD is the model which follows the development direction of the extraordinary flood prediction hoped for by Kirby and Moss (1987). Four publications of the CEVD (Liu et al. 2001; Liu 1982) and MCEVD (Liu et al. 2006, 2008) were cited as experimental evidence of prevention criteria for hurricane disasters (Chowdhury et al. 2009). Considering the regional differences, we will use feet for the USA and meters for China as the unit of water level in the process of analysis.

2 Development Process of the Multivariate Compound Extreme Value Distribution (MCEVD)

During the past years, CEVD and MCEVD have been applied to more than 50 coastal, offshore, and hydraulic projects in China and abroad. The theory of CEVD is also well cited in the international literature and used for extreme sea hazard study in the North Sea and around the Korean coast (Norwegian Det Norsk Company 1988; KORDI 2004), further justifying the use of MCEVD as a good model for typhoon (or hurricane) disaster prediction. Our proposed methods detailed in Liu et al. (2001, 2006, 2009) and Liu (1982) are used as design criteria of wind-structure interaction experimentation for mitigating hurricane-induced US coastal disasters (Chowdhury et al. 2009).

The derivation of the MCEVD is as follows:

Let N be a random variable (representing the number of storms in a given year), with their corresponding probability:

$$P\{N = k\} = p_k, k = 1, 2, \ldots;$$

and

$$(\xi_{11}, \ldots, \xi_{n1}) (\xi_{12}, \ldots, \xi_{n2}) \ldots \ldots$$

be an independent sequence of independent identically distributed random vectors (representing the observed extreme sea environments in the sense defined above within the successive storms) with common probability density $g(\bullet)$. Then we are interested in the distribution of:

$$(X_1, \ldots, X_n) = (\xi_{1i}, \ldots, \xi_{ni})$$

where ξ_{1i} is the maximum value of

$$\xi_{1j}, 1 \leq j \leq N, N = 1, 2, \ldots \ldots$$

This represents the maximum annual value of the principal variable, together with the simultaneously occurring values of the concomitant variables. There is a reasonable approximation in the definition of $(X_1, \ldots, X_n)$, also valid for $N = 0$, because no extreme value of interest can occur outside the storm in the case of $N = 0$. The more detailed discussion of the model correction in case of $p(N = 0)$ can be found in reference Liu et al. (2008, 2009).

When the multivariate continuous cumulative distribution is $G(x_1, \ldots x_n)$, then we can derive the MCEVD as:

$$F(x_1, \ldots, x_n) = \sum_{i=1}^{\infty} p_i \cdot i \cdot \int_{-\infty}^{x_n} \ldots \int_{-\infty}^{x_1} G_1^{i-1}(u) g(u_1, \ldots, u_n) \, \mathrm{d}u_1 \ldots \mathrm{d}u_n \quad (6.1)$$

where $G_1(u_1)$ is the marginal distribution of $G(x_1, \ldots, x_n)$ and $g(u_1, \ldots u_n)$ is the density function.

This can be proved as follows:

$$F(x, y, z) = P(X < x, Y < y, Z < z)$$

$$= P\left(\bigcup_{i=0}^{\infty} \{X < x, Y < y, Z < z\} \bigcap \{n = i\}\right)$$

$$= \sum_{i=0}^{\infty} P(X < x, Y < y, Z < z | n = i) \cdot P(n = i)$$

$$= \sum_{i=0}^{\infty} p_i P(X < x, Y < y, Z < z | n = i)$$

$$= p_0 \cdot Q(x, y, z) + \sum_{i=0}^{\infty} p_i P(X < x, Y < y, Z < z | n = i)$$

in which

$$P\left(X < x, Y < y, Z < z | n = i\right)$$

$$= P\left(\bigcup_{k=1}^{i} \{X < x, Y < y, Z < z\} \bigcap \left\{\max_{1 \leq j \leq i} \xi_j = \xi_k\right\} \Big| n = i\right)$$

$$= \sum_{k=1}^{i} P\left(\{X < x, Y < y, Z < z\} \bigcap \left\{\max_{1 \leq j \leq i} \xi_j = \xi_k\right\} \Big| n = i\right)$$

Let $\xi_k = \xi_1$, then

$$P(X < x, Y < y, Z < z | n = i)$$

$$= iP\left(\{X < x, Y < y, Z < z\} \bigcap \left\{\max_{1 \leq j \leq i} \xi_j = \xi_k\right\} \Big| n = i\right)$$

$$= i \cdot P\left(\xi_1 < x, \eta_1 < y, \varsigma_1 < z, \xi_1 > \xi_j, j = 2, 3, \ldots i | n = i\right)$$

$$= iE\left\{I_{\{\xi_1 < x\}}(\omega) I_{\{\eta_1 < y\}}(\omega) I_{\{\varsigma_1 < x\}}(\omega) I_{\{\xi_1 > \xi_j, j=2,3,\ldots i\}}(\omega) | n = i\right\}$$

$$= iE\left\{\begin{array}{l} E\left\{I_{\{\xi_1 < x\}}(\omega) I_{\{\eta_1 < y\}}(\omega) I_{\{\varsigma_1 < z\}}(\omega) I_{\{\xi_1 > \xi_j, j=2,3,\ldots i\}}(\omega)\right\} \\ |(\xi_1 = U, \eta_1 = V, \varsigma_1 = W) \end{array}\right\}$$

where (U, V, W) and $(\xi_1, \eta_1, \varsigma_1)$ are statistically independent and their probability distribution function is $G(x,y,z)$.

$$P\left(X < x, Y < y, Z < z \,|\, n = i\right)$$

$$= iE \left\{ \begin{array}{c} I_{(U<x)}\left(\omega\right) I_{\{V<y\}}\left(\omega\right) I_{\{W<z\}}\left(\omega\right) E\left\{I_{\{U>\xi_J,j=2,3,...i\}}\left(\omega\right)\right\} \\ |(\xi_1 = U, \eta_1 = V, \varsigma_1 = W) \end{array} \right\}$$

$$= iE\left\{I_{\{U<x\}}\left(\omega\right) I_{\{V<y\}}\left(\omega\right) I_{\{W<z\}}\left(\omega\right) G_1^{i-1}(u)\right\}$$

$$= i \cdot \int_{-\infty}^{2}\int_{-\infty}^{y}\int_{-\infty}^{x} G_1^{i-1}(u) \cdot \mathrm{dG}\left(u, v, w\right)$$

$$= i \cdot \int_{-\infty}^{2}\int_{-\infty}^{y}\int_{-\infty}^{x} G_1^{i-1}(u) g\left(u, v, w\right) \, dudvdw$$

where

$$I_A = \begin{cases} 1, x \in A \\ 0, x \notin A \end{cases}$$

is the characteristic function of A

$$F\left(x, y, z\right) = p_0 Q\left(x, y, z\right) + \sum_{i=1}^{\infty} p_i \cdot i \cdot \int_{-\infty}^{z}\int_{-\infty}^{y}\int_{-\infty}^{x} G_i^{i-1}(u) g\left(u, v, w\right) dudvdw$$

$$= p_0 Q\left(x, y, z\right) \sum_{i=1}^{\infty} p_i \cdot i \cdot \int_{-\infty}^{z}\int_{-\infty}^{y}\int_{-\infty}^{x} G_i^{i-1}(u) g\left(u, v, w\right) dudvdw$$

$$+ p_0 - p_0 \tag{6.2}$$

When the case of $n = 0$ is ignored, Eq. 6.2 can be approximated as formula (6.3):

$$F\left(x, y, z\right) = p_0 + \sum_{i=1}^{\infty} p_i \cdot i \cdot \int_{-\infty}^{z}\int_{-\infty}^{y}\int_{-\infty}^{x} G_i^{i-1}(u) g\left(u, v, w\right) dudvdw \tag{6.3}$$

Therefore, formula (6.1) is proved.

2.1 Poisson-Gumbel Compound Extreme Value Distribution (P-G CEVD) and Its Applications

When $G(x_1, \ldots, x_n)$ is the probability distribution function of the unit-variant random variable x, then formula (6.1) can be simplified to:

$$F(x) = \sum_{i=0}^{\infty} p_i [G(x)]^i \tag{6.4}$$

When typhoon occurrence frequency can be fitted to a Poisson distribution, typhoon-induced wave or wind is fitted to a Gumbel distribution, as in formula (6.5):

$$G(x) = e^{-e^{-x}} = \exp\{-\exp[-\alpha(x - \mu)]\} \qquad (6.5)$$

where α and μ are parameters of Gumbel distribution.

Then the Poisson-Gumbel compound extreme value distribution (P-G CEVD) can be derived as (Liu 1982):

$$F(x, y) = \sum_{i=0}^{\infty} p_i[G(x)]^i = \sum_{i=0}^{\infty} e^{-\lambda} \cdot \frac{\lambda^i}{i!}[G(x)]^i = e^{-\lambda[1-G(x)]} = 1 - P \qquad (6.6)$$

The typhoon-induced extreme wave (or wind speed) with return period T (1/p) can be calculated by formula (6.7):

$$H_P = \mu + X_P/\alpha \qquad (6.7)$$

where

$$X_P = -1n\left\{-1n\left(1 + \frac{1n(1 - P)}{\lambda}\right)\right\}$$

$\lambda = \frac{n}{N}$ is the yearly mean value of typhoon frequency.

N is the total number of years.
n is the total typhoon number.

$$\left.\begin{array}{l} \alpha = \sigma_n/S \\ \mu = \overline{H} - y_n/\alpha \end{array}\right\}$$

$\overline{H}, S$: mean value and standard deviation of typhoon-induced wave.
σ_n, y_n can be calculated by typhoon number.

2.2 Comparison Between P-G CEVD, Gumbel, and P-III Distributions

Observed typhoon-induced wave data in the East China Sea from 1953 to 2006 are used to statistically check for agreement with the Gumbel, P-III, and P-G CEVD distributions. The Kolmogorov-Smirnov test was used to measure the goodness of fit and based on the 20 years moving average data sampling used for calculation maximum deviation between empirical and theoretical distributions as in formula (6.8):

$$D_n = \sup_{-\infty < x < \infty} |F_n(x) - F_0(x)| \tag{6.8}$$

where $F_n(x)$ is the empirical distribution and $F_0(x)$ is the theoretical distribution.

The standard deviation is defined as:

$$d = \sqrt{\frac{\sum_{i=1}^{n} (pl - pj)^2}{n - 1}} \tag{6.9}$$

where pl and pj are the theoretical and empirical values, respectively.

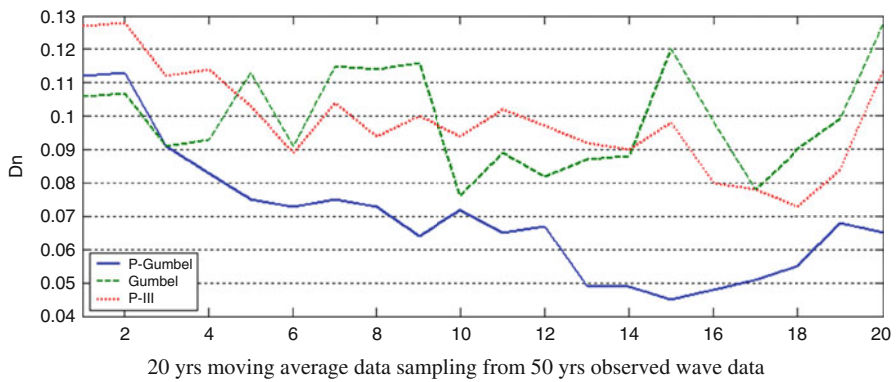The estimated Dn and d for the Gumbel, P-III, and P-G CEVD models are shown in Figs. 6.1 and 6.2.

Fig. 6.1 Comparison of calculated K-S statistic Dn between three statistical models for wave data in the East China Sea, 1953–2006
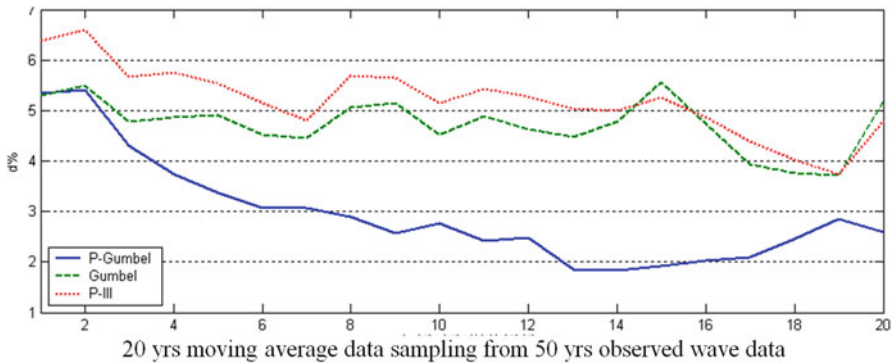
Fig. 6.2 The same as Fig. 6.1 for the comparison of calculated standard division d

Table 6.1 Relative error of predicted return value Δh between three models

	100 a	50 a	20 a
Model	Δh	Δh	Δh
Gumbel	26 %	25 %	23 %
P-III	26 %	25 %	22 %
P-Gumbel	18 %	17 %	16 %

Figures 6.1 and 6.2 and Table 6.1 show that P-G CEVD is a more reasonable model for extreme wave prediction than traditional models.

The P-G CEVD was used to design wave prediction for more than 40 coastal structures of China and was accepted in the 2013 "China Code for Sea Port Hydrology" as a recommended model for design wave prediction (China Code for Sea Port Hydrology 2013).

2.3 Poisson-Weibull Compound Extreme Value Distribution (P-W CEVD) and Its Application Along US Coasts

Long-term hurricane data show that frequencies of hurricane occurrence along the US Atlantic East Coast and Gulf of Mexico coast agree with the Poisson distribution (see Fig. 1 in Schwerdt et al. 1979). Hurricane central pressure, wind velocities, wave heights, and storm surges agree with the Weibull distribution. Therefore, a Poisson-Weibull compound extreme value distribution (P-W CEVD) is presented to predict hurricane central pressure, wind velocities, wave heights, and surges.

The Weibull distribution is given in formula (6.10):

$$G(x) = 1 - \exp\left\{-\left(\frac{x}{b}\right)^r\right\} \qquad (6.10)$$

The P-W CEVD can be derived as:

$$X_p = \left(-1n\left\{-\frac{1}{\lambda}1n\left(1-p\right)\right\}\right)^{\frac{1}{r}} - b \qquad (6.11)$$

where b and r are parameters of the Weibull distribution, while

$$\lambda = \frac{n}{N}$$

is the yearly mean value of hurricane frequency.
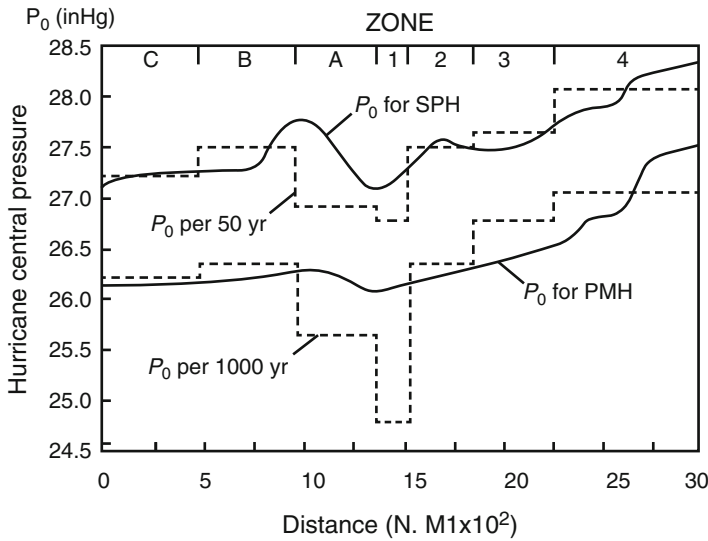
Fig. 6.3 Comparison of hurricane center pressures between CEVD predicted values and NOAA proposed design codes (see Liu 1982, Fig. 6)

2.4 Poisson-Nested Logistic Trivariate Compound Extreme Value Distribution (PNLTCEVD)

As mentioned above, the frequency of hurricane occurrence can be fitted to the Poisson distribution (Fig. 6.3):

$$P_i = \frac{e^{-\lambda}\lambda^i}{i!}$$

By substituting a nested-logistic trivariate distribution (Norwegian Det Norsk Company 1988) for the continuous distribution into formula (6.3), the PNLTCED can be obtained. The nested-logistic trivariate distribution is expressed as:

$$G\{x_1, x_2, x_3\} = \exp - \left[\left\{ \left[\left(1 + \xi_1 \frac{x_1 - \mu_1}{\sigma_1}\right)^{-1/(\alpha\beta\xi_1)} \right. \right. \right.$$
$$\left. \left. \left. + \left(1 + \xi_2 \frac{x_2 - \mu_1}{\sigma_2}\right)^{-1/(\alpha\beta\xi_2)} \right]^{\beta} + \left(1 + \xi_3 \frac{x_3 - \mu_3}{\sigma_3}\right)^{-1/(\alpha\beta\xi_3)} \right\}^{\alpha} \right] \quad (6.12)$$

in which ξ_j, μ_j, σ_j are the shape, location, and scale parameters of the marginal distributions $G(x_j)$ to x_j ($j = 1, 2, 3$), respectively. The dependent parameters α and β can be obtained by moment estimation:

$$\widehat{\alpha} = \frac{\sqrt{1 - r_{13}} + \sqrt{1 - r_{23}}}{2}$$

$$\widehat{\beta} = \frac{\sqrt{1 - r_{12}}}{\widehat{\alpha}}$$

where $r_{i,j}$ is correlation coefficient, $i \bullet j$, $i, j = 1, 2, 3$.

Let

$$s_j = \left(1 + \xi_j \frac{x_j - \mu_j}{\sigma_j}\right)^{-1/\xi_j} \quad j = 1, 2, 3$$

then formula (6.12) can be written as

$$G(x_1, x_2, x_3) = \exp\left\{-\left[\left(s_1^{1/(\alpha\beta)} + s_2^{1/(\alpha\beta)}\right)^{\beta} + s_3^{1/\alpha}\right]^{\alpha}\right\} \tag{6.13}$$

and the corresponding probability density function is

$$g(x_1, x_2, x_3) = \frac{\partial^3 G}{\partial x_1 \partial x_2 \partial x_3}$$
$$= \frac{1}{\sigma_1 \sigma_2 \sigma_3} e^{-u} u^{1-2/\alpha} v^{1/\alpha - 2/\alpha\beta} s_1^{1/(\alpha\beta) - \xi_1} s_2^{1/(\alpha\beta) - \xi_2} s_3^{1/\alpha - \xi_3} Q \tag{6.14}$$

in which

$$v = \left(S_1^{1/(\alpha\beta)} + S_2^{1/(\alpha\beta)}\right)^{\alpha\beta}$$

$$u = \left[\left(S_1^{1/(\alpha\beta)} + S_2^{1/(\alpha\beta)}\right)^{\beta} + S_3^{1/\alpha}\right] = \left(v^{1/\alpha} + s_3^{1/\alpha}\right)^{\alpha}$$

$$Q = \left(\frac{v}{u}\right)^{1/\alpha} Q_3(u; \alpha) + \frac{1 - \beta}{\alpha\beta} Q_2(u; \alpha)$$

$$Q_3(u; \alpha) = u + \frac{1}{\alpha} - 1$$

$$Q_3(u; \alpha) = u^2 + 3\left(\frac{1}{\alpha} - 1\right)u + \left(\frac{1}{\alpha} - 1\right)\left(\frac{2}{\alpha} - 1\right)$$

The trivariate layer structure (α – outside layer, β – inside layer) shows that the correlation between x_1 and x_2 is stronger than those among x_1, x_3 and x_2, x_3.

As shown above, PNLTCED can be obtained through the estimation of parameters of the marginal distributions and their dependent parameters.

The new model has some advantages:

(a) Considering the hurricane occurring frequency.
(b) Considering the combination of trivariate environmental factors induced by hurricane.
(c) Considering the dissymmetry of two dependent parameters.
(d) It has the simple structure and is easy to be applied in engineering applications.

2.5 Solution of MCEVD by Stochastic Simulation Method: P-ISP

Coastal engineering not only takes up coastline resources that are valuable and nonrenewable but also requires huge investment. Thus, the failure of coastal structures would cause enormous economic loss and possible environmental pollution. Therefore, the reliability analysis of coastal engineering in extreme sea state should be taken into account. Freudenthal was the first author who proposed the use of structural reliability theory. In recent years, reliability analysis has found more and more applications. The Monte Carlo method (MC method), the first-order reliability method (FORM), and the design point method (JC method) are the three methods that have been widely used to estimate the failure probability of structures. Compared with the FORM, JC method, and MC method, the MCEVD-based P-ISP method is regarded as a relative accurate method for reliability analysis of structure (Bea 2007; Blake and Gibney 2011; Casson and Coles 2000; China Code for Sea Port Hydrology 2013; China Ministry of Transportation 1986).

The multivariate joint probability distribution usually has a very complex mathematical form; solution of high-dimensional MCEVD needs a stochastic simulation method, such as a Monte Carlo method. However, the use of this method inevitably requires great computational efforts, and large variances exist when the analyzed joint probabilities are small. Hence, different sampling methods have been developed to reduce the number of simulations and to decrease the variance, among which the importance sampling procedure (ISP) is an efficient method (Liu et al. 2011c; Defu et al. 2015).

The basic idea of the ISP method consists of concentrating the distribution of the sampling points in the region of great importance, i.e., the part that mainly contributes to the joint probability instead of spreading them out evenly over the whole range of definition of the involved parameters. In particular, the multi-normal distribution centering on the design point (the most unfavorable design condition) is defined as the important sampling distribution. ISP thus requires an optimization procedure to find the design point. The joint probability can then be evaluated by a

weighted sampling procedure. A most significant advantage of ISP method is that it can also be used in the original space where data is deficient, regardless of the type of the basic random variables.

The transformation of the basic variables into a vector of independent standard normal variables, which may be difficult for correlated variables, is avoided. The weighted sampling is not affected by any non-Gaussian distribution because the actual joint probability is calculated by the use of the original distribution. For formula (6.1), we can generate N groups of $x_1, x_2, \ldots x_n$ and record the number of groups that lead to a limit state function ≤ 0; if this number is M, the evaluation of formula (6.1) can be estimated by:

$$F(x_1, x_2, \ldots x_n) = \lim_{N \to \infty} \frac{M}{N} \tag{6.15}$$

Let x denote an n-dimensional random vector. Its corresponding joint probability density function is $f_x(x)$ formula (6.1) which can be rewritten as:

$$F(x) = \underset{g(x) \leq 0}{\iint \cdots \int} I[g(x) \leq 0] \frac{f_x(x)}{h_x(x)} h_x(x) \mathrm{d}\mathbf{x} \tag{6.16}$$

in which x is the n-dimensional random vector, $x = x_1, x_2 \ldots x_n$; $g(x) \leq 0$ is the joint probability domain decided by limit state function, and $g(x) = 0$; $I[g(x) \leq 0] = \begin{cases} 1, g(x) \leq 0 \\ 0, g(x) > 0 \end{cases}$ is the characteristic function; $h_x(x)$ is usually called the weighting density function (Defu et al. 2015), from which the samples are generated in the simulation procedure. Then the expected value of joint probability is expressed as:

$$\widehat{F}(\mathbf{x}) = \frac{1}{N} \sum_{i=1}^{N} I[g(x) \leq 0] \frac{f_X(x_i)}{h_X(x_i)} \tag{6.17}$$

in which N denotes the simulation times and $\mathbf{x}_i$ is the i-th simulation vector.

As shown above, the main advantage of ISP is that samples are generated according to the density function $h_x(x)$ rather than the original density function $f_x(x)$. The efficiency of ISP is higher than basic Monte Carlo simulation.

The variance of $\widehat{F}(x)$ is derived as follows:

$$\mathrm{Var}\left(\widehat{F}(x)\right) = \frac{1}{N} \left[E\left(I[g(x) \leq 0] \cdot \frac{f_x(x)}{h_x(x)} \right)^2 - F(x)^2 \right] \tag{6.18}$$

It can be seen that if the forms of $h_x(x)$ and $f_x(x)$ are similar, the variance will be less.

The sampling procedure of MCEVD can be carried out as follows:

(a) For a given λ, a random number K which satisfies the Poisson distribution is initially generated.
(b) If $K > 0$, K groups of $x_1, x_2, \ldots x_n$ are then generated according to the multivariate joint normal density function $h_x(x)$. The design point $\mathbf{x}^*$ which is derived by using a second-moment method can be taken as the sampling center.
(c) From K groups of $(x_1, x_2, \ldots x_n)$, select $(x_1, x_2, \ldots x_n) | x_1 = \underset{1 \leq i \leq K}{\text{Max}} x_{1i}$ as the annual maximum value of the metoceanic factors(wind speed, wave height, and current) induced by the typhoon.
(d) Repeat step a to c for N times; the N year samples satisfying MCEVD are generated.

It should be noticed that $x_1, x_2, \ldots x_n$ are correlated variables with different kinds of non-Gaussian or Gaussian distributions. This method can be used to predict long-term joint probability of typhoon characteristics and other multivariate typhoon-induced environments with different kinds of marginal distributions and different correlation coefficients between variables.

These features affect disaster intensity and consequence directly. Thus, in our opinion, the analysis of typhoon characteristic combinations and the corresponding disaster consequences in different areas should be an important part of typhoon disaster zoning. The typhoon characteristics are usually described by using the maximum central pressure difference (ΔP), the radius of maximum wind speed (Rmax), the speed of movement of the typhoon center (s), the minimum distance between the typhoon center and the target site (δ), and the typhoon direction of movement (θ). But one of the chief advantages lies in taking the annual typhoon frequency (λ) into account as a discrete random variable in the MCEVD model. In addition, this model can take into account secondary typhoon disasters, for example, when Typhoon Nina occurred in 1975 in China and induced the dam collapse of the Banqiao Reservoir that led to a tragic loss of life or when Typhoon Bilis in 2006 caused a terrible loss of life in the land provinces. In this study, the typhoon duration from landfall to dissipation (t) is also considered in the prediction model. For the analysis procedure of the multivariate joint probability which combines a kind of discrete distribution (λ) and six kinds of continuous distributions (ΔP, Rmax, s, δ, θ, t), a stochastic simulation technique based on the theory of MCEVD is a valid way to solve such a six-dimensional non-Gaussian problem.

It should be noted that the solution of the multidimensional joint probability problem is a contour surface with some probability value. In the application process, when aiming at different objectives, for instance, (ΔP) reflects typhoon intensity, (Rmax) reflects the area influenced by the typhoon, (s) reflects the intensity of typhoon-induced surges and waves, and (t) reflects the inland areas affected intensely and should be selected as the dominant factors, respectively, to calculate the unique solution of joint probability for the assessment of different disaster consequences. This procedure is taken as the first layer of the double-layer-nested multi-objective probability model, which is offered as the basis for typhoon disaster zoning.

In the simulation procedure P-ISP, it is necessary to input the mean value of typhoon frequency (λ), the marginal distribution of the six kinds of typhoon characteristics (P-ISP is suitable for normal, uniform, exponential, Rayleigh, Gumbel, Weibull, lognormal, gamma, and Fréchet distributions), the mean value and standard deviation of each variable group, the matrix correlation coefficients among the variables, and the limit state equation. Then the joint probability of different typhoon characteristics with some typhoon occurrence frequency can be calculated as the output. Comparing this method with the basic Monte Carlo method, P-ISP performs more quickly and accurately, so it has been successfully applied to the joint probability analysis of typhoon-induced extreme sea environmental loads such as wind, wave, storm surge, current, etc., for different kinds of offshore structures, leading to a risk assessment of coastal and hydraulic structures (Defu et al. 2015).

3 Hurricanes Katrina and Rita of 2005 and Hurricane Sandy of 2012 as a Validation of CEVD 1982 Predicted Results

3.1 Comparison Between 1982 PWCEVD Predicted Results and NOAA-Proposed SPH and PMH

In 1979, the US National Oceanic and Atmospheric Administration (NOAA) divided the Gulf of Mexico and Atlantic coasts into seven areas according to hurricane intensity, in which corresponding standard project hurricane (SPH) and probable maximum hurricane (PMH) were proposed as hurricane disaster prevention criteria (Schwerdt et al. 1979). Using CEVD (Liu 1982; Harris 1963), the predicted hurricane central pressures with return period of 50 years and 1000 years were close to SPH and PMH, respectively, except that for the sea area nearby New Orleans (zone A) and East Florida (zone 1) coasts, hurricane intensities predicted using CEVD were more severe than NOAA proposed values. In these regions, SPH and PMH only correspond to CEVD predicted 30–40 years and 120 years return values, respectively.

In 2005, Hurricanes Katrina and Rita attacked coastal areas of the USA, causing the deaths of about 1833 people and an economic loss of $108 billion in the city of New Orleans (Blake and Gibney 2011; McTaggart-Cowan et al. 2008) and destroyed more than 110 oil platforms in the Gulf of Mexico. The disaster implied that using SPH as the flood-protective standard was a main reason for the catastrophic outcome (Liu et al. 2008; Bea 2007; Resio 2007; Mittal 2005a). Figure 6.3 and Table 6.2 indicate that CEVD predicted results are more reasonable than the safety regulations proposed by NOAA. An important reason for the hurricane Katrina and Rita disasters may be that NOAA proposed unreasonable SPH and PMH.

Table 6.2 Comparison between NOAA and PWCEVD predicted central pressure

Zone	NOAA In/hpa		CEVD In/hpa		Hurricane In/hpa
A	SPH	27.8/941.0	50 years	26.9/910.8	Katrina
	PMH	26.3/890.5	1000 years	25.6/866.8	26.6/902.0
1	SPH	27.1/919.3	50 years	26.7/904.0	Rita
	PMH	26.1/885.4	1000 years	24.6/832.9	26.4/894.9
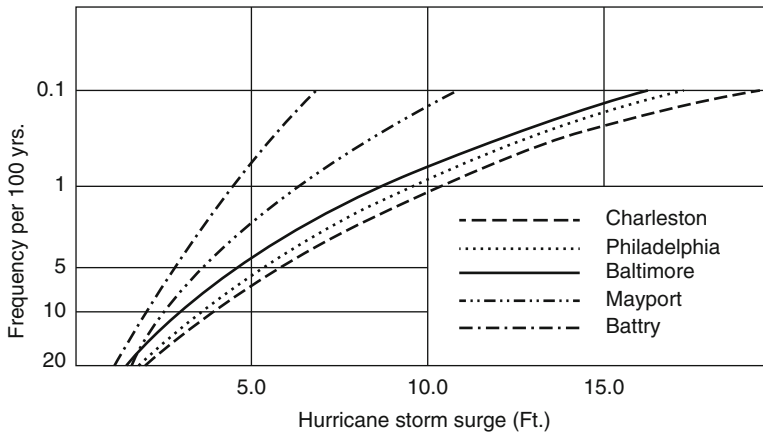
Fig. 6.4 CEVD predicted hurricane storm surge from Hurricane Sandy for locations along Atlantic coast (see Liu 1982, Fig. 8)

3.2   2012 Hurricane Sandy Induced Flooded Area as a Validation of the 1982 CEVD Predicted Storm Surge

Hurricane Sandy is the second costliest hurricane in the USA. Damage was $75 billion and at least 233 people killed (Wikipedia 2016). In 1982, based on the 1926–1960 observed data, we used CEVD to predict the storm surge which was induced by the 100-year return period hurricane for the Philadelphia area. We chose this site based on the following reasons:

(a) We have 1926–1960 observed data in this area.
(b) Philadelphia was indeed affected by Sandy's storm surge and that the area is vulnerable to hurricane-induced storm surges.

The result was about 10 ft and was close to the storm surge of 10.62 ft that was observed on October 30, 2012, at 08 h:06; the Hurricane Sandy-induced water level is shown by the dotted line in Fig. 6.4. But the surge predicted by NOAA was only 7.52 ft.

3.3 Hurricane Katrina and Hurricane Sandy as a Validation of MCEVD Predicted Results

Here, the 55-year (1950–2004) measured data of hurricane winds, hurricane effect duration (provided by NOAA and Unisys), and the simultaneous Mississippi water level (hurricane process data, provided by the USACE) are used for the long-term joint probability prediction of Hurricane Katrina. Sometime after the establishment of the seven zones (as shown in Fig. 6.3) was proposed, the Gulf of Mexico and Atlantic coasts were divided into 11 regions according to regional planning for hurricane hazard (Gray 2003).

Following the requirements of the MCEVD calculation procedure, a statistical check shows that the frequency of hurricane in this area fits to a Poisson distribution (Fig. 6.5). The diagnostic checks show that all of the data of the wind speed (Ws), water level (Wl), and hurricane duration (Wd) fit to the generalized extreme value distribution (Fig. 6.6a–c). Using MCEVD, a single contour surface for wind speed, hurricane inference duration, and water level for each joint return period can be obtained, as shown for the 100-year joint return period in Fig. 6.7. Thus, there should be different combinations of duration and wind speed that can result in the same joint return period of surge.

As shown in Tables 6.3 and 6.4 and Fig. 6.8, the MCEVD predicted 100 years of return values not only validated by 2005 Hurricane Katrina but also by 2012 Hurricane Sandy.

Fig. 6.5 Curve fitting of hurricane frequency for the Gulf of Mexico and Atlantic coast

annual occurrence frequency of hurricanes
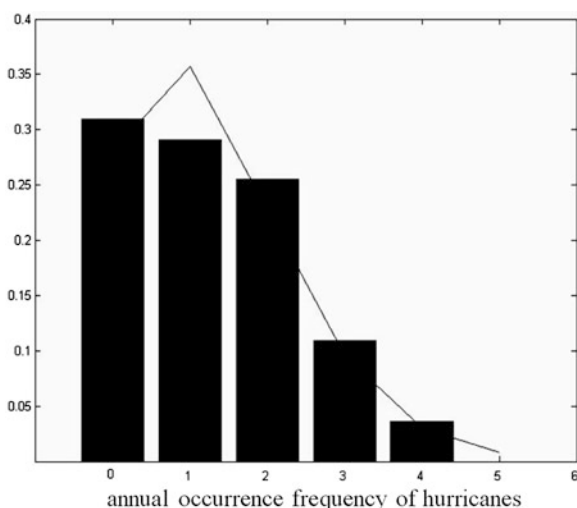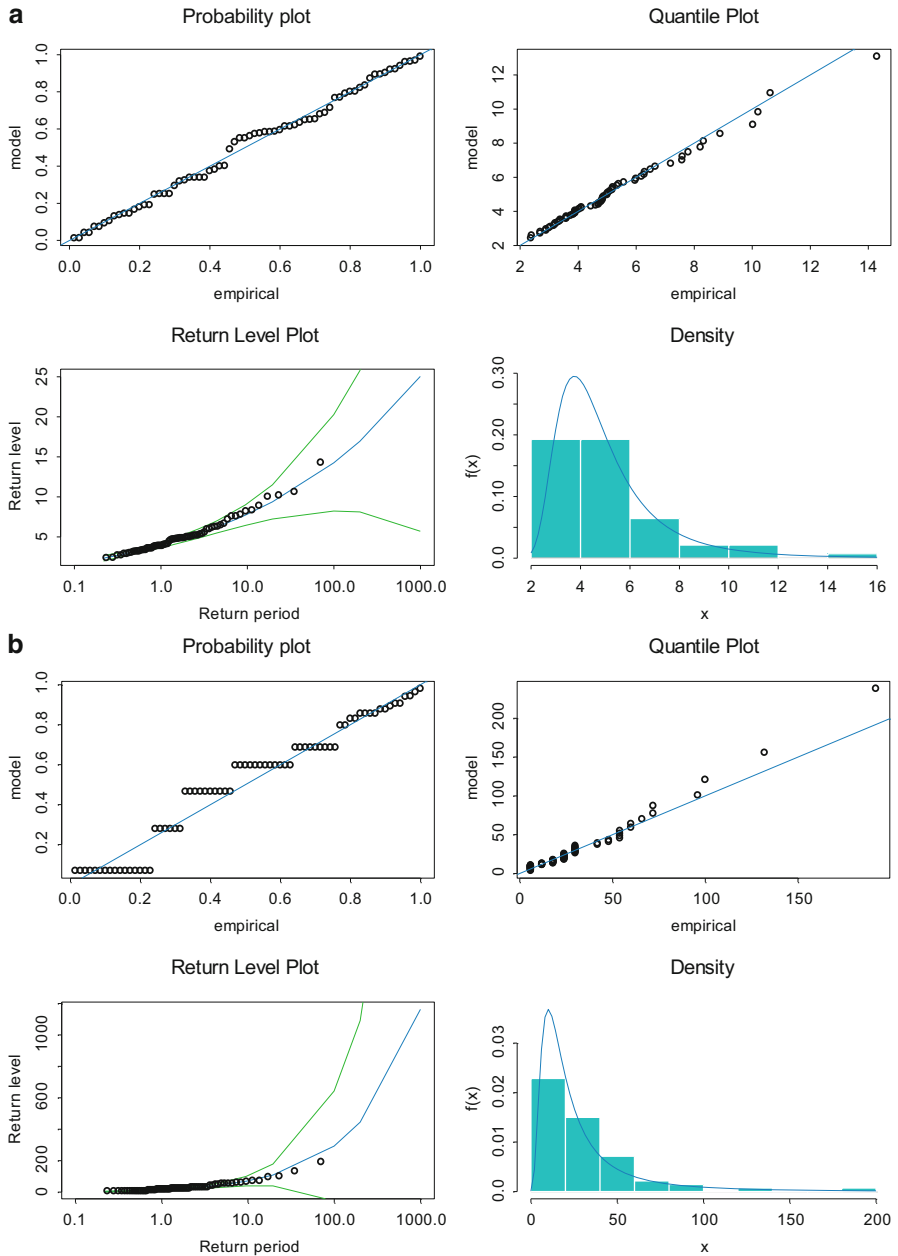
Fig. 6.6 (**a**) Distribution diagnostic testing of water level for the Gulf of Mexico and Atlantic coast. (**b**) Distribution diagnostic testing of hurricane duration for the Gulf of Mexico and Atlantic coast. (**c**) Distribution diagnostic testing of wind speed for the Gulf of Mexico and Atlantic coast

c

Probability plot

Quantile Plot

Return Level Plot

Density
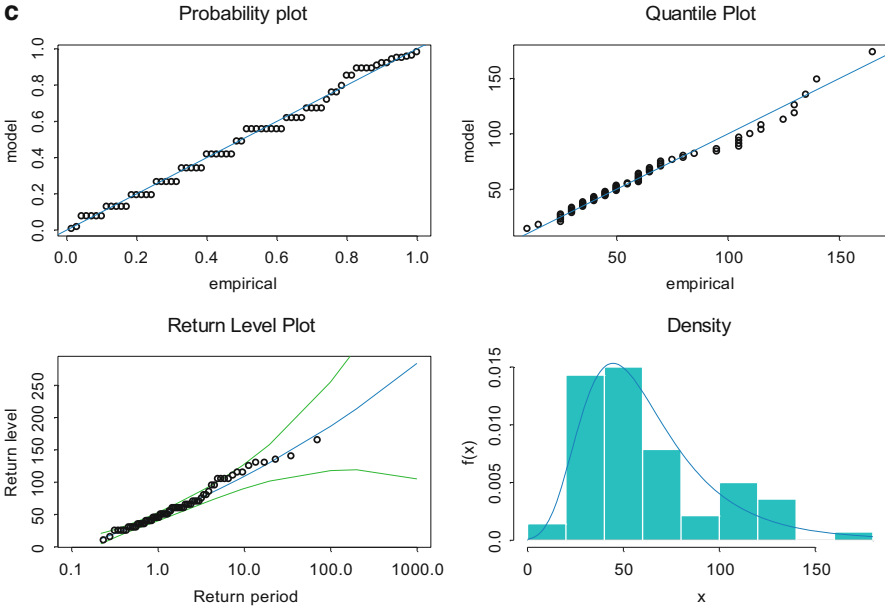
Fig. 6.6 (continued)
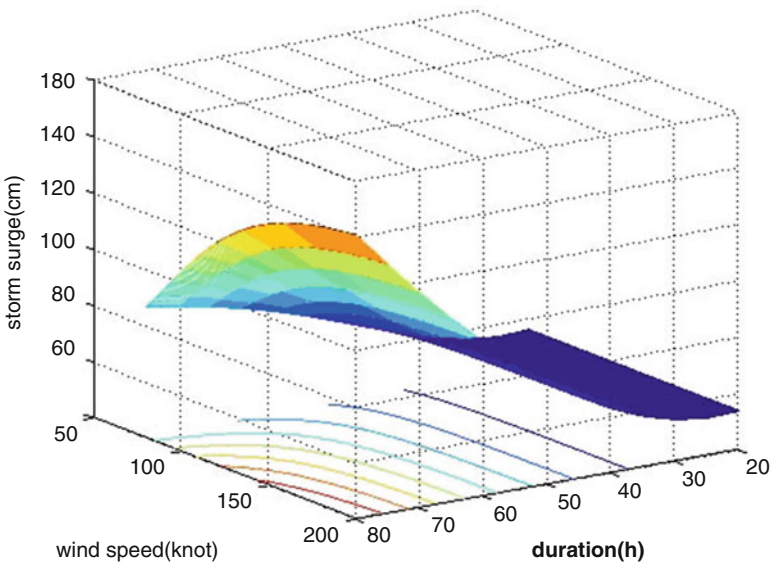
Fig. 6.7 Contour surface of storm surge with return period of 100 years for the Gulf of Mexico and Atlantic coast

Table 6.3 The calculated results with different joint return period for New Orleans

	1000 years	100 years	50 years	10 years
Ws (m/s)	89.4	70.6	64.2	44.1
Wl (m)	7.6	4.11	3.35	2.04
Wd (h)	149	107	96	60

Table 6.4 Comparison of 100-year wind speed (m/s) for New Orleans (2005) and New Jersey zones (2012)

Methods	Liu et al. (2006)	Coles and Simiu (2003)	Casson and Coles (2000)	Georgiou et al. (1983)
100-year return value for zone 3 (New Orleans)	70.0	46.0	38.0	39.0
100-year return value for zone 9 (New Jersey)	60.0	40.0	36.0	35.0
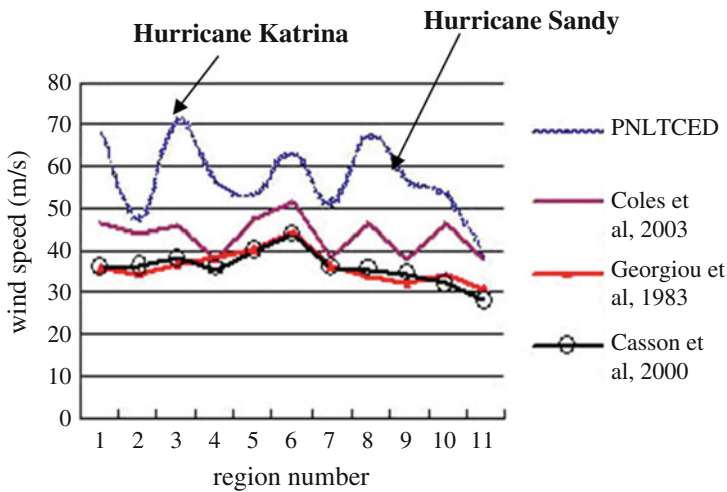
Fig. 6.8 Comparison of 100 years – hurricane wind speed using different methods over different regions (see Liu et al. 2009; Coles and Simiu 2003; Casson and Coles 2000; Georgiou et al. 1983, Fig. 6)

4 Corrections to SPH/PMH and API Recommendations Proposed by NOAA Based on Observed Wave Damage to Fixed Platforms by 2005 Hurricanes Katrina and Rita

In 2005, Hurricanes Katrina and Rita destroyed more than 110 platforms in the Gulf of Mexico (Fig. 6.9a). There were many platforms with reported wave-in-deck (WID) damage, attributed to the crest of the large hurricane wave hitting the platform decks and causing major damage. The catastrophic failures and damage of
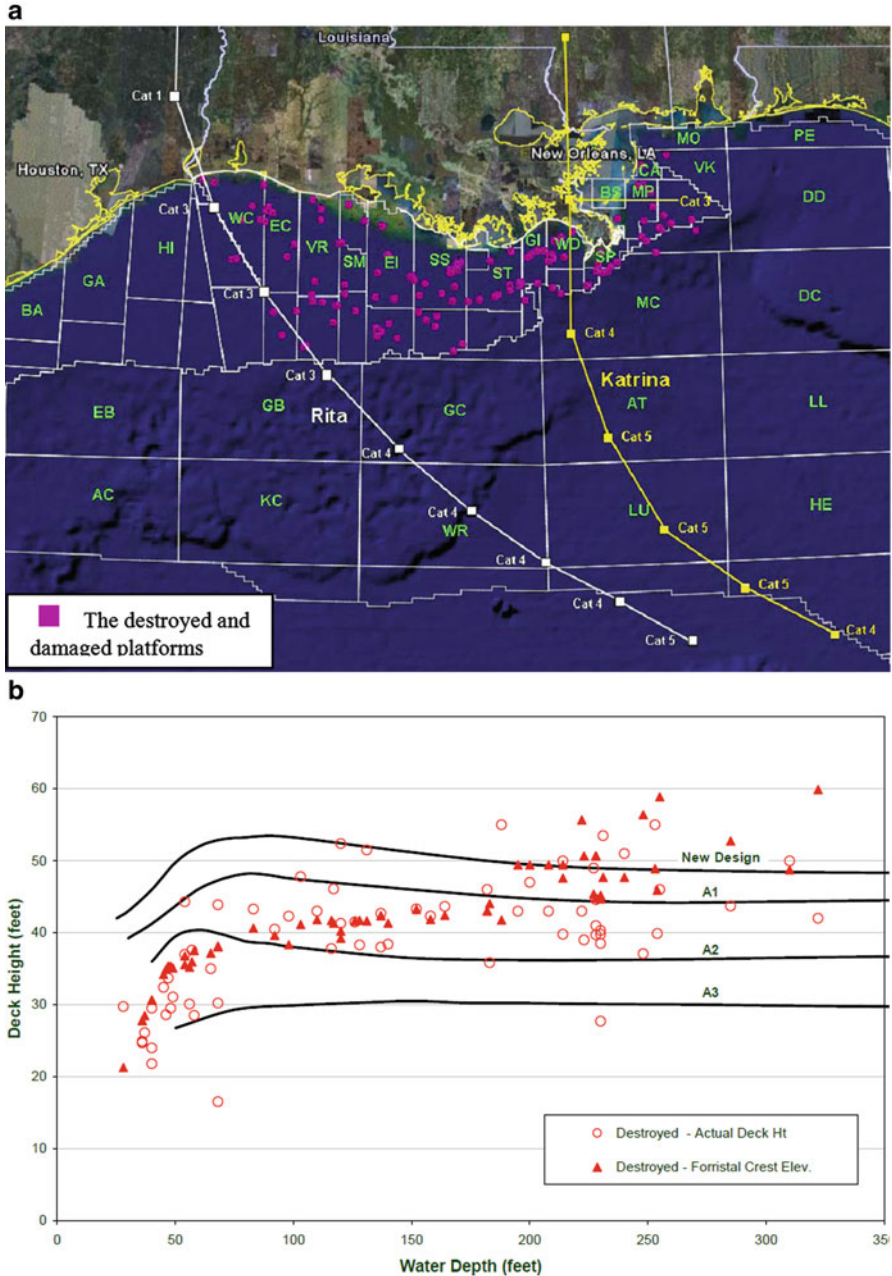
Fig. 6.9 (**a**) Hurricanes Katrina and Rita destroyed and damaged 110 platforms. (**b**) Platform deck height compared to predicted wave crest height, for A-1 (high consequence), A-2 (medium consequence), and A-3 (low consequence) API RP2A (2002) design deck height recommendations and the new design height proposed in the current study

platforms in GOM region show the deficiencies of API recommendations (American Petroleum Institute 2002, 2007; Det Norske Veritas 2002).

API RP2A (2002) categorizes platforms according to the consequence of failure, designated as A-1 for high consequence, A-2 for medium consequence, and A-3 as low consequence (American Petroleum Institute 2002). The report by Forristall shows a comparison of the deck elevation for the destroyed platforms (there were 76 cases where the deck elevation was available) at the location. The circles in Fig. 6.9b show the deck heights of individual platforms and the triangles show the wave crest heights predicted by Forristall. The curves A-1, A-2, and A-3 designate the deck heights recommended by API RP2A. For example, at a water depth of about 325 ft, the destroyed platform's deck height is about 42 ft and the wave crest height is about 60 ft. Thus, the wave crest height was almost 18 ft higher than platform deck clearance. It is then no surprise that the platform was destroyed (American Petroleum Institute 2002, 2007).

After Hurricanes Katrina and Rita, API issued Bulletin 2INT-DG, which provides procedures for using the hurricane conditions contained in BULL 2INT-MET for the associated type of platforms. API Bulletin 2DG updates specific recommendations for cellar deck elevation as the "new design" that accounts for a typical 5 m air gap above the 100-year wave crest and also an additional allowance of 15 % of the crest elevation to account for local wave effects (Energo Engineering 2007; Mittal 2005b).

Further, some of the primary causes of damage were wave, wind, and current forces greater than 100 years' conditions and foundations that were unable to support the fixed platform for the additional load level experienced from the increased metocean conditions beyond the industry-accepted standard for survival.

The SPH was the initial model used to determine how strong the hurricane protection system should be in order to protect the New Orleans, Louisiana, area from flooding due to hurricanes. The US Army Corps of Engineers began developing the model with the United States Weather Bureau (USWB). Subsequently, the USWB defined a probable maximum hurricane (PMH) as one that may be expected from the most severe combination of critical meteorological conditions that are "reasonably possible" for the region.

The original project designs of SPH were developed against the assumption that hurricane might strike the coastal Louisiana region once in 200–300 years. However, the standard was developed before the Saffir-Simpson hurricane scale came into use, and, in the SPH model, the features of the storm fit poorly with the scale. The model projected a storm roughly equivalent to a fast-moving Category 3 hurricane; other features more closely resemble a much more severe Category 4. In fact, Hurricane Katrina was a Category 5 hurricane before making landfall in Louisiana, and storm surge heights correlate better with pre-landfall wind speeds than wind speeds at landfall (Needham and Keim 2014).

In the design of a fixed platform, the topside structure should normally have adequate clearance above the design wave crest. Any topside structure of piping not

having adequate clearance would be affected by waves and current. The loss of the air gap and deck inundation has a large impact in reliability due to the following factors:

(a) Large increase in hydrodynamic loading
(b) Large increase in the uncertainty associated with hydrodynamic loading
(c) Potential increase in dynamic sensitivity

In order to provide adequate clearance to resist these large forces and overturning moments by waves, API (American Petroleum Institute 2002, 2007) gives some recommendations as follows:

(a) Omnidirectional guideline wave heights with a nominal return period of 100 years, together with the applicable wave theories and wave steepnesses, should be used to compute wave crest elevations above storm water level, including guideline storm tide.
(b) A safety margin, or air gap, of at least 5 ft should be added to the crest elevation to allow for platform settlement, water depth uncertainty, and the possibility of extreme waves in order to determine the minimum acceptable elevation of the bottom beam of the lowest deck to avoid waves striking the deck.

The predictions of the lowest deck height of the platforms by different designers may differ greatly for there is no clear definition of the "applicable wave theories" in the API recommendations. In addition, API just offers the reference standards of guideline storm tide in American sea regions by graphical interpretation; it cannot provide any reference value for platform design in other countries influenced by typhoons or hurricanes.

The definition of water level and deck height is shown in Fig. 6.10. The height of significant wave (Hs) is the average height of the highest one third of the waves in the record, and the crest height is the vertical distance from the top of the wave crest to the still water. LAT is the lowest astronomical tide. Still water level is the average water surface elevation at any instant, excluding local variation due to waves and wave setup, but including the effects of tides, storm surges, and long-period seiches. For other uncertain factors such as subsidence of the platform and sea bed, the present author gives 1.5 m recommended height in this study (Xie et al. 2010).

Therefore, Hs, storm surge, and tide are taken as variables in PNLTCED for calculation of the required deck height in this section.

Using PNLTCED, a single contour surface for wave, surge, and tide for a specified joint return period can be obtained. Because tide has its well-predicted law of motion, its periodical change is varied by other factors such as geographical influences. The astronomical tide height was taken as 2.45 m (19 years of return period) in the present paper, and then we obtain the combination of Hs, surge, and tide with 100-year return period (Fig. 6.10).

Different standards give different relations between the crest height, Hs, and maximum wave height (Hm). The ratio of crest height/Hm = 0.6 was adopted in the present paper (Xie et al. 2010). In the API standard, the relationship of Hs and

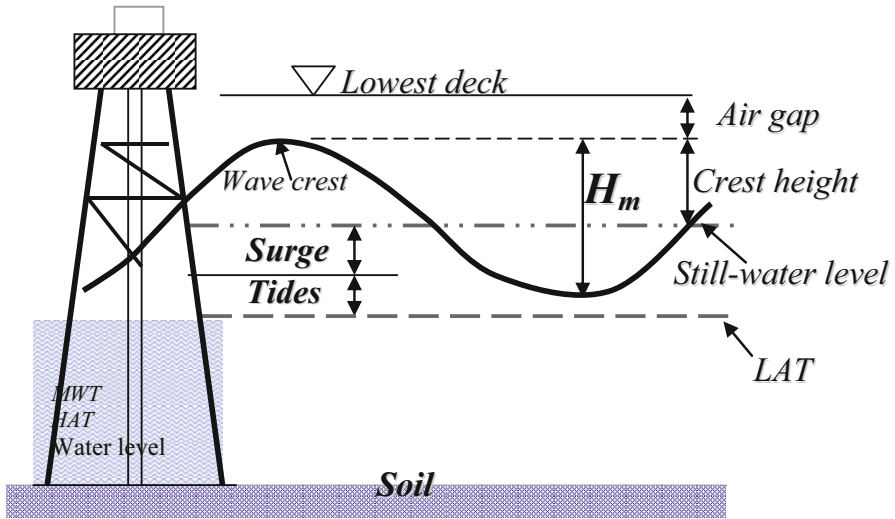**Fig. 6.10** The definition of water levels and the lowest deck height for marine platforms. *LAT* lowest astronomical tide

Table 6.5 H_s and concomitant surge samples of South China Sea (1979–1987)

Typhoon no.	H_s (m)	Surge (m)	Typhoon no.	H_s (m)	Surge (m)	Typhoon no.	H_s (m)	Surge (m)
197909[a]	4.6	0.46	198211	4.5	0.87	198508	3.2	0.24
197910	3.3	1.09	198219	3.4	0.29	198519	3.6	0.28
197915	3	0.21	198305	2.6	0.27	198607	2.1	0.35
197919	3.4	0.61	198310	3.3	0.58	198615	5.3	0.49
198001	2.1	0.18	198402	1.3	0.5	198617	2.5	0.39
198002	2.3	0.48	198403	1.6	0.15	198700	1.2	0.18
198003	5	0.26	198406	2	0.66	198701	1.5	0.26
198004	4.3	0.41	198407	2.5	0.19	198704	4.7	0.36
198101	4.5	0.93	198409	3.7	0.77	198705	2.2	0.17
198102	4.5	0.15	198504	2	0.19	198707	3.9	0.43
198209	2.2	0.52	198506	3.4	0.32	198711	2.8	0.69

[a]No. 9 typhoon in 1979

Hm is Hm/Hs = 1.7–1.9. According to the rules and regulations for the construction and classification of mobile offshore drilling rigs in China, Hm = min{2H$_{1/3}$, Hb}, where Hb is the critical wave height of breaking waves. In the South China Sea, water depth is 25.0 m, the sea bottom gradient is 1/300 (Xie et al. 2010).

A traditional addition method which defined the maximum level as the sum of MHWS (mean high water level spring tide), 100-year storm surge and 100-year crest height, was used to compare with the prediction by MCEVD. The comparison and calculated results were shown in Table 6.5 (1 and 2 in Table 6.6 are two combinations with 100-year return period) (Defu et al. 2015).

Table 6.6 Comparison of traditional method and MCEVD method

Traditional addition method	H_s (m)		Crest height with 100-year return period (m)	Surge with 100-year return period (m)	Tide and air gap (m)	Deck elevation above *LAT* (m)
	5.56		6.78	1.23		11.96
MCEVD method	Joint probability of 100-year return period				$2.45 + 1.5$	13.19
	H_s (m)		Crest height (m)	Surge (m)		12.91
	1.	5.95	7.26	1.98		
	2.	5.62	6.86	2.10		

Note that the tidal datum of deck elevation in this paper is different from the definition in API (Schwerdt et al. 1979). API adopted the mean lower low water (MLLW) which was only used in the USA. In order to extend its applicability and operability, LAT was used in the present paper (Defu et al. 2015), and the most severe combination of the surges, tides, and crests can be obtained by MCEVD.

This example shows results for 33 typhoons in the East China Sea and selects the significant wave height (Hs), concomitant surge, and corresponding tide of each process as samples (Table 6.6).

5 2013 Typhoon Fitow Validation of 2006 MCEVD Predicted Disaster in Shanghai City

Shanghai City is located in the estuarine area of Yangtze River in China. Historical observed data shows that the typhoon-induced storm surges and rainstorm flood, coupled with the astronomical spring tide, had threatened the security of Shanghai. Based on the long-term (1970–2005) typhoon characteristics around Shanghai area (Table 6.7), the double-layer-nested multi-objective probability model (Liu 1982) was used to predict combined effect of storm surge, rainstorm flood, and spring tide on Shanghai City (Liu et al. 2009; Defu et al. 2013).

In 2013, Typhoon Fitow induced significant losses in China. As shown in Table 6.8, the water level induced by 2013 Typhoon Fitow in Yangtze River was 5.15 m, but the recommended 500 years of return period warning water level calculated by the China design code was 4.80 m in this area, which only corresponds to the 50-year return value predicted by MCEVD.

Table 6.7 Marginal distribution of typhoon characteristics for Shanghai

Typhoon characters	Distribution type	Mean value	Standard deviation	Distribution parameters
λ	Poisson			$\lambda = 1.76$
ΔP (hPa)	Gumbel	21.89	14.96	$a = 0.073$, $b = 14.45$
R_{max} (km)	Lognormal	45.79	25.22	$\mu = 3.71$, $\sigma = 0.5$
s (m/s)	Gumbel	30.19	15.95	$a = 0.07$, $b = 22.4$
δ (km)	Uniform	44.37	169.63	$a = -294.57$, $b = 333.84$
θ (°)	Normal	15	37.36	$\mu = 15$, $\sigma = 37.36$

Table 6.8 Comparison between disaster prevention design criteria for Shanghai City

Model	Return period (a)	Design value (m)
MCEVD	100	5.89
	50	5.10
China design code	1000	5.86
Shanghai warning water level[a]	500	4.80
Typhoon Fitow observed water level		5.15

[a]Calculated by China Design Code

6 Risk Assessment for Nuclear Power Plant (NPP) Against Sea Hazards

6.1 Joint Probability Safety Assessment for NPP Coastal Defense Infrastructure Against Typhoon Disaster in the South China Sea

MCEVD can be used for joint probability safety assessment for NPP coastal defense along China coast against typhoon attacks (Harris 1963; Defu et al. 2013). Nuclear power plant L is located at the coast of the South China Sea, where the combined extreme external events are dominated by waves. Based on the China and IAEA safety regulations, the L-NPP calculated design water level is shown in Table 6.9.

The predicted results of storm surge, wave height, and spring tide with different joint return periods by MCEVD are shown in Table 6.10.

It can be seen from Table 6.9 that the MCEVD predicted 500-year return values of storm surge, spring tide (4.2 + 2.8 = 6.9 m), and wave height (7.9 m) should be

Table 6.9 Present design criteria for coastal defense of L-NPP

Design water level	Design value (m)
DBF	6.35
PMSS	5.30
Extreme wave height	6.6
Design low water level	−1.93

Harris (1963) and Liu et al. (2013)

Table 6.10 Joint probability of storm surge, wave height, and corresponding spring tide for L-NPP

Return period (year)	100	500	1000
Storm surge (m)	3.3	4.2	4.7
Spring tide (m)	2.4	2.7	3.2
Wave height (m)	6.9	7.9	8.7

more severe than DBF (6.35 m) with 100-year return period wave height (6.6 m), rather than the IAEA-recommended 10,000 years of return values (Defu et al. 2015).

6.2 Joint Probability Safety Assessment for QS NPP Defense Infrastructure in Qiantang River Estuarine Area, East China Sea

The combination of typhoon-induced storm surge with the strongest spring tide in the Qiantang River estuarine always leads to disasters. The observed maximum surge and spring tide is more than 9 m. The QS NPP is located on the south coast of the estuarine Qiantang River and faces to the East China Sea, where the highest severe spring tide in China always occurs.

The height of the constructed breakwater is 9.76 m. So the joint probability safety assessment of combined extreme external events for coastal defense infrastructure dominated by spring tide should be taken into account.

As the severest extreme external events for QS NPP are the combined effect of spring tide and surge, a two-dimensional joint probability model can be used to calculate the corresponding joint probability density function and cumulative distribution function (Fig. 6.11a, b). The joint probability distribution of spring tide, storm surge, and corresponding extreme wave with 1000-year joint return period can be seen in Fig. 6.12.

Risk assessment for NPP coastal defense is based on the as low as reasonably practicable (ALARP) principle (Fig. 6.13). Joint probability risk assessment for the abovementioned two constructed nuclear power plants shows that the coastal defense infrastructure of both NPPs cannot satisfy the 10^{-3} combined extreme external events risk according to the ALARP principle (Det Norske Veritas 2002). This means that the risk to constructed infrastructure is unacceptable.
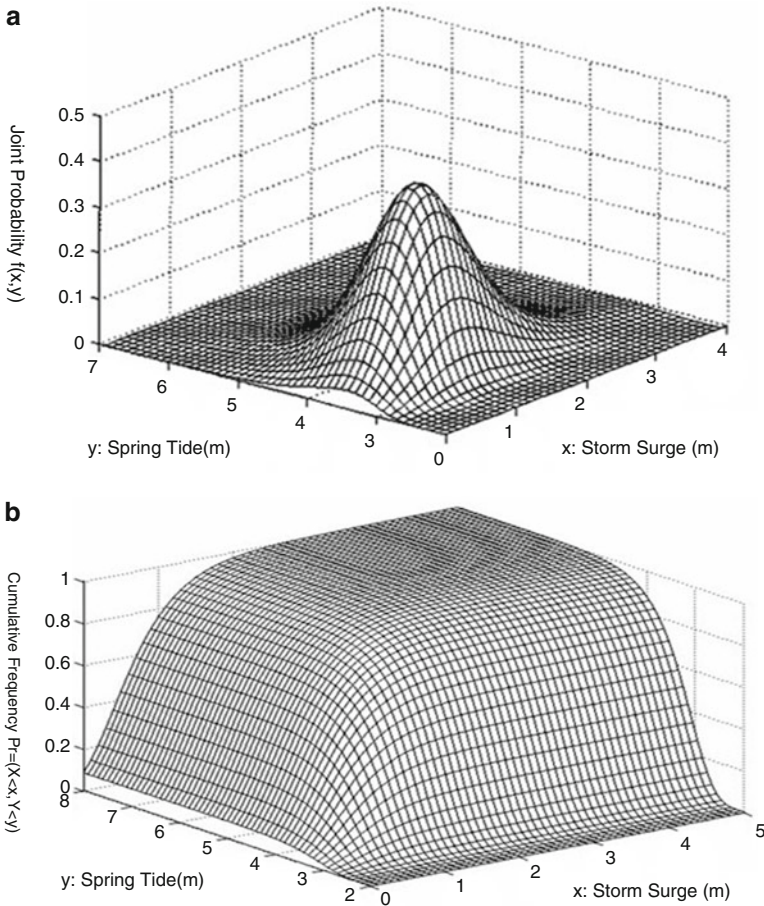
Fig. 6.11 (**a**) Probability density distribution of spring tide and storm surge for the QS NPP. (**b**) The same as (**a**) for the cumulative probability distribution of spring tide and storm surge

The joint probability safety assessment for NPP coastal defense infrastructure against extreme external hazards shows that the China and IAEA recommended safety regulations appear to have some vague definitions and different kinds of uncertainties. Both of the two constructed NPPs are located along the South China Sea and the East China Sea where the dominant external events are wave and spring tide, and the China and IAEA recommended safety regulations are much lower than 1000-year return period typhoon-induced sea hazards predicted by DLNMPM (Table 6.11).
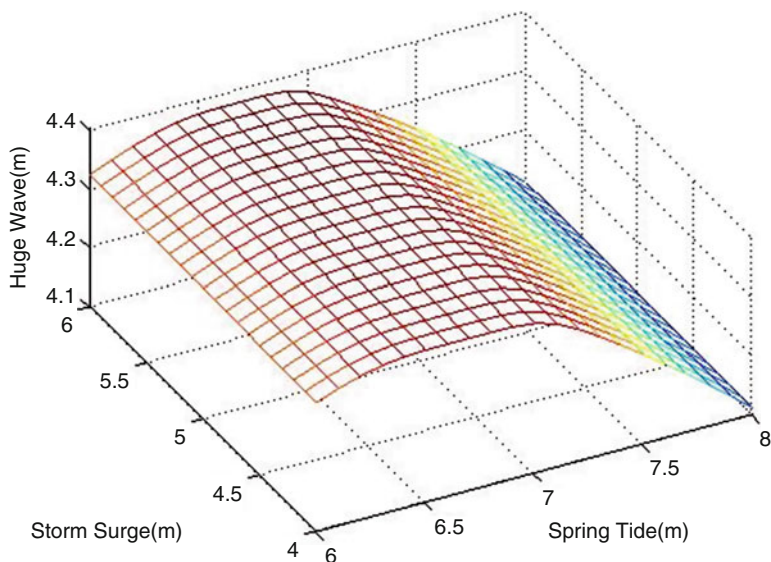
Fig. 6.12 Joint probability distribution of spring tide, storm surge, and extreme wave with 1000-year joint return period for the QS NPP
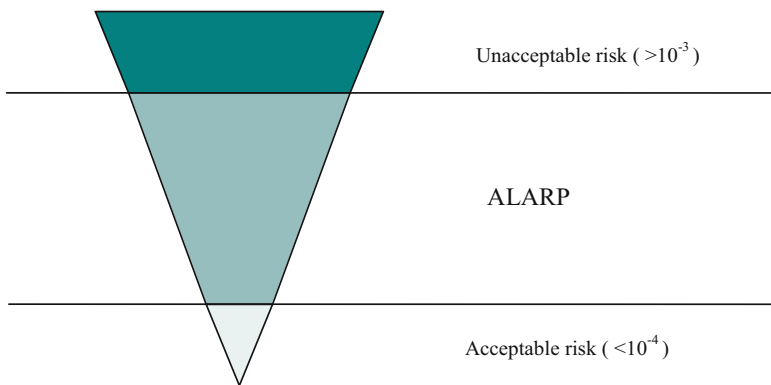
Fig. 6.13 Schematic diagram illustrating the "as low as reasonably practicable (*ALARP*)" concept, by Det Norske Veritas (Liu et al. 2012)

Table 6.11 Combined extreme external events with joint return period for QS NPP by PNLTCED

	Extreme event		
Joint probability	Spring tide (m)	Surge (m)	Wave (m)
100	4.2	3.0	2.5
500	5.0	3.5	3.0
1000	5.5	4.0	3.5
10,000	6.5	4.8	4.0

7   Conclusion

With the increasing tendency of the frequency of natural hazards and their intensity, from 1949 to 2014, during the past 55 years, vast coastal and hydrological disaster prevention levees and floodwalls have collapsed and led to more than 310,900 deaths and a severe economic loss in China. The first and second costliest hurricane disasters in the US history occurred only in an interval of 7 years. Extreme typhoon/hurricane hazards menaced some important construction engineering projects designed by traditional codes. For example, 2006 Typhoon Saomai induced a 3.76 m surge and 7 m waves, causing 240 deaths, sinking 952 ships, and damaging 1594 others in Shacheng Harbor. If the typhoon had landed 2 h later, then the simultaneous occurrence of the typhoon surge of 3.76 m and high spring tide of 3 m with a 7 m wave would have been close to the MCEVD predicted 500-year joint return period of 7.3 m wave, 3.5 m surge with simultaneous 3.0 spring tide, which is much over the height of the constructed 9.76 m breakwater for the nuclear power plant in this coastal area.

We hope that lessons from Hurricanes Katrina and Sandy and Typhoon Fitow are taken into account for NPP safety organizations in China and IAEA.

References

American Petroleum Institute (2007) API 2INT-MET: interim guidance on hurricane conditions in Gulf of Mexico. International Hurricane Research Center, Washington, DC

American Petroleum Institute (2002) API recommended practice 2A-WSD planning, designing, and constructing fixed offshore platforms – working stress design, 21st edn. API, Washington, DC

Bea R (2007) Reliability assessment and management lessons from hurricane Katrina. In: ASME 2007 26th International Conference on Offshore Mechanics and Arctic Engineering. American Society of Mechanical Engineers. pp 467–478

Blake ES, Gibney EJ (2011) The deadliest, costliest, and most intense United States tropical cyclones from 1851 to 2010 (and other frequently requested hurricane facts). National Weather Service, National Hurricane Center, Miami

Casson E, Coles S (2000) Simulation and extremal analysis of hurricane events. Appl Stat 49: 227–245

China Code for Sea Port Hydrology (2013) GTS 145-2-2013

China Ministry of Transportation (1986) Design wave criteria based on the short term observed data for Nouakchott port, Mauritania. China Ministry of Transportation, Beijing, China

Chowdhury AG, Huang E, Erwin J (2009) Novel full-scale wind-structure interaction experimentation for mitigating hurricane-induced coastal disasters. Far East J Ocean Res 2:1–27

Coles S, Simiu E (2003) Estimating uncertainty in the extreme value analysis of data generated by a hurricane simulation model. J Eng Mech 129:1288–1294

Defu L, Hongda S, Liang P (2006) Disaster prevention design criteria for the estuarine cities: New Orleans and Shanghai the lesson from Hurricane Katrina. Acta Oceanol Sin 25:131–142

Defu L, Hongda S, Guilin L, Fengqing W (2015) Risk assessment for nuclear power plants against natural disasters: probability prediction and disaster prevention infrastructures. Nova Science Publishers, New York

Det Norske Veritas (2002) DNV-OS-c201, structure design of offshore units (WESD method). Det Norske Veritas, Oslo

Energo Engineering (2007) Assessment of fixed offshore platform performance in hurricanes Katrina and Rita. US Department of the Interior, Mineral Management Service, Houston

Georgiou PN, Davenport AG, Vickery BJ (1983) Design wind speeds in regions dominated by tropical cyclones. J Wind Eng Ind Aerodyn 13:139–152

Gray WM (2003) Twentieth century challenges and milestones. In: Simpson R, Anthes R, Garstang M, Simpson J (eds) Hurricane! Coping with disaster: progress and challenges since Galveston, 1900. American Geophysical Union, Washington, DC, pp 3–37

Harris DL (1963) Characteristics of the hurricane storm surge. Department of Commerce, Weather Bureau, Washington, DC

Kirby WH, Moss ME (1987) Summary of flood-frequency analysis in the United States. J Hydrol 96:5–14

KORDI (2004) Prediction of extreme sea hazards around South Korean Sea. Korean Ocean Research and Development Institute, Seoul, Korea

Liu T (1982) Long-term distribution of hurricane characteristics. In: Offshore Technology Conference. Offshore Technology Conference

Liu DF, Li HJ, Wen SQ et al (2001) Prediction of extreme significant wave height from daily maxima. China Ocean Eng 15:97–106

Liu D, Pang L, Fu G et al (2006) Joint probability analysis of hurricane Katrina 2005. In: The Sixteenth International Offshore and Polar Engineering Conference. International Society of Offshore and Polar Engineers

Liu Y, Santos A, Wang SM et al (2007) Tsunami hazards along Chinese coast from potential earthquakes in south China Sea. Phys Earth Planet Inter 163:233–244

Liu D, Pang L, Xie B, Wu Y (2008) Typhoon disaster zoning and prevention criteria – a double layer nested multi-objective probability model and its application. Sci China Ser E: Technol Sci 51:1038–1048

Liu D, Pang L, Xie B (2009) Typhoon disaster in China: prediction, prevention, and mitigation. Nat Hazards 49:421–436

Liu DF, Li HJ, Liu GL, Wang FQ (2011a) Design code calibration of offshore, coastal and hydraulic energy development infrastructures. World Sci Eng Acad Soc (WSEAS) Int J Energy Environ 5:733–747

Liu DF, Liu GL, Li HJ, Wang FG (2011b) Risk assessment of coastal defense against typhoon attacks for nuclear power plant in China. In: Proceedings of ICAPP. pp 2484–2492

Liu D-F, Xie B-T, Li H-J (2011c) Design flood volume of the three gorges dam project. J Hydrol Eng 16:71–80

Liu G, Li H, Liu D et al (2012) Discussion on IAEA and China safety regulation for NPP coastal defense infrastructures against typhoon/hurricane attacks. World J Nucl Sci Tech 2:114–123. doi:10.4236/wjnst.2012.23017

Liu DF, Li HJ, Liu GL, Shi HD, Wang FQ (2013) Typhoon/Hurricane/Tropical Cyclone disasters: prediction, prevention and mitigation. In: Natural disasters: prevention, risk factors and management. NOVA Science Publishers Press, USA, pp 1–72

McTaggart-Cowan R, Deane GD, Bosart LF et al (2008) Climatology of tropical cyclogenesis in the north Atlantic (1948–2004). Mon Weather Rev 136:1284–1304

Mittal A (2005a) History of the Lake Pontchartrain and vicinity hurricane protection project. US Government Accountability Office, Washington, DC

Mittal AK (2005b) Lake pontchartrain and vicinity hurricane protection project

Muir LR, El-Shaarawi AH (1986) On the calculation of extreme wave heights: a review. Ocean Eng 13:93–118

Nafaa MG, Fanos AM, Elganainy MA (1991) Characteristics of waves off the Mediterranean coast of Egypt. J Coast Res 7:665–676

Needham HF, Keim BD (2014) Correlating storm surge heights with tropical cyclone winds at and before landfall. Earth Interact 18:1–26

Norwegian Det Norsk Company (1988) Extreme sea state prediction in North Sea. Norwegian Det Norsk Company, Trondheim, Norway

Ochi MK (1982) Stochastic analysis and probabilistic prediction of random seas. Adv Hydrosci 13:217–375

Quek S-T, Cheong H-F (1992) Prediction of extreme 3-sec. gusts accounting for seasonal effects. Struct Saf 11:121–129

Resio DT et al (2007). White paper on estimation Hurricane Inundation probabilities. U. S. Army Corps of Engineering Report, pp 1–10

Schwerdt RW, Ho FP, Watkins RR (1979) Meteorological criteria for standard project hurricane and probable maximum hurricane windfields, Gulf and East Coasts of the United States

Wikipedia (2016) Hurricane Sandy. Wikipedia, the free encyclopedia

Xie BT, Liu DF, Li HJ, Gong C (2010) Design code calibration of offshore platform against typhoon/hurricane attacks. China Ocean Eng 24(3):431–442

Chapter 7
The Use of Global Climate Models for Tropical Cyclone Risk Assessment

Alison Cobb and James Done

Abstract As tropical cyclones (TCs) make landfall in increasingly populated regions, the costs rise and are likely to continue rising in the future. The likely scenario of the TCs themselves changing in the future together with rising seas due to climate change will compound the problem. TC risk assessment needs to undergo a step change for society to properly confront this new era of TC risk. Next-generation global climate models (GCMs) are poised to bring about this change, and this chapter explores the potential role of GCMs in TC risk assessment. Long-term global climate model simulations are beginning to capture key TC characteristics that cause damage, thereby bringing a wealth of new risk-related information that presents a potentially powerful transformation of TC risk assessment. These physically based datasets will support better understanding of TC activity on longer timescales, exploration of events outside the range of the historical record, quantification of clustering, and discovery of teleconnected risks across TC basins. The integration of GCMs with risk assessment is a rapidly developing field, yet still in an exploratory phase, and a number of barriers need to be overcome including treatment of model error and understanding how to effectively integrate GCM information with risk assessment.

A. Cobb (✉)
Imperial College London, London, UK
e-mail: a.cobb15@imperial.ac.uk

J. Done
National Center for Atmospheric Research, Boulder, CO 80304, USA
e-mail: done@ucar.edu

1 Introduction

Tropical cyclones (TCs) are the largest contributor to weather and climate impacts in the USA (Smith and Katz 2013), driving 41 % of the inflation-adjusted US insured loss from 1995 to 2014. Annual TC losses are highly volatile: the 2004–2005 US hurricane seasons caused in excess of $150 billion in damages (Pielke Jr. et al. 2008), a significant increase from the annual average normalized damage of $10 billion. Most damage occurs when TCs make landfall, impacting all major societal infrastructure systems (transportation, communication, water supply, energy, sanitation) in addition to the potential for immediate loss of life and property.

It is not only the TC wind field but also heavy precipitation that drives damage. Subtropical storm Allison in 2001, for example, brought 940 mm of rain to the port of Houston, Texas (Beven et al. 2003), despite not reaching hurricane status and remains one of the deadliest and costliest subtropical storms to impact the USA. Storm surge also exacts a heavy toll, such as the heavy surge damage to New York, New Jersey, and Connecticut in 2012 brought by Hurricane Sandy (Blake et al. 2013). TCs can also cause significant damage while at sea, mainly to the offshore industry, where loading on offshore structures is a complex function of the wind field, ocean current, and ocean waves (Done et al. 2015). In addition to population and infrastructure impacts, TCs can have major impacts on the natural environment, including causing declines in fisheries and wildlife populations (Sheikh 2005). Hurricane Wilma, for example, resulted in drastic structural changes to the ecosystem in Lake Okeechobee, South Florida (Xuan and Chang 2014), the second largest freshwater lake in the USA.

Society is entering a new era of catastrophes in which TCs are causing more damage than in the past (Kunreuther and Michel-Kerjan 2009). Quantified economic losses have seen steep rises in recent years (Smith and Katz 2013; Weinkle et al. 2012; Pielke Jr et al. 2008), largely due to significant increase in exposure (Weinkle et al. 2012; Höppe and Pielke 2006; Stewart et al. 2003). The US population grew by 125 million from 1960 to 2008, with the coastal population increasing by 84 % (Lloyd's 2011), totaling more than $1.1 trillion in property exposure within storm-surge risk zones (King 2013). The trend in the losses (Fig. 7.1) indicates an approximate doubling of economic and insured losses every 15 years. Noneconomic sociocultural impacts have seen similar rises (Adger et al. 2013). Evidence that the TCs themselves have changed in recent decades (Holland and Bruyère 2014) together with sea-level rise (Solomon et al. 2007) has likely compounded the problem. For risk assessment to be a useful tool that can help society properly confront this new era of increasing TC risk, it must undergo a step change in its ability to simulate TCs; account for changes in exposure, sea level, hazard, and vulnerability; and better communicate the risk assessment results and the potential actions that could reduce risk.

Increases in risk are likely to continue in the future as populations continue to increase and migrate to vulnerable coastal regions. The likely scenario of the TCs themselves changing in the future due to climate change will compound the problem

Overall and insured losses 1980 to 2015 (in US$ bn)
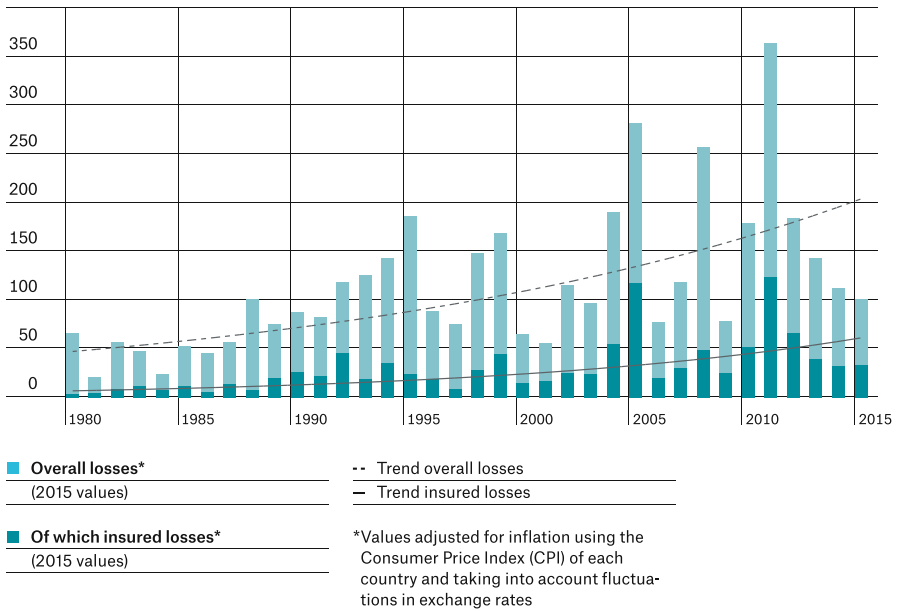
Source: Munich Re NatCatSERVICE

Fig. 7.1 Annual overall and insured losses (in US$ bn) 1980–2015 (Source: Topics GEO – Natural Catastrophes 2015 (Munich Re 2016))

(IPCC 2012; Walsh et al. 2016). TC potential intensity is directly related to the sea surface temperature (SST, Emanuel 1991; Holland 1997; Knutson et al. 2010) with a climate sensitivity of TC maximum wind speed of 5 % per degree Kelvin rise. It appears that the dominant effect of increasing carbon dioxide is increasing upper ocean temperatures (Zhao et al. 2013), with the 0–700 m layer experiencing 64 % of the total ocean warming to date (Rhein et al. 2013). The long-term impact of recent and future predicted increases in SSTs on the TC climate is hotly debated (e.g., Villarini and Vecchi 2012a, b; Bender et al. 2010; Emanuel et al. 2008; Holland and Webster 2007). However, there is general consensus on an increase in the incidence of high-intensity TCs (Murakami et al. 2012; Hill and Lackmann 2011; Elsner et al. 2008). There is less confidence on future changes in the frequency of weak to moderate intensity TCs.

In addition to changes to TC intensity, other important changes are anticipated. Maximum wind speeds have migrated poleward over the past decades and will continue to do so in a warming climate (Kossin et al. 2014), exposing new regions to TC impacts. There is also an indication that TCs may extend farther inland in the future (Vecchi, personal communication) and a substantial future increase in TC rainfall (Villarini et al. 2014). Compounding these expected changes in the TCs

themselves is rising sea level, and the rate of rise is perhaps accelerating (Church et al. 2013; IPCC 2012). There is less confidence in changes to TC tracks, TC size, and the incidence of extratropical transitioning storms (Emanuel, personal communication; Walsh et al. 2016).

These changes could lead to more damaging events in the future (Morss et al. 2011) and the possibility of high-impact events outside the range of our experience that would render traditional risk assessment practice ineffective (Milly et al. 2008). Indeed, studies point to future increases in TC-related insurance losses (Mendelsohn et al. 2012; Raible et al. 2012; Schmidt et al. 2010), largely driven by increased value and amounts of exposed coastal property. Mendelsohn et al. (2012) found that future increases in income are likely to more than double TC losses even without climate change, from US $26 billion per year to $53 billion by 2100, concentrated in North America, East Asia, and Central America-Caribbean. The recent rise and projected increases in TC losses further drive the need for risk assessment, risk communication, and accounting for changes in exposure, sea level, hazard, and vulnerability to undergo a step change to enable society to manage this increasing risk.

Next-generation global climate models (GCMs) are poised to bring about this change. Decades of government investment have supported the development of leading physical and dynamical representations of the climate system that provide a wealth of new information on key damaging parameters and present an opportunity to transform TC risk assessment by including climate physics.

GCMs are based on a set of equations of motion, thermodynamics, and radiative transfer and are the primary tools for developing a theory of climate and climate change. The atmosphere and ocean are broken down into a three-dimensional grid, over which the equations are calculated. The size of the grid boxes determines the resolution or scale that can be captured. As resolution increases, the realism of physical processes is enhanced, yet resolution is restricted by computational power; doubling resolution requires approximately ten times as much computing power. Other demands on computational power include the complexity of the representation of fine-scale physical processes such as radiation, rainfall and convection; the simulation length; and the number of simulations. However, novel approaches to focus detail in a region of interest while retaining a global grid (Slingo et al. 2009; Weller et al. 2010; see Chap. 8 for a full discussion) have shown success in simulating TC climate (Hashimoto et al. 2015; Zarzycki and Jablonowski 2015).

GCMs have the potential to transform risk assessment practice, yet a number of barriers need to be overcome. Some are exploring the use of TC climate information from GCMs in long-range planning fields such as water resources, infrastructure design, and catastrophe finance, but the use of GCM information is in its infancy. The full value of GCMs has yet to be realized, but presents an opportunity to align developing climate science with climate risk assessment to create potentially transformative strategies for reducing losses from future TCs.

The aim of this chapter is to explore the potential role of next-generation GCMs in TC risk assessment and is framed toward risk practitioners interested in understanding the potential role of GCMs in risk assessment and to physical

scientists interested in exploring TC risk problems. The information needed for TC risk assessment is established first in Sect. 2, together with an overview of current practice for risk assessment. Section 3 outlines the potential role of GCMs for TC risk assessment, starting with an overview of the TC climate information currently produced by GCMs, moving to an overview of the current use of GCMs in the risk arena, and ends by identifying the future potential role of next-generation GCMs for TC risk assessment. A summary is presented in Sect. 4.

2 Current Practice in TC Risk Assessment

Accurate assessments of TC risk are necessary for well-informed risk management. This includes planning future infrastructure and developing sound, informed policy. An enabling tool to identify and quantify risk is the catastrophe (CAT) model. CAT models are fundamental to risk management (Grossi et al. 2005) and were developed to address the need for more precise risk information. Public planners, disaster managers, and the insurance and reinsurance industries are increasingly reliant on CAT models. This increasingly diverse group of users is driving the need for the development of CAT models that are flexibly adaptable to inform emergency management, risk pricing, risk transfer structuring, insurer capital adequacy, and in assessing the financial strength of insurers and catastrophe bonds.

The four main components of a CAT model are hazard, exposure, vulnerability, and loss, as depicted in Fig. 7.2. First, the hazard phenomenon is defined (in our
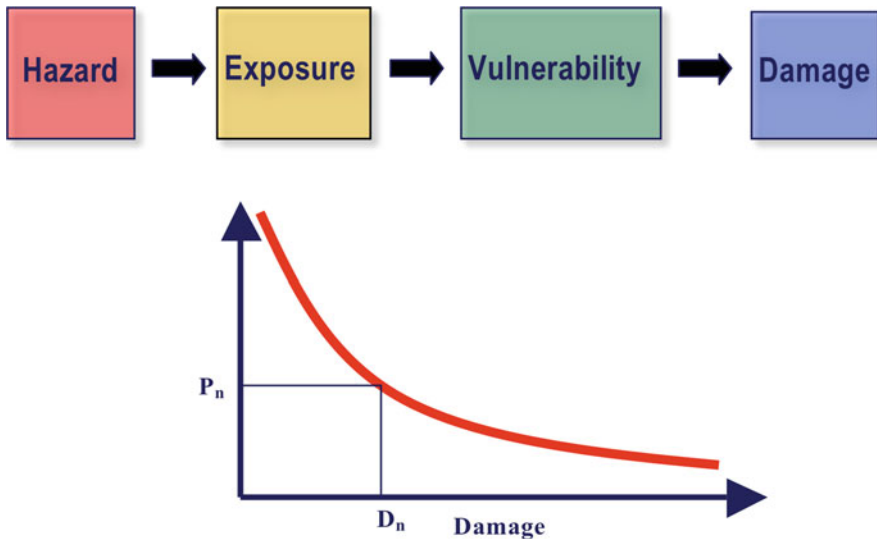
Fig. 7.2 (*Top*) Components of a catastrophe model. (*Bottom*) Schematic exceedance probability (EP) *curve*, showing the exceedance of loss amount Dn in a given time period given by probability Pn

case, a TC) and a hazard event set is generated. Each hazard event is defined by a specific magnitude and location and is assigned a probability of occurrence. Second, the exposure or infrastructure at risk is characterized using construction and occupancy types, building height, age, and design codes and assigned a geographic location. Third, the vulnerability or damage susceptibility of the exposure (World Bank 2014) is quantified, based on physical relationships between a characteristic or combination of characteristics of the hazard and damage. Finally, the expected loss is calculated, based on direct losses including the cost to repair and/or replace a structure and indirect losses including business interruption and relocation costs. Together, the hazard event set, exposure, and vulnerability components yield a probabilistic risk analysis. This probabilistic approach to catastrophe loss analysis is the most appropriate way to handle the abundant sources of uncertainty inherent to the hazard, exposure, and vulnerability components. CAT model output is quantified and presented in a way that is useful to the diverse range of stakeholders (often presented as an exceedance probability curve depicted in Fig. 7.2) Grossi et al. (2005).

A potential role for GCMs in TC risk assessment, as detailed in Sect. 3, would therefore be to inform the hazard component of a TC CAT model. The hazard component of hurricane loss models are computationally inexpensive to run, thereby allowing for the generation of a hazard event set large enough to develop robust statistics. The hazard event set is typically derived from a synthetic TC track database (e.g., Hall and Sobel 2013; Arthur et al. 2008; Hall and Jewson 2007; Rumpf et al. 2007; Vickery et al. 2000a). Tens of thousands of synthetic tracks are generated through repeated random sampling of local and regional historical TC parameters, such as track location, forward speed and heading, maximum wind speed, and rate of change of wind speed. Spatial wind fields, known as the wind footprints, are constructed along the synthetic tracks using simple parametric wind field models (e.g., Wang et al. 2015; Holland et al. 2010; Willoughby et al. 2006; Vickery et al. 2000b). These models are lacking in an important way for loss prediction. The Holland et al. (2010) wind field model goes some way to include major asymmetries and smaller-scale structural details such as double eye-walls, yet crucially these models behave particularly poorly at landfall. Hurricane wind fields change drastically when they make landfall, involving a complex interaction with the system and the underlying surface (Zhu 2008), yet it's common to use a simple wind speed decay function (Kaplan and DeMaria 1995). Attempts have been made to combine simple wind field models with dynamical atmospheric models of varying complexity (Vickery et al. 2009; Khare et al. 2009) to capture these complex surface effects.

Some models also capture changes in the storm wind field due to extratropical transition (Loridan et al. 2015). Storm surge is sometimes included using the synthetic storm footprints to drive a surge model (Lin et al. 2012), thereby creating coastal flood footprints. Rainfall is also sometimes included (e.g., Grieser and Jewson 2012) based on historical rainfall statistics (Lonfat et al. 2007) or physical principles (Langousis and Veneziano 2009). Hazard models vary widely in their

level of complexity, and differences among the resulting risk assessments are large, common, and critically dependent on model assumptions.

When CAT models were first used in the early 1990s, they revolutionized the way society understands and manages risk. However, despite their increasing level of sophistication, TC CAT models are deficient in a number of important ways. Traditional hazard modeling has relied on sampling from probability distributions fitted to historical TC data. The historic record of TC activity is the longest for the North Atlantic, where records start in 1851, yet the limitations of historical observations are well known, including undercounting in the pre-satellite era and intensity errors throughout (Vecchi and Knutson 2008; Landsea 2007).

Use of an historical archive as a base dataset has the following significant limitations:

- Possible artificial trends due to changes in data collection methods and unknown errors.
- The assumption of stationarity and not accounting for how risk may have changed in the past or how it may change in the future (Stewart et al. 2003). The impacts of recent climate variations and apparent shifts in TC climate (Holland and Webster (2007) and the resulting losses revealed deficiencies in the current state of CAT modeling.
- Unresolved temporal variability and trends by the short archive lengths. Estimates of hurricane wind risk based directly on the historical record suffer from the overall scarcity of events, particularly in regions that experience infrequent but sometimes devastating storms.
- Lack of information on critical hazard parameters that relate to loss such as TC size.
- Assumption of independence between perils and the occurrences of a peril.

Risk managers increasingly require predictive hazard information to enable appropriate planning and adaptation to the risk of today and tomorrow. Commonly missing risk-relevant processes include clustering of events in time and space (where occurrence rates are higher than expected by chance), inter-basin correlations of TC activity, information on events outside our historical experience, and on the relative importance of modes of climate variability. Many of these knowledge gaps may be met through inclusion of physical climate science to inform risk assessment. GCMs are one enabling tool (Shackley et al. 1998) to connect the needed information with developing climate science, as described in the next chapter.

3   The Role of Global Climate Models

This section outlines the role of GCMs for TC risk assessment, starting with an overview of the TC climate information currently produced by GCMs. An overview of the current use of GCMs in the risk arena follows and ends by identifying the future role of next-generation GCMs for TC risk assessment.

3.1 GCM-Simulated TC Climate

This subsection summarizes the capacity of GCMs to simulate the key damaging TC parameters, while Chap. 8 presents a more comprehensive overview of GCM-simulated TC climates in general.

GCMs with grid sizes in the range 20–100 km commonly perform well in capturing the geographic distribution of TCs, their frequencies, inter-basin differences and correlations, and interannual variability (e.g., Strachan et al. 2013; Zhao et al. 2009), but exhibit significant model sensitivity (Shaevitz et al. 2014; Zhao et al. 2013) even when used to reanalyze TCs in historical climate (Cobb et al. in preparation). At these grid sizes, however, details of TC wind fields are not captured (McDonald et al. 2005). Gentry and Lackmann (2010) found a grid size on the order of 1 km is needed to represent structural details of TCs and peak wind speeds.

Recent GCMs have been run using grid spacings of 10–25 km, at which many key damaging TC parameters start to become resolved (e.g., Shaevitz et al. 2014; Bacmeister et al. 2016). In particular, peak wind speeds are improved, yet there remains a need for bias correction (e.g., Tye et al. 2014). However, it's not only peak wind speed that drives damage. Recent work demonstrated the importance of TC size in driving losses (Zhai and Jiang 2014; Czajkowski and Done 2014), and Holland et al. (2016) recognized the importance of forward speed (and therefore duration of winds) for loss. GCMs are beginning to provide information on such details as the area of the damaging winds and forward speed that combined control the duration of damaging winds. GCMs can also quantify and elucidate the physical mechanisms of TC clustering (Jagger and Elsner 2012; Mumby et al. 2011; Camargo et al. 2007), and TC rainfall (Villarini et al. 2014). However, rainfall distribution and intensity result from complex processes and depend on multi-scale interactions, including track, intensity, topography, and environmental vertical shear. As a result, caution should be exercised in the direct use of rainfall from GCMs. Details that remain out of reach in current GCMs are eye-wall replacement cycles, rapid intensification, and TC-related tornadoes. Such detail can be obtained through statistical and dynamical downscaling, but are not discussed further here.

GCMs also bring benefits owing to their globally connected simulation system such as the physical connections between TC basins and other teleconnected risks, the occurrence and geographic locations of extratropical transitioning storms, the connections between basin and landfall activity, and the potential for upscaling of small-scale processes onto the large-scale climate (Schenkel and Hart 2015).

GCMs also provide a rich dataset to better understand TC activity on longer timescales, as it is influenced by climate change (as discussed in Sect. 1) and climate modes of variability such as the Indian Ocean Dipole (Saji et al. 1999), the Pacific Decadal Oscillation (Goh and Chan 2010), the Atlantic Multidecadal Oscillation (AMO, Wang et al. 2008), and the Atlantic Meridional Mode (Vimont and Kossin 2007). Such modes of variability have also been shown to control landfall occurrence (Villarini et al. 2012; Bove et al. 1998). Indeed, Elsner and

Bossak ([2004](#)) found elevated US coastal activity during La Niña and when the NAO is weak, with the strongest signals along the Gulf Coast and Florida.

3.2 Application to TC Risk Assessment

Decades of government investments have supported the development of leading GCMs that are today used in many applications in the public and private interest, including air quality, agriculture, transport, energy, and water resources. Yet, GCMs were not designed with such applications nor indeed TC risk assessment, in mind. Rather they were developed to inform a theory of climate. Only now has sufficient computational power become available to conduct global climate simulations in sufficient detail to capture key damaging characteristics of TCs, thereby bringing a wealth of new risk-related information that represents a potentially powerful transformation of TC risk assessment.

Many of the knowledge gaps outlined in the previous section may be met through inclusion of physical climate science to inform risk assessment. These full dynamical and physical models of TC climate can provide:

- Consistent data across spatial and temporal scales
- Sufficient simulation length to reliably sample extremes and resolve variability and change
- Physically based response to climate variability and change
- Physically based events outside the range of the historical record
- Information on key TC parameters that cause damage
- Information on TC clustering in time and space
- Comprehensive treatment of uncertainty

  Potential applications of GCMs to risk assessment include:

- A new view of TC climate from which to develop synthetic event sets and to better interpret the historical record and recent changes (Bonazzi et al. 2014; Strachan 2007)
- Views of future TC climate relevant decision-making (Douglas 2011)
- Application of simple TC risk indices and diagnostics to GCM output (Done et al. 2015)
- A base dataset to inform the development and calibration of simple, computationally efficient models
- Detailed reanalysis of past events
- Better understanding of the hazard drivers of loss

Although GCMs can generate temporally and spatially detailed projections of TC climate far into the future, this information is not without error and bias, and this has slowed the uptake of GCMs into risk assessment. Error and bias can arise from many sources including model physics and dynamics, model grid spacing, and internal model variability (Roberts et al. 2015; Strazzo et al. 2013). Compounding the

quantification of error are data sparseness and short historical records (McDonald et al. 2005), making it difficult to assess GCM skill. Raible et al. (2012) state that "these state-of-the-art models still yield contradicting results, and therefore they are not yet suitable to provide robust estimates of losses due to uncertainties in simulated hurricane intensity, location and frequency." However, errors in GCMs and the historical record are largely unrelated, thereby providing independent and complementary assessments of risk and improved estimates of uncertainty.

The integration of GCMs with risk assessment is a rapidly developing field, yet still in an exploratory phase and far from being operationally routine. Established public-private partnerships such as the Willis Research Network are applying the latest TC climate science to our understanding risk. Leading catastrophe modeling companies are also exploring the use of GCMs. A few pilot demonstration studies have recently appeared in the academic literature. Vitolo et al. (2010) demonstrated the use of a GCM-based event set for TC risk assessment in the West Pacific. Two hundred years of GCM tracks were bias corrected for intensity and resampled to generate a synthetic event set. The GCM-based event set provided assessment of multidecadal variations in TC risk and teleconnections to other basins that uncovered seemingly unrelated risk.

Emanuel (2013) applied the statistical-deterministic model of Emanuel et al. (2006, 2008) to simulate a large number of TCs. This approach seeds potential TCs into climate states statistically sampled from GCMs. GCM winds drive a beta and advection model to propagate the TCs, while SST, wind shear, and convective stability drive TC intensity. This is a computationally efficient creation of a large physically based event set. Emanuel (2011) applied this model to quantify a climate change emergence timescale in damage to an idealized portfolio of exposure along the US coast. There remains large uncertainty on how changes in future landfalling TCs will contribute to future TC damage (Emanuel 2011). Mendelsohn et al. (2012) further coupled this approach with exposure and vulnerability drivers of loss to quantify climate change impacts on TC damage. This approach has since been extended to assess storm-surge risk (Lin et al. 2012) and at city scales for Tampa in Florida, Cairns in Australia, and Dubai in the Persian Gulf (Lin and Emanuel 2016). Figure 7.3 shows synthetic TC tracks generated using the approach of Emanuel et al. (2006) within 200 km of Cairns, Australia. The storm-surge results are also highly sensitive to the climate model used, and this large variation among model predictions reflects uncertainties in GCM projections due to both systematic difference and internal climate variability (Lin et al. 2012).

Kishtawal (personal communication) seeded GCM climate change projections of steering flow over the Atlantic basin with passive tracers to infer future changes in US TC landfall risk. Gettelman (personal communication) used the Swiss Re hazard model to resample TC track data output from a small ensemble of high-resolution climate change GCM projections and coupled them with measures of exposure to explore plausible future damage scenarios. Raible et al. (2012) performed a similar approach using two different GCMs, noting the need to bias correct TC intensities and show even the sign of future losses depends on the GCM used, concluding that GCMs are not yet ready to be incorporated in loss assessments.
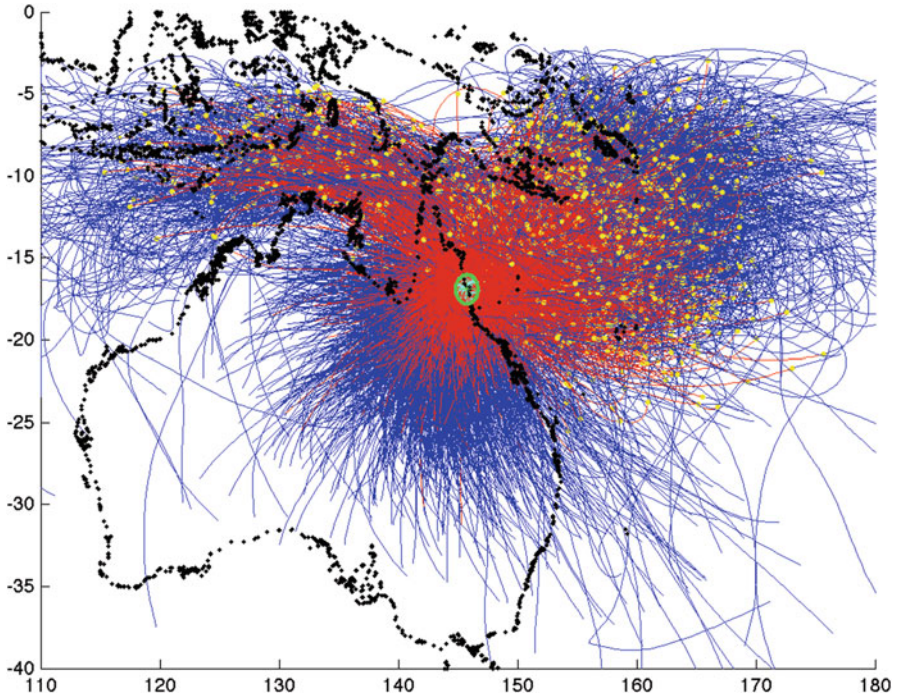
Fig. 7.3 Six thousand two hundred synthetic storms simulated using the Emanuel et al. (2006) model applied to NCEP-NCAR reanalysis data (1981–2000) that pass within 200 km of Cairns, Australia, with a maximum wind speed greater than 21 ms^{-1}. The *green circle* shows the 200-km-radius area around Cairns. The *red* portion of each track shows the 100-h period before and during landfall (Source: Ning Lin, Princeton, plotted using data from Lin and Emanuel (2016))

3.3 Future Potential of GCMs for TC Risk Assessment

The initial studies that incorporated GCM information into TC risk assessments were summarized in the previous section. In this section, the future potential of next-generation GCMs for risk assessment is outlined.

The direct use of today's GCM-simulated TC information is unlikely, given the high computational cost of generating sufficiently large event sets and known model bias and error. A more likely and more appropriate application of GCMs to risk assessment is to combine the information with the historical record. Risk managers do not necessarily seek explicit predictions, yet understanding the physical reasons for a change in TC climate may be evidence enough to reflect this in risk pricing and capital calculations.

Given the strong evidence that the TC climate is far from stationary, one immediate application of GCMs is to use their view of TC climate to inform interpretation of the historical record. This has the advantage of connecting the

use of GCMs to historical experience, something practitioners are more confident about than future projections. One fruitful entry point for the use of GCMs is to use their output to modify the results of CAT models. Connecting GCMs to current practice lowers the barriers to entry by practitioners tied by regulatory restrictions and increases credibility and familiarity by generally cautious sectors. One way this could be achieved is by using GCMs to provide scenarios of TC climate that can be used to adjust or weight event rates according to a user's confidence and opinion of a given outcome or collection of outcomes. Another immediate opportunity is to couple GCMs with simple measures of exposure to make simple, first-order assessments of risk and provide a risk-screening tool to alert risk managers on the need to investigate further.

Ranger and Niehörster (2012) suggested that natural variability would be the dominant driver of the level and volatility of wind-related tropical cyclone risk over the coming decade, but alongside climate change, it will be possible to experience new levels of risk within the decade. GCMs are now being run at TC-resolving resolution for 1,000s of years (Vecchi et al. personal communication). This unprecedented dataset allows for improved quantification of decadal and multidecadal variability of TC risk across the TC basins.

Emerging GCM large ensemble studies (e.g., Kay et al. 2015) provide the foundation to quantify the range in TC risk for a given future emissions scenario. For example, Done et al. (2014) used a dynamical ensemble to show up to 40 % of seasonal basin TC frequency is essentially unpredictable. TC risk models may benefit from accounting for this new view of uncertainty, in support of decisions robust to the quantified uncertainty. Computational resource constraints aside, the optimal approach to TC risk modeling is based on ensembles of high-resolution global simulations. Given finite resources and competition between model complexity, simulation length, and resolution, a combined statistical-dynamical approach (as described in the previous section, e.g., Lin and Emanuel 2016) offers a practical alternative and has significant scope for development.

Another important contribution next-generation GCMs can make to risk assessment derives from their global modeling framework, thereby allowing us to challenge the event independence assumption commonly made in risk assessments. From clustering in time and space and teleconnected risk across basins to joint probabilities of the multi-hazard nature of TCs, next-generation high-resolution GCM information promises a wealth of untapped risk information.

A key potential role for next-generation GCMs is in informing effective adaptation strategies in disaster risk reduction (DRR). A key decision in DRR is the choice of risk assessment methodology, and the demand for risk assessment data and modeling tools in the DRR community is high (World Bank 2014). Future changes in TC climate derived from GCM data may be used to quantify the protection levels needed for existing infrastructure, quantify the cost-benefit of stronger building codes accounting for future TC climates (Simmons, personal communication), support resilient agricultural practice (Lloyd's 2011), support land use planning (Burby 1998), and highlight previously unknown risk. For example, the landfall

of Hurricane Catarina in 2004 in Brazil, where it was commonly believed that TCs would not make landfall, caused devastating effects, as no buildings were designed for such an extreme event.

One recent example of the integration of GCM data into a community risk model is the National Center for Atmospheric Research's Global Risk Resilience and Impacts Toolbox (GRRIT). GRRIT is a public domain community model under development that aims to bring advanced techniques, data, and understanding within reach of decision-makers and planners to aid society in reducing weather and climate vulnerability, building economic resilience, and improving disaster recovery. A major component is access by the toolbox through web services to a variety of GCM datasets held in a number of different locations and varying widely in size and complexity. GRRIT provides a tool to understand the value of GCM data for risk assessment.

In all of these applications, transparency in risk assessment is becoming the standard required by regulators and rating agencies and a core principle as partnerships develop between academia, public policy institutions, and the insurance industry to improve our understanding of TC risk through collaborative and public research. The Florida Commission on Hurricane Loss Projection Methodology (FCHLPM) was set up (Grossi et al. 2005) such that any CAT model to be used in establishing residential rates must be publicly approved.

A key factor controlling the uptake of GCM data in risk assessment will be the alignment of the information produced with the information needed. Dilling and Lemos (2011) found that "nearly every case of successful use of climate knowledge involved some kind of iteration between knowledge producers and users," thereby necessitating the involvement of risk practitioners in the developmental trajectory of GCMs. Understanding current information needs is therefore a key first step (Wilby and Dessai 2010). Only then can we build capacity to generate the needed information. Realizing the full value of GCMs for TC risk assessment may proceed through iteration between information provision and information need. The value may indeed turn out to be negligible for some applications but many practitioners and climate science itself stand to benefit. Ultimately, this will transform how scientists and practitioners conceptualize global climate modeling.

Grand challenges such as these cannot be met in isolation. This transformation requires interdisciplinary expertise and training (Elsner et al. 2009) to understand interactions between climate risk, risk perception, and risk communication, but success ultimately hangs on sustained iteration of solutions. Societal response requires information that is useful and usable, and decision-makers must perceive the information to be scientifically sound, relevant, and produced and communicated in an unbiased conduct (Cash et al. 2003). The social sciences and humanities have a key role to play in helping society respond to the challenges posed by climatic and other environmental changes, from identifying stakeholders to establishing methods to convey scientific information in an applicable way. For example, the National Center for Atmospheric Research's Communicating Hazard Information in the Modern Environment project seeks to reduce harm and enhance resilience by

bringing together physical and social science expertise to study the flow of societal information and decisions as a hurricane approaches and arrives.

4   Summary

As tropical cyclones (TCs) make landfall in increasingly populated regions, the costs rise and are likely to continue rising due to future increases in exposure and wealth. The likely scenario of the TCs themselves changing in the future together with rising seas due to climate change will compound the problem. Current risk assessment practice leans heavily on catastrophe (CAT) models that have traditionally relied on historical data to assess risk. Use of historical data lacks accounting for how risk may have changed in the past or how it may change in the future. In addition, the short archives poorly capture temporal variability and trends, and records commonly lack information on critical TC parameters. Moreover, these models commonly assume independence between events. For risk assessment to be a useful tool that can help society properly confront this new era of increasing TC risk, it must undergo a step change in its ability to simulate TCs; account for changes in exposure, sea level, hazard, and vulnerability; and better communicate the risk assessment results and the potential actions that could reduce risk.

Next-generation global climate models (GCMs) are poised to bring in a new era of risk assessment capability. Only now has sufficient computational power become available to conduct global climate simulations in sufficient detail to capture key damaging TC characteristics on long timescales, thereby bringing a wealth of new risk-related information that presents a potentially powerful transformation of TC risk assessment.

Specifically, GCMs provide a rich physically based dataset to understand TC activity on longer timescales, influenced by climate change and variability, and the opportunity to explore events outside the range of the historical record. Events such as the devastating landfall of Hurricane Catarina in 2004 in Brazil, where it was commonly believed that TCs would not make landfall, could be anticipated. Moreover, emerging large GCM ensemble simulations provide the foundation to assess confidence in the simulated TC climates. Current state-of-the-art GCMs have been run using grid spacings of 10–25 km, at which many key damaging TC parameters such as TC size start to become resolved. GCMs can also quantify and elucidate the physical mechanisms of TC clustering, uncover teleconnected risks across TC basins, and quantify connections between basin and landfall rates.

The integration of GCMs with risk assessment is a rapidly developing field, yet still in an exploratory phase and a number of barriers need to be overcome. The direct use of today's GCM-simulated TC information is unlikely, given the high computational cost of generating sufficiently large event sets and known model bias and error. For example, error and bias may arise due to insufficient resolution of current GCMs to simulate all of the processes involved in tropical cyclone development. Direct use of single or sets of current GCMs in hurricane

risk management, without an appropriate treatment of uncertainty, could lead to potentially costly maladaptation and unnecessary risks (Ranger and Niehörster 2012), therefore inclusion of an estimate of uncertainty is vital.

One fruitful entry point for GCMs is to use the output to augment the historic record and modify the results of CAT models. Connecting GCMs to current practice lowers the barriers to entry by practitioners tied by regulatory restrictions and increases credibility and familiarity. In a changing climate with an increasing population, coordination between climate scientists and the risk management industry will help to reduce future damage. A key factor controlling the uptake of GCM data in risk assessment will be the alignment of the information produced with the information need, thereby necessitating the involvement of risk practitioners in the developmental trajectory of GCMs. GCM data are already being explored to support disaster risk reduction efforts, and GCM data are being incorporated into community risk models such as the National Center for Atmospheric Research's Global Risk Resilience and Impacts Toolbox to understand its full value.

The full value of GCMs has yet to be realized, but presents an opportunity to align developing climate science with climate risk assessment to create potentially transformative strategies for reducing losses from future TCs.

References

Adger WN, Barnett J, Brown K et al (2013) Cultural dimensions of climate change impacts and adaptation. Nat Clim Chang 3:112–117. doi:10.1038/nclimate1666

Arthur WC, Schofield A, Cechet RP, Sanabria LA (2008) Return period cyclonic wind hazard in the Australian Region. In: Abstracts of the 28th AMS conference on hurricanes and tropical meteorology, Orlando, Florida, USA, 28 April–2 May 2008

Bacmeister JT, Reed KA, Hannay C et al (2016) Projected changes in tropical cyclone activity under future warming scenarios using a high-resolution climate model. Clim Chang. doi:10.1007/s10584-016-1750-x

Bender MA, Knutson TR, Tuleya RE et al (2010) Modeled impact of anthropogenic warning on the frequency of intense Atlantic hurricanes. Science 327:454–458. doi:10.1126/science.1180568

Beven JL, Stewart SR, Lawrence MB et al (2003) ANNUAL SUMMARY: atlantic hurricane season of 2001. Mon Weather Rev 131:1454–1484. doi:10.1175/1520-0493(2003)131<1454:ASHSO>2.0.CO;2

Blake ES, Kimberlain TB, Berg RJ et al (2013) Tropical cyclone report: hurricane sandy. Natl Hurricane Cent 12:1–10

Bonazzi A, Dobbin AL, Turner JK et al (2014) A simulation approach for estimating hurricane risk over a 5-yr horizon. Weather Clim Soc 6:77–90. doi:10.1175/WCAS-D-13-00025.1

Bove MC, O'Brien JJ, Eisner JB et al (1998) Effect of el niño on U.S. landfalling hurricanes, revisited. Bull Am Meteorol Soc 79:2477–2482. doi:10.1175/1520-0477(1998)079<2477:EOENOO>2.0.CO;2

Burby RJ (ed) (1998) Cooperating with nature: confronting natural hazards with land-use planning for sustainable communities. Joseph Henry Press, Washington, DC

Camargo SJ, Robertson AW, Gaffney SJ et al (2007) Cluster analysis of typhoon tracks. Part II: large-scale circulation and ENSO. J Climate 20:3654–3676. doi:10.1175/JCLI4203.1

Cash DW, Clark WC, Alcock F et al (2003) Knowledge systems for sustainable development. Proc Natl Acad Sci 100:8086–8091. doi:10.1073/pnas.1231332100

Church JA, Clark PU, Cazenave A et al (2013) Sea level change. In: Stocker TF, Qin G-K, Plattner M et al (eds) Climate change 2013: the physical science basis. Contribution of Working Group I to the Fifth Assessment Report of the Intergovernmental Panel on Climate Change. Cambridge University Press, Cambridge, UK, pp 1137–1216

Czajkowski J, Done JM (2014) As the wind blows? Developing a deeper understanding of hurricane damages from a case study analysis. Weather Clim Soc 6(2):202–217

Dilling L, Lemos MC (2011) Creating usable science: opportunities and constraints for climate knowledge use and their implications for science policy. Glob Environ Chang 21(2):680–689. doi:10.1016/j.gloenvcha.2010.11.006

Done JM, Bruyère CL, Ge M, Jaye A (2014) Internal variability of North Atlantic tropical cyclones. J Geophys Res Atmos 119:6506–6519. doi:10.1002/2014JD021542

Done JM, PaiMazumder D, Towler E, Kishtawal CM (2015) Estimating impacts of North Atlantic tropical cyclones using an index of damage potential. Clim Chang. doi:10.1007/s10584-015-1513-0

Douglas R (2011) Financial markets drive demand for climate models. WMO Bull 60:34–37

Elsner JB, Bossak BH (2004) Hurricane landfall probability and climate. In: Murnane RJ, Liu KB (eds) Hurricanes and typhoons: past, present, and future. Columbia University Press. New York

Elsner JB, Kossin JP, Jagger TH (2008) The increasing intensity of the strongest tropical cyclones. Nature 455:92–95. doi:10.1038/nature07234

Elsner JB, Burch RK, Jagger TH (2009) Catastrophe finance: an emerging discipline. Eos Trans Ame Geophys Union 90:281. doi:10.1029/2009EO330001

Emanuel K (1991) The theory of hurricanes. Annu Rev Fluid Mech 23:179–196. doi:10.1146/annurev.fl.23.010191.001143

Emanuel K (2011) Global warming effects on U.S. hurricane damage. Weather Clim Soc 3:261–268. doi:10.1175/WCAS-D-11-00007.1

Emanuel K (2013) Downscaling CMIP5 climate models shows increased tropical cyclone activity over the 21st century. Proc Natl Acad Sci 110:12219. doi:10.1073/pnas.1301293110

Emanuel K, Ravela S, Vivant E, Risi C (2006) A statistical deterministic approach to hurricane risk assessment. Bull Am Meteorol Soc 87:299–314. doi:10.1175/BAMS-87-3-299

Emanuel K, Sundararajan R, Williams J (2008) Hurricanes and global warming: results from downscaling IPCC AR4 simulations. Bull Am Meteorol Soc 89:347–367. doi:10.1175/BAMS-89-3-347

Gentry MS, Lackmann GM (2010) Sensitivity of simulated tropical cyclone structure and intensity to horizontal resolution. Mon Weather Rev 138:688–704. doi:10.1175/2009MWR2976.1

Goh AZ-C, Chan JCL (2010) Interannual and interdecadal variations of tropical cyclone activity in the South China Sea. Int J Climatol 30:827–843. doi:10.1002/joc.1943

Grieser J, Jewson S (2012) The RMS TC-rain model. Meteorol Z 21(1):79–88

Grossi P, Kunreuther H, Patel CC (eds) (2005) Catastrophe modeling: a new approach to managing risk. Springer US, Boston

Hall TM, Jewson S (2007) Statistical modelling of North Atlantic tropical cyclone tracks. Tellus A 59:486–498. doi:10.1111/j.1600-0870.2007.00240.x

Hall TM, Sobel AH (2013) On the impact angle of hurricane Sandy's New Jersey landfall. Geophys Res Lett 40:2312–2315. doi:10.1002/grl.50395

Hashimoto A, Done JM, Fowler LD, Bruyere CL (2015) Tropical cyclone activity in nested regional and global grid-refined simulations. Clim Dyn 47:497–508. doi:10.1007/s00382-015-2852-2

Hill KA, Lackmann GM (2011) The impact of future climate change on TC intensity and structure: a downscaling approach. J Climate 24:4644–4661. doi:10.1175/2011JCLI3761.1

Holland GJ (1997) The maximum potential intensity of tropical cyclones. J Atmos Sci 54:2519–2541. doi:10.1175/1520-0469(1997)054<2519:TMPIOT>2.0.CO;2

Holland GJ, Bruyère CL (2014) Recent intense hurricane response to global climate change. Climate Dynam 42:617. doi:10.1007/s00382-013-1713-0

Holland GJ, Webster PJ (2007) Heightened tropical cyclone activity in the north Atlantic: natural variability or climate trend? Philos Trans R Soc A 365:2695–2716

Holland GJ, Belanger JI, Fritz A (2010) A revised model for radial profiles of hurricane winds. Mon Weather Rev 138:4393–4401. doi:10.1175/2010MWR3317.1

Holland GJ, Done JM, Ge M, Douglas R (2016) An index for cyclone damage potential. In: Abstracts of the 32nd conference on Hurricanes and Tropical Meteorology, San Juan, PR, USA, 17–22 April 2016

Höppe P, Pielke Jr RA (eds) (2006) Workshop on climate change and disaster losses: understanding and attributing trends and projections, final workshop report. Hohenkammer, Germany, 25–26 May 2006

IPCC (2012) Managing the risks of extreme events and disasters to advance climate change adaptation. In: Field CB, Barros V, Stocker TF et al (eds) A special report of working groups I and II of the Intergovernmental Panel on Climate Change. Cambridge University Press, Cambridge, UK, pp 3–21

Jagger TH, Elsner JB (2012) Hurricane clusters in the vicinity of Florida. J Appl Meteorol 51:869–877. doi:10.1175/JAMC-D-11-0107.1

Kaplan J, DeMaria M (1995) A simple empirical model for predicting the decay of tropical cyclone winds after landfall. J Appl Meteorol 34:2499–2512. doi:10.1175/1520-0450(1995)034<2499:ASEMFP>2.0.CO;2

Kay JE, Deser C, Phillips A et al (2015) The Community Earth System Model (CESM) large ensemble project: a community resource for studying climate change in the presence of internal climate variability. Bull Am Meteorol Soc 96:1333–1349. doi:10.1175/BAMS-D-13-00255.1

Khare SP, Bonazzi A, West N et al (2009) On the modelling of over-ocean hurricane surface winds and their uncertainty. QJR Meteorol Soc 135:1350–1365. doi:10.1002/qj.442

King RO (2013) Financing natural catastrophe exposure: issues and options for improving risk transfer markets. Congressional Research Service, Library of Congress

Knutson TR, McBride JL, Chan J et al (2010) Tropical cyclones and climate change. Nat Geosci 3:157–163. doi:10.1038/ngeo779

Kossin JP, Emanuel KA, Vecchi GA (2014) The poleward migration of the location of tropical cyclone maximum intensity. Nature 509:349–352. doi:10.1038/nature13278

Kunreuther H, Michel-Kerjan E (2009) At war with the weather: managing large-scale risks in a new era of catastrophes. MIT Press, New York, NY

Landsea C (2007) Counting Atlantic tropical cyclones back to 1900. Eos Trans AGU 88:197–202. doi:10.1029/2007EO180001

Langousis A, Veneziano D (2009) Long-term rainfall risk from tropical cyclones in coastal areas. Water Resour Res 45:W11430. doi:10.1029/2008WR007624

Lin N, Emanuel K (2016) Grey swan tropical cyclones. Nat Clim Chang 6:106–111. doi:10.1038/nclimate2777

Lin N, Emanuel KA, Oppenheimer M, Vanmarcke E (2012) Physically based assessment of hurricane surge threat under climate change. Nat Clim Chang 2(6):462–467. doi:10.1038/nclimate1389

Lloyd's (2011) Managing the escalating risks of natural catastrophes in the United States. https://www.lloyds.com/news-and-insight/risk-insight/library/natural-environment/us-nat-cat-report. Accessed 1 July 2016

Lonfat M, Rogers R, Marchok T, Marks FD (2007) A parametric model for predicting hurricane rainfall. Mon Weather Rev 135:3086–3097. doi:10.1175/MWR3433.1

Loridan T, Khare S, Scherer E et al (2015) Parametric modeling of transitioning cyclone wind fields for risk assessment studies in the Western North Pacific. J Appl Meteorol Climatol 54:624–642. doi:10.1175/JAMC-D-14-0095.1

McDonald RE, Bleaken DG, Cresswell DR et al (2005) Tropical storms: representation and diagnosis in climate models and the impacts of climate change. Climate Dynam 25:19–36. doi:10.1007/s00382-004-0491-0

Mendelsohn R, Emanuel K, Chonabayashi S, Bakkensen L (2012) The impact of climate change on global tropical storm damages. Nat Clim Chang 2:205–209. doi:10.1038/nclimate1357

Milly PCD, Betancourt J, Falkenmark M et al (2008) Stationarity is dead: whither water management? Science 319:573–574. doi:10.1126/science.1151915

Morss RE, Wilhelmi OV, Meehl GA, Dilling L (2011) Improving societal outcomes of extreme weather in a changing climate: an integrated perspective. Annu Rev Environ Resour 36:1–25. doi:10.1146/annurev-environ-060809-100145

Mumby PJ, Vitolo R, Stephenson DB (2011) Temporal clustering of tropical cyclones and its ecosystem impacts. Proc Natl Acad Sci 108:17626–17630. doi:10.1073/pnas.1100436108

Munich Re (2016) Topics Geo: natural catastrophes 2015 analyses, assessments, positions. Available at: www.munichre.com/topicsgeo2015

Murakami H, Wang Y, Yoshimura H et al (2012) Future changes in tropical cyclone activity projected by the new high-resolution MRI-AGCM. J Climate 25:3237–3260. doi:10.1175/JCLI-D-11-00415.1

Pielke RA Jr, Gratz J, Landsea CW et al (2008) Normalized hurricane damage in the United States: 1900–2005. Nat Hazards Rev. doi:10.1061/ASCE1527-698820089

Raible CC, Kleppek S, Wuest M et al (2012) Atlantic hurricanes and associate insurance loss potentials in future climate scenarios: limitations of high-resolution AGCM simulations. Tellus A 64:15672. doi:10.3402/tellusa.64i0.15672

Ranger N, Niehörster F (2012) Deep uncertainty in long-term hurricane risk: scenario generation and implications for future climate experiments. Glob Environ Chang 22:703–712. doi:10.1016/j.gloenvcha.2012.03.009

Rhein M et al (2013) Observations: ocean. In: Stocker TF et al (eds) Climate change 2013: the physical science basis. Contribution of working group I to the fifth assessment report of the Intergovernmental Panel on Climate Change. Cambridge University Press, Cambridge, UK

Roberts MJ, Vidale PL, Mizielinski MS et al (2015) Tropical cyclones in the upscale ensemble of high resolution global climate models. J Climate 28:574–596. doi:10.1175/JCLI871D-14-00131.1

Rumpf J, Weindl H, Höppe P et al (2007) Stochastic modelling of tropical cyclone tracks. Math Meth Oper Res 66:475–490. doi:10.1007/s00186-007-0168-7

Saji NH, Goswami BN, Vinayachandran PN, Yamagata T (1999) A dipole mode in the tropical Indian Ocean. Nature 401:360–363

Schenkel BA, Hart RE (2015) An analysis of the environmental moisture impacts of Western North Pacific tropical cyclones. J Climate 28:2600–2622. doi:10.1175/JCLI-D-14-00213.1

Schmidt S, Kemfert C, Höppe P (2010) The impact of socio-economics and climate change on tropical cyclone losses in the USA. Reg Environ Chang 10:13–26. doi:10.1007/s10113-008-0082-4

Shackley S, Young P, Parkinson S, Wynne B (1998) Uncertainty, complexity and concepts of good science in climate change modelling: are GCMs the best tools? Clim Change 38:159–205. doi:10.1023/A:1005310109968

Shaevitz DA, Camargo SJ, Sobel AH et al (2014) Characteristics of tropical cyclones in high-resolution models in the present climate. J Adv Model Earth Syst 6:1154–1172. doi:10.1002/2014MS000372

Sheikh PA (2005) The impact of hurricane Katrina on biological resources. Congressional Research Service, Library of Congress

Slingo J, Bates K, Nikiforakis N et al (2009) Developing the next-generation climate system models: challenges and achievements. Philos Trans R Soc London A: Math, Phys Eng Sci 367:815–831. doi:10.1098/rsta.2008.0207

Smith AB, Katz RW (2013) US billion-dollar weather and climate disasters: data sources, trends, accuracy and biases. Nat Hazards 67:387–410. doi:10.1007/s11069-013-0566-5

Solomon S et al (eds) (2007) Climate change 2007: the physical science basis. In: Contribution of working group I to the fourth assessment report of the IPCC, vol. 4. Cambridge University Press, Cambridge, UK

Stewart M, Rosowsky D, Huang Z (2003) Hurricane risks and economic viability of strengthened construction. Nat Hazards Rev 4:12–19. doi:10.1061/(ASCE)1527-6988(2003)4:1(12)

Strachan J (2007) The use of high-resolution global climate models for climate risk assessment. Catastrophe Modelling Forum Paper. New York

Strachan J, Vidale PL, Hodges K et al (2013) Investigating global tropical cyclone activity with a hierarchy of AGCMs: the role of model resolution. J Climate 26(1):133–152. doi:10.1175/JCLI-D-12-00012.1

Strazzo S, Elsner JB, LaRow T et al (2013) Observed versus GCM-generated local tropical cyclone frequency: comparisons using a spatial lattice. J Climate 26:8257–8268. doi:10.1175/JCLI-D-12-00808.1

Tye MR, Stephenson DB, Holland GJ, Katz RW (2014) A Weibull approach for improving climate model projections of tropical cyclone wind-speed distributions. J Climate 27:6119–6133. doi:10.1175/JCLI-D-14-00121.1

Vecchi GA, Knutson TR (2008) On estimates of historical North Atlantic tropical cyclone activity. J Climate 21:3580–3600. doi:10.1175/2008JCLI2178.1

Vickery PJ, Skerlj P, Twisdale L (2000a) Simulation of hurricane risk in the U.S. using empirical track model. J Struct Eng 10:1222–1237. doi:10.1061/(ASCE)07339445(2000)126

Vickery PJ, Skerlj P, Steckley A, Twisdale L (2000b) Hurricane wind field model for use in hurricane simulations. J Struct Eng 126(10):1203–1221

Vickery PJ, Masters FJ, Powell MD, Wadhera D (2009) Hurricane hazard modeling: the past, present, and future. J Wind Eng Ind Aerodyn. doi:10.1016/j.jweia.2009.05.005

Villarini G, Vecchi GA (2012a) Projected increases in North Atlantic tropical cyclone intensity from CMIP5 models. J Climate 26:3231–3240. doi:10.1175/JCLI-D-12-00441.1

Villarini G, Vecchi GA (2012b) Twenty-first-century projections of North Atlantic tropical storms from CMIP5 models. Nat Clim Chang 2:604–607. doi:10.1038/nclimate1530

Villarini G, Vecchi GA, Smith JA (2012) U.S. landfalling and North Atlantic hurricanes: statistical modeling of their frequencies and ratios. Mon Weather Rev 140:44–65

Villarini G, Lavers DA, Scoccimarro E, Zhao M et al (2014) Sensitivity of tropical cyclone rainfall to idealized global-scale forcings. J Climate 27:4622–4641. doi:10.1175/JCLI-D-13-00780

Vimont DJ, Kossin JP (2007) The Atlantic meridional mode and hurricane activity. Geophys Res Lett 34:L07709. doi:10.1029/2007GL029683

Vitolo R, Strachan J, Vidale PL, et al (2010) A global climate model based event set for tropical cyclone risk assessment in the West Pacific. In: Abstracts from EGU general assembly, Vienna, Austria, 2–7 May 2010

Walsh KJE, McBride JL, Klotzbach PJ et al (2016) Tropical cyclones and climate change. WIREs Clim Chang 7:65–89. doi:10.1002/wcc371

Wang C, Lee S-K, Enfield DB (2008) Atlantic warm pool acting as a link between Atlantic multidecadal oscillation and Atlantic tropical cyclone activity. Geochem Geophys Geosyst 9:Q05V03. doi:10.1029/2007GC001809

Wang S, Toumi R, Czaja A, Kan AV (2015) An analytic model of tropical cyclone wind profiles. Q J R Meteorol Soc 141:3018–3029. doi:10.1002/qj.2586

Weinkle J, Maue R, Pielke R (2012) Historical global tropical cyclone landfalls*. J Climate 25:4729–4735. doi:10.1175/JCLI-D-11-00719.1

Weller H, Ringler T, Piggott M, Wood N (2010) Challenges facing adaptive mesh modeling of the atmosphere and ocean. Bull Am Meteorol Soc 91:105–108. doi:10.1175/2009BAMS2907.1

Wilby RL, Dessai S (2010) Robust adaptation to climate change. Weather 65:180–185. doi:10.1002/wea.543

Willoughby HE, Darling RWR, Rahn ME (2006) Parametric representation of the primary hurricane vortex. Part II: a new family of sectionally continuous profiles. Mon Weather Rev 134:1102–1120. doi:10.1175/MWR3106.1

World Bank (2014) Understanding risk: review of open source and open access software packages available to quantify risk from natural hazards. World Bank Group, Washington, DC

Xuan Z, Chang N-B (2014) Modeling the climate-induced changes of lake ecosystem structure under the cascade impacts of hurricanes and droughts. Ecol Model 288:79–93. doi:10.1016/j.ecolmodel.2014.05.014

Zarzycki C, Jablonowski C (2015) Experimental tropical cyclone forecasts using a variable-resolution global model. Mon Weather Rev 143:4012–4037. doi:10.1175/MWR-D-15-0159.1

Zhai AR, Jiang JH (2014) Dependence of US hurricane economic loss on maximum wind speed and storm size. Environ Res Lett 9:64019. doi:10.1088/1748-9326/9/6/064019

Zhao M, Held IM, Lin S-J, Vecchi GA (2009) Simulations of global hurricane climatology, interannual variability, and response to global warming using a 50-km resolution GCM. J Climate 22:6653–6678. doi:10.1175/2009JCLI3049.1

Zhao M et al (2013) Robust direct effect of increasing atmospheric CO2 concentration on global tropical cyclone frequency. US CLIVAR Var 11:17–23

Zhu P (2008) A multiple scale modeling system for coastal hurricane wind damage mitigation. Nat Hazards 47:577–591. doi:10.1007/s11069-008-9240-8

Chapter 8
High-Resolution Multi-decadal Simulation of Tropical Cyclones

Michael F. Wehner, Kevin A. Reed, and Colin M. Zarzycki

Abstract Recent advances in high-performance computing technologies are enabling multiple climate modeling groups to perform global multi-decadal simulations at tropical cyclone-permitting resolutions. This chapter discusses the developing state of the art of such high-resolution modeling. These global atmospheric models, with horizontal resolutions in the 10–50 km range, simulate strong gradients in temperature and moisture far more realistically than contemporary mainstream climate models at coarser resolution. With these models, simulated tropical cyclones exhibit a surprising degree of realism in terms of both the physical characteristics of individual storms and their long-term statistical behavior. Experience with the Community Atmospheric Model version 5 is used as an example to demonstrate the strengths and weaknesses of this new class of climate models.

Keywords Tropical cyclones • Hurricanes • High-resolution global climate models • Variable-resolution • Hurricane tracking • Cyclogenesis • Climate change • High-performance computing

1 Introduction

The numerical simulation of tropical cyclones has a rich history, and its roots can be traced back to some of the earliest studies in atmospheric models with the successful implementation of convective parameterizations (Kuo 1965; Ooyama 1969). The

---

M.F. Wehner (✉)
Lawrence Berkeley National Laboratory, Berkeley, CA 94720, USA
e-mail: mfwehner@lbl.gov

K.A. Reed
School of Marine and Atmospheric Sciences, Stony Brook University,
Stony Brook, NY 11794, USA
e-mail: kevin.a.reed@stonybrook.edu

C.M. Zarzycki
National Center for Atmospheric Research, Boulder, CO 80307, USA
e-mail: zarzycki@ucar.edu

use of atmospheric models for decadal simulations of tropical cyclones (TCs) has been in practice for well over two decades. The first study to utilize a general circulation model (GCM) to perform decade-long simulations of tropical cyclones was produced by Broccoli and Manabe (1990) and consisted of experiments at two horizontal resolutions of roughly 500 and 200 km. The simulations resulted in a reasonable global climatology of tropical storm-like features compared to the observed climatology; however, the regional distribution lacked skill. The Broccoli and Manabe (1990) study was also the first to perform simulations with increased greenhouse gas concentrations to quantify how tropical cyclones may change in an altered climate. This work was expanded upon at finer grid spacings of approximately 125 km with noted improvement in storm climatology (Bengtsson et al. 1995, 1996). Numerous studies with various models at grid spacing greater than 100 km followed these initial studies and a more complete summary can be found in Walsh (2008).

In addition to these early GCM simulations, limited-area models have also been used in recent decades for decadal projections of tropical cyclone statistics in present-day and future climates for specific ocean basins. These downscaling studies have often utilized grid spacings as fine as approximately 20 km. Examples of experiments that use limited-area models with prescribed sea surface temperatures to investigate cyclone statistics for the North Atlantic are Knutson et al. (2008) and Bender et al. (2010). For such studies, the large-scale atmospheric conditions at the lateral domain boundaries, such as temperature, water vapor, and wind velocities, are often derived from low-resolution coupled GCM climatologies or reanalysis data. Furthermore, coupled-atmosphere-ocean configurations of such models (e.g., Knutson et al. 2001) have been utilized to explore the impact of ocean coupling on tropical cyclones.

While the use of limited-area models to simulate tropical cyclone statistics is reasonably well established, the forcing from lateral boundary conditions can have a strong impact on the climatology of the atmospheric state within limited-area models. Errors in these boundary conditions can have profound effects on tropical cyclogenesis due to biases in wind shear, steering flow, sea surface temperature, and atmospheric thermodynamics which can lead to errors in storm track density and pattern. Hence, direct downscaling of current generation coupled climate models such as those in the database of the Coupled Model Intercomparison Project version 5 (CMIP5) is subject to larger errors in tropical cyclone statistics that are downscalings of observationally constrained reanalysis products.

The usage of GCMs for simulating tropical cyclones has been limited by insufficient horizontal and vertical grid spacings, which are limited by computational resources. Despite these limitations, conventional GCMs have demonstrated the ability to produce tropical cyclones, even at coarse horizontal resolutions on the order of 100 km (Knutson et al. 2010; Wehner et al. 2014). However, tropical cyclones simulated in GCMs at these resolutions are of much weaker intensity and larger size than observed storms (Walsh 2008). Because of the reduced intensities, the number of trackable storms in coarse resolution GCMs is generally substantially lower than observed.

Recent advancements in computer architectures currently permit multi-decadal high-resolution GCM simulations with grid spacings in the 10–50 km range. However, such models still face many challenges in accurately representing both the physical and statistical behavior of tropical cyclones. The storm size and count, the representation of the intense convection, and the interplay of large-scale and small-scale processes have not been demonstrated to have converged. Subgrid-scale parameterizations have generally been adopted from the tuned coarser models and are usually not aware of the change in scale. Nonetheless, comparison of the tropical cyclone statistics between this class of global simulations with observations of the last two to three decades show a remarkable degree of realism (Bacmeister et al. 2014; Reed et al. 2015; Roberts et al. 2015; Strachan et al. 2013; Wehner et al. 2014; Zhao et al. 2009). For climate change experiments, the impact of increased carbon dioxide (and other greenhouse gases) and/or increased, prescribed sea surface temperatures (SSTs) has been investigated. Recent examples of such studies include Oouchi et al. (2006), Zhao et al. (2009), Sugi et al. (2009), Wehner et al. (2010), Murakami and Sugi (2010), Held and Zhao (2011), Murakami et al. (2012), Villarini et al. (2014), Scoccimarro et al. (2014), Lin et al. (2015), and Wehner et al. (2015).

In addition to advances in uniform high-resolution GCMs, recent progress has also been made in techniques permitting local mesh refinement within GCMs. Mesh refinement techniques allow for limited regions of high resolution within the global domain. These refinement areas can be tailored to particular research questions and, therefore, offer an attractive approach to simulating regional tropical cyclone activity in GCMs. There are two main types of mesh refinement used in models. Static mesh refinement techniques, where a multi-resolution grid is fixed at initialization and remains the same for the entirety of the model run, have been included in GCM frameworks for tropical cyclone investigations (Caron et al. 2011; Chauvin et al. 2006). A more recent example of such an approach is Zarzycki and Jablonowski (2014) which utilized an unstructured variable resolution mesh of approximately 25 km over the North Atlantic basin. An alternative technique is adaptive mesh refinement, where a grid dynamically refines/coarsens based on a particular features being present in the model. For example, a certain vorticity threshold in tropical regions within a 100 km simulation may trigger an automatic refinement to 25 km to better resolve cyclogenesis and the corresponding storm lifetime. Challenges such as multi-scale subgrid physical parameterizations, dynamic computational load balancing in massively parallel simulations, and the development of suitable refinement threshold criteria for cyclogenesis are areas of ongoing research before adaptive techniques could be a viable option for long-term simulations of tropical cyclones in climate models.

2   Uniform High-Resolution Global Atmospheric Modeling

The Community Atmospheric Model version 5 (CAM5) is typical of the global atmospheric component sub-models in the broader class of coupled general circulation models found in the CMIP5 database. The public-release version of the

model is supported at a horizontal resolution of approximately 100 km at the equator and 30 vertical levels extending into the lower stratosphere (Ghan et al. 2012; Neale et al. 2012). Increases in the horizontal resolution to an approximate grid spacing of 25 km using the finite volume (FV) dynamical core with minimal changes to the physical parameterizations have shown marked improvements to the realism of individual storms, including tropical cyclones (Bacmeister et al. 2014; Wehner et al. 2014). These improvements are most apparent in the sharper gradients of moisture and temperature in the higher-resolution version of the model when compared to lower-resolution models. As a result, many characteristics of extreme storms compare favorably with available observations. Depending on the details of the storm-tracking algorithm, the global number of simulated tropical cyclones in multi-decadal integrations can match present-day climatology. This high-resolution version of CAM5-FV even produces some intense hurricanes (Categories 4 and 5), although not all other current models at this resolution can also do so. The low-resolution (100 km) public-release configuration is typical of CMIP5-class climate models and is revealed to produce far too few tropical cyclones. Relaxation of tracking algorithm thresholds can increase the storm counts, albeit with less physical realism, but not to a significant fraction of the observed values (Wehner et al. 2015).

Despite the good performance in simulating the total number of tropical cyclones with the 25 km version of CAM5-FV, the simulated spatial distribution has some significant biases. Figure 8.1 shows the tropical cyclone track density
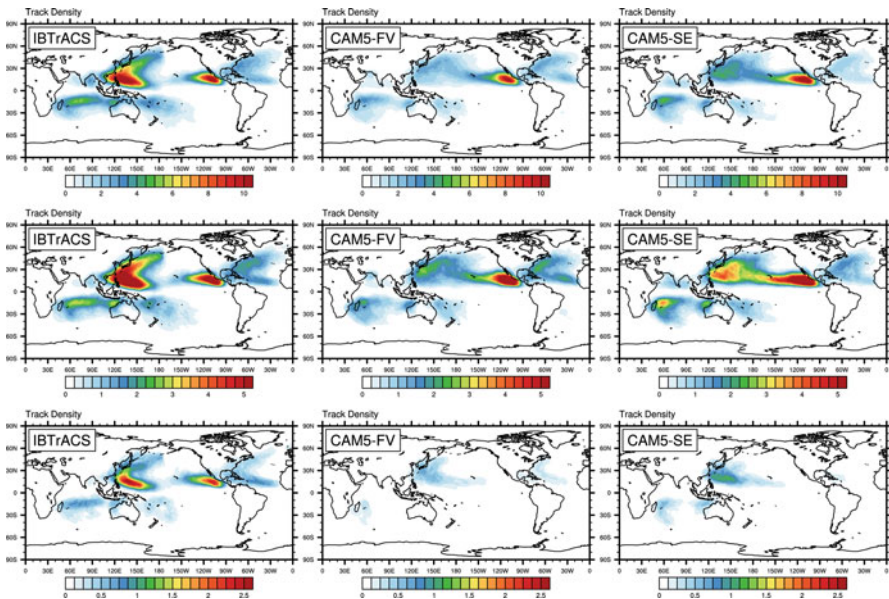
Fig. 8.1 Distribution of tropical cyclone track density of tropical cyclones that reach (*top row*) tropical storm (cat. 0–5), (*middle row*) hurricane (cat. 1–5), and (*bottom row*) intense hurricane (cat. 4 and 5) wind speeds for observations, CAM5-FV, and CAM5-SE (see labels). Track density is defined as the number of storm tracks within a 5° radius of a given point per year. Note that the color scale differs for each row

of the high-resolution version for CAM5-FV compared to observations. Note that the observations, the International Best Track Archive for Climate Stewardship (IBTrACS, Knapp et al. 2010), are shown over the same time period (1980–2005) as the CAM5 simulations. The largest discrepancy in the high-resolution model is in the central Pacific with the model generating far too many storms there than are observed, as well as the western Pacific where CAM5-FV produced too few storms, although the total number of simulated Pacific storms is reasonable. Such errors are likely the result of biases in the large-scale circulation simulated by the climate model. Each tropical cyclone-permitting global climate model has its own unique set of large-scale errors. Increases in horizontal resolution alone do not generally reduce these errors in regions without significant local orography (Bacmeister et al. 2014; Wehner et al. 2014). Rather, such errors are more likely the results of deficiencies in subgrid-scale parameterizations. As most modeling groups have tuned these parameterizations of unresolved processes to coarser resolutions, errors in large-scale circulation features can actually be greater at the higher resolution necessary for tropical cyclogenesis.

Recent work by Reed et al. (2015) has suggested that the simulation of tropical cyclone climatology in CAM5 is also sensitive to the choice of dynamical core. The dynamical core is the main fluid flow component of an atmospheric model and is a discretization of the Navier–Stokes equations, the relevant equations of motion for the atmosphere. As the largest errors in simulated large-scale climatological fields are often traceable to errors arising from the subgrid-scale parameterizations, it is not obvious that the dynamical core should have such a large effect on simulated tropical cyclone properties. CAM5 permits the selection of three different dynamical core approaches and two different sets of physical parameterizations. Reed et al. (2015) showed that a spectral-element (SE) dynamical core produces stronger storms, resulting in more hurricanes and major hurricanes over a 26-year simulation than does the FV approach when using nearly identical physical parameterization packages. This is despite the fact that the CAM5-FV simulation produces a slightly more favorable environment for intense storms based on analysis of the large-scale climatology. Figure 8.1 also displays the track density for the CAM5-SE simulation from Reed et al. (2015) and Bacmeister et al. (2016). When comparing CAM5-SE to CAM5-FV, there is a reduction in the bias of track density in the west Pacific, but the bias in the central Pacific is worse. CAM5-SE also shows decreased tropical cyclone activity in the North Atlantic. This work demonstrates that internal uncertainties due to model design choices are not fully understood in the current generation of high-resolution simulations. It is worth noting that many previous studies have investigated the more commonly understood sensitivity of tropical cyclones to the choice of physical parameterizations (e.g., Bacmeister et al. 2014; Kim et al. 2012; Reed and Jablonowski 2011a,b; Zhao et al. 2012), which is not discussed here.

Tropical cyclone-permitting climate models are a critical tool toward developing a theoretical understanding of the effect of climate change on tropical cyclone statistics (Walsh et al. 2015). The Hurricane Working Group (HWG) of the US Climate Variability and Predictability Research Program (CLIVAR) developed four idealized test configurations to explore the effects of increased sea surface

temperature (SST) and increased atmospheric carbon dioxide concentrations both separately and jointly on future tropical storm behavior in warmer climates (http://www.usclivar.org/working-groups/hurricane; Held and Zhao 2011). The warmer configurations imposed a uniform 2K increase to a base case 1990 SST climatology. Model performance in simulating the 1990 baseline case varied considerably. However, most of the models that contributed to the study, including the high-resolution version of CAM5-FV, produced stronger storms in the tail of their tropical storm distributions as measured by wind speed and minimum central pressures. A likely mechanism for such behavior is that when an intense tropical cyclone occurs, the large-scale conditions of low wind shear, high sea surface temperature, and high humidity are ideal. In the warmer simulations, the average wind shear conditions in tropical cyclogenesis regions do not change much, but average values of sensible and latent heat are larger due to increases in temperature and humidity. Hence, when the conditions are ripe for an intense storm to occur, it becomes stronger due to the increase in available energy. The models were less conclusive in regard to the number of lower intensity storms (Walsh et al. 2015). Most of the models, including the high-resolution version of CAM5 (Wehner et al. 2015), produced significantly fewer storms in the uniform 2K warmer configurations. This reduction was demonstrated to be a result of both the warmer surface and elevated air temperature aloft (driven by the increased greenhouse gas concentration), with the latter being the larger contributor.

The US CLIVAR HWG test problems present an opportunity to test conceptual models of the response of tropical cyclones to changes in the relevant large-scale climatological fields. The maximum potential intensity (MPI) index gives a bulk measure estimate of the highest possible wind speed and lowest possible central pressures of a "perfect" tropical cyclone modeled as a Carnot engine transporting energy from the ocean surface to the stratosphere (Emanuel 1987). Using changes in the monthly averaged surface temperatures and pressures as well as the vertical profiles of air temperature and humidity from the high-resolution version of CAM5.1, changes in MPI correctly predicted that the most intense simulated storms had higher winds and lower central pressures in the warmer test problems (Wehner et al. 2015). The magnitude of the MPI changes in maximum wind speed was also reasonable when compared to the changes in the ten most intense simulated storms in each configuration. The genesis potential index (GPI) uses the MPI together with vorticity, humidity, and wind shear to estimate the cyclogenesis density and has been tuned to observe values through reanalyses (Camargo et al. 2007; Emanuel and Nolan 2004). However, this bulk measure of tropical storm activity fails to correctly predict the decrease in the number of storms in the high-resolution CAM5.1 US CLIVAR HWG test problems as SST is uniformly increased (Wehner et al. 2015). A more sophisticated approach follows a downscaling approach designed by (Emanuel 2013) which "seeds" small-scale vorticity disturbances into the large-scale climatological conditions. This approach also predicts an increase in tropical cyclone activity (Walsh et al. 2015). Similarly, the low-resolution version of CAM5.1 also fails to predict the sign of the response

of its high-resolution counterpart. Since neither bulk measures of cyclogenesis nor direct tracking results in low-resolution models are guaranteed to faithfully replicate the behavior of models capable of actually producing hurricane category winds, confidence in projected future changes in tropical cyclone statistics derived from the low-resolution models in the CMIP5 database is undermined.

Fixed SST numerical experiments imply that the ocean is of infinite heat capacity. This is of course not true, and a cold wake of reduced SST is often observed behind large tropical cyclones due to the mixing of colder water at depth to the surface (Mei and Pasquero 2013; Price 1981). This serves as a negative feedback on storm intensity (Cione and Uhlhorn 2003). In addition to the effect on the tropical cyclone itself, this mixing also transports warmer surface waters to the subsurface thermocline (Li et al. 2015; McClean et al. 2011). Fully coupled global ocean–atmosphere models at tropical cyclone-permitting resolutions are at the very limit of existing computational technologies. The requisite multi-century spin-ups of such models demanded by the long time scales in the ocean are currently prohibitively computationally intensive, and experience is limited. Long-term biases in ocean sea surface temperatures may also deleteriously impact tropical cyclone climatology, as demonstrated by Small et al. (2014) using a 25 km version of CAM coupled to a prognostic ocean model. However, preliminary simulations reveal that the cold wake phenomena can be reproduced (Li et al. 2015; McClean et al. 2011). Furthermore, the relaxation time of the cold wake back to "normal" temperatures was recently found to be sensitive to ocean model resolution, with mesoscale eddy-permitting configurations responding more quickly (Li et al. 2015). As an alternative, long spin-up simulations can be avoided through the use of slab or mixed-layer ocean models, and early attempts to develop such configurations are ongoing (e.g., Hirons et al. 2015).

3 Variable-Resolution Global Modeling

Recent developments in numerical techniques have allowed for global simulations to be performed with regional refinement. Variable-resolution GCMs (VRGCMs) allow for targeted use of computing resources, as in regional climate or limited-area models, but do so within a global framework, allowing for a more physically and mathematically consistent treatment of the atmosphere in addition to eliminating the need for lateral boundary conditions to drive nested domains. Tropical cyclones are a natural fit for these frameworks as their spatial distribution is well defined, leading to obvious choices for refinement location. Storms are also generally restricted based on their genesis location, allowing for individual ocean basins to be easily isolated for regional studies, provided any nonlocal TC genesis precursor features remain adequately resolved in unrefined regions of the mesh (such as North Atlantic tropical waves and El Nino–Southern Oscillation (ENSO) teleconnections in Zarzycki and Jablonowski (2014) and Zarzycki et al. (2015)).
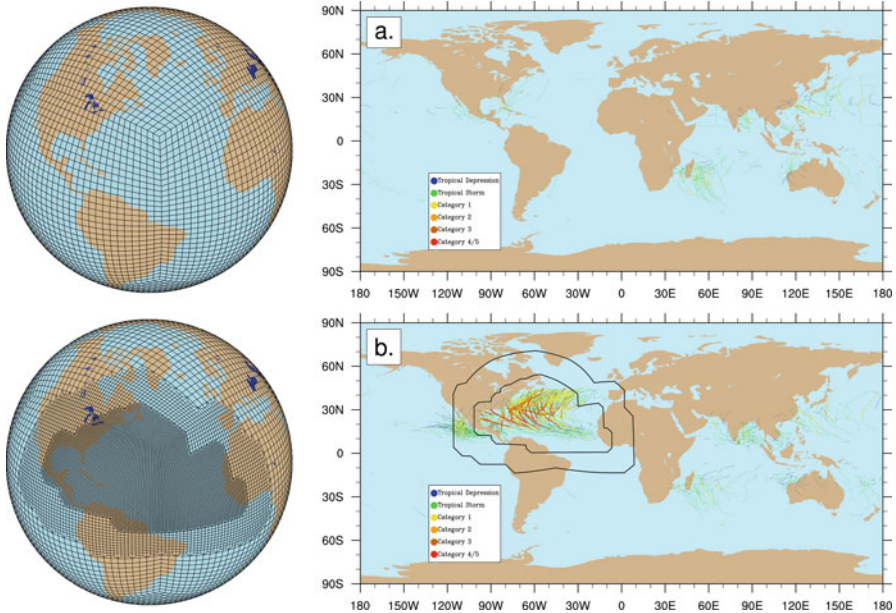
Fig. 8.2 Two different grids in the Community Atmosphere Model (*left*) with simulated tropical cyclone trajectories (*right*) from 23-year historical AMIP simulations. Tropical cyclone trajectories are color-coded by storm intensity on the Saffir–Simpson scale. Horizontal resolution of top model grid and base resolution of bottom model grid is 100 km. Static refinement in lower panels results in 25 km grid spacing over the North Atlantic (Results from Zarzycki and Jablonowski 2014)

Recently, a variable-resolution option (Zarzycki et al. 2014b) has been implemented into the SE dynamical core of CAM5 (Dennis et al. 2012a; Taylor et al. 1997; Taylor 2011), allowing for regionally refined simulations using the same framework as the uniform simulations discussed above. An example of tracked tropical cyclones from Zarzycki and Jablonowski (2014) is shown in Fig. 8.2. The top panels show results from a multi-decadal Atmospheric Model Intercomparison Project (AMIP, Gates 1992) historical simulation on an unrefined, CMIP-class, 100 km grid. The bottom panels show results from an identical model setup except using a grid with 100 km grid spacing everywhere except over the North Atlantic, where the horizontal resolution is increased to 25 km. The impact of finer grid spacing is clearly highlighted in the trajectories shown on the right in Fig. 8.2, with the regionally refined simulations able to achieve a significantly more realistic representation of both the spatial distribution and intensity of Atlantic storms. The fact that the bottom right panel is well matched to the results seen with the globally uniform simulations seen in Fig. 8.1 (albeit a simulation using a different dynamical core, but with the same set of subgrid parameterizations), lends further credence to the use of VRGCMs as a tool for regional tropical cyclone assessments. While VRGCM development remains in the early stages, other studies using different

models have found similar promising results with respect to tropical cyclones (Caron et al. 2011; Hashimoto et al. 2015).

The variable-resolution mesh in Fig. 8.2 (bottom) contains 13,340 elements, compared to 86,400 for a globally uniform mesh of the same resolution (25 km). Assuming a variable-resolution model that is able to scale with the number of grid cells (as CAM-SE has demonstrated (Zarzycki et al. 2014a)), regional tropical cyclone studies can be dramatically improved by decreasing the computational cost to simulate at a particular horizontal resolution. In the case above, the variable-resolution simulation only cost one-sixth of the CPU hours of an equivalent simulation utilizing high-resolution over the entire global domain. For a fixed computing load, this opens up additional simulation enhancements, such as increased resolution or longer run-time. It also may allow for the addition of ensemble members, which has been shown to improve the interannual correlation of tropical cyclones in high-resolution hindcasts forced with historical observed SSTs (LaRow et al. 2008). However, we note that while variable-resolution runs can be substantially less computationally expensive than uniform resolution calculations, they are by their very nature more targeted simulations and of less general applicability in a spatial sense. Hence, the decision to use variable resolution methods is a trade-off between reduced computational cost and limitations on the variety of analyses that can be performed on the model output.

4 Tracking

A wealth of automated detection algorithms has been developed to objectively find and quantify tropical cyclones in gridded climate data. The majority of published techniques employ a similar strategy. First, cyclone centers are defined by either a near-surface (generally 850 hPa) vorticity maximum or sea-level pressure minimum. Following this, warm-core criteria are typically applied to exclude mid-latitude cyclones. A surface wind speed threshold must also be surpassed, and all of these criteria need to be met for a minimum period of time, typically 1–3 days.

While the general formulation is similar among popular detection mechanisms, a great deal of variety exists in the particular criteria used. The choice of vorticity maximum or sea-level pressure minimum as the tropical cyclone center, as well as the applicable threshold value for either, differs between schemes. The warm-core detection criteria are also variable, with some schemes seeking a particular air temperature anomaly at one or multiple pressure surfaces (e.g., Murakami et al. 2012; Vitart et al. 1997; Zhao et al. 2009), others utilizing geopotential thicknesses (e.g., Tsutsui and Kasahara 1996), and others focusing on a negative gradient in vorticity with height (indicating a warm core via the thermal wind relation (e.g., Bengtsson et al. 2007; Strachan et al. 2013). Additionally, some apply basin- (Camargo and Zebiak 2002) or resolution-specific (Murakami and Sugi 2010; Walsh et al. 2007) thresholds to produce results which more closely match observed tropical cyclones,

others implement additional exclusionary criteria based on geographic location (such as latitude restrictions in many trackers or the removal of monsoon lows in Murakami et al. 2012), and others tune based on PDFs of relevant variables generated within a particular climate simulation (Camargo and Zebiak 2002).

As the horizontal grid spacings of climate models increase, analyzing data sets becomes more cumbersome due to growing file size. Recently, MapReduce-style (Dean and Ghemawat 2008) techniques have been used to parallelize existing code (e.g., Prabhat et al. 2012; Zarzycki and Jablonowski 2014) to leverage high-performance computing capabilities for tropical cyclone-tracking purposes. In these cases, candidate cyclones are first detected in a time-independent fashion, allowing for data files (generally ranging from three hourly to daily) to be spread out among many processors. Following the completion of this processing, candidate cyclones are sorted and then connected to other nearby points in space and time to merge tropical cyclones into their particular trajectories.

Of particular concern is whether the wide range of algorithms used contributes to uncertainty in tropical cyclone results. Extremely intense tropical cyclones generally have very well-defined features (vorticity maximum, warm core, etc.) that are picked up universally across algorithms. However, weaker storms are likely more difficult to track, particularly since the observational record of less intense, short-lived storms is questionable itself (Landsea et al. 2010). Some techniques may miss these storms altogether, although schemes that track large numbers of weaker storms may be more susceptible to false alarms. Using CLIVAR HWG data, Horn et al. (2014) found broad agreement in projected changes in future tropical cyclone count, particularly when homogenizing for certain thresholds which are common among tracking algorithms, such as wind speed and storm duration. However, other differences still existed, likely due to fundamental differences across the mechanics of the algorithms, implying that additional work is necessary to close the gap between published schemes. Recently, tracking on reanalysis products provided a potential avenue for this assessment (e.g., Murakami 2014; Strachan et al. 2013). The utility of using the current class of reanalysis products (at or coarser than approximately 50 km grid spacing) may be questionable due to a systematic weak bias when comparing reanalysis TCs to observations (Schenkel and Hart 2012), but as higher-resolution reanalysis products become available, it is likely their usefulness in developing and tuning tracking algorithms will increase.

5 Assessing Model Quality of Tropical Cyclone Statistics Simulation

Model intercomparison studies of CMIP5 class are often constrained to large-scale metrics of seasonally or annually averaged quantities (Myhre et al. 2013). Multi-model assessment of extreme weather in these models has been confined mostly to daily or longer indices averaged over large regions (Grotjahn et al. 2015; Sillmann et al. 2013). The improved realism of simulated storms from

high-resolution climate models offers additional opportunities to assess model quality. Short-duration hindcast experiments of actual individual or idealized storms can provide valuable insight into errors arising from dynamical cores and the physical parameterizations of the climate model (Reed and Jablonowski 2011a,b, 2012; Zarzycki and Jablonowski 2015). However, the present discussion will be confined to performance metrics describing the statistical behavior of simulated tropical cyclones in multi-decadal simulations.

The simulated annual average distribution of tropical cyclones is perhaps the most fundamental measure of a model's ability to characterize the statistics of these intense storms. However, as noted in Sect. 4, identifying tropical cyclones in long simulations is subject to uncertainties. Furthermore, even during the satellite era, observations do not provide a fully complete record of the global climatology of tropical cyclones. In particular, short-duration weak storms were not uniformly tracked by the hurricane centers as observational technologies advanced, resulting in spurious trends (Landsea et al. 2010). As most of the errors in tracking simulated storms also arise from weak storms, comparison of simulated and observed storm statistics at wind speeds above a critical threshold, say 33 m/s (or category 1 or greater on the Saffir–Simpson scale), is less dependent on the choice of tracking scheme. However, this can be problematic for some models, even in the less than 30 km resolution class, if their distributions of wind speeds are biased low. In fact, the number and intensity distribution of simulated tropical cyclones is highly dependent on a large number of factors as discussed in Sect. 2 and has not yet been demonstrated to converge in any model as resolution is increased. Nonetheless, given its importance, modeling groups often compare to the global number of tropical cyclones and in some cases tune their models to that number, although this may bias climate change studies. The spatial distribution of simulated tropical cyclones is also of fundamental importance if high-resolution climate models are to provide useful information to the impact community. The simplest model performance metric in this regard is to divide the ocean basins into somewhat arbitrary regions and count the simulated storms and/or their fraction of the total in each of the regions. Table 8.1 shows the annual global and selected basin number of storms for several high-resolution models under contemporary forcing factors and an observational estimates as for three different instantaneous maximum wind speeds defined by the Saffir–Simpson scale. The observations are from the International Best Track Archive for Climate Stewardship (IBTrACS) observed track database (Knapp et al. 2010).

Comparison of tracked storms from simulations to observational datasets such as IBTrACS should be performed with caution. The observations are a hand-crafted product constructed in an entirely different manner than a model storm tracker. Likewise, as discussed in Sect. 4, comparison between model results that are obtained by different tracking methods can also be problematic. In Table 8.1, two different sets of storm counts are provided for CAM5-FV. The set labeled CAM5-FV[a] comes from Wehner et al. (2014) using the GFDL method and threshold values published in (Knutson et al. 2007). The set labeled CAM5-FV[b] comes from the same tracker used with CAM5 in Reed et al. (2015) which is based on a more

Table 8.1 Annual frequency of simulated and observed tropical cyclones that reach tropical storm (cat. 0–5), hurricane (cat. 1–5), and intense hurricane (cat. 4 and 5) wind speeds for selected ocean basins. Uncertainty ranges, if available, are the interannual standard deviation

Tropical storm (U>17 m/s)	Global	North Atlantic	East Pacific	West Pacific	North Indian	South Indian	South Pacific
Observations	91.6 ± 8.5	11.8 ± 5.1	17.5 ± 4.9	27.3 ± 4.2	4.9 ± 1.9	17.9 ± 3.3	12.1 ± 4.1
CAM5-FV[a] (25 km)	82.6 ± 8.8	9.3 ± 2.9	30.5 ± 7.2	12.7 ± 3.9	4.5 ± 2.4	13.4 ± 4.4	12 ± 4.2
CAM5-FV[b] (25 km)	66.4 ± 8.5	10.5 ± 3.0	21.5 ± 6.5	10.2 ± 3.5	3.0 ± 1.8	13.5 ± 3.4	6.8 ± 2.8
CAM5-SE (25 km)	73.3 ± 10.6	7.6 ± 2.8	24.6 ± 7.5	13.8 ± 3.7	3.5 ± 2.0	15.8 ± 5.1	7.3 ± 2.8
HIRAM (50 km)	113.1	12	23.5	36.5	6.7	20.7	13.7
GA3 n216 (60 km)	75	4	15	16	3	14	8.5
GA3 n512 (25 km)	85	6.5	17	16	2.5	17	10
MRI AGCM203.2 (20 km)	84.7	7.6	18.3	23.4	6.1	16.0	12.9
Hurricane (U>33 m/s)	Global	North Atlantic	East Pacific	West Pacific	North Indian	South Indian	South Pacific
Observations	47.1 ± 5.5	6.5 ± 3.1	9.7 ± 3.6	15.4 ± 3.5	1.2 ± 1.0	8.7 ± 2.6	5.6 ± 2.6
CAM5-FV[a] (25 km)	51.7 ± 7.2	7.1 ± 3.2	18.4 ± 6.0	8.3 ± 2.9	2.4 ± 1.6	7.8 ± 2.8	7.5 ± 2.5
CAM5-FV[b] (25 km)	42.5 ± 6.5	7.8 ± 2.7	14.1 ± 5.1	7.3 ± 2.7	1.6 ± 1.1	7.8 ± 2.7	3.4 ± 2.0
CAM5-SE (25 km)	50.4 ± 8.3	5.7 ± 2.5	17.2 ± 6.1	10.5 ± 3.2	2.2 ± 1.5	10.4 ± 4.1	4.3 ± 2.5
HIRAM (50 km)	49.3	5.6	9.6	22.2	2.1	9.1	5.7
Intense hurricane (U>63 m/s)	Global	North Atlantic	East Pacific	West Pacific	North Indian	South Indian	South Pacific
Observations	10.7 ± 3.3	1.5 ± 1.5	3.0 ± 2.2	3.2 ± 2.0	0.2 ± 0.4	1.8 ± 1.6	0.9 ± 1.3
CAM5-FV[a] (25 km)	8.9 ± 2.7	1.8 ± 1.6	2.3 ± 1.9	2.8 ± 1.5	0.2 ± 0.4	1.1 ± 1.1	0.5 ± 0.7
CAM5-FV[b] (25 km)	3. ± 1.9	0.6 ± 0.8	0.5 ± 0.7	1.2 ± 1.0	0.0 ± 0.0	0.5 ± 0.8	0.2 ± 0.4
CAM5-SE (25 km)	4.2 ± 1.9	0.3 ± 0.5	0.5 ± 0.9	1.8 ± 1.3	0.2 ± 0.5	1.2 ± 1.0	0.2 ± 0.4

Data sources: IBTraCS observations (Knapp et al. 2010), CAM5-FV[a] (Wehner et al. 2014), CAM5-FV[b] (Reed et al. 2015), CAM5-SE (Reed et al. 2015), HIRAM (Zhao and Held 2012), MRI AGCM203.2 (Murakami et al. 2012), GA3 (Roberts et al. 2015)

recent method from GFDL (Zhao et al. 2009) with substantially lower counts than the earlier analysis despite being applied to exactly the same model output. However, the comparison of CAM5-FV[b] and CAM5-SE used the same tracker (Reed et al. 2015), revealing a true difference in tropical cyclone statistics between a few models.

The basins in Table 8.1 are perhaps the most natural division of the world's oceans, but more detailed comparison of simulated and observed track and cyclogenesis densities are also revealing. Also, models typically produce a few storms in the South Atlantic. Although only a few tropical cyclones have been observed there, it is not a well-observed region. Another interesting metric is the fraction of Atlantic storms that originate in the Caribbean (Camp et al. 2015; Roberts et al. 2015). This detail has proven to be difficult for contemporary 25 km models to reproduce. A further refinement on basin-wide storm counts is to separately account for land-falling storms (Camp et al. 2015; Vecchi and Villarini 2014). While many simulated storms recurve poleward at some point in their evolution, in some models with cyclogenesis biases too far to the east, the fraction of storms that make landfall is too low even if their simulation of the basin-wide number of storms is correct. Such errors can limit the usefulness of a model for tropical cyclone impact studies.

The simulated tropical cyclone frequencies in Table 8.1 can be further augmented by considering the number of storm days per year as a measure of basin-wide cyclonic activity as typically used by the hurricane seasonal forecast community (Gray 1979; Wehner et al. 2010). However, measures based on Saffir–Simpson categories are defined by point-wise maximum wind speeds only. Integrated measures of tropical cyclone properties such as accumulated cyclonic energy, ACE (Bell et al. 2000), Power Dissipation Index, PDI (Emanuel 2005, 2007), and integrated kinetic energy, IKE (Powell and Reinhold 2007) provide a more holistic description of overall storm intensities. Wind speeds alone provide an incomplete measure of the impacts of tropical storms (Wendel 2015). The Cyclone Damage Potential (Holland et al. 2016) and the Hurricane Hazard Index (Wendel 2006) also incorporate the spatial extent of high winds to assess the potential for impacts from tropical storms. Application of model evaluation metrics based on observational estimates of these quantities to high-resolution atmospheric models will likely prove more informative than simple counting based on the Saffir–Simpson scale.

Each ocean basin has its own seasonal cycle of tropical cyclogenesis. The timing of the beginning and end of these stormy periods provides another model performance metric. Depending on the basin, the seasonality is a function of the magnitude of sea surface temperature and wind shear in the cyclogenesis regions. Figure 8.3 shows seasonal cycle of North Atlantic tropical cyclones as simulated by the variable-resolution model described in Sect. 3, compared to the IBTraCS observations. The model (25 km CAM-SE, red) reproduces the correct observed (IBTraCS, blue) annual peak for all TCs (Fig. 8.3a) with September being the most active month, followed by August, and then October. When only hurricanes and major hurricanes are considered (Fig. 8.3b–c), the peak is shifted 1 month too early in the simulations, although the model does an adequate job reproducing the peridocity of storm formation. When absolute values are plotted (Fig. 8.3d–f), it is
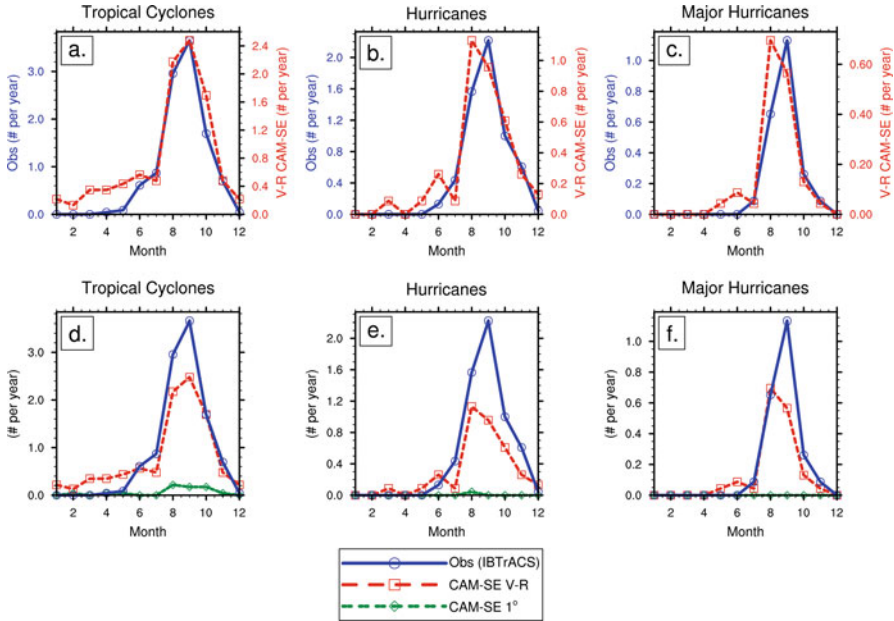
Fig. 8.3 Simulated seasonal cycle of (*left*) TC, (*middle*) hurricane, and (*right*) major hurricane formation rates in North Atlantic ocean. (**a–c**) Comparison between (*red*, right y-axis) a 25 km variable-resolution CAM5 simulation and (*blue*, left y-axis) IBTraCS observations and are normalized using separate axes. (**d–f**) Storm formation rates on the same scale and also include a 100 km coarse simulation (*dark green*). The calendar month (in numeric format) is labeled on the x-axis in all figures (From Zarzycki and Jablonowski 2014)

clear that the model is biased slightly low in the overall number of TCs produced (similar to the CAM-SE North Atlantic results in Table 8.1), but that the cycle is significantly more realistic than that demonstrated by a coarser 100 km model (dark green) (Zarzycki and Jablonowski 2014).

Improvement in the seasonal cycle of TCs as a function of resolution is not limited to the North Atlantic. In the North Indian, the observed tropical cyclone seasonality is bimodal with a peak in March and a second larger peak in November before and after the monsoon season (Li et al. 2013). In prescribed SST experiments, models can reproduce this bimodality (Wehner et al. 2014). Other studies utilizing high-resolution configurations have shown similar reproductability in other ocean basins as well (e.g., Zhao et al. 2009).

The interannual variations in tropical cyclone number in some basins are strongly controlled by the state of the oceans. For instance, in the North Atlantic, both the El Nino–Southern Oscillation (ENSO) and the Atlantic Meridional Mode (AMM) modulate tropical cyclogenesis (Gray 1984; Patricola et al. 2014). Several analyses of prescribed SST experiments examined the relationships between simulated and observed time series of annual tropical cyclone counts finding relatively high correlations in some basins (Roberts et al. 2015; Zhao et al. 2009).
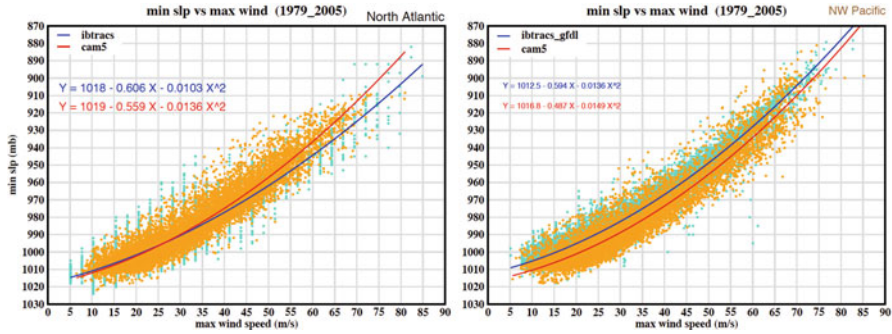
Fig. 8.4 Scatterplot of instantaneous maximum wind speed versus minimum central pressure of tracked storms in CAM5-FV and the IBTRACS observations over the period 1979–2005. *Left*: North Atlantic. *Right*: Northwest Pacific (Figure courtesy of Cheng-Ta Chen, National Taiwan Normal University)

Performance metrics describing the physical characteristics of simulated tropical cyclones are also an important part of a complete model assessment. A scatterplot of the instantaneous maximum wind speed versus minimum pressure for each tracked storm provides a picture of how well the dynamical core responds to high vorticity flow. Figure 8.4 shows this pressure–wind relationship for North Atlantic and West Pacific basins as simulated the CAM5-FV model at a resolution of approximately 25 km compared to the IBTrACS observations. Quadratic fits to each scatterplot are shown in the background of Fig. 8.4. Further quantitative analysis could also be performed when comparing such scatterplots. Other scatterplots, such as storm radii versus maximum wind speed or minimum pressure would also reveal much about how resolution impacts the structure of simulated tropical cyclones.

Direct usage of simulated paths and statistics for studies of tropical cyclone impacts must be made with caution. Systematic errors in the position of simulated tracks may under- or overestimate landfall frequency although corrections could be imposed. Errors in the total basin-wide storm count and/or seasonality must also be carefully considered. Furthermore, cumulus convection parameterizations are still necessary for models in the 10–50 km range. As these parameterizations were not developed for these resolutions, errors in total precipitation may also need to be corrected for usage in tropical cyclone-related inland flooding analyses.

6 Computational Performance Issues, Analysis, and Scalability

Since the seminal study by Oouchi et al. (2006), computers have continued to increase in peak speed enabling other modeling groups to extend their models to tropical cyclone-permitting horizontal resolutions. Although Moore's law continues

to increase peak speeds of the largest available supercomputers, the doubling of transistor density approximately every 18 months is no longer used to increase processor clock speeds because of energy consumption and cooling considerations (Donofrio et al. 2009). Rather, machine designers have used these additional components to increase the number of on-chip processors. This has important implications for the software design of climate models. Scalability to large number of processors, at least tens of thousands, is necessary to fully utilize the most recent hardware designs (Dennis et al. 2012b). Scalability to 100,000 processor cores or more will likely be indispensable in the not too distant future to fully exploit many-core chip based machines (Wehner et al. 2011).

As spatial resolution increases, sub-daily output becomes ever more interesting due to the increased realism of the simulated weather. For some tropical cyclone-tracking schemes, eight surface variables are required at six hourly intervals. For other studies, three hourly or even hourly outputs can be informative about the diurnal cycle. Furthermore, the sub-daily output of variables at multiple vertical levels can inform about the structure of storms. Tens to hundreds of terabytes of model output can justifiably be saved from multi-decadal simulations at order 25 km resolution. However, overall throughput of model simulations can be adversely affected by this volume and frequency of data output. For instance, the CAM-SE will scale without output to well over 30,000 processor cores through a combination of MPI tasks and OpenMP threads (Dennis et al. 2012b; Mirin and Worley 2011). At such processor counts, careful usage of parallel i/o libraries is required in order to avoid serial bottlenecks. Attention must be paid to the specifics of the parallel file systems (e.g., Mizielinski et al. 2014). However, available high-performance machines such as edison.nersc.gov, a Cray XC30, have a limited number of i/o nodes. Hence, parallel output does not scale past more than 256 pio tasks (pio is a parallel i/o library using pnetcdf) for the 25 km version of CAM-SE on that machine when a large three hourly output dataset is specified. As a practical matter, overall performance is degraded by this poor i/o scaling such that using more than about 8000 processor cores is ineffective. Such limitations have been found on other, very different architectures such as the Blue Gene Q (mira.alcf.gov). There are a number of yet to be implemented fixes to this problem, including more effective usage of the parallel file systems (in this case, LUSTRE) by pnetcdf/pio as well as asynchronous i/o protocols to overlap output with computation on a separate set of i/o processors.

Some might argue that such large volumes of output data are unnecessary as some analyses, such as parts of the tracking algorithm, can be performed in-core during the model integration. In fact, this statement is true if the analysis to be performed is independent of time or can be simply accumulated as model time advances. However, multi-decadal, tropical cyclone-permitting climate model simulations are so computationally intensive that only a few groups can perform them. We argue here that this class of integration is most effectively used as a community-shared resource. Since it is impossible for a modeling group to anticipate how external users may creatively use the model output, distribution of large datasets is unavoidable if the model output is to be used by the wider scientific community. Fortunately,

advanced file transfer protocols such as GLOBUS (www.globus.org) fully utilize network bandwidth to facilitate the movement of large amounts of data between computing centers.

Such large datasets present significant challenges for offline analyses. In order to reduce the workflow turnaround time, analysts must restructure their algorithms to use parallel, multiprocessor programs. Many common analyses can indeed be structured so that at least one dimension is embarrassingly parallel, that is not requiring any interprocessor communications. In many cases, as noted in the previous paragraph, this dimension can be time. For example, the interpolation from an irregular model mesh to a regular latitude–longitude mesh or the construction of spatial averages falls into this category. By contrast, calculating time-dependent quantities such as monthly averages or values above a threshold may be cast as embarrassingly parallel in space. Such parallel processing tasks are easily programmed by dividing the entire problem up at the start of the analysis calculation and reassembling at the end. Bottlenecks often occur during the i/o phase of analysis calculations. This can be particularly acute when trying to read many files simultaneously to initialize the analysis as the parallel tasks can be in contention for the available i/o resources. This reinforces the notion that well-designed climate modeling supercomputer centers must invest in special purpose analysis machines (e.g., Lawrence et al. 2013), with large memories and fast i/o in addition to the large number crunchers necessary to run the actual climate models.

7   Future Directions

Direct simulation of the multi-decadal statistics of tropical cyclones has only recently become possible. This new area of climate modeling offers many new challenges and opportunities as available computational resources continue to increase. Certainly, coupling of tropical cyclone-permitting atmospheric models to mesoscale eddy-permitting ocean models is among the most difficult of current research efforts. Consortia in both Europe (the PRIMAVERA project[1]) and in the USA (the ACME program[2]) has been formed to specifically develop new climate models of this class. These efforts, in addition to existing ones, recognize that the increased realism in simulated weather systems, of which tropical cyclones are just one class, leads to more credible local and regional simulation of present and future climate. Public and private decision-makers require much more localized information than current CMIP5-class models can easily provide. The significant resources currently being devoted to developing global atmospheric models resolved in the range of 10–25 km is motivated in part by these policy needs.

---

[1]https://www.primavera-h2020.eu/

[2]http://climatemodeling.science.energy.gov/projects/accelerated-climate-modeling-energy/

Internationally, the endorsement by the CMIP panel of the HighResMIP protocol (https://dev.knmi.nl/projects/highresmip) for the next climate model intercomparison, CMIP6, is an important step in advancing both stand-alone and coupled tropical cyclone-permitting climate models as well as quantifying the structural uncertainty in future projected changes in tropical cyclone properties. The protocol defines multiple century-scale numerical experiments from the mid-twentieth century to the mid-twenty-first century under two different future external climate-forcing scenarios. In order to permit research on storm statistics, a variety of output fields at six hourly intervals are prescribed which will more than likely result in a multi-petabyte data set.

The need for ensemble simulations is as critical for tropical cyclone-permitting models as it is for more conventional resolution climate models (Deser et al. 2014). Analysis of variance (ANOVA) techniques can be applied to such integrations to explore forced and unforced climate variability. As was the case with conventional resolution models, early ensemble simulations will be small (the HighResMIP protocol is only three realizations), but will grow in size as computational resources expand.

As the amount of data available to study tropical cyclones increases due to both higher resolution and larger ensembles, further efforts in developing flexible, highly parallelized tracking algorithms (such as those previously discussed in this chapter) will be required. Techniques where TCs are tracked "online" during the actual model run may become popular as a way of alleviating post-simulation data analysis bottlenecks. This would allow users to continue to output high-resolution, high-frequency TC data, but without the need for this data to be first generated at the global scale for initial detection purposes, significantly reducing the data storage required for investigating TCs. As the structure of simulated TCs grows closer to those observed in nature, machine-learning algorithms may also be viable future detection and tracking paths (e.g., Liu et al. 2016). An example would be using observations of historical TCs (such as satellite images or wind fields) to be used as training data sets, which can then be applied to find storms in climate model data.

As mentioned earlier, the subgrid-scale parameterizations in current tropical cyclone-permitting models were not specifically developed for usage at such high resolutions. Research in "scale aware" formulations, particularly of cumulus convective processes, will likely improve the mean climatology of models down to approximately 10 km resolution. As computational resources permit resolutions finer than about 10 km, more dramatic changes in model formulation are dictated. Below this resolution, non-hydrostatic effects in the fluid motion equations must be accounted for, requiring new formulations of the dynamical cores of some models. Furthermore, for resolutions below 10 km, deep cumulus convection cannot be rigorously parameterized and some portion of convection is actually directly simulated. The range of resolutions from about 1 km to about 10 km has been called a "gray zone" where some combination of explicit and parameterized convection is required. One option is to remove the convective parameterization altogether (Satoh et al. 2014). Another approach to unify this combination (Arakawa and Wu

2013; Wu and Arakawa 2014) defines a scaling factor between 0 and 1 to multiply a parameterized convective contribution to temperature and moisture tendencies; this is still an active area of research.

8 Conclusions

High-resolution multi-decadal simulation of tropical cyclones can now be performed by a few groups using the largest available supercomputers. This new class of models, with horizontal resolution in the range of 10–50 km, enables more realistic simulation of many classes of extreme storms in addition to tropical cyclones. However, increased resolution alone will not decrease the large-scale model errors that result from deficiencies in subgrid-scale physical parameterizations. Many aspects of simulated tropical cyclones in these models are surprisingly realistic, including their frequency, seasonality, and interannual variability. Wind speeds up to category 5 on the Saffir–Simpson scale are simulated by some models with correspondingly realistic central low-pressure values. Fixed SST models are the most practical, in terms of computational burden, at the present time. Carefully constructed climate change experiments with these models are beginning to confirm some theoretical expectations of the behavior of tropical cyclones in future warmer climates. Fully coupled global ocean atmosphere models are more challenging to integrate due to the need to spin up or initialize the ocean state, and multi-decadal simulations are just beginning to be made. Such models can offer insight into the effect of tropical cyclones on the climate through the poleward transport of energy and moisture as well as more realistically simulate the interaction of storms with the upper ocean.

Nearly every tropical cyclone-permitting model produces stronger storms in the tail of their simulated wind speeds under warmer ocean conditions. What the total number of tropical cyclones in a warmer world will be is less clear as results vary between models and are dependent on both the magnitude and pattern of ocean temperature change. As more modeling groups are enabled to perform multi-decadal tropical cyclone-permitting simulations, structural uncertainties in the behavior of future storm statistics will be better quantified. This is a critical part of the development of a climate change theory of tropical cyclones.

References

Arakawa A, Wu CM (2013) A unified representation of deep moist convection in numerical modeling of the atmosphere. Part I. J Atmos Sci 70:1977–1992. doi: 10.1175/JAS-D-12-0330.1

Bacmeister JT, Wehner MF, Neale RB, Gettelman A, Hannay C, Lauritzen PH, Caron JM, Truesdale JE (2014) Exploratory high-resolution climate simulations using the community atmosphere model (CAM). J Clim 27:3073–3099. doi: 10.1175/JCLI-D-13-00387.1

Bacmeister JT, Reed KA, Hannay C, Lawrence PJ, Bates SC, Truesdale JT, Rosenbloom NA, Levy ML (2016, in press) Projected changes in tropical cyclone activity under future warming scenarios using a high-resolution climate model. Clim Change. doi: 10.1007/s10584-016-1750-x

Bell GD, Halpert MS, Schnell RC, Higgins RW, Lawrimore J, Kousky VE, Tinker R, Thiaw W, Chelliah M, Artusa A (2000) Climate assessment for 1999. Bull Am Meteorol Soc 81(6):1328

Bender MA, Knutson TR, Tuleya RE, Sirutis JJ, Vecchi GA, Garner ST, Held IM (2010) Modeled impact of anthropogenic warming on the frequency of intense Atlantic hurricanes. Science 327:454–458. doi: 10.1126/science.1180568

Bengtsson L, Botzet M, Esch M (1995) Hurricane-type vortices in a general circulation model. Tellus 47:175–196. doi: 10.1034/j.1600-0870.1995.t01-1-00003.x

Bengtsson L, Botzet M, Esch M (1996) Will greenhouse gas-induced warming over the next 50 years lead to higher frequency and greater intensity of hurricanes? Tellus 48:57–73. doi: 10.1034/j.1600-0870.1996.00004.x

Bengtsson L, Hodges KI, Esch M (2007) Tropical cyclones in a T159 resolution global climate model: comparison with observations and re-analyses. Tellus A 59(4):396–416. doi: 10.1111/j.1600-0870.2007.00236.x

Broccoli AJ, Manabe S (1990) Can existing climate models be used to study anthropogenic changes in tropical cyclone climate? Geophys Res Lett 17:1917–1920. doi: 10.1029/GL017i011p01917

Camargo S, Emanuel K, Sobel A (2007) Tropical cyclone activity and global climate. J Clim 20:4819–4834. doi: 0.1175/JCLI4282.1

Camargo SJ, Zebiak SE (2002) Improving the detection and tracking of tropical cyclones in atmospheric general circulation models. Weather Forecast 17(6):1152–1162

Camp J, Roberts M, MacLachlan C, Wallace E, Hermanson L, Brookshaw A, Arribas A, Scaife AA (2015) Seasonal forecasting of tropical storms using the Met Office GloSea5 seasonal forecast system. Q J R Meteorol Soc 141:2206–2219. doi: 10.1002/qj.2516

Caron LP, Jones CG, Winger K (2011) Impact of resolution and downscaling technique in simulating recent Atlantic tropical cyclone activity. Clim Dyn 37(5–6):869–892. doi: 10.1007/s00382-010-0846-7

Chauvin F, Royer JF, Déqué M (2006) Response of hurricane-type vortices to global warming as simulated by ARPEGE-Climat at high resolution. Clim Dyn 27(4):377–399. doi: 10.1007/s00382-006-0135-7

Cione JJ, Uhlhorn EW (2003) Sea surface temperature variability in hurricanes: implications with respect to intensity change. Mon Weather Rev 131(8):1783–1796. doi: 10.1175//2562.1

Dean J, Ghemawat S (2008) Mapreduce: simplified data processing on large clusters. Commun ACM 51(1):107–113

Dennis JM, Edwards J, Evans KJ, Guba O, Lauritzen PH, Mirin AA, St-Cyr A, Taylor MA, Worley PH (2012a) CAM-SE: a scalable spectral element dynamical core for the Community Atmosphere Model. Int J High Perform Comput Appl 26(1):74–89. doi: 10.1177/1094342011428142

Dennis JM, Vertenstein M, Worley PH, Mirin AA, Craig AP, Jacob R, Mickelson S (2012b) Computational performance of ultra-high-resolution capability in the Community Earth System Model. Int J High Perform Comput Appl 26(1):5–16. doi: 10.1177/1094342012436965, http://hpc.sagepub.com/content/26/1/5.abstract, http://hpc.sagepub.com/content/26/1/5.full.pdf+html

Deser C, Phillips AS, Alexander MA, Smoliak BV (2014) Projecting North American climate over the next 50 years: uncertainty due to internal variability. J Clim 27:2271–2296

Donofrio D, Oliker L, Shalf J, Wehner MF, Rowen C, Krueger J, Kamil S, Mohiyuddin M (2009) Energy-efficient computing for extreme-scale science. Computer 42(11):62–71. http://doi.ieeecomputersociety.org/10.1109/MC.2009.353

Emanuel K (1987) The dependence of hurricane intensity on climate. Nature 326:483–485

Emanuel K (2005) Increasing destructiveness of tropical cyclones over the past 30 years. Nature 436:686–688

Emanuel K (2007) Environmental factors affecting tropical cyclone power dissipation. J Clim 20:5497–5509

Emanuel K (2013) Downscaling CMIP5 climate models shows increased tropical cyclone activity over the 21st century. Proc Natl Acad Sci 110(30):12219–12224. doi: 10.1073/pnas.1301293110

Emanuel K, Nolan D (2004) Tropical cyclone activity and global climate. Preprints, 26th conference on hurricanes and tropical meteorology, Miami, pp 240–241 (Am Meteorol Soc)

Gates WL (1992) AMIP: the Atmospheric Model Intercomparison Project. Bull Am Meteorol Soc 73:1962–1970

Ghan SJ, Liu X, Easter RC, Zaveri R, Rasch PJ, Yoon JH, Eaton B (2012) Toward a minimal representation of aerosols in climate models: comparative decomposition of aerosol direct, semidirect, and indirect radiative forcing. J Clim 25:6461–6476

Gray WM (1979) Hurricanes: their formation, structure and likely role in the tropical circulation. In: Meteorology over the tropical oceans, 21–25 Aug 1979, vol 77. Royal Meterological Society, Bracknell, pp 155–218

Gray WM (1984) Atlantic seasonal hurricane frequency. Part I: El Niño and 30 MB Quasi-Biennial Oscillation influences. Mon Weather Rev 112(9):1649–1668. doi: 10.1175/1520-0493(1984)112<1649:ASHFPI>2.0.CO;2

Grotjahn R, Black R, Leung R, Wehner MF, Barlow M, Bosilovich M, Gershunov A, Gutowski W, Katz RW, Lee YY, Lim YK, Prabhat (2015) North American extreme temperature events and related large scale meteorological patterns: statistical methods, dynamics, modeling, and trends. Clim Dyn 96:1–34. doi: 10.1007/s00382-015-2638-6

Hashimoto A, Done JM, Fowler LD, Bruyère CL (2015) Tropical cyclone activity in nested regional and global grid-refined simulations. Clim Dyn 1–12. doi: 10.1007/s00382-015-2852-2

Held IM, Zhao M (2011) The response of tropical cyclone statistics to an increase in CO_2 with fixed sea surface temperatures. J Clim 24:5353–5364. doi: 10.1175/JCLI-D-11-00050.1

Hirons LC, Klingaman NP, Woolnough SJ (2015) MetUM-GOML1: a near-globally coupled atmosphere-ocean-mixed-layer model. Geosci Model Dev 8:363–379. doi: 10.5194/gmd-8-363-2015

Holland GJ, Done JM, Douglas R, Ge M (2016, submitted) Global tropical cyclone damage potential. Technical Report, National Center for Atmospheric Research, Boulder, Colorado

Horn M, Walsh K, Zhao M, Camargo SJ, Scoccimarro E, Murakami H, Wang H, Ballinger A, Kumar A, Shaevitz DA, Jonas JA, Oouchi K (2014) Tracking scheme dependence of simulated tropical cyclone response to idealized climate simulations. J Clim 27(24):9197–9213. doi: 10.1175/JCLI-D-14-00200.1

Kim D, Sobel AH, Del Genio AD, Chen Y, Camargo SJ, Yao MS, Kelley M, Nazarenko L (2012) The tropical subseasonal variability simulated in the NASA GISS general circulation model. J Clim 25:4641–4659. doi: 10.1175/JCLI-D-11-00447.1

Knapp KR, Kruk MC, Levinson DH, Diamond HJ, Neumann CJ (2010) The international best track archive for climate stewardship (IBTrACS). Bull Am Meteorol Soc 91:363–376. doi: 10.1175/2009BAMS2755.1

Knutson TR, Tuleya RE, Shen W, Ginis I (2001) Impact of CO_2-induced warming on hurricane intensities as simulated in a hurricane model with ocean coupling. J Clim 14:2458–2468. doi: 10.1175/1520-0442(2001)014

Knutson TR, Sirutis JJ, Garner ST, Held IM, Tuleya RE (2007) Simulation of the recent multidecadal increase of Atlantic hurricane activity using an 18-km-grid regional model. Bull Am Meteorol Soc 88:1549–1565. doi: 10.1175/BAMS-88-10-1549

Knutson TR, Sirutis JJ, Garner ST, Vecchi GA, Held IM (2008) Simulated reduction in Atlantic hurricane frequency under twenty-first-century warming conditions. Nat Geosci 1:359–364. doi: 10.1038/ngeo202

Knutson TR, McBride JL, Chan J, Emanuel K, Holland G, Landsea C, Held I, Kossin JP, Srivastava AK, Sugi M (2010) Tropical cyclones and climate change. Nat Geosci 3:157–163. doi: 10.1038/ngeo779

Kuo HL (1965) On formation and intensification of tropical cyclones through latent heat release by cumulus convection. J Atmos Sci 22:40–63

Landsea CW, Vecchi GA, Bengtsson L, Knutson TR (2010) Impact of duration thresholds on Atlantic tropical cyclone counts. J Clim 23(10):2508–2519. doi: 10.1175/2009JCLI3034.1

LaRow TE, Lim YK, Shin DW, Chassignet EP, Cocke S (2008) Atlantic basin seasonal hurricane simulations. J Clim 21(13):3191–3206. doi: 10.1175/2007JCLI2036.1

Lawrence BN, Bennett VL, Churchill J, Juckes M, Kershaw P, Pascoe S, Pepler S, Pritchard M, Stephens A (2013) Storing and manipulating environmental big data with JASMIN. In: IEEE international conference on Big Data, 2013. IEEE, pp 68–75

Li H, Sriver RL, Goes M (2015) Modeled sensitivity of the northwestern pacific upper-ocean response to tropical cyclones in a fully coupled climate model with varying ocean grid resolution. J Geophys Res: Oceans. doi: 10.1002/2015JC011226

Li Z, Yu W, Li T, Murty V, Tangang F (2013) Bimodal character of cyclone climatology in the Bay of Bengal modulated by monsoon seasonal cycle*. J Clim 26(3):1033–1046

Lin Y, Zhao M, Zhang M (2015) Tropical cyclone rainfall area controlled by relative sea surface temperature. Nat Commun 6:6591. doi: 10.1038/ncomms7591

Liu Y, Racah E, Prabhat, Correa J, Khosrowshahi A, Lavers D, Kunkel K, Wehner M, Collins WD (2016) Application of deep convolutional neural networks for detecting extreme weather in climate datasets. CoRR abs/1605.01156

McClean J, Bader D, Bryan F, Maltrud M, Dennis J, Mirin A, Jones P, Kim Y, Ivanova D, Vertenstein M, Boyle J, Jacob R, Norton N, Craig A, Worley P (2011) A prototype two-decade fully-coupled fine-resolution CCSM simulation. Ocean Model 39:10–30. doi: 10.1016/j.ocemod.2011.02.011

Mei W, Pasquero C (2013) Spatial and temporal characterization of sea surface temperature response to tropical cyclones*. J Clim 26(11):3745–3765. doi: 10.1175/JCLI-D-12-00125.1

Mirin AA, Worley PH (2011) Improving the performance scalability of the community atmosphere model. Inter J High Perform Comput Appl. doi: 10.1177/1094342011412630

Mizielinski MS, Roberts MJ, Vidale PL, Schiemann R, Demory ME, Strachan J, Edwards T, Stephens A, Lawrence BN, Pritchard M, Chiu P, Iwi A, Churchill J, del Cano Novales C, Kettleborough J, Roseblade W, Selwood P, Foster M, Glover M, Malcolm A (2014) High-resolution global climate modelling: the UPSCALE project, a large-simulation campaign. Geosci Model Dev 7:1629–1640. doi: 10.5194/gmd-7-1629-2014

Murakami H (2014) Tropical cyclones in reanalysis data sets. Geophys Res Lett 41(6):2133–2141. doi: 10.1002/2014GL059519

Murakami H, Sugi M (2010) Effect of model resolution on tropical cyclone climate projections. Sci Online Lett Atmos 6:73–76. doi: 10.2151/sola.2010-019

Murakami H, Wang Y, Yoshimura H, Mizuta R, Sugi M, Shindo E, Adachi Y, Yukimoto S, Hosaka M, Kusunoki S, Ose T, Kitoh A (2012) Future changes in tropical cyclone activity projected by the new high-resolution MRI-AGCM*. J Clim 25:3237–3260. doi: 10.1175/JCLI-D-11-00415.1

Myhre G, Shindell D, Breon FM, Collins W, Fuglestvedt J, Huang J, Koch D, Lamarque JF, Lee D, Mendoza B, Nakajima T, Robock A, Stephens G, Takemura T, Zhang H (2013) Anthropogenic and natural radiative forcing, book section 8. Cambridge University Press, Cambridge, UK/New York, pp 659–740. doi: 10.1017/CBO9781107415324.018, www.climatechange2013.org

Neale RB, Chen CC, Gettelman A, Lauritzen PH, Park S, Williamson DL, Conley AJ, Garcia R, Kinnison D, Lamarque JF, Marsh D, Mills M, Smith AK, Tilmes S, Vitt F, Morrison H, Cameron-Smith P, Collins WD, Iacono MJ, Easter RC, Ghan SJ, X Liu X, Rasch PJ, Taylor M (2012) Description of the NCAR community atmosphere model: CAM5.0. Technical Report NCAR/TN-486+STR;National Center for Atmospheric Research; Boulder, p 268pp

Oouchi K, Yoshimura J, Yoshimura H, Mizuta R, Kusunoki S, Noda A (2006) Tropical cyclone climatology in a global-warming climate as simulated in a 20 km-mesh global atmospheric model: frequency and wind intensity analyses. J Meteorol Soc Jpn 84(2):259–276

Ooyama K (1969) Numerical simulation of the life cycle of tropical cyclones. J Atmos Sci 26:3–40. doi: 10.1175/1520-0469(1969)026<0003:NSOTLC>2.0.CO;2

Patricola CM, Saravanan R, Chang P (2014) The impact of the El Niño – Southern Oscillation and Atlantic meridional mode on seasonal Atlantic tropical cyclone activity. J Clim 27:5311–5328

Powell MD, Reinhold TA (2007) Tropical cyclone destructive potential by integrated kinetic energy. Bull Am Meteorol Soc 88(4):513–526

Prabhat, Rübel O, Byna S, Wu K, Li F, Wehner M, Bethel W (2012) TECA: a parallel toolkit for extreme climate analysis. Proc Comput Sci 9:866–876. doi: 10.1016/j.procs.2012.04.093. Proceedings of the international conference on computational science, 2012

Price JF (1981) Upper ocean response to a hurricane. J Phys Oceanogr 11(2):153–175

Reed KA, Jablonowski C (2011a) Assessing the uncertainty of tropical cyclone simulations in NCAR's community atmosphere model. J Adv Model Earth Syst 3:M08002. doi: 10.1029/2011MS000076

Reed KA, Jablonowski C (2011b) Impact of physical parameterizations on idealized tropical cyclones in the community atmosphere model. Geophys Res Lett 38:L04805. doi: 10.1029/2010GL046297

Reed KA, Jablonowski C (2012) Idealized tropical cyclone simulations of intermediate complexity: a test case for AGCMs. J Adv Model Earth Syst 4:M04001. doi: 10.1029/2011MS000099

Reed KA, Bacmeister JT, Wehner MF, Rosenbloom NA, Bates SC, Lauritzen PH, Truesdale JT, Hannay C (2015) Impact of the dynamical core on the direct simulation of tropical cyclones in a high-resolution global model. Geophys Res Lett 42(9):3603–3608. doi: 10.1002/2015GL063974

Roberts MJ, Vidale PL, Mizielinski MS, Demory ME, Schiemann R, Strachan J, Hodges K, Bell R, Camp J (2015) Tropical cyclones in the upscale ensemble of high resolution global climate models. J Clim 28:574–596. doi: 10.1175/JCLI-D-14-00131.1

Satoh M, Tomita H, Yashiro H, Miura H, Kodama C, Seiki T, Noda AT, Yamada Y, Goto D, Sawada M, Miyoshi T, Niwa Y, Hara M, Ohno T, Iga Si, Arakawa T, Inoue T, Kubokawa H (2014) The non-hydrostatic icosahedral atmospheric model: description and development. Prog Earth Planet Sci 1:18. doi: 10.1186/s40645-014-0018-1

Schenkel BA, Hart RE (2012) An examination of tropical cyclone position, intensity, and intensity life cycle within atmospheric reanalysis datasets. J Clim 25(10):3453–3475. doi: 10.1175/2011JCLI4208.1

Scoccimarro E, Gualdi S, Villarini G, Vecchi GA, Zhao M, Walsh K, Navarra A (2014) Intense precipitation events associated with landfalling tropical cyclones in response to a Warmer climate and increased CO_2. J Clim 27:4642–4654. doi: 10.1175/JCLI-D-14-00065.1

Sillmann J, Kharin VV, Zhang X, Zwiers FW, Bronaugh D (2013) Climate extremes indices in the CMIP5 multimodel ensemble: Part 1. Model evaluation in the present climate. J Geophys Res Atmos 118(4):1716–1733

Small RJ, Bacmeister J, Bailey D, Baker A, Bishop S, Bryan F, Caron J, Dennis J, Gent P, Hsu HM et al (2014) A new synoptic scale resolving global climate simulation using the Community Earth System Model. J Adv Model Earth Syst 6(4):1065–1094. doi: 10.1002/2014MS000363

Strachan J, Vidale PL, Hodges K, Roberts M, Demory ME (2013) Investigating global tropical cyclone activity with a hierarchy of AGCMs: the role of model resolution. J Clim 26(1):133–152. doi: 10.1175/JCLI-D-12-00012.1

Sugi M, Murakami H, Yoshimura J (2009) A reduction in global tropical cyclone frequency due to global warming. SOLA 5:164–167. doi: 10.2151/sola.2009-042

Taylor M, Tribbia J, Iskandarani M (1997) The spectral element method for the shallow water equations on the sphere. J Comput Phys 130:92–108

Taylor MA (2011) Conservation of mass and energy for the moist atmospheric primitive equations on unstructured grids. In: Lauritzen PH, Jablonowski C, Taylor MA, Nair RD (eds) Numerical techniques for global atmospheric models. Lecture notes in computational science and engineering, vol 80. Springer, Berlin/London, pp 357–380

Tsutsui Ji, Kasahara A (1996) Simulated tropical cyclones using the National Center for Atmospheric Research community climate model. J Geophys Res: Atmospheres 101(D10):15013–15032. doi: 10.1029/95JD03774

Vecchi GA, Villarini G (2014) Next season's hurricanes. Science 343:618–619. doi: 10.1126/science.1247759

Villarini G, Lavers DA, Scoccimarro E, Zhao M, Wehner MF, Vecchi GA, Knutson TR, Reed KA (2014) Sensitivity of tropical cyclone rainfall to idealized global-scale forcings. J Clim 27:4622–4641. doi: 10.1175/JCLI-D-13-00780.1

Vitart F, Anderson JL, Stern WF (1997) Simulation of interannual variability of tropical storm frequency in an ensemble of GCM integrations. J Clim 10(4):745–760

Walsh KJE (2008) The ability of climate models to generate tropical cyclones: implications for prediction. In: Peretz L (ed) Climate change research progress. Nova Publishers, New York, pp 313–329

Walsh KJE, Fiorino M, Landsea CW, McInnes KL (2007) Objectively determined resolution-dependent threshold criteria for the detection of tropical cyclones in climate models and reanalyses. J Clim 20:2307. doi: 10.1175/JCLI4074.1

Walsh KJE, Camargo S, Vecchi G, Daloz AS, Elsner J, Emanuel K, Horn M, Lim YK, Roberts M, Patricola C, Scoccimarro E, Sobel A, Strazzo S, Villarini G, Wehner M, Zhao M, Kossin J, LaRow T, Oouchi K, Schubert S, Wang H, Bacmeister J, Chang P, Chauvin F, Jablonowski C, Kumar A, Murakami H, Ose T, Reed K, Saravanan S, Yamada Y, Zarzycki C, Vidale PL, Jonas J, Henderson N (2015) Hurricanes and climate: the U.S. CLIVAR working group on hurricanes. Bull Am Meteorol Soc 96:997–1017. doi: 10.1175/BAMS-D-13-00242.1

Wehner MF, Bala G, Duffy P, Mirin AA, Romano R (2010) Towards direct simulation of future tropical cyclone statistics in a high-resolution global atmospheric model. Adv Meteorol 2010:915303. doi: 10.1155/2010/915303

Wehner MF, Oliker L, Shalf J, Donofrio D, Drummond LA, Heikes R, Kamil S, Kono C, Miller N, Miura H, Mohiyuddin M, Randall D, Yang WS (2011) Hardware/software co-design of global cloud system resolving models. J Adv Model Earth Syst 3(4):n/a–n/a. doi: 10.1029/2011MS000073, http://dx.doi.org/10.1029/2011MS000073, m10003

Wehner MF, Reed KA, Li F, Prabhat, Bacmeister JT, Chen CT, Paciorek C, Gleckler PJ, Sperber KR, Collins WD, Gettelman A, Jablonowski C (2014) The effect of horizontal resolution on simulation quality in the Community Atmospheric Model, CAM5.1. J Adv Model Earth Syst 6(4):980–997. doi: 10.1002/2013MS000276

Wehner MF, Prabhat, Reed KA, Stone D, Collins WD, Bacmeister JT (2015) Resolution dependence of future tropical cyclone projections of CAM5.1 in the US CLIVAR hurricane working group idealized configurations. J Clim 28:3905–3925. doi: 10.1175/JCLI-D-14-00311.1

Wendel J (2006) Time to replace the Saffir–Simpson hurricane scale? Eos 87(1):3–6

Wendel J (2015) Does U.S. hurricane rating scale get the danger right? Eos 96. doi: 10.1029/2015EO034841

Wu CM, Arakawa A (2014) A unified representation of deep moist convection in numerical modeling of the atmosphere. Part II. J Atmos Sci 71:2089–2103. doi: 10.1175/JAS-D-13-0382.1

Zarzycki CM, Jablonowski C (2014) A multidecadal simulation of Atlantic tropical cyclones using a variable-resolution global atmospheric general circulation model. J Adv Model Earth Syst 6:805–828. doi: 10.1002/2014MS000352

Zarzycki CM, Jablonowski C (2015) Experimental tropical cyclone forecasts using a variable-resolution global model. Mon Weather Rev 143(10):4012–4037. doi: 10.1175/MWR-D-15-0159.1

Zarzycki CM, Jablonowski C, Taylor MA (2014a) Using variable resolution meshes to model tropical cyclones in the Community Atmosphere Model. Mon Weather Rev 142(3):1221–1239. doi: 10.1175/MWR-D-13-00179.1

Zarzycki CM, Levy MN, Jablonowski C, Overfelt JR, Taylor MA, Ullrich PA (2014b) Aquaplanet experiments using CAM's variable-resolution dynamical core. J Clim 27(14):5481–5503. doi: 10.1175/JCLI-D-14-00004.1

Zarzycki CM, Jablonowski C, Thatcher DR, Taylor MA (2015) Effects of localized grid refinement on the general circulation and climatology in the Community Atmosphere Model. J Clim 28(7):2777–2803. doi: 10.1175/JCLI-D-14-00599.1

Zhao M, Held IM (2012) TC-Permitting GCM simulations of hurricane frequency response to Sea Surface Temperature anomalies projected for the late-twenty-first century. J Clim 25:2995–3009. doi: 10.1175/JCLI-D-11-00313.1

Zhao M, Held IM, Lin SJ, Vecchi GA (2009) Simulations of global hurricane climatology, interannual variability, and response to global warming using a 50-km resolution GCM. J Clim 22:6653–6678

Zhao M, Held IM, Lin SJ (2012) Some counterintuitive dependencies of tropical cyclone frequency on parameters in a GCM. J Atmos Sci 69(7):2272–2283. doi: 10.1175/JAS-D-11-0238.1

Chapter 9
Analysis of Atlantic Tropical Cyclone Landfall Forecasts in Coupled GCMs on Seasonal and Decadal Timescales

Joanne Camp and Louis-Philippe Caron

Abstract In this chapter we present advances in forecasting Atlantic tropical cyclone (TC) landfall statistics at both seasonal and multi-annual timescales using coupled global climate models. First, we demonstrate potential for forecasting TC landfall frequency on seasonal timescales using the Met Office seasonal forecast system, GloSea5, in some regions: statistically significant skill is found in the Caribbean and moderate skill is found for Florida. In contrast, low skill is found along the US Coast as a whole. We show that the skill over the Caribbean is likely due to a good model response to El Niño–Southern Oscillation (ENSO) forcing. Lack of skill along the US Coast may be due to a weaker influence from ENSO compounded by a low bias in model storm tracks crossing the US coastline. Secondly, we demonstrate that it is possible to construct reliable 4-year mean forecasts of landfalling hurricane numbers in the Atlantic using initialised global climate models to predict an index that relies on subpolar gyre temperature and subtropical sea level pressure, two quantities with links to hurricane activity. Furthermore, we give evidence that the forecast system anticipates large changes in at least one of the two components of this index, which suggests that the technique could be used to forecast shifts between active and inactive regimes of hurricane activity in the Atlantic.

J. Camp (✉)
Met Office Hadley Centre, Exeter, UK
e-mail: joanne.camp@metoffice.gov.uk

L.-P. Caron
Earth Science Department, Barcelona Supercomputing Center, Nexus II building, carrer Jordi Girona 29, 08034 Barcelona, Spain
e-mail: louis-philippe.caron@bsc.es

213

1   Introduction

Atlantic tropical cyclone (TC) activity fluctuates on various timescales, ranging from intra-seasonal to decadal (and possibly longer). The El Niño–Southern Oscillation (ENSO) is the dominant climate mode influencing this variability on a year-to-year basis (Camargo et al. 2010), modulating both basin-wide activity and hurricane landfalls in the USA (e.g. Klotzbach 2011a) and Caribbean (e.g. Klotzbach 2011b; Tartaglione et al. 2003). Indeed, recognising the link between ENSO and Atlantic hurricane frequency led to the first Atlantic hurricane seasonal forecasts in the 1980s (Gray 1984a,b).

Since then, many other climate factors modulating Atlantic hurricane activity have been identified (see Caron et al. 2015a for an overview), and to the extent that these climate influences are predictable, they can be used (individually or in combination) to estimate upcoming hurricane activity. This is done explicitly in statistical forecasts, which are constructed using past observations of seasonal hurricane activity and precursive climate indices. However, the short period of reliable observational data (typically since the 1970s with the advent of satellite data) can limit the sample size that can be used to develop such statistical models. Furthermore these methods rely on *past* observed relationships between climate predictors and TC activity, which may not remain stationary with changing climate (e.g. Klotzbach 2007).

Over the last two decades, there has been increasing interest in seasonal dynamical predictions of TC activity with initialised general circulation models (GCMs). These have been used to explicitly forecast TC statistics (e.g. Camp et al. 2015; Vitart et al. 1997), as well as predicted parameters (e.g. sea surface temperatures (SSTs)) within statistical forecasting models (e.g. Vecchi et al. 2011). It has long been recognised that even low-resolution climate models (grid spacing of 100 km or coarser at midlatitudes) are capable of reproducing tropical cyclone-like vortices (Bengtsson et al. 1982, 1996; Vitart et al. 1997; Walsh and Watterson 1997). These model representations of TCs tend to have lower wind speeds and larger diameters than observed storms, but have realistic climatology in terms of geographical distribution and season of occurrence (Camargo and Wing 2015). The observed relationship between ENSO and Atlantic hurricane activity is also well captured (e.g. Vitart et al. 1997), and, as a result, the predictive skill of Atlantic TC frequency using such methods is competitive with statistical forecasts (e.g. Vecchi et al. 2014; Vitart et al. 2007). Dynamical seasonal predictions of Atlantic TC activity have been issued by various centres, including the UK Met Office (Camp et al. 2015), European Centre for Medium-Range Weather Forecasts (ECMWF; Vitart and Stockdale 2001), Florida State University (LaRow et al. 2010) and the National Oceanic and Atmospheric Administration's (NOAA) Geophysical Fluid Dynamics Laboratory (GFDL; Vecchi et al. 2011, 2014). Such forecasts typically provide predictions of basin-wide numbers of TCs, hurricanes and accumulated cyclone energy (ACE) index (a measure of the combined strength and duration of TCs) during the season; dynamical forecasts of TS landfall are not currently available.

As dynamical models become more advanced in terms of resolution, physics and dynamical core, their ability to resolve characteristics of observed TCs—such as their geographical distribution, track, frequency, interannual variability, structure and intensity—also tends to improve (e.g. Caron et al. 2010; Murakami et al. 2012; Reed et al. 2015; Roberts et al. 2015; Shaevitz et al. 2014; Strachan et al. 2013; Zhao et al. 2009). However, such models are computationally expensive to run, and therefore it has only been in recent years that increases in supercomputing power have enabled high-resolution GCMs (grid spacing of 50 km or finer at midlatitudes) to be used for seasonal TC predictions (e.g. Camp et al. 2015; Chen and Lin 2011, 2013; Vecchi et al. 2014; Zhao et al. 2010). The increase in resolution, combined with more realistic TC tracks, now provides an opportunity for seasonal forecasts of TC landfall risk to be explored.

In comparison, decadal or multi-annual hurricane forecasts are still in their experimental stage. Multi-annual forecasts are already being produced by some catastrophe modelling firms which typically construct them using a range of statistical forecasting models. Recently, it has also been shown (Caron et al. 2014; Smith et al. 2010; Vecchi et al. 2013) that it is possible to produce skilful predictions of Atlantic hurricane activity over lead times of several years using initialised coupled GCMs. For those vulnerable to losses from TC damage, forecasts covering multiple seasons may be more readily incorporated into planning and management strategies, because the lead time allows greater opportunity to integrate forecasts with fixed planning schedules. For example, TC forecasts covering a 5-year horizon can be used in the pricing of contracts by the insurance and reinsurance industry (Jewson et al. 2009), for which hurricane damage can be the leading cause of losses during a given year.

On longer (multi-decadal) timescales, many of the climate factors influencing interannual Atlantic hurricane variability, such as ENSO, tend to average out, and prolonged periods of high and low hurricane activity are usually attributed to Atlantic multi-decadal variability (AMV) of SSTs, also referred to as the Atlantic Multi-decadal Oscillation (AMO) (Dunstone et al. 2013; Goldenberg et al. 2001; Knight et al. 2006; Zhang and Delworth 2006). The link between the AMO/AMV and Atlantic hurricane activity is well documented (Kossin and Vimont 2007; Vimont and Kossin 2007; Zhang and Delworth 2006) and has been shown to operate through a modulation of various climate factors influencing cyclogenesis: SSTs, vertical wind shear, low-level convergence and low-level vorticity over the tropical Atlantic and a shift in the intertropical convergence zone. Periods of high (low) Atlantic TC activity have been associated with the positive (negative) phase of the AMO/AMV.

In this chapter, we present recent advances in seasonal and multi-annual forecasting of Atlantic hurricane activity using general circulation models, with a particular focus on the skill of these systems at predicting landfall statistics. A list of acronyms used in this chapter is given in Table 9.1.

Table 9.1 Frequently used acronyms

ACC	Anomaly correlation coefficient
AMO	Atlantic multi-decadal oscillation
AMV	Atlantic multi-decadal variability
BSS	Brier skill score
CGCM	Coupled global climate model
EN	El Niño
ENSO	El Niño Southern Oscillation
GCM	Global climate model
LN	La Niña
MDR	Main Development Region
MME	Multi-model ensemble
RMSSS	Root mean square skill score
SLP(A)	Sea level pressure (anomaly)
SPG	Sub polar gyre
SST(A)	Sea surface temperature (anomaly)
TC	Tropical cyclone

2 Seasonal Forecasting of Landfall Risk

Seasonal forecasts of TC landfall risk are not currently issued operationally from dynamical models. While such systems have been shown to have skill forecasting Atlantic basin-wide numbers of TCs (e.g. Vitart et al. 2007), the basin-wide frequency is not strongly correlated with US hurricane landfalls and therefore has limited use as a proxy for forecasting TC landfall frequency. An alternative is to forecast landfall using the model TC tracks directly; however, this also presents problems: low-resolution GCMs—generally used for operational seasonal forecasting—typically tend to simulate larger TC vortices than observed, which can lead to biases in TC track (e.g. Camargo 2013). Furthermore, observed TC tracks and landfall are also largely governed by weather conditions prior to landfall, which are only predictable on shorter range (e.g. 1–5 days) rather than seasonal timescales. Nevertheless, seasonal average preferences in TC track, such as those associated with ENSO (e.g. Wang et al. 2014), may be predictable on seasonal timescales. High-resolution GCMs, which can better represent observed TC track and geographical distribution, now provide the opportunity for seasonal forecasts of TC landfall risk to be explored further.

Two recent studies—Vecchi et al. (2014) and Camp et al. (2015)—examined the ability of fully coupled ocean-atmosphere GCMs with ∼50 km midlatitude resolution to predict changes in landfall risk in the North Atlantic basin. Both studies, despite using different techniques and models, yielded similar results: significant skill was shown for regional TC landfall predictions in the Caribbean, whereas low skill was found for the US Coast.

Here we expand the work of Camp et al. (2015) to more closely examine landfalls in the North Atlantic basin. The purpose of this assessment is twofold: to investigate

potential causes of both the low predictive skill of TC landfalls along the US Coast and the comparatively higher skill in the Caribbean. To do this, we look at various landfall statistics in GloSea5 and observations, including frequency, interannual variability, genesis locations and the relationship with ENSO. We also examine landfalls over smaller regions of the USA (such as the US Gulf Coast) and the Caribbean, to identify whether GloSea5 has any subregional skill.

2.1 Models, Data and Analysis

The Met Office Global Seasonal Forecast System 5 (GloSea5; MacLachlan et al. 2014) is used in this study. GloSea5 is a fully coupled ocean-atmosphere GCM: the atmospheric component has a horizontal resolution of 0.83° longitude x 0.55° latitude (N216; ~53 km at 55 °N and ~93 km at the equator) and 85 levels in the vertical; the ocean component has a horizontal resolution of 0.25° and 75 vertical levels.

The performance of GloSea5 is examined using retrospective forecasts (also known as hindcasts) for the North Atlantic TC season (June–November) over the 22-year period 1992–2013. The hindcasts are initialised on three consecutive weeks centred around 1 May (25 April, 1 May and 9 May) using reanalyses from the ECMWF Interim Reanalysis project (ERA-Interim; Dee et al. 2011). For each of the three weeks, ten ensemble members are run for each year, providing a total of 30 members per year.

TCs are detected and tracked in each ensemble member using a feature-based algorithm (TRACK; Bengtsson et al. 2007; Hodges 1995, 1996, 1999), with the same configuration as described in Camp et al. (2015). Observed data for the North Atlantic basin are obtained from the National Hurricane Center's best-track Hurricane Database (HURDAT2; Landsea and Franklin 2013). In this analysis, the term "tropical cyclone" is used to describe all observed storms which reach a maximum intensity of tropical storm strength or higher; we have not included the contribution from subtropical storms, which make up a very small portion of the observed database (only three such storms were recorded during the study period, and none of these made landfall).

A TC in observations and model data is considered to have made landfall when its track—generated from 6-hourly positions of mean sea level pressure minima—crosses a coastline. We consider landfalls across a total of seven coastal regions: the US Coast (further subdivided into the Gulf, Florida and East Coast) and the Caribbean (further subdivided into the Eastern and Western Caribbean). The coastline boundaries for each of these seven regions are shown in Fig. 9.1. The US Coast and Caribbean regions are the same as those used in Camp et al. (2015); however, we reproduce the results again here for completeness and comparison. The counting method is as follows: for each region we simply count the number of TCs crossing the coastline. Each storm can only count towards the landfall total
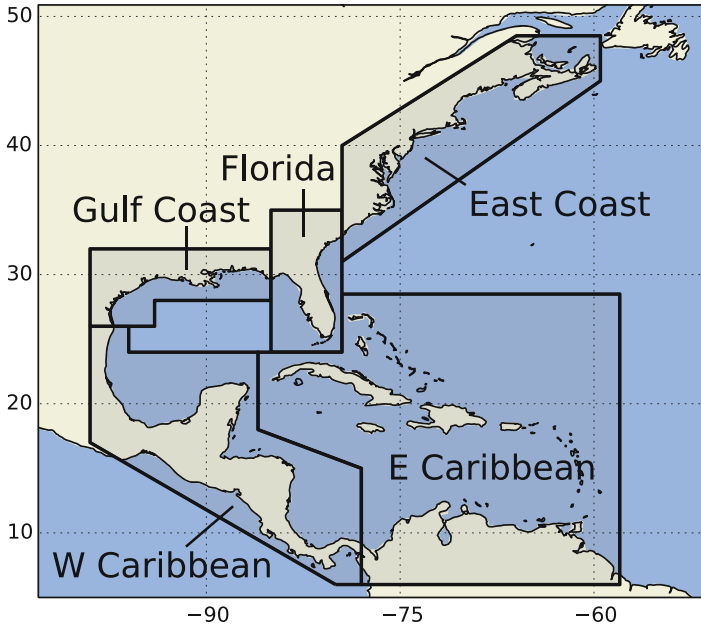
Fig. 9.1 Tropical cyclone landfall regions: US Gulf Coast, Florida, East Coast (including Nova Scotia), Western Caribbean and Eastern Caribbean. The "US Coast" encompasses the US Gulf, Florida and East Coast, and the "Caribbean" encompasses the Eastern and Western Caribbean. Note that a TC is considered to have made landfall when its track crosses the coastline within a region boundary. Both the US Coast and the Caribbean regions are the same as those defined in Camp et al. (2015)

in each region once. Therefore, because a single storm can make landfall in more than one region during its lifetime, the total number of landfalling storms in the Caribbean, for example, may not equal the combined total for the Eastern and Western Caribbean; likewise, the landfall frequency along the US Coast may not equal the combined total for the Gulf, Florida and East coasts.

To assess the relationship between TC landfall frequency and ENSO, observed SST anomalies (SSTAs) for the equatorial Pacific Niño3.4 region (120°–170°W, 5°S–5°N) are obtained from the NOAA Climate Prediction Center (CPC 2015).

2.2 Results

2.2.1 US and Caribbean Landfall Frequency

Over the 22-year period June–November 1992–2013, a total of 294 observed TCs formed in the North Atlantic (average 13.4 per year), and of these 152 (52%)

made landfall in the USA and Caribbean (average 6.9 landfalls per year). Along the US Coast, the Gulf and East Coast experienced the greatest average number of landfalls per year (2.0 and 1.8, respectively) and Florida the fewest (1.3); and in the Caribbean, the Eastern Caribbean experienced more landfalls (2.7) than the Western Caribbean (2.3).

In GloSea5, an average of 6.1 TCs formed in the Atlantic basin per member per year. Of these, an average of 1.8 TCs (29 %) made landfall in the USA and Caribbean: just over half the percentage of landfalling storms per year compared to observations. Along the US Coast, GloSea5 simulates the greatest average number of landfalls per year over Florida (0.4) and the fewest along the Gulf (0.2) and East (0.3) coasts, which is the opposite pattern to that seen in observations. However, we note that the landfall rates for these regions are low and the sample of 22 years is relatively small; thus the difference may not be statistically significant. In the Caribbean, GloSea5 simulates a greater average number of landfalls per year in the Eastern Caribbean (1.1) compared to the Western Caribbean (0.4), as seen in observations, although the difference is more pronounced.

2.2.2 US and Caribbean Landfall Track Density

The track density of all TCs that made landfall in the USA and Caribbean during June–November 1992–2013 is shown for GloSea5 and observations in Fig. 9.2. A corresponding track density difference (GloSea5 minus observations) is also provided.

In observations, the greatest frequency of landfalling TC tracks is concentrated in the western half of the basin: in the western Atlantic hurricane Main Development Region (MDR; 10–20 °N, 20–60 °W), Caribbean Sea, Gulf of Mexico and to the east of Florida (Fig. 9.2a). This pattern is well simulated by GloSea5 (Fig. 9.2b); however, the frequency of landfalling TC tracks is much lower than observed, particularly in the western Caribbean Sea, Gulf of Mexico and along the US Gulf Coast (Fig. 9.2c). This may in part be due to a deficit in the total *basin-wide* TC track density in these regions, which was highlighted in Camp et al. (2015) and also seen in other GCMs (e.g. Mei et al. 2014; Strazzo et al. 2013; Vecchi et al. 2014) and regional climate models (Caron and Jones 2011). Deficits in landfall track density are also seen along the eastern US Coast, suggesting that model storms may not reach higher latitudes as frequently as observed storms and/or that too few storms recurve towards the eastern US Coast from the Atlantic MDR and Caribbean.

The higher frequency of landfalls in Florida and the Eastern Caribbean in GloSea5 is likely due to the mean location of model storm tracks, which take a preferential path from the Atlantic MDR towards the Eastern Caribbean and Florida (Fig. 9.2b). In contrast, too few storms move from the MDR into the Caribbean Sea and Gulf of Mexico and into higher latitudes along the US East Coast, therefore resulting in a lower landfall frequency in these regions.
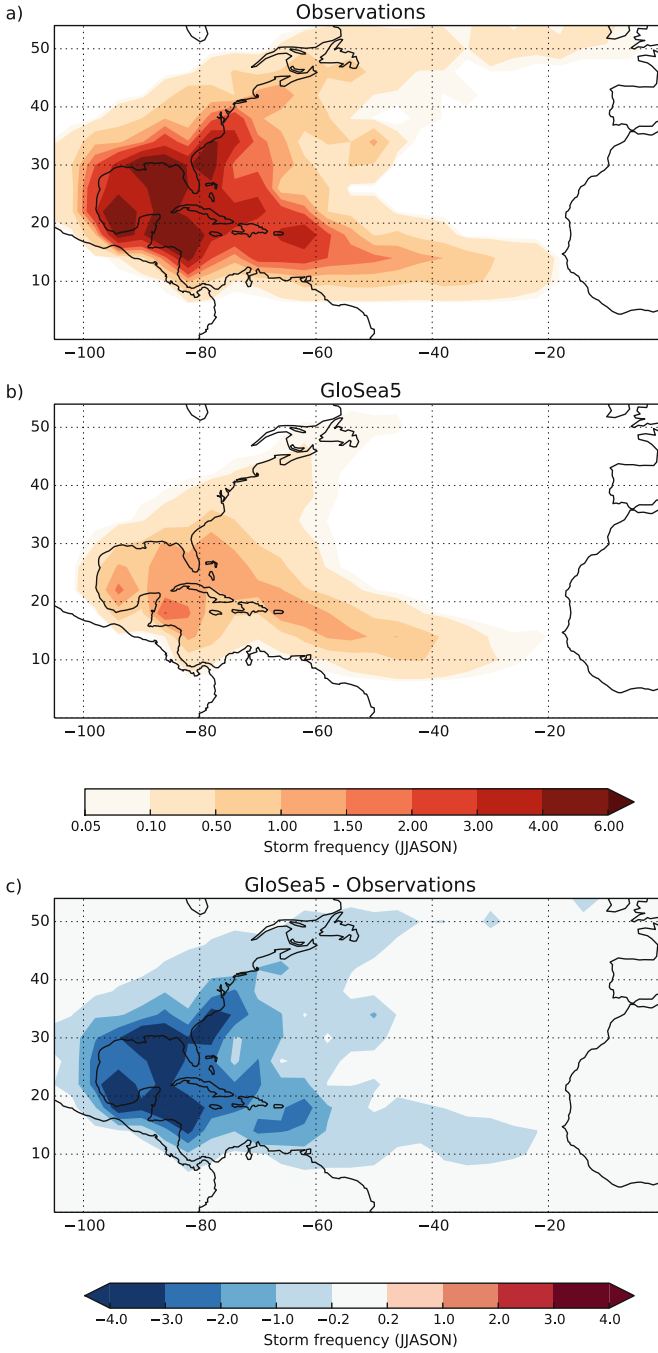
Fig. 9.2 Average seasonal track density (transits per 4°×4° box) of US and Caribbean landfalling TCs in (**a**) observations, (**b**) GloSea5 and (**c**) GloSea5 minus observations over the period June–November (JJASON) 1992–2013. GloSea5 results are averaged over all ensemble members

2.2.3 Genesis Locations

In addition to the low frequency of landfalling TC tracks passing through
the Caribbean Sea, Gulf of Mexico and close to the US Coast, it is possible
that the number of landfalling storms *forming* in these regions is also too low.
To investigate this, we examine the genesis location of all landfalling TCs in the
USA and Caribbean from June–November 1992–2013. In order to aid comparison
between GloSea5 and observations, we divide the genesis density for each year by
the total number of landfalling storms. Results are presented in Fig. 9.3.
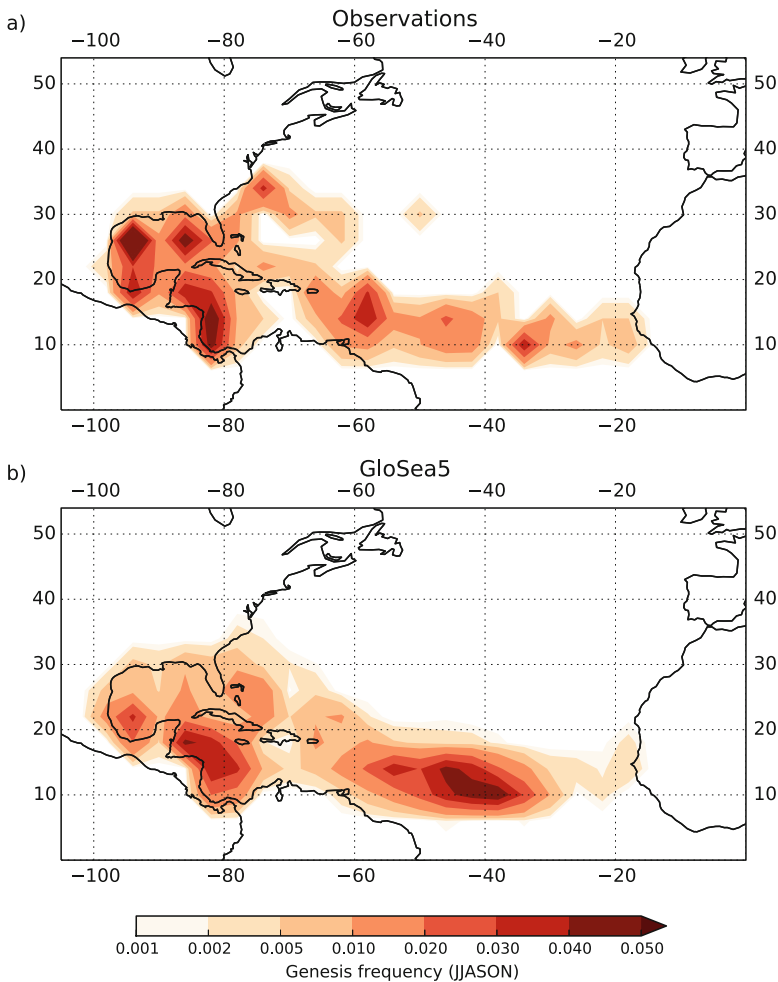
Fig. 9.3 Average seasonal genesis density (per 4°×4° box) of all US and Caribbean landfalling
TCs, measured as a proportion of the total number of landfalling US and Caribbean TCs, in (**a**)
observations and (**b**) GloSea5 (all ensemble members) over the period June–November (JJASON)
1992–2013

In observations, the majority of US and Caribbean landfalling storms form in the western tropical Atlantic MDR or close to the coastline in the western Caribbean Sea and Gulf of Mexico. An additional minor peak in TC genesis is found in the western subtropical Atlantic close to the US East Coast. This pattern of genesis is generally well captured by GloSea5; however, the frequency of genesis, relative to the total landfall frequency, is too high in the central MDR and too low in the Gulf of Mexico and off the US East Coast.

In GloSea5, the high frequency of genesis in the MDR, combined with the preference in tracks to move towards the Eastern Caribbean and Florida, is the likely cause of the high frequency of landfalls in the latter regions. It may also be the primary reason why the greatest number of landfalls along the US Coast occurs in Florida in GloSea5, compared to the US Gulf and East Coast as seen in observations. It could also account for the greater difference in landfall frequency between the Eastern and Western Caribbean in GloSea5 compared to observations. Conversely, the low genesis frequency in the Gulf of Mexico is the likely reason why the Gulf Coast sees the fewest landfalls in GloSea5, since many observed TCs that form in the Caribbean Sea and Gulf of Mexico later make landfall here (Lyons 2004). Finally, the low frequency of genesis off the US East Coast, combined with the low frequency of TC tracks from the Atlantic MDR that reach higher latitudes, is the likely cause of the low landfall frequency along the US East Coast in GloSea5, compared to observations.

We can also speculate that the low proportion of landfalling TCs in GloSea5 compared to the total basin-wide count may also be due to preferred regions of TC genesis and tracks. For example, many of the storms in GloSea5 form in the Atlantic MDR: some of these make landfall in the Eastern Caribbean and Florida; however many recurve without making landfall (not shown). In contrast, very few storms in GloSea5 form in the Gulf of Mexico, many of which make landfall along the US Gulf Coast in observations.

2.2.4 Interannual Variability

Time series of TC landfalls along the US Coast, Caribbean and each of the individual subregions are shown for observations and GloSea5 over the period June–November 1992–2013 in Fig. 9.4. Corresponding linear correlations between observations and the GloSea5 ensemble-mean landfall count are shown in Table 9.2.

Overall, we find moderate, but significant, skill (at the 5 % level) for predictions of TC landfall frequency in the Caribbean (linear correlation of 0.69), Eastern Caribbean (0.52), Florida (0.41) and Western Caribbean (0.39). Along the US Coast, we find low skill (0.22, not significant), and along the US Gulf and East Coasts, we find no skill (−0.01 and −0.06, respectively). However, it is worth noting that the landfall regions assessed here are small and the frequency of landfalling storms is low both in observations and GloSea5; thus small differences between observed and model-predicted landfalls, particularly over this short time period, can have a large impact on correlation scores.
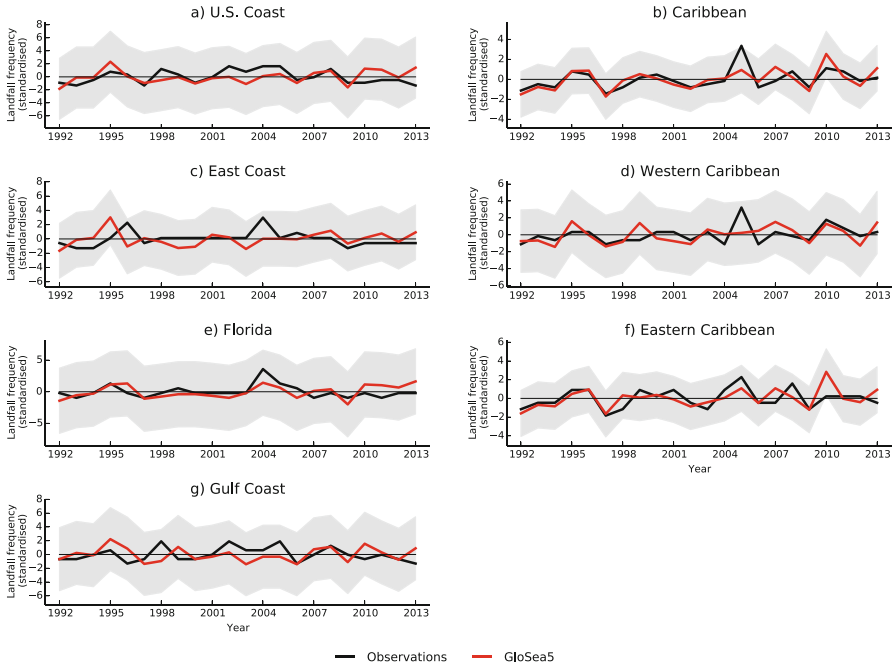
Fig. 9.4 Standardised TC landfall frequency in each of the regions defined in Fig. 9.1 over the period June–November 1992–2013. Observations are in *black*; GloSea5 ensemble mean is in *red*. The *grey shading* illustrates the model ensemble spread measured as ± 1 standard deviation about the ensemble mean for each year. Results are standardised for each year by subtracting the mean of the whole ensemble for all years and then dividing by the standard deviation of the ensemble means

Table 9.2 Pearson's linear correlations (top) and p-values (bottom) between observed and the GloSea5 ensemble-mean TC landfall frequency along the US Coast, East Coast, Florida, Gulf Coast, Caribbean (Carib), Western Caribbean (W Carib) and Eastern Caribbean (E Carib) over the period June–November 1992–2013. Bold implies statistical significance at the 95 % confidence level

	U.S. Coast	East Coast	Florida	Gulf Coast	Carib	W Carib	E Carib
r	0.22	−0.06	**0.41**	−0.01	**0.69**	**0.39**	**0.52**
p-value	0.16	0.40	0.03	0.49	0.00	0.04	0.01

2.2.5 Relationship with ENSO

One of the most important factors influencing TC landfall variability on interannual timescales is ENSO. In the tropical North Atlantic, hurricane landfalls in the USA and Caribbean are reduced during El Niño (EN) events, whereas they are enhanced during La Niña (LN) events (e.g. Bove et al. 1998; Klotzbach 2011a; Larson et al. 2005; Lyons 2004; Tartaglione et al. 2003).

To investigate whether this relationship is represented in GloSea5, we examine the difference in landfall track density in the USA and Caribbean between EN and LN events and compare these to observations. EN and LN events are here defined as years in which the 3-month (August–October) averaged Niño3.4 SSTA is $\geq 0.5\,°C$ and $\leq$-0.5 $°C$, respectively. Over the period 1992–2013, five years are classified as EN (1997, 2002, 2004, 2006 and 2009) and seven years as LN (1995, 1998, 1999, 2000, 2007, 2010 and 2011). The track density of landfalling TCs during EN and LN events, as well as the track density difference (EN minus LN), is shown for observations and GloSea5 in Fig. 9.5.

In observations, we find a reduction in landfalling TC tracks throughout the MDR, western Atlantic and far western Caribbean Sea and Gulf of Mexico during EN events compared to LN events (Fig. 9.5e). However, in contrast to the literature (e.g. Klotzbach 2011a; Smith et al. 2007; Xie et al. 2002), we do not find a reduction in TC landfalls in the central Caribbean or along the US Coast. This could be due to differences in the classification of EN events (e.g. Klotzbach (2011a) do not include 2004, which was a marginal EN year but had strongly favourable conditions for TC development) as well as the small sample size of observed EN and LN years used. Further investigation reveals that either removing 2004 from the analysis or by using observations over a longer period (we used 1950–2014 as this is the longest period for which CPC SST data are available; see Fig. 9.6) provides results that are in better agreement with the literature. We note, however, that the two main regions of lower track density in the western Atlantic and in the western Caribbean Sea and Gulf of Mexico during EN years relative to LN years are evident in both Figs. 9.5e and 9.6.

In GloSea5 there is a clear reduction in TC landfall frequency throughout the Caribbean and tropical Atlantic during EN events relative to LN events (Fig. 9.5f). Indeed, in the western MDR, GloSea5 shows a statistically significant reduction in track density, which matches the long-term observed response well (Fig. 9.6). Similar observed regions of low track density are also evident over the shorter period 1992–2013 (Fig. 9.5e), although these are not statistically significant. The good response of TC landfall track frequency to ENSO forcing is the likely reason for relatively high skill of interannual predictions of TC landfall in the Caribbean in GloSea5.

Around the US Coast, GloSea5 shows reduced activity (not statistically significant) along the Gulf and Florida coastline, as seen in Klotzbach (2011a). However, GloSea5 shows a significant reduction in TC landfall frequency around the southern tip of Florida, which is not present in observations (Figs. 9.5e and 9.6). Along the US East Coast, we find no significant difference in TC landfall frequency between EN and LN events in GloSea5. In observations, we find a small decrease in TC landfalls during EN events relative to LN events over the period 1950–2014 (Fig. 9.6) and slightly enhanced activity during the period 1992–2013 (Fig. 9.5e), although neither of these are statistically significant. The absence of a strong (i.e. statistically significant) response of TC landfalls to ENSO in observations is likely one of the main reasons why skilful seasonal predictions of TC landfall risk along the US Coast are difficult to provide.
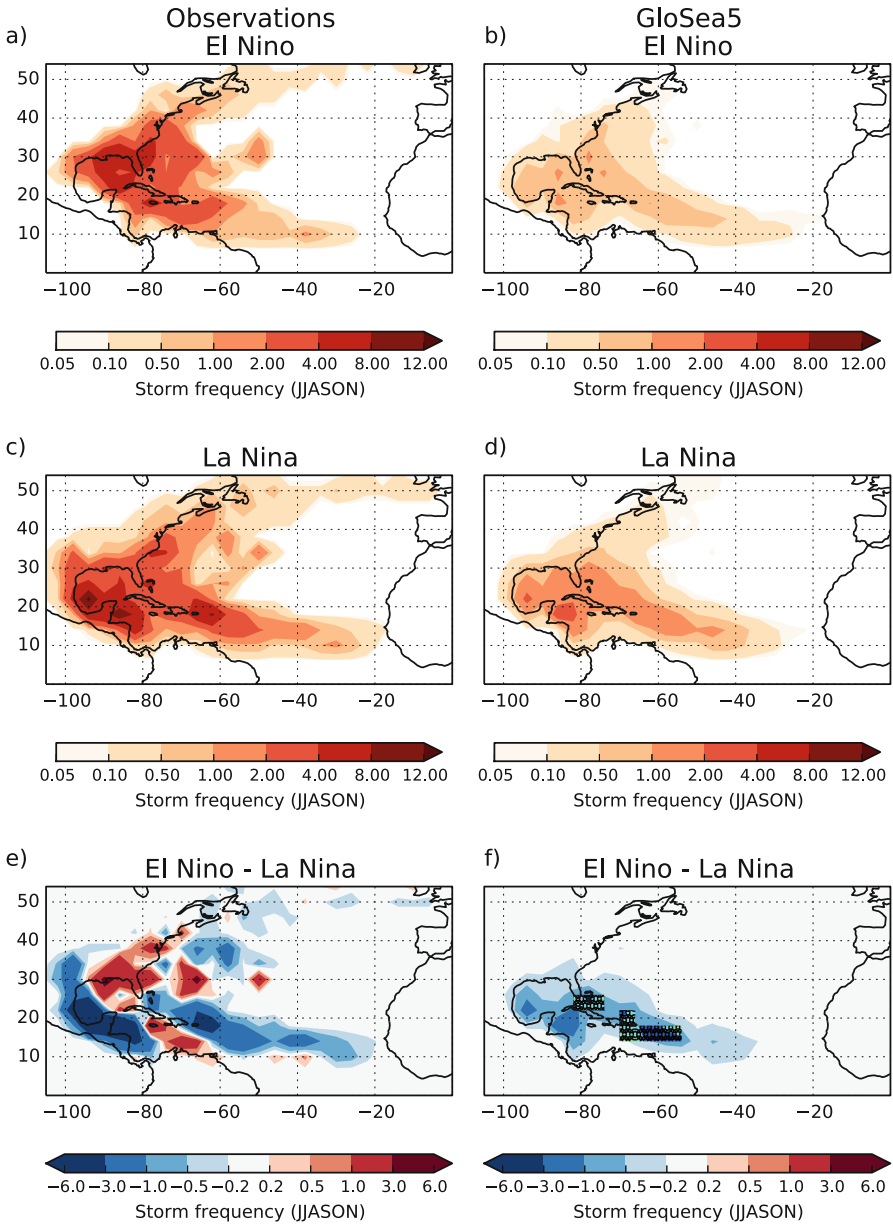
Fig. 9.5 Observed (*left*) and GloSea5 ensemble-mean (*right*) storm track density (number of storm tracks per 4°×4° box) for all landfalling TCs along the US and Caribbean coasts during (**a**, **b**) El Niño and (c, d) La Niña events during June–November (JJASON). (**e**, **f**) show the track density difference (El Niño minus La Niña events): *red* (*blue*) regions show where the track density is enhanced (reduced) during El Niño relative to La Niña events. *Black boxes* show where changes have a p-value < 0.1 using a two-tailed Student's t-test. El Niño years: 1997, 2002, 2004, 2006 and 2009; La Niña years: 1995, 1998, 1999, 2000, 2007, 2010 and 2011
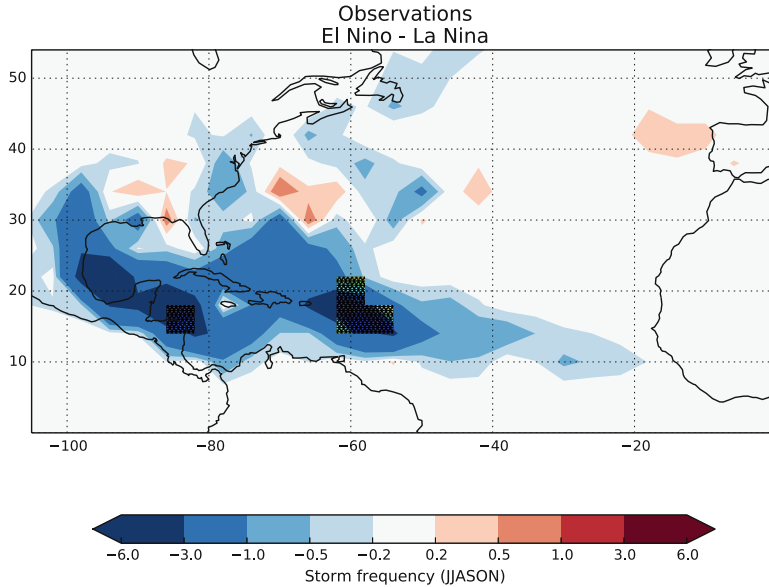
Fig. 9.6 As Fig. 9.5e, but for the US and Caribbean landfall track density difference between EN and LN events averaged over the longer period 1950–2014. There are 18 EN and 16 LN events in total. *Black boxes* show where changes have a p-value < 0.1 using a two-tailed Student's t-test. El Niño years: 1951, 1953, 1957, 1963, 1965, 1969, 1972, 1976, 1977, 1982, 1986, 1987, 1991, 1997, 2002, 2004, 2006 and 2009; La Niña years: 1950, 1954, 1955, 1964, 1970, 1971, 1973, 1975, 1988, 1995, 1998, 1999, 2000, 2007, 2010 and 2011

2.2.6 Conclusion

TC landfalls in the North Atlantic basin are assessed using a fully coupled GCM over the period June–November 1992–2013. Overall, we find significant skill for predictions of TC landfall in the Caribbean and moderate skill (not statistically significant) over Florida; however, low skill is found along the US Coast as a whole. In the Caribbean, the GCM shows a realistic response to ENSO forcing, and the interannual variability in landfall rates is well simulated for both the Eastern and Western Caribbean. In contrast, along the US Coast, we find a deficit of landfalling TCs, particularly along the Gulf and East coasts. This is due to a combination of too few storms forming and tracking through the Caribbean and Gulf of Mexico as well as too few storms reaching higher latitudes from the tropical Atlantic MDR. In addition, we find no significant difference in TC landfall rates along the US Coast between El Niño and La Niña events in either GloSea5 or observations. The absence of a strong relationship between ENSO and US landfalls is one possible reason why skilful seasonal predictions of landfall risk along the US Coast are not presently available. However, the relationship between ENSO and US landfalls is stronger for more intense storms (e.g. Bove et al. 1998); therefore investigating this relationship in GloSea5 would be worthwhile.

3   Decadal Forecasting of Landfall Risk

While tracking tropical cyclone-like disturbances directly (as in the previous section) has the merit of being very intuitive, it is also very computationally expensive and can be difficult to apply in the context of multi-model ensemble decadal forecast studies. This is in large part due to the large volume of data required wherein a set of retrospective decadal predictions typically requires running 5200 years of simulations (10 members, 52 start dates, 10 forecast years) combined with the fact that tracking storms requires high frequency ($\sim$12 h or less) of surface and multiple levels of atmospheric data. As such, it is of interest to devise alternative techniques by which TC activity can easily be estimated using large-scale fields that are readily available by way of international efforts such as the Coupled Model Intercomparison Project (CMIP). Such a first attempt was made by Vecchi et al. (2013), which investigated the use of a statistical relationship between tropical SSTs and Atlantic hurricane activity; however they concluded that most of the skill they had obtained originated from persisting the initial conditions. Of particular interest was the failure to predict the upward shift in hurricane activity that occurred in the mid-1990s. Skilful predictions of such consequential climate shifts are a prerequisite for decadal forecasts to be considered useful.

Smith et al. (2010) and Dunstone et al. (2011) argue that much of the long-term hurricane predictability that they identified in their GCM could be traced back to the North Atlantic subpolar gyre (SPG), a region where initialised climate simulations show a high level of skill at the multi-annual timescale. They showed that changes in surface temperature over the SPG could be linked to changes in the atmospheric circulation over the Atlantic MDR, more specifically the ascending branch of the Hadley circulation, which in turn impacted TC formation in their climate simulations. Caron et al. (2015b) suggested taking advantage of the relatively high skill displayed by decadal forecast systems over the northern North Atlantic by using a proxy index of the AMV (Klotzbach and Gray 2008) to produce multi-annual forecasts of Atlantic TC activity. Constructed using SSTs over the SPG as well as tropical and extratropical Atlantic sea level pressures (SLPs), this index has been shown to vary with Atlantic hurricane activity over the course of the twentieth century (ibid.) and is defined such that

$$AMV_{index} = SSTA - SLPA \qquad (9.1)$$

where *SSTA* is the standardised annual mean SST anomaly over the North Atlantic subpolar gyre ($50\,^{\circ}N$, $60\,^{\circ}N$, $50\,^{\circ}W$, $10\,^{\circ}W$) and *SLPA* is the standardised annual mean sea level pressure anomaly over the tropical and extratropical North Atlantic ($0\,^{\circ}$, $50\,^{\circ}N$, $70\,^{\circ}W$, $10\,^{\circ}W$; see boxes in Fig. 9.8). Caron et al. (2015b) showed that an ensemble of initialised forecasts showed skill at predicting this index over a 5-year horizon, which led to useful information on multi-annual levels of ACE index. Here, we expand on this work by investigating whether this technique can further be used to make reliable forecasts of hurricane landfall statistics over multiple seasons.

3.1 Methodology

3.1.1 Models and Observational Data

Our analysis relies on two different multi-model ensembles (MMEs) of 10-year long simulations performed within the context of the CMIP5 project (GFDL-CM2.1 (Delworth et al. 2006); HadCM3 (Gordon et al. 2000); MIROC5 (Watanabe et al. 2010)) and SPECS project (MPI-ESM (Matei et al. 2012)), for a total of four forecast systems, each with start dates available every year from 1961 to 2010. The first ensemble is constructed using simulations initialised with contemporaneous observations, thus aligning the simulated natural variability with the observed variability. The multi-model ensemble-mean anomalies are computed by giving an equal weight to each model mean, regardless of the number of ensemble members available for a particular model. This ensemble is referred to as Ini. The second ensemble is composed of 10-year long simulations constructed using the CMIP5 historical and RCP 4.5 scenario (Meinshausen et al. 2011) simulations. This second ensemble is referred to as NoIni. The difference in skill between Ini and NoIni is a measure of the added value of initialisation. The number of members for each ensemble is shown in Table 9.3. We note that we have added one start date and increased the ensemble size using new simulations that have become available since Caron et al. (2015b).

In both ensembles, external forcings (greenhouse gases, solar activity, stratospheric aerosols associated with volcanic eruptions and anthropogenic aerosols) are taken from observations for the period 1961–2005 and the RCP 4.5 scenario afterwards. Because any significant unexpected changes in external forcing (e.g. large volcanic eruption) cannot be taken into account in a true forecast, the skill obtained by using observed forcings is somewhat overestimated. However, the difference in skill between Ini and NoIni should not be affected. Unlike Caron et al. (2015b) which showed the skill of 5-year mean forecasts, here we show results of 4-year mean forecasts, using only forecast years 2–5, which is a standard procedure when evaluating decadal forecasts (Goddard et al. 2013).

Finally, reference data for SSTAs are taken from NOAA's Extended Reconstructed Sea Surface Temperatures (ERSST; version 3b) (Smith et al. 2008), the SLPAs are taken from the JRA-55 reanalyses (Kobayashi et al. 2015) and the hurricane data are taken from HURDAT2 (Landsea and Franklin 2013). The number of landfall events is calculated as the number of times hurricane tracks (linearly interpolated to 1 h) cross over onto a land mass. A storm is considered to have made

Table 9.3 Models (and their respective number of members) used to construct the ensembles used in this study

Model I.D.	No. Ini members	No. NoIni members
GFDL-CM2.1	10	10
HadCM3	20	10
MIROC5	6	3
MPI-ESM	10	3
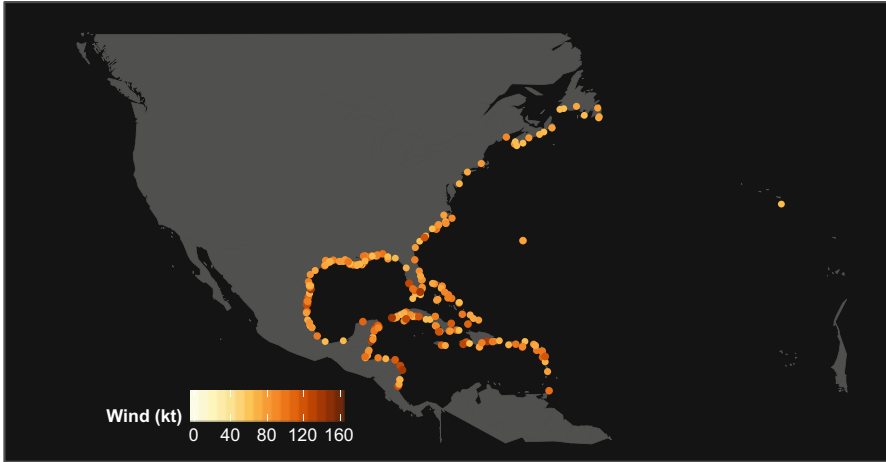
Fig. 9.7 Landfalling hurricane locations for the 1962–2014 period

multiple landfalls if it continued back over a large body of open water (e.g. Gulf of Mexico, Atlantic Ocean) after a first landfall (e.g. a storm passing over Florida, the Gulf of Mexico and Louisiana would be considered as two landfalls). Storms were required to be of hurricane strength upon landfall to be considered, but could have transitioned to extratropical status. Figure 9.7 shows all of the hurricane landfall locations for the period 1962–2014.

3.1.2 Forecast Skill Assessment

Different measures are used to evaluate the skill of the forecasts: the anomaly correlation coefficient (ACC), the root mean square skill score (RMSSS) and the Brier skill score (BSS).

ACCs are computed by correlating the MME anomalies with the observed anomalies across the start date dimension, using both standard Pearson's correlation and Kendall's rank correlation. The RMSSS shows the improvement relative to a climatological forecast and is defined as

$$RMSSS = 1 - \frac{RMSE_{for}}{RMSE_{clim}} \tag{9.2}$$

where $RMSE_{for}$ and $RMSE_{clim}$ are, respectively, the root mean square error of our forecast and of the reference forecast. RMSSS = 1 shows a perfect forecast and RMSSS ≤ 0, a forecast with no improvement over the benchmark (in this case, climatology). In both cases, a t-test, after a Fisher-z transformation, is performed to assess the significance level. Autocorrelation in the various time series is accounted for by following (Von Storch and Zwiers 2001).

Finally, the BSS measures the improvement of a probabilistic forecast relative to a benchmark, in this case either climatology or NoIni. It is defined as

$$BSS = 1 - \frac{BS_{for}}{BS_{ref}} \tag{9.3}$$

where BS_{for} and BS_{ref} are the Brier scores of the actual and reference forecast, respectively. The Brier score itself is defined as the average of the squared differences between each forecast probability and the corresponding binary observations (1 if the event is observed, 0 if it is not). Our binary probabilities are constructed as follows: for each 4-year period we calculate, using forecast years 2–5 of each model, the probability that the index will be positive based on the number of members for which the index is positive. We then average the model probabilities to obtain the probability of the MMEs, giving an equal weight to each model, regardless of the number of ensemble members available for that particular model. This result is then compared to the observed 4-year mean number of hurricane landfalls.

3.2 Multi-annual Forecast Skill of AMV index

Figure 9.8 shows the ACCs between the Ini MME and observations for 4-year mean SSTAs (Fig. 9.8a) and SLPAs (Fig. 9.8b). For SSTA, high and significant skill is found over almost the entire domain, but a large portion of this skill originates from the radiatively driven upward trend in SSTs captured by the MME. This can be seen in Fig. 9.8c, which shows the difference in ACCs between the Ini and NoIni MMEs. However, for a large part of the region considered in the construction of the AMV index (black box), the skill of the Ini MME is significantly higher than the NoIni MME. In comparison, skill for SLPA is more modest (Fig. 9.8b), but subtracting the ACC from the NoIni MME (Fig. 9.8d) has a much lesser impact than for SSTA since the NoIni MME shows very poor skill at predicting SLPA. In effect, Fig. 9.8 shows that initialised GCMs have skill at capturing multi-annual variations in the large-scale fields that are used in the construction of the AMV index.

Figure 9.9 shows the time series for standardised 4-year mean SSTA (Fig. 9.9a) and SLPA (Fig. 9.9b) for both the Ini (red) and the NoIni (blue) MME as well as the observational reference (black). Both time series show significant ACCs for the Ini ensemble, but only the SSTA forecasts show a RMSSS greater than 0. Figure 9.9c shows the value of a 4-year mean forecasted index for both ensembles and for observations. For the Ini ensemble, both the ACC and the RMSSS are statistically significant, with values of 0.78 and 0.37, respectively. The timing of the downward shift (1969–1970) towards negative values is fairly well captured, while the upward shift of the mid-1990s occurs somewhat too early, the latter being driven by the early drop in simulated SLPA in the Ini MME.

Figure 9.10 (top) compares the 4-year mean index forecasted by the Ini MME and the 4-year mean number of hurricane landfalls (expressed as anomalies) observed during the corresponding period. Both the linear (0.65) and the ranked (0.48)
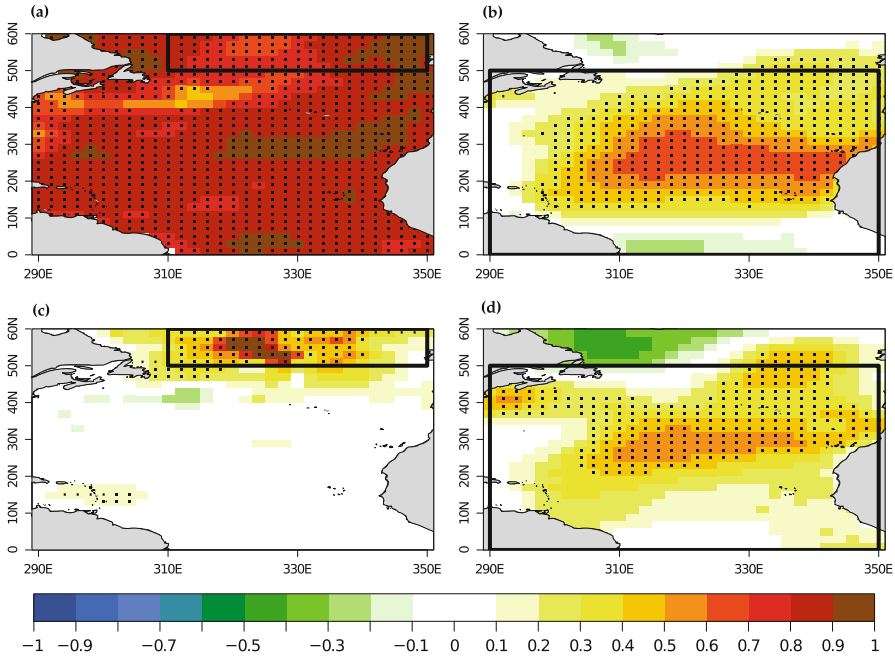
Fig. 9.8 *First row*: Anomaly correlation coefficients (ACCs) for 4-year mean (**a**) SSTA and (**b**) SLPA in Ini MME forecasts. *Second row*: Difference in ACCs between the Ini MME and NoIni MME for (**c**) SSTA and (**d**) SLPA. The *black dots* indicate the regions where the results are significant at the 5 % level, and the *black boxes* indicate the area considered in the construction of the index

correlation coefficients are statistically significant, confirming the skill of our MME at forecasting multi-annual hurricane landfall numbers. In fact, the index explains ∼40 % of the variability in total hurricane landfalls in the Atlantic basin. We also evaluate the skill of our forecasts using a binary probability forecast verification technique, wherein a high (>50 %) probability of a positive index is suggestive of above-normal hurricane landfall numbers. The result is shown in the form of a reliability diagram (Fig. 9.10, bottom), which compares the forecasted frequencies with the actual observed frequencies. The reliability diagram is constructed by grouping the probabilistic forecasts into three bins (0–33 %, 34 %–66 %, 67 %–100 %) on the horizontal axis according to the probability derived from the MME (as described in the methodology section). For perfect reliability, the forecast probability and the frequency of occurrence should be equal, and the predictions should align along the diagonal (solid line in the figure). However, due to the finite number of predictions, a forecast system may still be deemed reliable even if its predictions do not lie precisely along the diagonal. To address this issue, we include consistency bars, showing the 5 % and 95 % quantiles. A histogram with the distribution of the forecasts within the different bins is shown in the bottom right of the diagram, and the BSSs (using both climatology and NoIni MME as a benchmark) are shown in the upper-left corner.

Fig. 9.9 4-year mean (**a**) standardised SSTA, (**b**) standardised SLPA and (**c**) AMV index. Observations are in *black*, the Ini MME in *red* and the NoIni MME in *blue*. The *red shading* represents the 95 % confidence interval. ACCs and RMSSSs are shown in the *bottom left* and *right corners*, respectively. Significant values are in bold
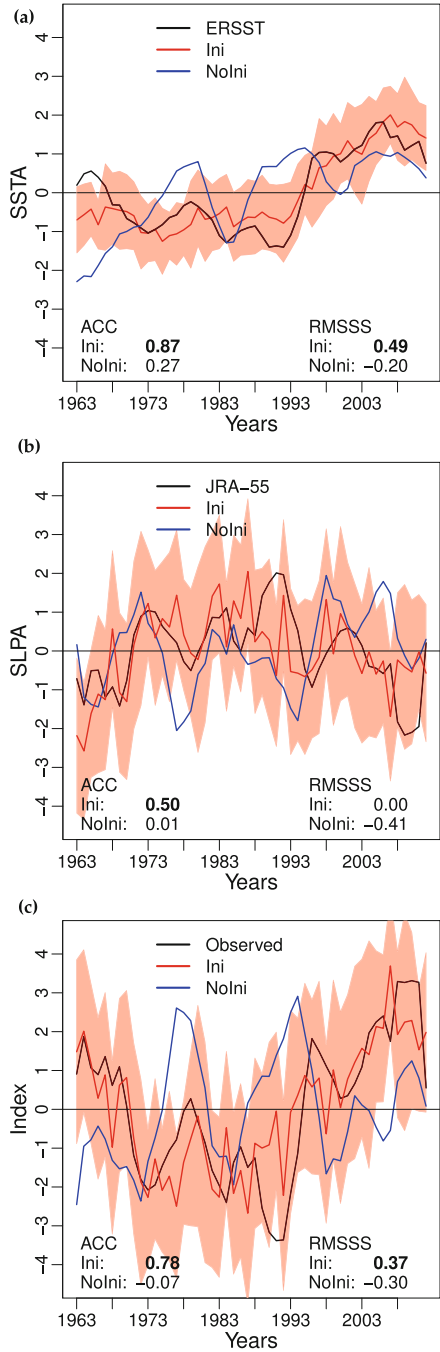
Fig. 9.10 *Top*: Time series of 4-year mean hurricane landfall numbers (*bars*) and 4-year mean Ini MME forecasted index (forecast year 2–5; *red line*). Hurricane landfalls are expressed as anomalies with respect to the 1962–2014 average. Pearson's linear correlation and Kendall's ranked correlation indices are indicated in the *upper-left corner*. Both are statistically significant at the 5 % level. *Bottom*: Reliability diagrams of 4-year mean Ini MME forecasts for landfalling hurricanes. Brier skill scores using both climatology and NoIni MME as benchmark are shown in the *upper-left corner*. Both are statistically significant at the 5 % level. The probabilistic forecasts represent the probability that the activity level will be above the climatological average
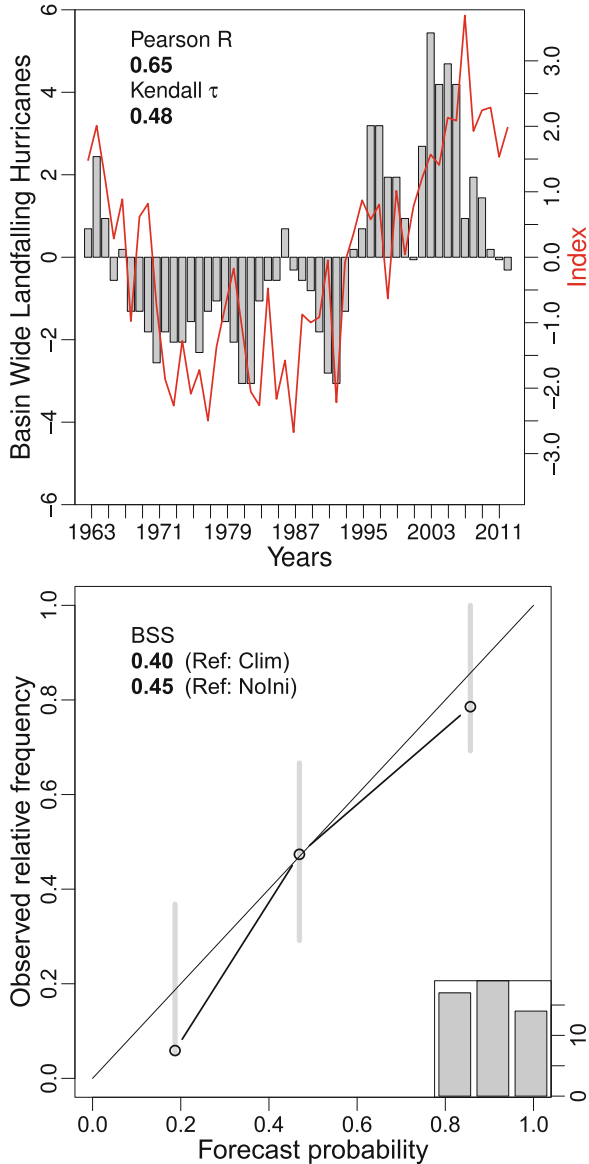
The forecasts are reliable, with all points of the Ini MME lying close to the diagonal, within the consistency bars. Furthermore, the Ini ensemble is capable of predicting relatively high or low probabilities of 4-year mean hurricane landfalls, as evidenced by the fairly even number of predictions in each of the three forecast categories. In effect, this graph shows that above-average periods of activity tend to occur when the MME forecasts return high probabilities (>66 %) and that such

high activity will occur. Similarly, low activity periods tend to occur when the MME returns low probabilities (<33 %) of high activity. Finally, BSSs are both positive and significant, thus further confirming the skill of our MME forecasts.

3.3 Persistence or Predictability?

As stated earlier, for decadal forecasts to be truly useful, their skill must not originate solely from the persistence of anomalies introduced at the initialisation stage. Particularly desirable (arguably, necessary) is the ability of the MME to predict the shifts between active and inactive regimes. For the period covered here, such a downward shift was observed in 1969–1970, while an upward shift was observed in 1994–1995. We note that these shifts in activity were matched by similar shifts in the index itself (see Figs. 9.9c and 9.10). Both shifts in the AMV index were driven by simultaneous changes in SLPA and SSTA (Fig. 9.9a,b): the first shift is driven by a decrease in SSTA and an increase in SLPA (the opposite is true for the second shift). Thus, for forecasts initialised in the years leading up to the 1969–1970 shift, we would expect, on average, the SSTA (SLPA) of the later years to be smaller (larger) than that of the earlier years. For the upward shift of the mid-1990s, we would expect the opposite.

In Fig. 9.11, we show the distribution of the difference between the average of forecast years 2–5 and that of forecast year 1 for both SSTA and SLPA using (i) hindcasts from all start dates (grey), (ii) only hindcasts initialised in the years leading up to the downward shift (1965–1968; blue) and (iii) only hindcasts initialised in the years leading up to the upward shift (start dates: 1990–1993; red). For SLPA (Fig. 9.11b), the distribution, when all the hindcasts are considered, is centred around zero. When only the years leading up to the shifts are considered, small differences in the distribution are observed, but these differences are not statistically significant. This suggests that most of the skill in SLPA results from persistence, since there is no tendency towards higher (lower) SLPAs in the years leading up to a decrease (increase) in AMV index value. However, for SSTA, a clear shift in the distribution towards lower (1969–1970 shift) and higher (1994–1995) values can be seen. A Kolmogorov–Smirnov test confirms that these differences are significant at the 1 % level. This suggests that the MME has some predictive power at the multi-annual level for SSTs over this particular region. This skill in initialised MME has been identified in previous studies (Robson et al. 2012, 2014) and has been linked to the ability of the GCMs at capturing the ocean dynamics of the Atlantic Meridional Overturning Circulation (AMOC). This latter result suggests that this technique could indeed be used to predict shifts in prolonged periods of high or low hurricane activity in the Atlantic.
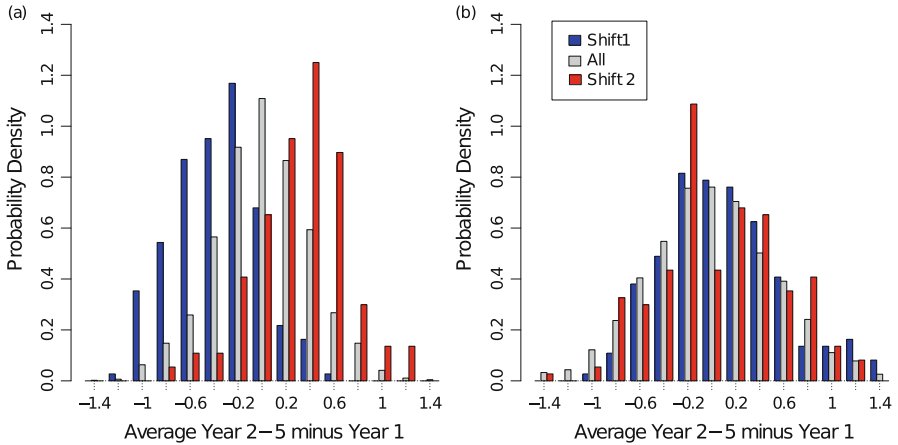
Fig. 9.11 Empirical probability density function (PDF) for changes in Ini MME forecasted (**a**) SSTA and (**b**) SLPA. The three distributions are constructed using all the start dates (*grey*) and the four start dates preceding the 1969–1970 (*blue*) and 1994–1995 (*red*) shifts. The PDF is based on the differences between the mean values of forecast year 2–5 and forecast year 1 values

3.4 Discussion

The results presented here suggest that initialised GCMs offer an opportunity to develop reliable forecasts of multi-annual (∼5 years) hurricane landfall statistics in the Atlantic basin and could predict shifts between prolonged periods of high and low hurricane activity. There are caveats to this approach however. First, the skill at predicting one of the components (SLPA) of the AMV index originates from persistence and, as such, shows no true predictive skill. This might change with improvements in initialisation procedures and climate models, but it might also be the case that changes in SLPA over the tropical and extratropical Atlantic are not predictable at the multi-annual timescale. Furthermore, the forecasted quantity is an index as opposed to an estimated storm number. In a climate service context, the latter is much easier to use (e.g. insurance loss models expect a storm number as input, not an index). Both issues could potentially be addressed by using a multiple regression technique (similar to that of Vecchi et al. 2011), where SLPA and SSTA are used as predictors for hurricane landfall numbers and wherein the variable with the best skill (SSTA) is given more weight than the one with more limited skill (SLPA). This approach is likely to improve on the results shown here, and such work is currently underway. Nonetheless, even in its current form, this technique appears useful in estimating upcoming hurricane activity levels and could be used to shed some light on whether we have indeed entered a new era of lower Atlantic TC activity (Klotzbach et al. 2015).

4 Concluding Remarks

In the last few years, significant progress has been made both in improving global climate models and their representation of TCs and in understanding the TC climate connection. This has led to the development of dynamical forecasts of TC activity at various timescales, with two such examples given here. Skill of dynamical seasonal forecasts over the entire Atlantic is already fairly high for basin-wide activity (Camp et al. 2015; Chen and Lin 2011, 2013; Vecchi et al. 2014; Zhao et al. 2010); however, operational seasonal forecasts of TC landfall are not presently available. In this study we show that a high-resolution GCM shows promising skill for predictions of TC landfall in the Caribbean region, likely due to a good model response of TC landfall frequency to ENSO forcing. However, along the US Coast, the absence of a strong observed response of TC landfalls to ENSO, combined with a deficit of landfalling storms in the model, limits the skill of seasonal TC landfall forecasts for the US Coast using the present forecasting system. Nevertheless, improvements in GCM resolution and physics offer the opportunity for seasonal TC forecasts of landfall risk along the US Coast to be investigated further.

Recently, multi-annual predictions of Atlantic TC activity using GCMs have been developed and show promising skill (e.g. Caron et al. 2014, 2015b; Smith et al. 2010; Vecchi et al. 2013). In the present study, we also show that an initialised GCM offers the opportunity to provide reliable forecasts of hurricane landfall statistics on ∼5-year timescales. Such forecasts may be of use to those vulnerable to TC damage and losses, but require decisions to be made at lead times longer than presently available from seasonal forecasts (such as in the insurance and reinsurance industry). Furthermore, with the continuous increase in computing power and the improvement in coupled GCMs, multi-model ensembles of dynamical forecasts should become possible, further improving the skill of such forecasts.

References

Bengtsson L, Bottger H, Kanamitsu M (1982) Simulation of hurricane-type vortices in a general circulation model. Tellus A 34:440–457. doi: 10.3402/tellusa.v47i2.11500

Bengtsson L, Botzet M, Esch M (1996) Will greenhouse gas-induced warming over the next 50 years lead to higher frequency and greater intensity of hurricanes? Tellus A 48:57–73

Bengtsson L, Hodges KI, Esch M, Keenlyside N, Kornblueh L, Luo JJ, Yamagata T (2007) How may tropical cyclones change in a warmer climate? Tellus A 59(4):539–561. doi: 10.1111/j.1600-0870.2007.00251.x, http://dx.doi.org/10.1111/j.1600-0870.2007.00251.x

Bove MC, O'Brien JJ, Eisner JB, Landsea CW, Niu X (1998) Effect of El Niño on U.S. landfalling hurricanes, revisited. Bull Am Meteorol Soc 79(11):2477–2482. doi: 10.1175/1520-0477(1998)079%3C2477:eoenoo%3E2.0.co;2, http://dx.doi.org/10.1175/1520-0477(1998)079%3C2477:eoenoo%3E2.0.co;2

Camargo SJ (2013) Global and regional aspects of tropical cyclone activity in the CMIP5 models. J Clim 26(24):9880–9902. doi: 10.1175/jcli-d-12-00549.1, http://dx.doi.org/10.1175/jcli-d-12-00549.1

Camargo SJ, Wing AA (2015) Tropical cyclones in climate models. WIREs Clim Change p n/a. doi: 10.1002/wcc.373, http://dx.doi.org/10.1002/wcc.373

Camargo SJ, Sobel AH, Barnston AG, Klotzbach PJ (2010) The influence of natural climate variability on tropical cyclones, and seasonal forecasts of tropical cyclone activity, vol 4. World Scientific, Singapore, pp 325–360. doi: 10.1142/9789814293488_0011, http://dx.doi.org/10.1142/9789814293488_0011

Camp J, Roberts M, MacLachlan C, Wallace E, Hermanson L, Brookshaw A, Arribas A, Scaife AA (2015) Seasonal forecasting of tropical storms using the Met Office GloSea5 seasonal forecast system. QJR Meteorol Soc p n/a. doi: 10.1002/qj.2516, http://dx.doi.org/10.1002/qj.2516

Caron LP, Jones CG (2011) Understanding and simulating the link between African easterly waves and Atlantic tropical cyclones using a regional climate model: the role of domain size and lateral boundary conditions. Clim Dyn 39(1–2):113–135. doi: 10.1007/s00382-011-1160-8, http://link.springer.com/10.1007/s00382-011-1160-8

Caron LP, Jones CG, Winger K (2010) Impact of resolution and downscaling technique in simulating recent Atlantic tropical cyclone activity. Clim Dyn 37(5–6):869–892. doi: 10.1007/s00382-010-0846-7, http://link.springer.com/10.1007/s00382-010-0846-7

Caron LP, Jones CG, Doblas-Reyes F (2014) Multi-year prediction skill of Atlantic hurricane activity in CMIP5 decadal hindcasts. Clim Dyn 42:2675–2690. doi: 10.1007/s00382-013-1773-1, http://link.springer.com/10.1007/s00382-013-1773-1

Caron LP, Boudreault M, Bruyère CL (2015a) Large-scale control of Atlantic tropical cyclone activity as a function of the Atlantic multi-decadal oscillation phase. Clim Dyn 44:1801–1821. doi: 10.1007/s00382-014-2186-5

Caron LP, Hermanson L, Doblas-Reyes FJ (2015b) Multiannual forecasts of Atlantic U.S. tropical cyclone wind damage potential. Geophys Res Lett 42:2417–2425. doi: 10.1002/2015GL063303

Chen JH, Lin SJ (2011) The remarkable predictability of inter-annual variability of Atlantic hurricanes during the past decade. Geophys Res Lett 38(11):L11804+. doi: 10.1029/2011gl047629, http://dx.doi.org/10.1029/2011gl047629

Chen JH, Lin SJ (2013) Seasonal predictions of tropical cyclones using a 25-km-resolution general circulation model. J Clim 26(2):380–398. doi: 10.1175/jcli-d-12-00061.1, http://dx.doi.org/10.1175/jcli-d-12-00061.1

CPC (2015) Historical El Nino/ La Nina episodes (1950-present). CPC. [Available online at http://www.cpc.ncep.noaa.gov/products/analysis_monitoring/ensostuff/ensoyea%rs.shtml]

Dee DP, Uppala SM, Simmons AJ, Berrisford P, Poli P, Kobayashi S, Andrae U, Balmaseda MA, Balsamo G, Bauer P, Bechtold P, Beljaars ACM, van de Berg L, Bidlot J, Bormann N, Delsol C, Dragani R, Fuentes M, Geer AJ, Haimberger L, Healy SB, Hersbach H, Hólm EV, Isaksen L, Kållberg P, Köhler M, Matricardi M, McNally AP, Monge-Sanz BM, Morcrette JJ,

Park BK, Peubey C, de Rosnay P, Tavolato C, Thépaut JN, Vitart F (2011) The ERA-Interim reanalysis: configuration and performance of the data assimilation system. QJR Meteorol Soc 137(656):553–597. doi: 10.1002/qj.828, http://dx.doi.org/10.1002/qj.828

Delworth TL, Broccoli AJ, Rosati A, Stouffer RJ, Balaji V, Beesley JA, Cooke WF, Dixon KW, Dunne J, Dunne KA, Durachta JW, Findell KL, Ginoux P, Gnanadesikan A, Gordon CT, Griffies SM, Gudgel R, Harrison MJ, Held IM, Hemler RS, Horowitz LW, Klein SA, Knutson TR, Kushner PJ, Langenhorst AR, Lee HC, Lin SJ, Lu J, Malyshev SL, Milly PCD, Ramaswamy V, Russell J, Schwarzkopf MD, Shevliakova E, Sirutis JJ, Spelman MJ, Stern WF, Winton M, Wittenberg AT, Wyman B, Zeng F (2006) GFDL's CM2 global coupled climate models – Part 1: formulation and simulation characteristics. J Clim 19:643–674. doi: 10.1175/JCLI3629.1

Dunstone NJ, Smith DM, Eade R (2011) Multi-year predictability of the tropical Atlantic atmosphere driven by the high latitude North Atlantic Ocean. Geophys Res Lett 38:L14701. doi: 10.1029/2011GL047949, http://doi.wiley.com/10.1029/2011GL047949

Dunstone NJ, Smith DM, Booth BBB, Hermanson L, Eade R (2013) Anthropogenic aerosol forcing of Atlantic tropical storms. Nat Geosci 6(7):1–6. doi: 10.1038/ngeo1854, http://www.nature.com/doifinder/10.1038/ngeo1854

Goddard L, Kumar a, Solomon a, Smith D, Boer G, Gonzalez P, Kharin V, Merryfield W, Deser C, Mason SJ, Kirtman BP, Msadek R, Sutton R, Hawkins E, Fricker T, Hegerl G, Ferro CaT, Stephenson DB, Meehl Ga, Stockdale T, Burgman R, Greene aM, Kushnir Y, Newman M, Carton J, Fukumori I, Delworth T (2013) A verification framework for interannual-to-decadal predictions experiments. Clim Dyn 40(1–2):245–272. doi: 10.1007/s00382-012-1481-2

Goldenberg SB, Landsea CW, Mestas-Nunez AM, Gray WM (2001) The recent increase in Atlantic hurricane activity: causes and implications. Science 293(5529):474–479

Gordon C, Cooper C, Senior C, Banks H, Gregory J, Johns T, Mitchell J, Wood R (2000) The simulation of SST, sea ice extents and ocean heat transports in a version of the Hadley Centre coupled model without flux adjustments. Clim Dyn 16:147–168

Gray WM (1984a) Atlantic seasonal hurricane frequency. Part I: El Niño and 30MB Quasi-Biennial Oscillation influences. Mon Weather Rev 112:1649–1668

Gray WM (1984b) Atlantic seasonal hurricane frequency. Part II: forecasting its variability. Mon Weather Rev 112:1669–1683

Hodges KI (1995) Feature tracking on the unit sphere. Mon Weather Rev 123(12):3458–3465. doi: 10.1175/1520-0493(1995)123%3C3458:ftotus%3E2.0.co;2, http://dx.doi.org/10.1175/1520-0493(1995)123%3C3458:ftotus%3E2.0.co;2

Hodges KI (1996) Spherical nonparametric estimators applied to the UGAMP model integration for AMIP. Mon Weather Rev 124(12):2914–2932. doi: 10.1175/1520-0493(1996)124%3C2914:sneatt%3E2.0.co;2, http://dx.doi.org/10.1175/1520-0493(1996)124%3C2914:sneatt%3E2.0.co;2

Hodges KI (1999) Adaptive constraints for feature tracking. Mon Weather Rev 127(6):1362–1373. doi: 10.1175/1520-0493(1999)127%3C1362:acfft%3E2.0.co;2, http://dx.doi.org/10.1175/1520-0493(1999)127%3C1362:acfft%3E2.0.co;2

Jewson S, Bellone E, Khare S, Laepple T, Lonfat M, Shay AO, Penzer J, Coughlin K (2009) 5-Year prediction of the number of hurricanes which make U.S. landfall. In: Elsner JB, Jagger TH (eds) Hurricanes and climate change. Springer, New York, pp 73–99. doi: 10.1007/978-0-387-09410-6_5

Klotzbach P, Gray W, Fogarty C (2015) Active Atlantic hurricane era at its end? Nat Geosci 8(10):737–738. doi: 10.1038/ngeo2529, http://dx.doi.org/10.1038/ngeo2529

Klotzbach PJ (2007) Revised prediction of seasonal Atlantic basin tropical cyclone activity from 1 August. Weather Forecast 22(5):937–949. doi: 10.1175/waf1045.1, http://dx.doi.org/10.1175/waf1045.1

Klotzbach PJ (2011a) El Niño-Southern oscillation's impact on Atlantic basin hurricanes and U.S. landfalls. J Clim 24(4):1252–1263. doi: 10.1175/2010jcli3799.1, http://dx.doi.org/10.1175/2010jcli3799.1

Klotzbach PJ (2011b) The influence of El Niño-Southern oscillation and the Atlantic mul-
    tidecadal oscillation on Caribbean tropical cyclone activity. J Clim 24(3):721–731. doi:
    10.1175/2010jcli3705.1, http://dx.doi.org/10.1175/2010jcli3705.1

Klotzbach PJ, Gray WM (2008) Multidecadal variability in North Atlantic tropical cyclone activity.
    J Clim 21(15):3929–3935. doi: 10.1175/2008JCLI2162.1, http://journals.ametsoc.org/doi/abs/
    10.1175/2008JCLI2162.1

Knight JR, Folland CK, Scaife AA (2006) Climate impacts of the Atlantic Multidecadal Oscilla-
    tion. Geophys Res Lett 33(17):L17,706. doi: 10.1029/2006GL026242, http://doi.wiley.com/10.
    1029/2006GL026242

Kobayashi S, Ota Y, Harada Y, Ebita A, Moriya M, Onoda H, Onogi K, Kamahori H, Kobayashi
    C, Endo H, Miyaoka K, Takahashi K (2015) The JRA-55 reanalysis: general specifications and
    basic characteristics. J Meteorol Soc Jpn 93:5–48. doi: 10.2151/jmsj.2015-001

Kossin JP, Vimont DJ (2007) A more general framework for understanding Atlantic hurricane vari-
    ability and trends. Bull Am Meteorol Soc 88(11):1767–1781. doi: 10.1175/BAMS-88-11-1767,
    http://journals.ametsoc.org/doi/abs/10.1175/BAMS-88-11-1767

Landsea CW, Franklin JL (2013) Atlantic hurricane database uncertainty and presentation of a
    new database format. Mon Weather Rev 141(10):3576–3592. doi: 10.1175/mwr-d-12-00254.1,
    http://dx.doi.org/10.1175/mwr-d-12-00254.1

LaRow TE, Stefanova L, Shin DW, Cocke S (2010) Seasonal Atlantic tropical cyclone hindcast-
    ing/forecasting using two sea surface temperature datasets. Geophys Res Lett 37(2):L02,804+.
    doi: 10.1029/2009gl041459, http://dx.doi.org/10.1029/2009gl041459

Larson J, Zhou Y, Higgins RW (2005) Characteristics of landfalling tropical cyclones in the
    United States and Mexico: climatology and interannual variability. J Clim 18(8):1247–1262.
    doi: 10.1175/jcli3317.1, http://dx.doi.org/10.1175/jcli3317.1

Lyons SW (2004) U.S. tropical cyclone landfall variability: 1950–2002. Weather Forecast
    19(2):473–480. doi: 10.1175/1520-0434(2004)019%3C0473:utclv%3E2.0.co;2, http://dx.doi.
    org/10.1175/1520-0434(2004)019%3C0473:utclv%3E2.0.co;2

MacLachlan C, Arribas A, Peterson KA, Maidens A, Fereday D, Scaife AA, Gordon M, Vellinga
    M, Williams A, Comer RE, Camp J, Xavier P, Madec G (2014) Global seasonal forecast system
    version 5 (GloSea5): a high-resolution seasonal forecast system. QJR Meteorol Soc p n/a. doi:
    10.1002/qj.2396, http://dx.doi.org/10.1002/qj.2396

Matei D, Pohlmann H, Jungclaus J, Müller W, Haak H, Marotzke J (2012) Two tales of
    initializing decadal climate prediction experiments with the ECHAM5/MPI-OM model. J Clim
    25(24):8502–8523. doi: 10.1175/JCLI-D-11-00633.1, http://journals.ametsoc.org/doi/abs/10.
    1175/JCLI-D-11-00633.1

Mei W, Xie SP, Zhao M (2014) Variability of tropical cyclone track density in the North
    Atlantic: observations and high-resolution simulations. J Clim 27(13):4797–4814. doi:
    10.1175/jcli-d-13-00587.1, http://dx.doi.org/10.1175/jcli-d-13-00587.1

Meinshausen M, Smith SJ, Calvin K, Daniel JS, Kainuma MLT, Lamarque JF, Matsumoto K,
    Montzka Sa, Raper SCB, Riahi K, Thomson a, Velders GJM, Vuuren DP (2011) The RCP
    greenhouse gas concentrations and their extensions from 1765 to 2300. Clim Change 109(1–
    2):213–241. doi: 10.1007/s10584-011-0156-z, http://link.springer.com/10.1007/s10584-011-
    0156-z

Murakami H, Wang Y, Yoshimura H, Mizuta R, Sugi M, Shindo E, Adachi Y, Yukimoto
    S, Hosaka M, Kusunoki S, Ose T, Kitoh A (2012) Future changes in tropical cyclone
    activity projected by the new high-resolution MRI-AGCM*. J Clim 25(9):3237–3260. doi:
    10.1175/jcli-d-11-00415.1, http://dx.doi.org/10.1175/jcli-d-11-00415.1

Reed KA, Bacmeister JT, Rosenbloom NA, Wehner MF, Bates SC, Lauritzen PH, Truesdale
    JE, Hannay C (2015) Impact of the dynamical core on the direct simulation of tropical
    cyclones in a high-resolution global model. Geophys Res Lett 42(9):2015GL063,974+. doi:
    10.1002/2015gl063974, http://dx.doi.org/10.1002/2015gl063974

Roberts MJ, Vidale PL, Mizielinski MS, Demory ME, Schiemann R, Strachan J, Hodges K, Bell R,
    Camp J (2015) Tropical cyclones in the UPSCALE ensemble of high-resolution global climate
    models. J Clim 28(2):574–596. doi: 10.1175/jcli-d-14-00131.1, http://dx.doi.org/10.1175/jcli-
    d-14-00131.1

Robson J, Sutton R, Lohmann K, Smith D, Palmer MD (2012) Causes of the rapid warming of the North Atlantic ocean in the Mid-1990s. J Clim 25(12):4116–4134. doi: 10.1175/JCLI-D-11-00443.1, http://journals.ametsoc.org/doi/abs/10.1175/JCLI-D-11-00443.1

Robson J, Sutton R, Smith D (2014) Decadal predictions of the cooling and freshening of the North Atlantic in the 1960s and the role of ocean circulation. Clim Dyn 42(9–10):2353–2365. doi: 10.1007/s00382-014-2115-7, http://link.springer.com/10.1007/s00382-014-2115-7

Shaevitz DA, Camargo SJ, Sobel AH, Jonas JA, Kim D, Kumar A, LaRow TE, Lim YK, Murakami H, Reed KA, Roberts MJ, Scoccimarro E, Vidale PL, Wang H, Wehner MF, Zhao M, Henderson N (2014) Characteristics of tropical cyclones in high-resolution models in the present climate. J Adv Model Earth Syst 6(4):1154–1172. doi: 10.1002/2014ms000372, http://dx.doi.org/10.1002/2014ms000372

Smith DM, Eade R, Dunstone NJ, Fereday D, Murphy JM, Pohlmann H, Scaife AA (2010) Skilful multi-year predictions of Atlantic hurricane frequency. Nat Geosci 3(12):846–849. doi: 10.1038/ngeo1004, http://www.nature.com/doifinder/10.1038/ngeo1004

Smith SR, Brolley J, O'Brien JJ, Tartaglione CA (2007) ENSO's impact on regional U.S. hurricane activity. J Clim 20(7):1404–1414. doi: 10.1175/jcli4063.1, http://dx.doi.org/10.1175/jcli4063.1

Smith TM, Reynolds RW, Peterson TC, Lawrimore J (2008) Improvements to NOAA's historical merged Land-Ocean surface temperature analysis (1880–2006). J Clim 21(10):2283–2296. doi: 10.1175/2007JCLI2100.1, http://journals.ametsoc.org/doi/abs/10.1175/2007JCLI2100.1

Strachan J, Vidale PL, Hodges K, Roberts M, Demory ME (2013) Investigating global tropical cyclone activity with a hierarchy of AGCMs: the role of model resolution. J Clim 26(1):133–152. doi: 10.1175/jcli-d-12-00012.1, http://dx.doi.org/10.1175/jcli-d-12-00012.1

Strazzo S, Elsner JB, LaRow T, Halperin DJ, Zhao M (2013) Observed versus GCM-generated local tropical cyclone frequency: comparisons using a spatial lattice. J Clim 26(21):8257–8268. doi: 10.1175/jcli-d-12-00808.1, http://dx.doi.org/10.1175/jcli-d-12-00808.1

Tartaglione CA, Smith SR, O'Brien JJ (2003) ENSO impact on hurricane landfall probabilities for the Caribbean. J Clim 16(17):2925–2931. doi: 10.1175/1520-0442(2003)016%3C2925:eiohlp%3E2.0.co;2, http://dx.doi.org/10.1175/1520-0442(2003)016%3C2925:eiohlp%3E2.0.co;2

Vecchi GA, Zhao M, Wang H, Villarini G, Rosati A, Kumar A, Held IM, Gudgel R (2011) Statistical-dynamical predictions of seasonal North Atlantic hurricane activity. Mon Weather Rev 139(4):1070–1082. doi: 10.1175/2010mwr3499.1, http://dx.doi.org/10.1175/2010mwr3499.1

Vecchi GA, Msadek R, Anderson W, Chang YS, Delworth T, Dixon K, Gudgel R, Rosati A, Stern B, Villarini G, Wittenberg A, Yang X, Zeng F, Zhang R, Zhang S (2013) Multi-year predictions of North Atlantic hurricane frequency: promise and limitations. J Clim 26:5337–5357. doi: 10.1175/JCLI-D-12-00464.1

Vecchi GA, Delworth T, Gudgel R, Kapnick S, Rosati A, Wittenberg AT, Zeng F, Anderson W, Balaji V, Dixon K, Jia L, Kim HS, Krishnamurthy L, Msadek R, Stern WF, Underwood SD, Villarini G, Yang X, Zhang S (2014) On the seasonal forecasting of regional tropical cyclone activity. J Clim 27(21):7994–8016. doi: 10.1175/jcli-d-14-00158.1, http://dx.doi.org/10.1175/jcli-d-14-00158.1

Vimont DJ, Kossin JP (2007) The Atlantic meridional mode and hurricane activity. Geophys Res Lett 34(7):L07,709. doi: 10.1029/2007GL029683, http://doi.wiley.com/10.1029/2007GL029683

Vitart F, Stockdale TN (2001) Seasonal forecasting of tropical storms using coupled GCM integrations. Mon Weather Rev 129(10):2521–2537. doi: 10.1175/1520-0493(2001)129%3C2521:sfotsu%3E2.0.co;2, http://dx.doi.org/10.1175/1520-0493(2001)129%3C2521:sfotsu%3E2.0.co;2

Vitart F, Anderson JL, Stern WF (1997) Simulation of interannual variability of tropical storm frequency in an ensemble of GCM integrations. J Clim 10(4):745–760. doi: 10.1175/1520-0442(1997)010<0745:SOIVOT>2.0.CO;2

Vitart F, Huddleston MR, Déqué M, Peake D, Palmer TN, Stockdale TN, Davey MK, Ineson S, Weisheimer A (2007) Dynamically-based seasonal forecasts of Atlantic tropical storm activity issued in June by EUROSIP. Geophys Res Lett 34(16):L16815+. doi: 10.1029/2007gl030740, http://dx.doi.org/10.1029/2007gl030740

Von Storch H, Zwiers F (2001) Statistical analysis in climate research. Cambridge University Press, Cambridge, UK

Walsh K, Watterson IG (1997) Tropical cyclone-like vortices in a limited area model: comparison with observed climatology. J Clim 10(9):2240–2259

Wang H, Long L, Kumar A, Wang W, Schemm JKE, Zhao M, Vecchi GA, Larow TE, Lim YK, Schubert SD, Shaevitz DA, Camargo SJ, Henderson N, Kim D, Jonas JA, Walsh KJE (2014) How well do global climate models simulate the variability of Atlantic tropical cyclones associated with ENSO? J Clim 27(15):5673–5692. doi: 10.1175/jcli-d-13-00625.1, http://dx.doi.org/10.1175/jcli-d-13-00625.1

Watanabe M, Suzuki T, O'ishi R, Komuro Y, Watanabe S, Emori S, Takemura T, Chikira M, Ogura T, Sekiguchi M, Takata K, Yamazaki D, Yokohata T, Nozawa T, Hasumi H, Tatebe H, Kimoto M (2010) Improved climate simulation by MIROC5: mean states, variability, and climate sensitivity. J Clim 23:6312–6335. doi: 10.1175/2010JCLI3679.1

Xie L, Pietrafesa L, Wu K (2002) Interannual and decadal variability of landfalling tropical cyclones in the Southeast Coastal States of the United States. 19(4):677–686. doi: 10.1007/s00376-002-0007-y, http://dx.doi.org/10.1007/s00376-002-0007-y

Zhang R, Delworth TL (2006) Impact of Atlantic multidecadal oscillations on India/Sahel rainfall and Atlantic hurricanes. Geophys Res Lett 33(17):L17712. doi: 10.1029/2006GL026267, http://doi.wiley.com/10.1029/2006GL026267

Zhao M, Held IM, Lin SJ, Vecchi GA (2009) Simulations of global hurricane climatology, interannual variability, and response to global warming using a 50-km resolution GCM. J Clim 22(24):6653–6678. doi: 10.1175/2009jcli3049.1, http://dx.doi.org/10.1175/2009jcli3049.1

Zhao M, Held IM, Vecchi GA (2010) Retrospective forecasts of the hurricane season using a global atmospheric model assuming persistence of SST anomalies. Mon Weather Rev 138(10):3858–3868. doi: 10.1175/2010mwr3366.1, http://dx.doi.org/10.1175/2010mwr3366.1

Chapter 10
Tropical Cyclone Rainfall Changes in a Warmer Climate

Enrico Scoccimarro, Gabriele Villarini, Silvio Gualdi, Antonio Navarra, Gabriel Vecchi, Kevin Walsh, and Ming Zhao

Abstract Heavy precipitation and flooding associated with tropical cyclones (TCs) are responsible for a large number of fatalities and economic damage worldwide. Due to the societal and economic relevance of this hazard, studies have focused on the potential changes in heavy rainfall associated with TCs in a warmer climate. Despite the overall agreement about the tendency of TC rainfall to increase with greenhouse warming, the uncertainty of the projected changes is large, ranging from 3 to 37 %. Models project an increase in rainfall over land, both in terms of average and extremes, and a large spatial variability is associated with changes in projected rainfall amount.

The goal of this study is to quantify the contribution of landfalling TCs to rainfall at different latitudes, as well as its dependence on different idealized climate change scenarios.

Possible changes in the intensity of rainfall events associated with TCs are investigated under idealized forcing scenarios, with a special focus on landfalling storms. A new set of experiments designed within the US CLIVAR Hurricane Working Group allows disentangling the relative role of changes in atmospheric carbon dioxide from that played by sea surface temperature (SST) in changing the amount of rainfall associated with TCs in a warmer world. Compared to the present-day simulation, we found an increase in TC rainfall under the scenarios involving SST increases. On the other hand, in a CO_2 doubling-only scenario, the changes in TC rainfall are small and we found that, on average, TC rainfall tends

E. Scoccimarro (✉) • S. Gualdi • A. Navarra
Istituto Nazionale di Geofisica e Vulcanologia, INGV Italy, Centro euro-Mediterraneo sui Cambiamenti Climatici, CMCC, Via M. Franceschini 31, 40128 Bologna, Italy
e-mail: enrico.scoccimarro@ingv.it

G. Villarini
IIHR-Hydroscience & Engineering, The University of Iowa, Iowa City, IA, USA

G. Vecchi • M. Zhao
NOAA/Geophysical Fluid Dynamics Laboratory (GFDL), Princeton, NJ, USA

K. Walsh
School of Earth Sciences, The University of Melbourne, Parkville, VIC, Australia

to decrease compared to the present-day climate. The results of this study highlight the contribution of landfalling TCs to the projected increase in the rainfall changes affecting the tropical coastal regions. Scenarios involving SST increases project a TC rainfall strengthening more evident over land than over ocean. This is linked to the increased lifting effect on the landfalling TCs, induced by a more moist air at low levels.

1   Introduction

Heavy rainfall and flooding associated with tropical cyclones are responsible for a large number of fatalities and economic damage worldwide (e.g., Rappaport 2000; Pielke et al. 2008; Mendelsohn et al. 2012). Despite their large socioeconomic impacts, research into heavy rainfall and flooding associated with tropical cyclones (TCs) has received limited attention to date and still represents a major challenge. Despite the overall agreement about the tendency of TC rainfall to increase with greenhouse warming (Knutson et al. 2010; Villarini et al. 2014), the uncertainty of the projected changes is large, ranging from $+3\%$ to $+37\%$ (Knutson et al. 2013). Our capability to adapt to future changes in heavy rainfall and flooding associated with TCs is inextricably linked to and informed by our understanding of the sensitivity of TC rainfall to likely future forcing mechanisms.

Here we use a set of idealized high-resolution (between 50 and 80 km as horizontal grid spacing, Scoccimarro et al. 2014) atmospheric model experiments produced as part of the US CLIVAR Hurricane Working Group (Walsh et al. 2015) activity to examine TC response to idealized global-scale perturbations: the doubling of CO_2, uniform 2K increases in global sea surface temperature (SST), and their combined impact.

The goal of this study is to quantify changes in the rainfall amount associated with landfalling TCs at different latitudes, as well as its dependence on different idealized climate change scenarios. A possible explanation for the more pronounced TC rainfall increase over land, when compared to the global effect, is also provided.

2   Data and Method

The reference data used in this study are TC tracks and precipitation. For the former, we use TC observational datasets available as six-hourly data from the National Hurricane Center (NHC, Landsea and Franklin 2013) and the US Joint Typhoon

Warning Center (JTWC report 2013). These datasets include the location of the center of circulation, maximum wind, and minimum pressure for all the TCs during the period 1997–2006. Over the same period, the Global Precipitation Climatology Project (GPCP, Huffman et al. 2001; Bolvin et al. 2009) represents the reference data to quantify the precipitation associated with TCs (TCP). GPCP dataset is obtained by combining satellite and rain gage data to provide daily global rainfall estimates with a one degree resolution.

To investigate the ability of GCMs to represent TCP and its possible changes in a warmer climate, we employ a set of simulations performed within the US-CLIVAR Hurricane Working Group. Here we focus on two models, one run by the Geophysical Fluid Dynamics Laboratory (GFDL) and one by the Centro Euro-Mediterrraneo sui Cambiamenti Climatici (CMCC).

Rather than running the same TC tracking algorithm on both the GFDL (Zhao et al. 2009) and CMCC (Roeckner et al. 2003) models, we used the tracks provided by each modeling group. Detailed information on the ability of the climate models to represent TCs can be found in Walsh et al. (2013). Also, a specific discussion on the tracking scheme dependence of simulated TC in the considered runs can be found in Horn et al. (2014).

In this study we consider a subset of the simulations available from the US-CLIVAR Hurricane Working Group dataset. More specifically, we use the following four experiments:

- CLIM: this is a climatological run obtained by repeating the seasonally varying SST climatology over the period 1982–2005 for 10 years. TC genesis locations in the control run are shown in Fig. 10.1, compared to the observations over the 1997–2006 period. The control run is used to provide a baseline to contrast with the perturbation studies.
- 2C: this is a doubling CO2 experiment. It is obtained by integrating the models with climatological SST (as in CLIM) but with a doubled concentration of atmospheric CO2 with respect to the CLIM experiment for 10 years.
- 2K: this experiment is obtained by integrating the models with climatological SST (as in CLIM) and adding a 2K globally uniform SST anomaly for 10 years.
- 2C2K: this experiment is made by combining the 2K and 2C perturbations.

A more detailed explanation of models and simulations can be found in Scoccimarro et al. (2014), Shaewitz et al. (2014), and Walsh et al. (2015).

The amount of rainfall associated with a TC, both in models and observations, is computed by considering the daily precipitation in a $10 \times 10°$ box around the center of the storm (extending 5° from the center of the TC to the north, south, east, and west). According to previous studies (e.g., Lonfat et al. 2004; Larson et al. 2005; Kunkel et al. 2010), a $10 \times 10°$ window is sufficient to include the majority of TC-related precipitation in most of the cases.

3 Results

The control simulation (CLIM) performed with the two models represent reasonably well the TC count at the global scale for the present climate, with a 9 % underestimation for the CMCC model and a 16 % overestimation for the GFDL model, compared to the reference value of 93.3 TCs/year obtained from the observation for the period 1997–2006. The CMCC model also tends to significantly underestimate the TC count in the Atlantic basin and Eastern Pacific (Fig. 10.1) as found by similar analyses using the coupled version of the ECHAM5 atmospheric model (Scoccimarro et al. 2011). A difficulty in representing TC activity in the Atlantic Basin is common to many climate models, as discussed in Lim et al. (2014).

In this work, we aim to assess the models' ability in simulating precipitation associated with TCs and quantifying their relative changes for the three different idealized global forcing scenarios. To examine the TCP contribution to total precipitation, we accumulated TCP over the 10-year period, representing the
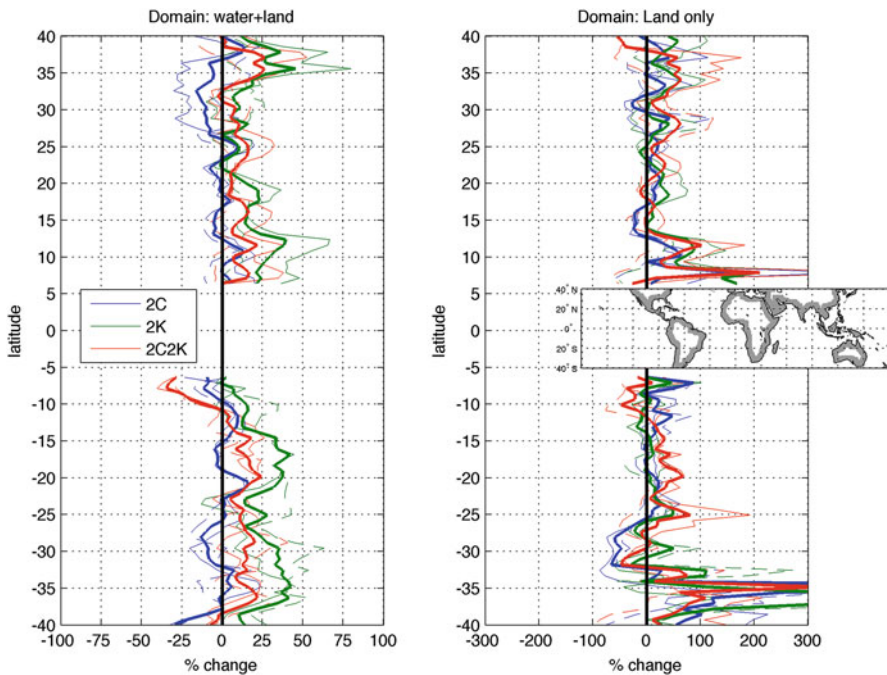
Fig. 10.1 Changes in TC-related precipitation amount (TCPn) in the 2C (*blue*), 2K (*green*), and 2C2K (*red*) experiments as a function of latitude. Results are shown with respect to the CLIM experiment. *Solid thin lines* represent CMCC results. *Dashed thin lines* represent GFDL results. The *solid thick lines* represent the average of the two models. Units are [%]. *Left* panel refers to the entire TC track. *Right* panel refers to TC track over land only (the *gray* region represented in the small map)
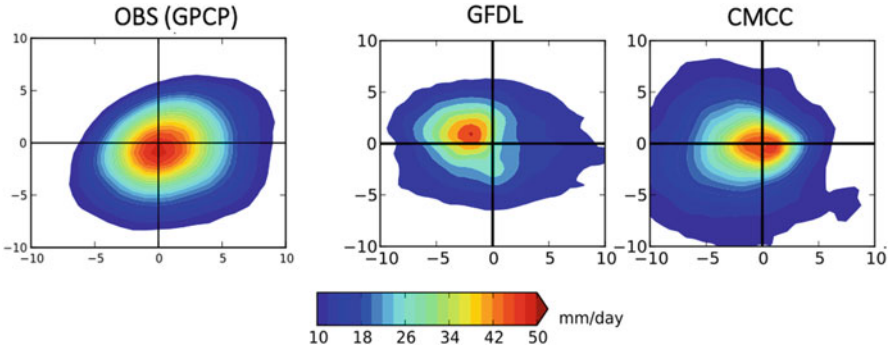
Fig. 10.2 Composite mean observed (GPCP, *left* panel) and modeled (CMCC/GFDL *central/right* panels) daily rainfall rate patterns associated to the 10 % most intense TCs. The units are mm/day and the x and y axes correspond to degrees from the TC center

present climate, and we compared it to the total precipitation for the same period. Figure 10.2 shows the composite of rainfall during the top 10 % rainiest TCs for the observations (left panel) and models (middle and right panels). TC rainfall patterns are reasonably well represented by models, as described by Villarini et al. (2014).

In the observations the TC rainfall represents a large contribution to the total rainfall over the Northwest Pacific, the Northeast Pacific, and the northwestern part of the Australian Basin (Fig. 10.3, upper panel). Over these regions, the amount of precipitation contribution due to TCs is as large as 40 %, reaching a maximum of 50 % in the Northwest Pacific. These features are captured by the simulations, despite the tendency of the CMCC model to underestimate the TCP fraction (Fig. 10.3 central panel). Both CMCC and GFDL models are able to represent the basic aspects of the latitudinal distribution of TCP, with the GFDL model showing a better agreement with the observations (Fig. 10.3 lower panel). In terms of absolute values, the modeled TCP zonal average, normalized by TC days (hereafter TCPn), shows maximum values at about 15° in both hemispheres (not shown).

Changes in TCPn are very similar for the two models and show a global increase in the 2K and 2C2K experiments but not for the 2C one (Fig. 10.4). The meridional distribution of TCPn changes (Fig. 10.4 left panel) in the 2C case shows the less pronounced changes within the three synthetic scenarios, with negative values over most of the latitudes, especially in the Northern Hemisphere. On the other hand, the 2K and 2C2K experiments show positive changes up to 45 % when considering the average of the two models (Fig. 10.4, red and green bold lines). The positive increase is more pronounced in the 2K experiment if compared to the 2C2K one. These results are consistent with Villarini et al. (2014) who found a widespread decrease in rainfall for the most intense TCs for the 2C experiment and a general increase in rainfall when SST was increased by 2K. This statement holds regardless of the distance from the center of circulation and for all the ocean basins.
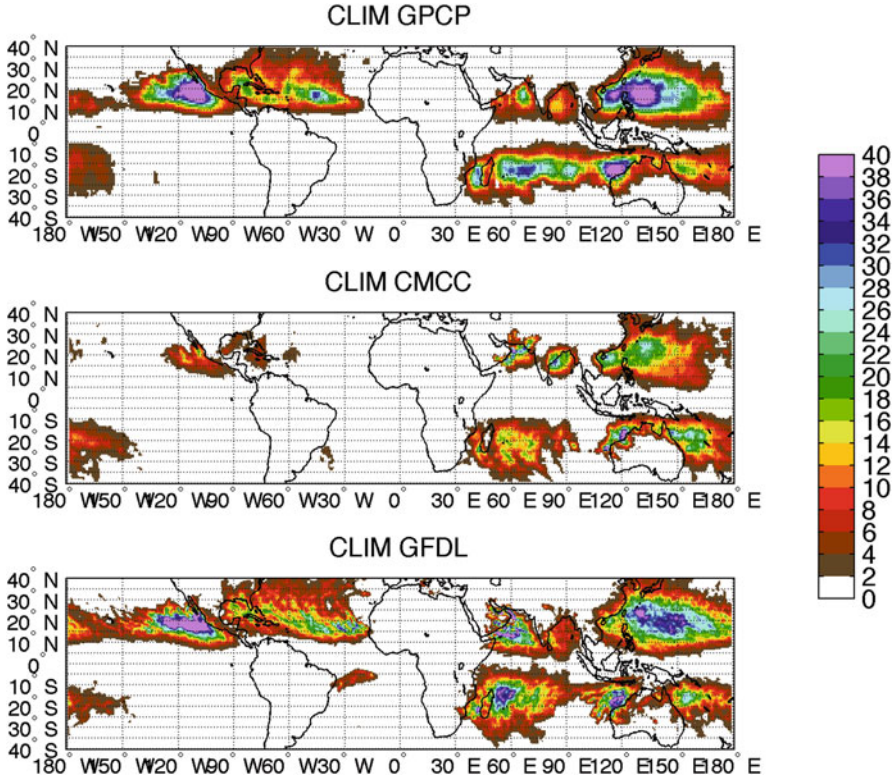
Fig. 10.3 Percentage of precipitation associated with TCs in the control simulation CLIM with respect to the total annual precipitation. The accumulation is performed by taking a $10 \times 10°$ window centered on the center of circulation. The *upper* panel refers to the observations, while the *central* and *lower* panels to the CMCC and GFDL models, respectively. Units are [%]

Focusing on the coastal region (shaded gray area in small map shown in Fig. 10.4), the TCPn increase in 2K and 2C2K is even more pronounced (Fig. 10.4, right panels), up to 200 %. In these areas even the 2C experiment shows positive changes in most latitudes. The resulting changes are spread out almost evenly over the coastal domain prone to TC landfall (not shown).

4 Discussion and Conclusion

It is well known that atmospheric moisture content tends to increase at a rate roughly governed by the Clausius–Clapeyron equation, while the energy available to drive convection increases more slowly (e.g., Knutson and Manabe 1995; Allen and Ingram 2002; Held and Soden 2006; Meehl et al. 2007). Therefore, in a warmer
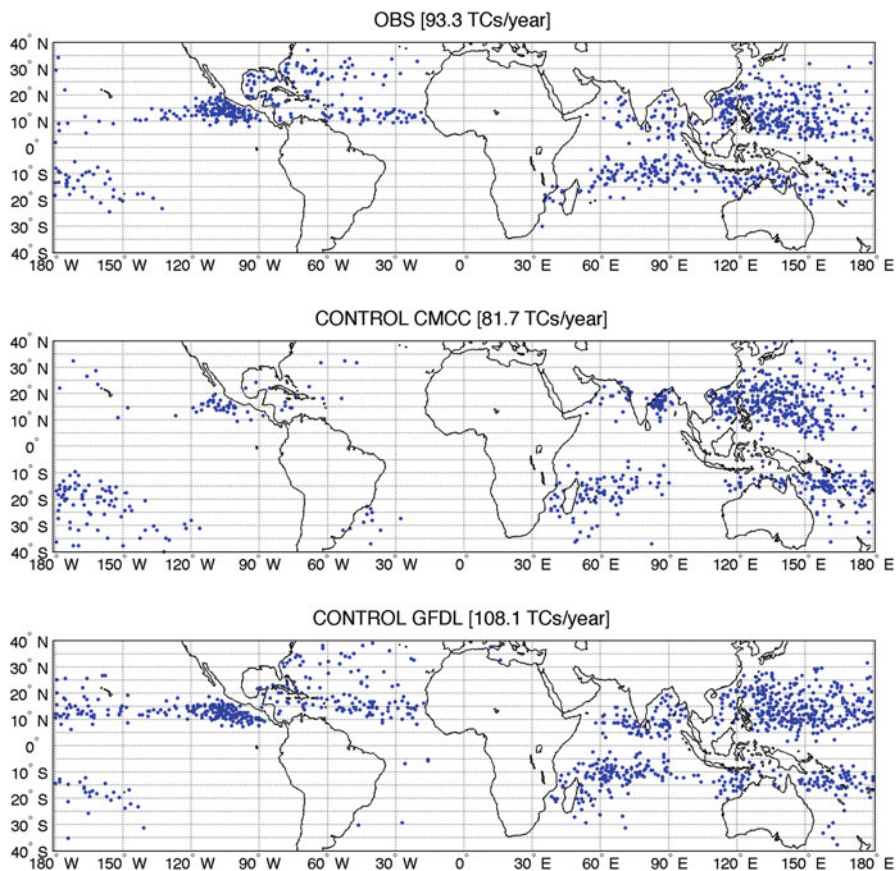
Fig. 10.4 TC genesis points in CMCC (*central* panel) and GFDL (*lower* panel) models, compared to the observations (*upper* panel) over the period 1981–1990

climate, we expect an increase in the water amount associated with phenomena leading to intense precipitation (such as TCs) larger than what it is expected in moderate events (Scoccimarro et al. 2013).

Our results show that the TC-associated precipitation is increased in the experiments with a 2K-SST increase. On the other hand, in the simulation with doubling of atmospheric CO_2, the changes in TC rainfall are small and we found that, on average, the simulated TC rainfall tends to decrease compared to the present-day climate (Fig. 10.4). Since environmental humidity was found to correlate with a larger hurricane rain field (Matyas 2010), and because we should expect a strong relationship between changes in available precipitable water and changes in TC precipitation, we investigated changes in the vertically integrated atmospheric water vapor content under the different idealized warming scenarios. All the

considered experiments show an increase in the water content over the tropical belt. The water content percentage increase (not shown here, see Scoccimarro et al. (2014), their Fig. 8) is about 1 % in 2C, 18 % in 2K, and 19 % in 2C2K, suggesting that the 1 % increment between 2K and 2C2K is mainly due to the higher atmospheric capability to hold moisture induced by the doubling of CO_2, as shown in the 2C experiment. According to the Clausius–Clapeyron relationship, the lower-tropospheric temperature change found in the different experiments (about 0.1 K in the 2C, 2.2 K in the 2K, and 2.4 K in the 2C2K) should lead to a water content increase of about 1 %, 18 %, and 19 %, respectively, which is fully consistent with that obtained from the models.

Despite the increase in water content in all of the three warming experiments, the doubling of CO_2 tends to reduce TCP, whereas the increase of 2K in SST tends to increase TCP. The reason should be found in the water balance at the surface: in 2K and 2C2K experiments (2Ks), we found a strong increase of the evaporation rate over the tropics (Fig. 10.5, left panel, green and red lines, respectively) due to the increase in saturated water vapor pressure at the surface. The 2K increase in SST leads to a net increase of the evaporation rate (E). This can be easily explained considering that E is proportional to the difference between saturated water vapor at the surface (es) and water vapor pressure of the lower tropospheric layers (ea) and that es depends on surface temperature following an exponential law, whereas ea follows the same law, scaled by a factor (less than 1) represented by the relative humidity. Therefore, an increase in temperature has different impacts on es and ea. The doubling of CO_2, on the other hand, tends to reduce E (Fig. 10.5, blue line) independently of the boundary conditions. The doubling of CO_2 in forced experiments (prescribed SST) induces a weakening effect on E, since the increase in the lower tropospheric temperature leads to an increase in ea, associated with no changes in es due to the fixed temperature forcing at the surface. This effect results in an increase of the atmospheric static stability in the 2C experiment.

The CO_2 doubling tends to slow down the global hydrological cycle by about 2 % (see Table 2 in Scoccimarro et al. 2014). This is also evident in the meridional distribution of evaporation and precipitation changes (blue lines in Fig. 10.5 left and right panels, respectively) during the TC season. The 2K SST increase induces an acceleration of the hydrological cycle of the order of 6–7 % that is reduced to 4–5 % if associated with the CO_2 doubling (Fig. 10.5). The changes found in the hydrological cycle are strongly influenced by the TC precipitation: a 4 %/6 % (2C2K/2K) increase in the average precipitation corresponds to an increase of about 20 %/30 % in TC-related precipitation.

In summary, bearing in mind the limitation of the considered models in representing tropical convection (Lim et al. 2014), and the difficulty to provide a measure of reliability due to the low number of models involved (just two), the precipitation
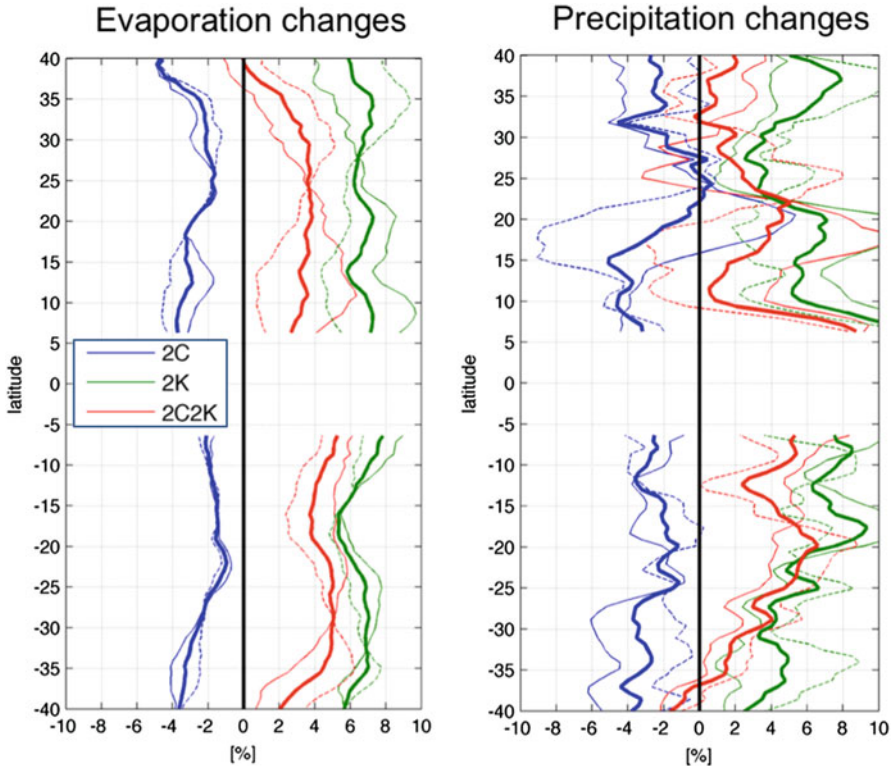
Fig. 10.5 Changes in evaporation (*left* panel) and precipitation (*right* panel) in 2C (*blue*), 2K (*green*) and 2C2K (*red*) experiments as a function of latitude with respect to the CLIM experiment. *Solid thin lines* represent CMCC results. *Dashed thin lines* represent GFDL results. *Solid thick lines* represent averaged values. Northern Hemisphere values are computed over June–November and Southern Hemisphere values are computed over December–May. Units are [%]

associated with TCs results in an increase in the experiments with a 2K-SST increase and to a decrease when atmospheric CO2 is doubled. This is consistent with the water balance at the surface, as a 2K increase in SST leads to a net increase of the evaporation rate, while doubling the atmospheric CO2 has the opposite effect.

Unexpectedly, between 7 and 12° in the Southern Hemisphere, the 2C2K experiment shows a reduction of the TC-associated precipitation. This feature will be the object of future work.

As already mentioned, the TCPn increase projected in all of the considered 2K-SST warming scenarios is more pronounced over land than what is expected considering also the TC path over the ocean (Fig. 10.4). It is well known that in some cases, during landfall, the TC precipitation tends to increase (Dong et al. 2010). This is mainly due to the lifting effect induced by orographic features (Huang et al. 2013). In our 2K-SST warming experiment, the more pronounced increase of
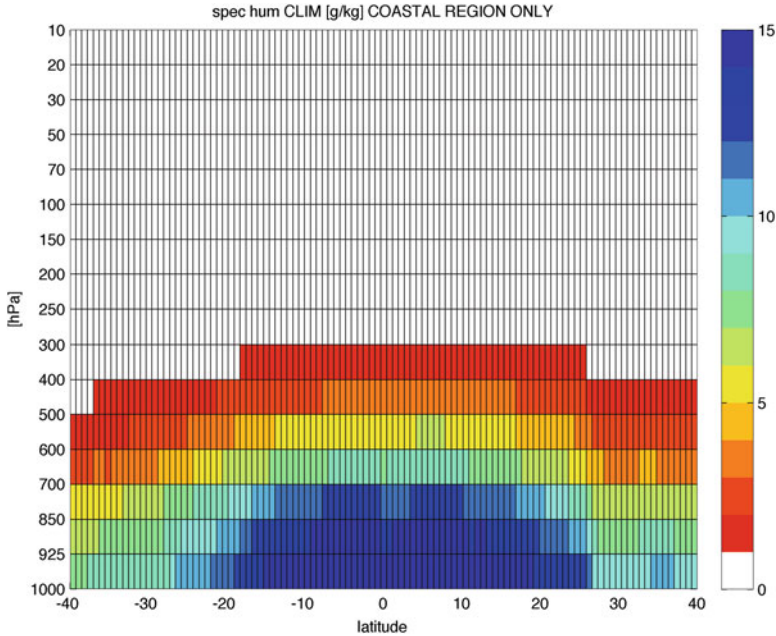
Fig. 10.6 Meridional distribution of the specific humidity in CLIM experiment during the TC season (June–November for the Northern Hemisphere and December–May for the Southern Hemisphere) considering coastal region only. Ensemble averages are shown. Units are [g/kg]

the precipitation over land might be related to an additional lifting effect on the TC-associated air masses, when landfall occurs. Keeping in mind the possibility of an induced lifting effect source, we examined how humidity of the air is projected to change in the considered 2K-SST experiments. The specific humidity over the coastal regions (Fig. 10.6) in the CLIM experiment is very similar to what is found over the entire domain including its ocean portion, with differences of the order of mg/Kg (not shown). In the 2C experiment, no significant differences are found in the specific humidity over land (Fig. 10.7, upper panel). On the other hand, the two experiments implying 2K-SST warming show substantial changes in the meridional distribution of the specific humidity: in the first levels of the atmospheric column (between the surface and 300 hPa), there are positive changes, over most of the tropical latitudes (Fig. 10.7 central and lower panels): the specific humidity increase is up to 20 % of the CLIM value. The more pronounced increase in TCPn over land in 2K-SST experiments is consistent with such specific humidity increase in the lower levels of the atmospheric column: TCs at landfall are projected to encounter a less stable atmospheric column, since the air at the lower levels is wetter in this experiment due to increased SSTs. A more unstable atmospheric column, induced by the availability of more moist air at low levels, leads to increased updrafts, thus to an increased condensation into droplets.
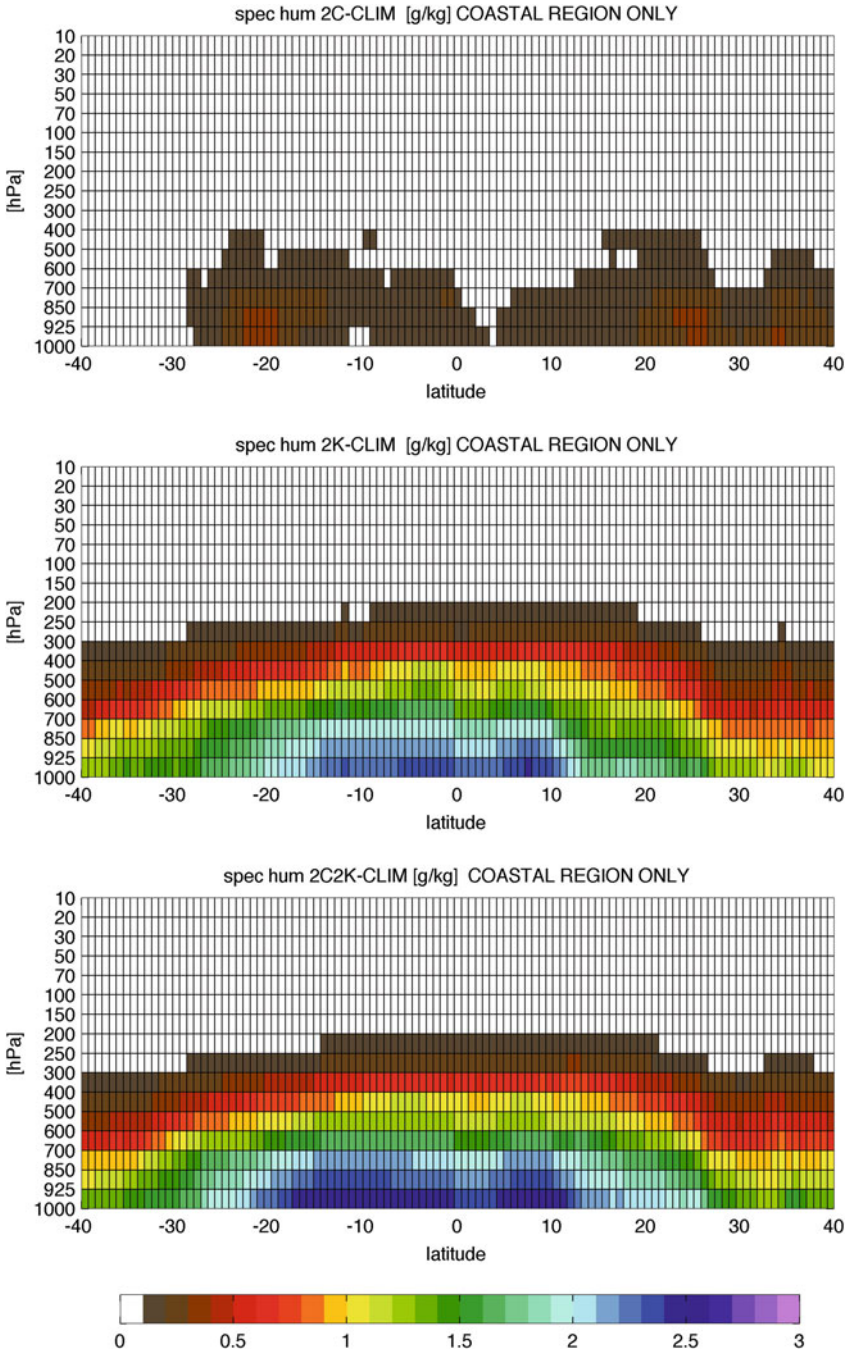
Fig. 10.7 Meridional distribution of the specific humidity changes during the TC season (June–November for the Northern Hemisphere and December–May for the Southern Hemisphere). Figure shows specific humidity changes in the three different scenarios (2C/2K/2C2K in *upper-right/central-right/lover-right* panels), compared to the CLIM experiment. Only land regions are considered. Ensemble averages are shown. Units are [g/kg]

References

Allen MR, Ingram WJ (2002) Constraints on future changes in climate and the hydrologic cycle. Nature 419:224–232. doi:10.1038/nature01092

Bolvin DT, Adler RF, Huffman GJ et al (2009) Comparison of GPCP monthly and daily precipitation estimates with high-latitude gauge observations. J Appl Meteorol Climatol 48:1843–1857. doi:10.1175/2009JAMC2147.1

Dong M, Chen L, Li Y, Lu C (2010) Rainfall reinforcement associated with landfalling tropical cyclones. J Atmos Sci 67:3541–3558. doi:10.1175/2010JAS3268.1

Held IM, Soden BJ (2006) Robust responses of the hydrological cycle to global warming. J Climate 19:5686–5699. doi:10.1175/JCLI3990.1

Horn M, Walsh K, Zhao M et al (2014) Tracking scheme dependence of simulated tropical cyclone response to idealized climate simulations. J Climate 27:9197–9213. doi:10.1175/JCLI-D-14-00200.1

Huang H-L, Yang M-J, Sui C-H (2013) Water budget and precipitation efficiency of typhoon Morakot (2009). J Atmos Sci 71:112–129. doi:10.1175/JAS-D-13-053.1

Huffman GJ, Adler RF, Morrissey MM et al (2001) Global precipitation at one-degree daily resolution from multisatellite observations. J Hydrometeorol 2:36–50. doi:10.1175/1525-7541(2001)002<0036:GPAODD>2.0.CO;2

JTWC (2013) Annual tropical cyclone report. Joint Typhoon Warning Center, Pearl Harbor

Knutson TR, Manabe S (1995) Time-mean response over the tropical pacific to increased C02 in a coupled Ocean-Atmosphere Model. J Climate 8:2181–2199. doi:10.1175/1520-0442(1995)008<2181:TMROTT>2.0.CO;2

Knutson TR, McBride JL, Chan J et al (2010) Tropical cyclones and climate change. Nat Geosci 3:157–163. doi:10.1038/ngeo779

Knutson TR, Sirutis JJ, Vecchi GA et al (2013) Dynamical downscaling projections of twenty-first-century Atlantic hurricane activity: CMIP3 and CMIP5 model-based scenarios. J Climate 26:6591–6617. doi:10.1175/JCLI-D-12-00539.1

Kunkel KE, Easterling DR, Kristovich DAR et al (2010) Recent increases in U.S. heavy precipitation associated with tropical cyclones. Geophys Res Lett. doi:10.1029/2010GL045164

Landsea CW, Franklin JL (2013) Atlantic hurricane database uncertainty and presentation of a new database format. Mon Weather Rev 141:3576–3592. doi:10.1175/MWR-D-12-00254.1

Larson J, Zhou Y, Higgins RW (2005) Characteristics of landfalling tropical cyclones in the United States and Mexico: climatology and interannual variability. J Climate 18:1247–1262. doi:10.1175/JCLI3317.1

Lim Y-K, Schubert SD, Reale O et al (2014) Sensitivity of tropical cyclones to parameterized convection in the NASA GEOS-5 model. J Climate 28:551–573. doi:10.1175/JCLI-D-14-00104.1

Lonfat M, Marks FD, Chen SS (2004) Precipitation distribution in tropical cyclones using the Tropical Rainfall Measuring Mission (TRMM) microwave imager: a global perspective. Mon Weather Rev 132:1645–1660. doi:10.1175/1520-0493(2004)132<1645:PDITCU>2.0.CO;2

Matyas CJ (2010) Associations between the size of hurricane rain fields at landfall and their surrounding environments. Meteorol Atmos Phys 106:135–148. doi:10.1007/s00703-009-0056-1

Meehl GA, Stocker TF, Collins WD et al (2007) Global climate projections. In: Solomon S, Qin D, Manning M et al (eds) Climate change 2007: the physical science basis. Cambridge University Press, Cambridge, UK, pp 748–845

Mendelsohn R, Emanuel K, Chonabayashi S, Bakkensen L (2012) The impact of climate change on global tropical cyclone damage. Nat Clim Chang 2:205–209. doi:10.1038/nclimate1357

Pielke RA Jr, Gratz J, Landsea CW et al (2008) Normalized hurricane damage in the United States: 1900–2005. Nat Hazards Rev 9:29–42. doi:10.1061/(ASCE)1527-6988(2008)9:1(29)

Rappaport EN (2000) Loss of life in the United States associated with recent Atlantic Tropical Cyclones. Bull Am Meteorol Soc 81:2065–2073. doi:10.1175/1520-0477(2000)081<2065:LOLITU>2.3.CO;2

Roeckner E, Bäuml G, Bonaventura L et al (2003) The atmospheric general circulation model ECHAMM5. Part 1: model description. Max-Planck-Institut für Meteorologie, Hamburg

Scoccimarro E, Gualdi S, Bellucci A et al (2011) Effects of tropical cyclones on ocean heat transport in a high-resolution coupled general circulation model. J Climate 24:4368–4384. doi:10.1175/2011JCLI4104.1

Scoccimarro E, Gualdi S, Bellucci A et al (2013) Heavy precipitation events in a warmer climate: results from CMIP5 models. J Climate 26:7902–7911. doi:10.1175/JCLI-D-12-00850.1

Scoccimarro E, Gualdi S, Villarini G et al (2014) Intense precipitation events associated with landfalling tropical cyclones in response to a warmer climate and increased CO_2. J Climate 27:4642–4654. doi:10.1175/JCLI-D-14-00065.1

Shaevitz DA, Camargo SJ, Sobel AH et al (2014) Characteristics of tropical cyclones in high-resolution models in the present climate. J Adv Model Earth Syst 6:1154–1172. doi:10.1002/2014MS000372

Villarini G, Lavers DA, Scoccimarro E et al (2014) Sensitivity of tropical cyclone rainfall to idealized global-scale forcings. J Climate 27:4622–4641. doi:10.1175/JCLI-D-13-00780.1

Walsh K, Lavender S, Scoccimarro E, Murakami H (2013) Resolution dependence of tropical cyclone formation in CMIP3 and finer resolution models. Clim Dyn 40:585–599. doi:10.1007/s00382-012-1298-z

Walsh KJE, Camargo SJ, Vecchi GA et al (2015) Hurricanes and climate: the U.S. CLIVAR Working Group on hurricanes. Bull Am Meteorol Soc 96:997–1017. doi:10.1175/BAM-S-D-13-00242.1

Zhao M, Held IM, Lin S-J, Vecchi GA (2009) Simulations of global hurricane climatology, interannual variability, and response to global warming using a 50-km resolution GCM. J Climate 22:6653–6678. doi:10.1175/2009JCLI3049.1